

Dissertation zur Erlangung des Doktorgrades
der Fakultät für Chemie und Pharmazie
der Ludwig-Maximilians-Universität München

**Biomimetic hydroxylation catalysis
with bis(pyrazolyl)methane copper peroxo complexes
and structural studies on
transition metal bis(pyrazolyl)methane complexes**

Claudia Gerlinde Wilfer

aus

Dachau

2015

Erklärung

Diese Dissertation wurde im Sinne von §7 der Promotionsordnung vom 28. November 2011 von Frau Prof. Dr. Herres-Pawlis betreut.

Eidesstattliche Versicherung

Diese Dissertation wurde eigenständig und ohne unerlaubte Hilfe erarbeitet.

München, den 23.02.2015

.....

Dissertation eingereicht am 24.02.2015

1. Gutachterin: Prof. Dr. Sonja Herres-Pawlis

2. Gutachter: Prof. Dr. Peter Klüfers

Mündliche Prüfung am 26.03.2015

Kurzzusammenfassung

Im Hinblick auf die Entwicklung biomimetischer Tyrosinasemodelle wurde im Rahmen dieser Arbeit $\text{HC}(3\text{-}t\text{BuPz})_2(1\text{-MeIm})$ als Bis(pyrazolyl)methan-Ligand zweiter Generation entwickelt, der in der Lage ist, den Cu_2O_2 -Peroxo-Komplex $(\mu\text{-}\eta^2:\eta^2)\text{-}[\text{Cu}_2\text{O}_2\{\text{HC}(3\text{-}t\text{BuPz})_2(1\text{-MeIm})\}_2][\text{SbF}_6]_2$ zu stabilisieren. Er konnte sowohl UV/Vis- und röntgenabsorptionsspektroskopisch als auch massenspektrometrisch nachgewiesen werden. Hierbei wurde eine Blau-Verschiebung der für Komplexe dieser Art bekannten Charge-Transfer-Banden beobachtet. Dieser Effekt wurde mit dichtefunktionaltheoretischen Methoden untersucht und zeigte eine starke Donorfähigkeit der Imidazolyl-Einheit des Liganden als Ursache. Es wurde festgestellt, dass der Komplex $[\text{Cu}_2\text{O}_2\{\text{HC}(3\text{-}t\text{BuPz})_2(1\text{-MeIm})\}_2][\text{SbF}_6]_2$ außerdem eine effiziente Oxidations- und Oxygenierungsfähigkeit aufweist. In Analogie zur Tyrosinase konnte die selektive Übertragung eines Sauerstoffatoms auf verschiedene Substrate nach dem auch bei der Tyrosinase vorherrschenden "*inner-sphere*" Sauerstoffatomtransfermechanismus bewiesen werden. Neben dem neu entwickelten Liganden $\text{HC}(3\text{-}t\text{BuPz})_2(1\text{-MeIm})$ wurde der bekannte Ligand $\text{HC}(3\text{-}t\text{BuPz})_2(\text{Qu})$ auf sein Sauerstoffaktivierungspotential sowie seine Sauerstoffübertragungsfähigkeit getestet. Hierbei konnte eine sich langsamer bildende, aber ebenfalls zur Sauerstoffaktivierung und dem π -transfer befähigte, Cu_2O_2 -Peroxo Spezies charakterisiert werden. Aufbauend auf einer bereits existierenden Ligandenbibliothek wurde der *iso*-Propyl Substituent an den Pyrazolyl-Einheiten eingeführt und so die Liganden $\text{HC}(3\text{-}i\text{PrPz})_2(\text{Py})$ und eine Mischung aus $\text{HC}(3\text{-}i\text{PrPz})_2(\text{Qu})$ und $\text{HC}(3\text{-}i\text{PrPz})(5\text{-}i\text{PrPz})(\text{Qu})$ erhalten. Während der Synthese wurde der Effekt der Isomerisierung von Alkylgruppen an diesen Systemen von der 3- in die 5-Position beobachtet und ein Protokoll zur Rückisomerisierung eingeführt. Des Weiteren wurden acht monofaciale Bis(pyrazolyl)methan-Komplexe mit den Übergangsmetallen Kupfer, Cobalt und Zink, sowie drei bisfaciale Cobalt-Bis(pyrazolyl)methan-Komplexe synthetisiert und charakterisiert. Die monofacialen Komplexe wurden eingehend dichtefunktionaltheoretisch untersucht und dabei eine Donorkonkurrenz zwischen Pyrazolyl- und Pyridinyl- bzw. Quinolinyl- oder Imidazolyl-Einheiten festgestellt. Drei monofaciale Nitratkomplexe wiesen außerdem eine seltene Mischung aus mono- und bidentat gebundenen Nitratgruppen in einem Komplex auf. Im Hinblick auf die Aktivierung von anderen kleinen Molekülen wie Stickstoffmonoxid bestätigten erste Versuche mit dem NO-Donorreagenz Diazald®, dessen NO-Übertragungsfähigkeit auf einen Bis(pyrazolyl)methan-Kupferkomplex.

Abstract

With regard to the development of a biomimetic tyrosinase model, HC(3-*t*BuPz)₂(1-Melm) was developed in this thesis as an example for a second generation bis(pyrazolyl)methane ligand that is capable of stabilising the Cu₂O₂-peroxo complex $(\mu-\eta^2:\eta^2)$ -[Cu₂O₂{HC(3-*t*BuPz)₂(1-Melm)}₂][SbF₆]₂. This compound could be verified UV/Vis and X-Ray absorption spectroscopically as well as mass spectrometrically, showing a blue-shift in the UV/Vis bands compared to other known complexes of this kind. This effect was investigated by means of density functional theory calculations and attributed to the strong donor ability of the imidazolyl moiety at the ligand. Furthermore the [Cu₂O₂{HC(3-*t*BuPz)₂(1-Melm)}₂][SbF₆]₂ complex exhibits an efficient oxidation- as well as oxygenation ability. In analogy to tyrosinase, the selective oxygen atom transfer (OAT) onto different substrates according to the inner-sphere OAT mechanism was shown.

In addition to the newly designed HC(3-*t*BuPz)₂(1-Melm) ligand, the already established HC(3-*t*BuPz)₂(Qu) ligand was tested for its oxygen activation and -transfer potential. Hereby a slowly forming Cu₂O₂-peroxo species, which is also able to activate and transfer oxygen, was characterised.

Based on the already existing ligand library, the *isopropyl* substituent was introduced to the pyrazolyl moieties leading to the ligands HC(3-*i*PrPz)₂(Py) and a mixture of HC(3-*i*PrPz)₂(Qu) and HC(3-*i*PrPz)(5-*i*PrPz)(Qu). During the synthesis of these ligands the isomerisation effect of the alkyl groups from 3- to 5-position of the pyrazolyl unit was observed and a protocol for their reisomerisation was established.

Moreover eight monofacial bis(pyrazolyl)methane complexes with the transition metals copper, cobalt and zinc as well as three bisfacial cobalt-bis(pyrazolyl)methane complexes were synthesised and characterised. The monofacial complexes were investigated by means of density functional theory (DFT), including structural optimisation and NBO calculations. Here a donor competition between pyrazolyl and pyridinyl, quinolinyl or imidazolyl substituents, respectively, was observed. Three monofacial nitrate complexes exhibit a rare mixture of monofacially and bisfacially bound nitrate groups in one complex.

Concerning the activation of another small molecule, first experiments with the NO donor reagent diazald® confirmed its ability to transfer NO onto a bis(pyrazolyl)methane copper complex.

Danksagung

Mein besonderer Dank gilt Prof. Dr. Sonja Herres-Pawlis für die Möglichkeit, mich während meiner Dissertation in ihrem Arbeitskreis mit diesem interessanten und vielfältigen Thema beschäftigen zu dürfen. Ich konnte dadurch Einblick in verschiedene Gebiete sowie Analysemethoden erlangen. Des Weiteren danke ich für die hilfreichen Anregungen, sowie die stetige Unterstützung und intensive Betreuung. Außerdem bedanke ich mich für die Möglichkeit des Besuches zahlreicher Tagungen in In- und Ausland, bei denen ich Erfahrung sammeln und Anregungen mitnehmen konnte.

Bei Prof. Dr. Peter Klüfers möchte ich mich besonders für die Übernahme des Zweitgutachtens bedanken.

Prof. Dr. Peter Klüfers, Prof. Dr. Hans-Christian Böttcher, Prof. Dr. Anja Hoffmann-Röder, Prof. Dr. Konstantin Karaghiosoff und Dr. Thomas Magauer danke ich für ihren Beisitz im Prüfungskomitee.

Dr. Alexander Hoffmann gilt mein Dank für die Einführung in das Thema dieser Arbeit, sowie seine Vorarbeit auf diesem Gebiet, sodass ich auf bereits bestehendem Wissen aufbauen konnte. Des Weiteren danke ich für das Lösen aller Kristallstrukturen und die Durchführung zahlreicher theoretischer Rechnungen. Außerdem danke ich herzlich für das Lesen und die Korrektur dieser Arbeit.

Prof. Dr. Ivana Ivanović-Burmazović von der Friedrich-Alexander-Universität Erlangen-Nürnberg gilt mein Dank für die Zusammenarbeit im Bereich der Cryo-UHR ESI Spektrometrie. Besonders danke ich M. Dürr für die Durchführung der Messungen in diesem Bereich.

Prof. Dr. Matthias Bauer sowie R. Schepper und R. Dick von der Universität Paderborn danke ich für die Durchführung der Messungen im Bereich der Röntgenabsorptionsspektroskopie.

Der Analytikabteilung des Departments Chemie und Pharmazie der LMU München danke ich für die Durchführung von NMR-Analytik, Massenspektrometrie und Elementaranalyse.

Besonderer Dank gilt Dr. P. Mayer für das röntgenkristallographische Vermessen zahlreicher Proben.

Ich danke all meinen ehemaligen und aktuellen Kollegen für das gute Arbeitsklima und die dadurch sehr angenehme und schöne Zeit während meiner Promotion: Anton, Mouala, Ramona, Britta, Ulrich, Katharina, Julian, Thomas, Patricia, Angela, Julia, Johannes, Robert und Kerstin.

Darüber hinaus gilt mein Dank Ulrich und Katharina für das gründliche und gewissenhafte Lesen meiner Dissertation.

Bei all meinen Praktikanten möchte ich mich für die motivierte und sehr gute Zusammenarbeit bedanken, die unter anderem zum Gelingen dieser Dissertation beigetragen hat.

Uli, Kathy, Mouala und Anton danke ich dafür, dass sie mir auch abseits der Arbeit zu guten Freunden geworden sind.

Meinen Freunden Amelie, Lydia, Francisco, Konstantin, Anna und Jens danke ich für die gegenseitige Unterstützung während des Studiums, sowie die gemeinsamen Urlaube und vielen schönen Abende.

Judith danke ich für ihre Freundschaft seit über 20 Jahren, in denen wir einiges zusammen erlebt haben und dafür, dass sie mein Sport-„Buddy“ ist.

Von ganzem Herzen danke ich meinen Eltern für ihre Liebe und bedingungslose Unterstützung während meines gesamten Studiums.

*Unsere Wünsche sind Vorgefühle der Fähigkeiten, die in uns liegen,
Vorboten desjenigen, was wir zu leisten imstande sein werden.*

Johann Wolfgang von Goethe

Abbreviations

aliph	aliphatic
arom	aromatic
d	doublet (NMR)
DFT	density functional theory
EA	elemental analysis
ESI	electrospray ionisation (MS)
Et	ethyl
EXAFS	extended X-ray absorption fine structure
FAB	fast atom bombardment (MS)
<i>i</i> Pr	<i>isopropyl</i>
IR	infrared spectroscopy
<i>J</i>	coupling constant (NMR)
M	molar mass
m	multiplet (NMR), medium (IR)
Me	methyl
MeCN	acetonitrile
MS	mass spectrometry
NBO	natural bond orbital
<i>n</i> Bu	<i>n</i> -butyl
NMR	nuclear magnetic resonance spectroscopy
NTO	natural transition orbital
OTf	triflate, trifluoromethanesulphonate
Ph	phenyl
ppm	parts per million
Py	pyridinyl rest
Pz	pyrazolyl rest
Qu	quinolinyl rest
R	alkyl rest
rt	room temperature
s	singlet (NMR), strong (IR)

sept	septet (NMR)
t	triplet (NMR)
<i>t</i> Bu	<i>tert</i> butyl
TD-DFT	time-dependent density functional theory
THF	tetrahydrofuran
UHR	ultra high resolution
vs	very strong (IR)
vw	very weak (IR)
w	weak (IR)
XANES	X-ray absorption near edge structure
XAS	X-ray absorption spectroscopy
δ	chemical shift (NMR)
ν	stretching vibration (IR)
ρ	structural parameter
$\tilde{\nu}$	wave number (IR)

List of contents

With * marked compounds are already known and have been resynthesised.

Ligands

L1	HC(3- <i>t</i> BuPz) ₂ (1-Melm)	L4'	HC(3- <i>i</i> PrPz)(5- <i>i</i> PrPz)(Qu)
L2*	HC(3- <i>t</i> BuPz) ₂ (Qu)	L5*	HC(3- <i>t</i> BuPz) ₂ (Py)
L3	HC(3- <i>i</i> PrPz) ₂ (Py)	L6*	HC(Pz) ₂ (Py)
L3'	HC(3- <i>i</i> PrPz)(5- <i>i</i> PrPz)(Py)	L7*	HC(Pz) ₂ (Qu)
L4	HC(3- <i>i</i> PrPz) ₂ (Qu)		

Complexes

C1	[CuCl ₂ {HC(3- <i>t</i> BuPz) ₂ (1-Melm)}]	C7	[Zn(NO ₃) ₂ {HC(3- <i>i</i> PrPz) ₂ (Py)}]
C2	[CuCl{HC(3- <i>t</i> BuPz) ₂ (Qu)}]	C8	[Co{HC(Pz) ₂ (Py)} ₂][Co(NO ₃) ₄]
C3	[CuCl{HC(3- <i>t</i> BuPz) ₂ (Py)}]	CC8²⁺	[Co{HC(Pz) ₂ (Py)} ₂] ²⁺
C4	[CuBr ₂ {HC(3- <i>t</i> BuPz) ₂ (Py)}]	C9	[Co{HC(Pz) ₂ (Qu)} ₂][OTf] ₂
CC4*	[CuCl ₂ {HC(3- <i>t</i> BuPz) ₂ (Py)}]	C10	[Co{HC(3- <i>i</i> PrPz) ₂ (Qu)} ₂][(NO ₃) ₂]
C5	[Co(NO ₃) ₂ {HC(3- <i>t</i> BuPz) ₂ (Py)}]	C11*	[CoCl ₂ {HC(3- <i>t</i> BuPz) ₂ (Py)}]
C6	[Co(NO ₃) ₂ {HC(3- <i>i</i> PrPz) ₂ (Py)}]		

Table of Figures

Figure 1. Structures of type I, II and III copper enzymes.	4
Figure 2. A, active centre of the met-form of tyrosinase complexed with ORF 378. B, active centre of the inhibitor-bound potato catechol oxidase. C, active centre of the oxy-form of octopus hemocyanin. ^[34]	5
Figure 3. O ₂ -derived metalloenzyme intermediates, structurally characterised by X-ray crystallography.	11
Figure 4. Left side: Structure of β -ketiminate ligands as used by Tolman. ^[65] ; right side: Structure of bidentate (1) and tridentate (2) 2-(2-pyridyl)ethylamin ligands as used by Itoh. ^[64]	13
Figure 5. Structure of peralkylated diamine ligands (L ^{PDA}) as used by Stack. ^[63]	14
Figure 6. Top: Structure of bis- μ -oxo copper(III)-species with ligands TMPD, DMPD and PD.; bottom: active centre of particulate methane monooxygenase (pMMO). ^[70]	14
Figure 7. Structure of <i>N,N,N',N',N''</i> -pentakis[(1-methyl-2-benzimidazolyl)methyl] dipropylene-triamine (8) and <i>N,N</i> -bis(2- <i>N</i> -methylbenzimidazol-2-yl)ethyl)benzylamine (9) as used by Casella. ^{[71][72]}	15
Figure 8. Structures of an imine/pyridine (10), a bis(imine) (11), a bis(pyridine) (12), a benzimidazole/imine (13), an imine/pyridine containing ligand with biphenyl spacer (14) and a bis(pyrazolyl)(pyridinyl)methane ligand (15, L5). ^[18,77-79]	16
Figure 9. Coordination motives of the reaction of Co(II) species with oxygen. ^[83]	20
Figure 10. Structure of the corrin ring.....	20
Figure 11. Structure of Co(tpy) ₂ and [CoCl ₄] ²⁻ . ^[83]	21
Figure 12. Structure of tris(pyrazolyl)borate and tris(pyrazolyl)methane.	23
Figure 13. Boat conformation of a bis(pyrazolyl)methane complex.....	25
Figure 14. Structure of bis(pyrazolyl)methane ligands with <i>N,S</i> -, <i>N,N'</i> - and <i>N,O</i> -donors.	26
Figure 15. Structure of “third generation” scorpionate ligands. ^[123]	27
Figure 16. Possible coordination modes of Cu(I) and Cu(II) bis(pyrazolyl)methane complexes.....	27
Figure 17. Imidazolyl containing ligands applied in the activation of oxygen. ^[128-130]	32
Figure 18. Molecular structure of L1.	34
Figure 19. Molecular structure of [CuCl ₂ {HC(3- <i>t</i> BuPz) ₂ (1-Melm)}] (C1).....	35
Figure 20. Electronic structure of the peroxide-Cu(II) bond in (μ - η^2 : η^2) bridged species. ^{adapted from[31]} ..	38
Figure 21. UV/Vis spectrum of [Cu ₂ O ₂ {HC(3- <i>t</i> BuPz) ₂ (1-Melm)} ₂][SbF ₆] ₂ (P1[SbF ₆] ₂).	40
Figure 22. Theoretical model of [Cu ₂ O ₂ {HC(3- <i>t</i> BuPz) ₂ (1-Melm)} ₂] ²⁺ (P1). (Gaussian09, TPSSh/6-31G(d). Hydrogen atoms are omitted for clarity). ^[135,137,141]	42
Figure 23. Calculated UV/Vis spectrum of [Cu ₂ O ₂ {HC(3- <i>t</i> BuPz) ₂ (1-Melm)} ₂][SbF ₆] ₂ (P1[SbF ₆] ₂) (TD-DFT, Gaussian09, TPSSh, 6-31G(d)). ^[135,137,141]	42
Figure 24. NTO-analysis of [Cu ₂ O ₂ {HC(3- <i>t</i> BuPz) ₂ (1-Melm)} ₂] ²⁺ (P1). ^[141]	44
Figure 25. Cryo UHR-ESI mass spectrum of [Cu ₂ O ₂ {HC(3- <i>t</i> BuPz) ₂ (1-Melm)} ₂][SbF ₆] ⁺ . ^[145]	46
Figure 26. Cu K-edge XANES spectrum of P1[SbF ₆] ₂ . ^[148]	47
Figure 27. Filtered Fourier backtransformed Cu K-edge EXAFS spectrum (black solid line: experiment, grey dashed line: fitted function) of P1[SbF ₆] ₂ . ^[148]	48
Figure 28. Structure of the active site of tyrosinase. Green: Carbon, blue: Nitrogen, orange: Copper, red: Oxygen. ^[34]	49
Figure 29. Reaction of <i>para</i> -substituted phenols with oxygen under Cu-catalysis. ^[80]	50

Figure 30. UV/Vis spectrum of the formation of $[\text{Cu}_2\text{O}_2\{\text{HC}(3\text{-tBuPz})_2(1\text{-Melm})\}_2][\text{SbF}_6]_2$ (orange) and the formation of the quinone (blue). Between 260 and 310 nm the spectrum does not follow Lambert Beer's law due to high concentration.	51
Figure 31. UV/Vis spectrum of the formation of $[\text{Cu}_2\text{O}_2\{\text{HC}(3\text{-tBuPz})_2(1\text{-Melm})\}_2][\text{SbF}_6]_2$ (black) and the formation of the quinone (all colours).....	52
Figure 32. Molecular structure of $[\text{CuCl}\{\text{HC}(3\text{-tBuPz})_2(\text{Qu})\}]$ (C2).....	55
Figure 33. Molecular structures of $[\text{CuCl}\{\text{HC}(3\text{-tBuPz})_2(\text{Py})\}]$ (C3a, b).	56
Figure 34. Molecular structure of $[\text{CuBr}_2\{\text{HC}(3\text{-tBuPz})_2(\text{Py})\}]$ (C4).	57
Figure 35. Molecular structure of CC4. ^[125]	57
Figure 36. UV/Vis spectrum of $[\text{Cu}_2\text{O}_2\{\text{HC}(3\text{-tBuPz})_2(\text{Qu})\}_2][\text{SbF}_6]_2$ (P2 $[\text{SbF}_6]_2$) (red: experimental, black: theoretical ^[141]) and the final UV/Vis spectrum of the formation of the quinone in the self-assembly mode (green) ^[168]	64
Figure 37. Pseudo-first order plot for the determination of the rate constant of the formation of P1. Red: linear fit (R = 0.997).....	65
Figure 38. NTO-analysis of $[\text{Cu}_2\text{O}_2\{\text{HC}(3\text{-tBuPz})_2(\text{Qu})\}_2]^{2+}$ (P2). ^[141]	66
Figure 39. Molecular structures of $[\text{Co}(\text{NO}_3\text{-}\kappa\text{O})(\text{NO}_3\text{-}\kappa^2\text{OO}')\{\text{HC}(3\text{-tBuPz})_2(\text{Py})\}]$ (C5) and $[\text{Co}(\text{NO}_3\text{-}\kappa\text{O})(\text{NO}_3\text{-}\kappa^2\text{OO}')\{\text{HC}(3\text{-iPrPz})_2(\text{Py})\}]$ (C6).....	70
Figure 40. Molecular structure of $[\text{Co}(\text{NO}_3\text{-}\kappa\text{O})(\text{NO}_3\text{-}\kappa^2\text{OO}')\{\text{HC}(3\text{-iPrPz})_2(\text{Py})\}]$ (C6).	71
Figure 41. Quantification of the binding mode for the nitrate groups. ^[175]	74
Figure 42. Structure of NO transferring reagents diazald® and tritylthionitrite (TTN).	79
Figure 43. Experimental UV/Vis spectra of the reaction of $[\text{Cu}\{\text{HC}(3\text{-tBuPz})_2(\text{Py})\}]^+$ with nitrosobenzene.....	80
Figure 44. Structural optimisation of singlet $[\text{Cu}\{\text{HC}(3\text{-tBuPz})_2(\text{Py})\}(\text{PhNO-}\kappa\text{O})]^+$ and $[\text{Cu}\{\text{HC}(3\text{-tBuPz})_2(\text{Py})\}(\text{PhNO-}\kappa\text{N})]^+$ (B3LYP, 6-31G(d), Gaussian09). ^[186]	81
Figure 45. UV/Vis spectra of the reaction of $[\text{Cu}\{\text{HC}(3\text{-tBuPz})_2(\text{Py})\}]^+$ with diazald® (black) and NO gas (blue).	83
Figure 46. Expected reaction product of the reaction of $[\text{Cu}\{\text{HC}(3\text{-tBuPz})_2(\text{Py})\}]^+$ with NO donor agents.	83
Figure 47. Structures of ligands L1–L7 as well as L3' and L4'. With * marked ligands were resynthesised according to [117].	85
Figure 48. Molecular structures of $\text{HC}(3\text{-tBuPz})_2(\text{Qu})$ (L2) and $\text{HC}(3\text{-iPrPz})(5\text{-iPrPz})(\text{Py})$ (L3').	87
Figure 49. Molecular structure of $[\text{Co}\{\text{HC}(\text{Pz})_2(\text{Py})\}_2]^{2+}$ ^[194] (C8 ²⁺) in crystals of $[\text{Co}\{\text{HC}(\text{Pz})_2(\text{Py})\}_2][\text{Co}(\text{NO}_3)_4]$ (C8) and of $[\text{Co}\{\text{HC}(\text{Pz})_2(\text{Qu})\}_2]^{2+}$ (C9 ²⁺) in crystals of $[\text{Co}\{\text{HC}(\text{Pz})_2(\text{Qu})\}_2][(\text{OTf})_2]$ (C9). In C8 pyrazolyl and pyridinyl moieties are disordered. Here only one isomer is shown for clarity.....	89
Figure 50. Molecular structure of $[\{\text{HC}(3\text{-iPrPz})(5\text{-iPrPz})(\text{Qu})\}_2\text{Co}]^{2+}$ (C10 ²⁺) in crystals of $[\text{Co}\{\text{HC}(3\text{-iPrPz})(5\text{-iPrPz})(\text{Qu})\}_2][(\text{NO}_3)_2]$ (C10).	91
Figure 51. Molecular structure of $[\text{CoCl}_2\{\text{HC}(3\text{-tBuPz})_2(\text{Py})\}]$ (C11).....	92
Figure 52. Structures of newly synthesised bis(pyrazolyl)methane ligands L1, L3 and L4/L4'.	95
Figure 53. Structures of newly synthesised transition metal bis(pyrazolyl)methane complexes.....	97
Figure 54. Molecular structure of $\text{HC}(3\text{-tBuPz})_2(1\text{-Melm})$ (L1, top) and $[\text{CuCl}_2\{\text{HC}(3\text{-tBuPz})_2(1\text{-Melm})\}]$ (C1, bottom). Thermal ellipsoids represent 50% particular probability.	133
Figure 55. Molecular structure of $[\text{CuCl}\{\text{HC}(3\text{-tBuPz})_2(\text{Qu})\}]$ (C2, top) and $[\text{CuCl}\{\text{HC}(3\text{-tBuPz})_2(\text{Py})\}]$ (C3, bottom). Thermal ellipsoids represent 50% particular probability.....	135
Figure 56. Molecular structure of $[\text{CuBr}_2\{\text{HC}(3\text{-tBuPz})_2(\text{Py})\}]$ (C4, top) and $[\text{Co}(\text{NO}_3\text{-}\kappa\text{O})(\text{NO}_3\text{-}\kappa^2\text{OO}')\{\text{HC}(3\text{-tBuPz})_2(\text{Py})\}]\cdot\text{CH}_2\text{Cl}_2$ (C5, bottom). In C5 it was not possible to model the disordered	

solvent molecules of CH ₂ Cl ₂ in an adequate manner, so the data set was treated with the SQUEEZE facility of PLATON. ^[216,217] Thermal ellipsoids represent 50% particular probability.	137
Figure 57. Molecular structure of [Co(NO ₃ -κO)(NO ₃ -κ ² OO'){HC(3- <i>i</i> PrPz) ₂ (Py)}] (C6, top) and [Zn(NO ₃ -κO)(NO ₃ -κ ² OO'){HC(3- <i>i</i> PrPz) ₂ (Py)}] (C7, bottom). Thermal ellipsoids represent 50% particular probability.	139
Figure 58. Molecular structure of HC(3- <i>t</i> BuPz) ₂ (Qu) (L2, top) and of HC(3- <i>i</i> PrPz)(5- <i>i</i> PrPz)(Qu) (L3', bottom). In L2 three molecules are present, two of which have one threefold disordered <i>t</i> Bu-group each. Refinement of those was not possible due to the minor quality of the data set. Thermal ellipsoids represent 50% particular probability.	141
Figure 59. Molecular structure of [Co{HC(Pz) ₂ (Py)} ₂][Co(NO ₃) ₄]·C ₃ H ₆ O (C8, top) and of [Co{HC(Pz) ₂ (Qu)} ₂][(OTf) ₂] (C9, bottom). In C8 it was not possible to model the disordered solvent molecules of acetone in an adequate manner, the data set was treated with the SQUEEZE facility of PLATON. ^[216,217] Thermal ellipsoids represent 50% particular probability.	143
Figure 60. Molecular structure of [Co{HC(<i>i</i> PrPz) ₂ (Qu)} ₂][(NO ₃) ₂]·2MeOH (C10, top) and of [CoCl ₂ {HC(Pz) ₂ (Py)}]·THF (C11, bottom). Thermal ellipsoids represent 50% particular probability....	145
Figure 61. Overview of all newly synthesised bis(pyrazolyl)methane ligands and transition metal bis(pyrazolyl)methane complexes.....	145

Table of Schemes

Scheme 1. Monophenolase and diphenolase reaction, catalysed by tyrosinase. ^{adapted from [46]}	6
Scheme 2. Reaction of tyrosinase to dopaquinone, catalysed by tyrosinase. ^[49]	7
Scheme 3. Catalytic cycle of tyrosinase. ^[50,51]	8
Scheme 4. Left side: reaction of [Cu(HB(3,5- <i>i</i> Pr ₂ Pz) ₃)] with oxygen; right side: reaction of [Cu(TMPA)] with oxygen. ^[61,68]	12
Scheme 5. Reaction of [Cu(I)(R-PYAN)] with oxygen. ^[57]	18
Scheme 6. Reaction mechanism of NO-synthases. ^[88]	21
Scheme 7. Reactions of the microbial denitrification.	22
Scheme 8. Reaction scheme of the synthesis of substituted tris(pyrazolyl)methanes. ^[111]	25
Scheme 9. Reaction from pyrazole to bis(pyrazolyl)methane by using triphosgene and 2-hydroxybenzaldehyde. ^[116]	25
Scheme 10. Reaction mechanism of the Co-catalysed Peterson-like rearrangement.....	26
Scheme 11. Different routes for the synthesis of 1-methyl-2-imidazolecarboxaldehyde.	33
Scheme 12. Applied route for the synthesis of 1-methyl-2-imidazolecarboxaldehyde.....	33
Scheme 13. Synthesis of [HC(3- <i>t</i> BuPz) ₂ (1-Melm)] (L1).	34
Scheme 14. Synthesis of [CuCl ₂ {HC(3- <i>t</i> BuPz) ₂ (1-Melm)}] (C1).	35
Scheme 15. Synthesis of the precursor complex [Cu{HC(3- <i>t</i> BuPz) ₂ (1-Melm)}][SbF ₆].	39
Scheme 16. Formation of [Cu ₂ O ₂ {HC(3- <i>t</i> BuPz) ₂ (1-Melm)} ₂][SbF ₆] ₂ (P1[SbF ₆] ₂).	39
Scheme 17. Proposed reaction pathway for model complexes of tyrosinase. ^{adapted from [46]}	49
Scheme 18. Competitive pathways in catalytic aerobic oxidations of phenols. ^{adapted from [156]}	50
Scheme 19. Synthesis of [CuCl{HC(3- <i>t</i> BuPz) ₂ (Qu)}] (C2).	55
Scheme 20. Synthesis of [CuCl{HC(3- <i>t</i> BuPz) ₂ (Py)}] (C3a, b).	56
Scheme 21. Synthesis of [CuBr ₂ {HC(3- <i>t</i> BuPz) ₂ (Py)}] (C4).	56
Scheme 22. Oxygenation of Cu(I)-tris(1,2-dimethyl-1 <i>H</i> -imidazole) in 2-MeTHF. ^[144]	62
Scheme 23. Synthesis of [Cu ₂ O ₂ {HC(3- <i>t</i> BuPz) ₂ (Qu)} ₂][SbF ₆] ₂ (P2[SbF ₆] ₂).	63

Scheme 24. Synthesis of $[\text{Co}(\text{NO}_3\text{-}\kappa\text{O})(\text{NO}_3\text{-}\kappa^2\text{OO}')\{\text{HC}(3\text{-}t\text{BuPz})_2(\text{Py})\}]$ (C5), $[\text{Co}(\text{NO}_3\text{-}\kappa\text{O})(\text{NO}_3\text{-}\kappa^2\text{OO}')\{\text{HC}(3\text{-}i\text{PrPz})_2(\text{Py})\}]$ (C6) and	70
Scheme 25. Structure of tris(3,5-dimethyl(pyrazolyl))methylamine (21) and synthesis of $[\text{Ni}(21)(\text{O}_2\text{NO})][\text{NO}_3]$ (22) and $[\text{Cd}(21)(\text{O}_2\text{NO})(\text{ONO}_2)]$. ^{adapted from [174,175]}	73
Scheme 26. Synthesis of $[\text{Me}_6\text{trenCu}(\text{PhNO-}\kappa\text{O})]^+$ adapted from [184]	79
Scheme 27. Synthesis of $\text{HC}(3\text{-}i\text{PrPz})_2(\text{Py})$ (L3) and a mixture of $\text{HC}(3\text{-}i\text{PrPz})_2(\text{Qu})$ (L4) and $\text{HC}(3\text{-}i\text{PrPz})(5\text{-}i\text{PrPz})(\text{Qu})$ (L4').	86
Scheme 28. Synthesis of $[\text{Co}\{\text{HC}(\text{Pz})_2(\text{Py})\}_2][\text{Co}(\text{NO}_3)_4]$ (C8) and $[\text{Co}\{\text{HC}(\text{Pz})_2(\text{Qu})\}_2][(\text{OTf})_2]$ (C9).	88
Scheme 29. Synthesis of $[\text{Co}\{\text{HC}(3\text{-}i\text{PrPz})(5\text{-}i\text{PrPz})(\text{Qu})\}_2][(\text{NO}_3)_2]$ (C10).	90
Scheme 30. Synthesis of $[\text{CoCl}_2\{\text{HC}(3\text{-}t\text{BuPz})_2(\text{Py})\}]$ (C11). ^[125]	92

Tables

Table 1. Structural features of Cu_2O_2 and CuO_2 species. ^[55]	9
Table 2. Spectroscopic features of $(\mu\text{-}\eta^2\text{-}\eta^2)$ - and bis(μ -oxo)-complexes. ^[47,55]	10
Table 3. Overview of built species concerning the reaction of $[\text{Cu}(\text{I})(\text{R-PYAN})]$ with oxygen. Reactions were performed at -78°C . Content in brackets symbolises minor product. ^[57]	19
Table 4. Selected bond lengths and angles of L1.	35
Table 5. Selected bond lengths and angles for C1.	36
Table 6. Charge-transfer energies for C1 and P1. (Gaussian09, TPSSh/6-31G(d) and NBO 6.0). ^[135,137,142]	41
Table 7. Calculated atom distances in P1 (Gaussian09, TPSSh, 6-31G(d)). ^[135,137,141]	43
Table 8. Most important isotopes of $[\text{Cu}_2\text{O}_2\{\text{HC}(3\text{-}t\text{BuPz})_2(1\text{-MeIm})\}_2][\text{SbF}_6]^+$	45
Table 9. Structural parameters obtained by fitting the experimental EXAFS functions with theoretical models. ^[148]	48
Table 10. Catalytic efficiency of $[\text{Cu}_2\text{O}_2\{\text{HC}(3\text{-}t\text{BuPz})_2(1\text{-MeIm})\}_2][\text{SbF}_6]_2$ with phenolic substrates.	52
Table 11. Yield of catechol after treatment of $[\text{Cu}_2\text{O}_2\{\text{HC}(3\text{-}t\text{BuPz})_2(1\text{-MeIm})\}_2][\text{SbF}_6]_2$ with stoichiometric amounts of <i>para</i> -substituted phenol.	53
Table 12. Selected bond lengths [Å] of C2–C4 and CC4.	58
Table 13. Selected bond angles [°] of C2–C4 and CC4 and according τ -values.	59
Table 14. Calculated key bond lengths [Å] of C2–C4 and CC4 (Gaussian09, TPSSh/6-31G(d)). ^[135,137] ..	60
Table 15. Calculated key bond angles [°] of C2–C4 and CC4 (Gaussian09, TPSSh/6-31G(d)). ^[135,137]	61
Table 16. Charge-transfer energies [kcal mol^{-1}] for C2–C4, as well as CC4 and P2 (Gaussian09, TPSSh/6-31G(d) and NBO 6.0). ^[135,137,142]	61
Table 17. Selected bond lengths for C5, C6 and C7.	71
Table 18. Selected bond angles for C5, C6 and C7.	72
Table 19. Selected octahedron angles of C5–C7.	72
Table 20. Binding modes for nitrate groups of C5, C6 and C7.	75
Table 21. Charge-transfer energies [kcal mol^{-1}] for C5–C7 (Gaussian09, BP86/6-31G(d) and NBO 6.0). ^[135,142,162]	76
Table 22. NBO charge distribution in C5, C6 and C7 (Gaussian09, BP86/6-31G(d) and NBO 6.0). ^[135,142,162]	76
Table 23. Overview of extinction coefficients of the reaction of $[\text{Cu}\{\text{HC}(3\text{-}t\text{BuPz})_2(\text{Py})\}]^+$ with nitrosobenzene at $\lambda = 454$ and $\lambda = 558$ nm.	80

Table 24. TD-DFT calculated UV/Vis absorption maxima for singlet $[\text{Cu}\{\text{HC}(3\text{-}t\text{BuPz})_2(\text{Py})\}(\text{PhNO-}\kappa\text{O})]^+$ and $[\text{Cu}\{\text{HC}(3\text{-}t\text{BuPz})_2(\text{Py})\}(\text{PhNO-}\kappa\text{N})]^+$ (B3LYP, 6-31G(d), Gaussian09) in comparison to experimental values. ^[186]	82
Table 25. Key bond lengths [Å] and angles [°] in L2 and L3'	87
Table 26. Key bond lengths [Å] and angles [°] in C8 ²⁺ , CC8 ²⁺ and C9 ²⁺	89
Table 27. Key bond lengths [Å] and angles [°] in C10 ²⁺	91
Table 28. Key bond lengths [Å] and angles [°] in C11 and CC11 ^[125] and τ_5 -values of both.	93
Table 29. Crystallographic data collection and refinement information for L1 and C1.	132
Table 30. Crystallographic data collection and refinement information for C2 and C3.	134
Table 31. Crystallographic data collection and refinement information for C4 and C5.	136
Table 32. Crystallographic data collection and refinement information for C6 and C7.	138
Table 33. Crystallographic data collection and refinement information for L2 and L3'.	140
Table 34. Crystallographic data collection and refinement information for C8 and C9.	142
Table 35. Crystallographic data collection and refinement information for C10 and C11.	144

Table of Contents

1	Introduction.....	1
1.1	Catalysis in Bioinorganic Chemistry.....	1
1.2	Enzyme modelling	2
1.3	Metalloxygenases and Metallooxidases	3
1.4	Copper enzymes ^[31]	4
1.5	Tyrosinase, catechol oxidase and hemocyanin	5
1.6	Reaction mechanism of tyrosinase	6
1.7	Oxygen activation	9
1.8	State of research in oxygen activation	11
1.9	(μ - η^2 : η^2)-peroxo dicopper(II) vs. bis(μ -oxo) dicopper(III)	18
1.10	Cobalt complex chemistry ^[83]	19
1.11	NO in Bioinorganic Chemistry	21
1.12	Microbial denitrification.....	22
1.13	Poly(pyrazolyl)methanes.....	23
2	Objectives & Contents.....	28
2.1	Objectives	28
2.2	Contents	29
3	Results & Discussion.....	31
3.1	Synthesis of a new bis(pyrazolyl)methane ligand and its copper(II) complex	31
3.1.1	Optimisation of reaction conditions for the synthesis of 1-methyl-2-imidazolecarboxaldehyde.....	32
3.1.2	Structural characterisation of HC(3- <i>t</i> BuPz) ₂ (1-Melm) and [CuCl ₂ {HC(3- <i>t</i> BuPz) ₂ (1-Melm)}]	34
3.1.3	Definition of the τ -parameter.....	37
3.2	Efficient biomimetic hydroxylation catalysis with a bis(pyrazolyl)imidazolylmethanecopper-peroxide complex.....	38
3.2.1	General Introduction	38
3.2.2	Characterisation of [Cu ₂ O ₂ {HC(3- <i>t</i> BuPz) ₂ (1-Melm)} ₂][SbF ₆] ₂	39
3.2.3	Catalytic studies on P1[SbF ₆] ₂	49
3.2.4	Summary.....	54
3.3	Biomimetic hydroxylation catalysis through self-assembly of a bis(pyrazolyl)methanecopper-peroxo complex ^[160]	55
3.3.1	Structural characterisation of bis(pyrazolyl)methanecopper complexes	55
3.3.2	Biomimetic hydroxylation catalysis through self-assembly of [Cu ₂ O ₂ {HC(3- <i>t</i> BuPz) ₂ (Qu)} ₂][SbF ₆] ₂	62

3.3.3	Theoretical investigations	66
3.3.4	Summary.....	67
3.4	Analysis and Characterisation of bis(pyrazolyl)methane nitrate complexes	69
3.4.1	Introduction.....	69
3.4.2	Structural characterisation of bis(pyrazolyl)methane nitrate complexes.....	69
3.4.3	Calculation of the binding mode	73
3.4.4	Evaluation of NBO calculations	75
3.4.5	Summary.....	77
3.5	Investigations towards a copper(II)-superoxide mimic and NO activation with bis(pyrazolyl)methanes	79
3.5.1	Introduction.....	79
3.5.2	Copper nitrosobenzene species as superoxide mimics.....	80
3.5.3	Diazald and TTN as NO transferring agents.....	82
3.5.4	Summary.....	83
3.6	Basic studies on bis(pyrazolyl)methane ligands and their complexation behaviour	85
3.6.1	Isomerisation and structural properties.....	85
3.6.2	Structural studies on cobalt bis(pyrazolyl)methane complexes	88
3.6.3	Summary.....	93
4	Conclusion & Outlook.....	95
4.1	Conclusion	95
4.2	Outlook.....	98
5	Experimental Section.....	100
5.1	General	100
5.2	Physical Methods	100
5.3	Computational details	102
5.4	Chemicals.....	103
5.5	Syntheses.....	103
5.5.1	Synthesis of starting materials	103
5.5.2	Synthesis of 1-methyl-2-imidazolealdehyde ^{adapted from [215]}	104
5.5.3	Synthesis of ligands L2, L5, L6 and L7	104
5.5.4	Synthesis of transition metal complexes.....	108
5.5.5	Synthesis of Bis(2-(1-Methylimidazolyl))bis(3- <i>tert</i> butylpyrazolyl)methane)- copper(II)peroxide dihexafluoridoantimonate [Cu ₂ O ₂ {HC(3- <i>t</i> BuPz) ₂ (1-Melm)} ₂][SbF ₆] ₂ (P1[SbF ₆] ₂).....	115

5.5.6	Synthesis of Bis(bis(3- <i>tert</i> -butylpyrazolyl)(2-Quinoliny)methanecopper(II)-peroxide dihexafluoridoantimonate [Cu ₂ O ₂ {HC(3- <i>t</i> BuPz) ₂ (Qu)} ₂] [SbF ₆] ₂ (P2[SbF ₆] ₂)	115
5.5.7	Oxidation of catalytic amounts of exogenous substrate with (P1[SbF ₆] ₂) (25 eq of phenol, 50 eq. of NEt ₃)	116
5.5.8	Oxidation of catalytic amounts of exogenous substrate with (P2[SbF ₆] ₂) (25 eq of phenol, 50 eq. of NEt ₃) ^[160,168]	116
5.5.9	Oxidation of stoichiometric amounts (5 eq) of exogenous substrate with (P1(SbF ₆) ₂).....	117
5.5.10	Conversion of [Cu{HC(3- <i>t</i> BuPz) ₂ (Py)}][SbF ₆] with nitrosobenzene.....	118
5.5.11	Conversion of [Cu{HC(3- <i>t</i> BuPz) ₂ (Py)}][SbF ₆] with NO gas.....	119
5.5.12	Conversion of [Cu{HC(3- <i>t</i> BuPz) ₂ (Py)}][SbF ₆] with diazald [®]	119
6	References.....	120
7	Appendix.....	132

1 Introduction

1.1 Catalysis in Bioinorganic Chemistry

With enzymes being Nature's highly efficient motors of reactions, the great effort in the search for new efficient, ecological and stereospecific ways to catalyse chemical reactions, as well as to understand enzyme reaction pathways does not surprise.

While the two big branches to distinguish are homogenous and heterogeneous catalysis, this work will only focus on homogenous catalysis, which can be divided into three sub domains:

- *Transition metal catalysis* with the important section of coordination and metal-organic catalysis, in which transition metal complexes act as catalysts and allow for a broad spectrum of possible reactions.^[1-4]
- *Biocatalysis*, also known as enzymatic catalysis, which is substrate- and reaction specific due to the unique composition of the enzymes' active centres.^[5-10]
- *Organocatalysis*, in which small organic molecules function as metal free catalysts.^[11,12]

Organocatalysts offer certain advantages compared to bio- or metal-organic catalysts. Mostly they are soluble in organic solvents, which offers an additional substrate spectrum. Furthermore examples for many synthetic reactions show a practicability of organo catalysed reactions compared to their metal-organic catalysed counterparts, resulting in simplified versions of formerly challenging reactions.^[11] Typical organocatalysts include proline and thiourea, which are available from biological materials, are inexpensive and easy to prepare, simple to use and stable in air and water.^[12] Moreover, based on its metal free and therefore often less cytotoxic species, organocatalysis is of major importance in the field of drug development.^[13,14]

Transition metal catalysis offers its potential in its flexibility, as the central atom and ligands can be varied as desired in order to create the ideal catalyst for a specific reaction.^[1-4] Here, depending on the metal, disadvantages include toxicity of the metal complexes, high costs for the metals, difficult purification and instability towards oxidation.^[15]

Enzymes are essential for almost every reaction taking place in the human body.^[16,17] They are Nature's perfect combination of organo- and metal catalysis and their reactions have become highly specific and efficient throughout evolution.^[18,19] The sheer number of

enzymes (> 10000) already stresses their importance. Reactions take place at their active site, which consists of a metal centre that is surrounded by specific peptide chains. Common metals in the centre of enzymes belong to the first row of transition metals, including copper, iron, manganese and zinc. Enzymes always catalyse very specific reactions, so that mostly different enzymes are necessary to convert a substrate to its desired end form that can be metabolised by the human body. This fact is known as substrate specificity.^[18,19] Enzymes also work very efficiently, which is determined by their turnover number (TON). Turnover is the number of substrate molecules that can be converted by an enzyme per active site per unit of time.^[20] Here efficiency is optimised by nature, but good enzymatic models can achieve remarkable TONs as well.

Because of their physiological environment they function under the influence of oxygen and are mostly soluble in water. Problems arise, when working on corresponding model systems outside the human body, as their organic ligands are not soluble in water.^[21,22]

The field of Bioinorganic Chemistry is a combination of complex chemistry and enzymology.^[23] By merging coordination catalysis with biocatalysis, each method's advantages can be combined. The high efficiency of metal enzymes and the modification possibilities of metal complexes lead to a larger substrate variety. Additional variation of solvent and reaction conditions result in a maximum optimisation potential.^[19]

1.2 Enzyme modelling

As nature optimised reaction ways over millions of years^[18,19] – and enzyme extraction is sometimes expensive, as well as challenging – chemists have attempted to recreate these natural motors of reactions *in vitro* for a long time. To achieve this task, scientists have to firstly decode the structure of a specific enzyme. Obtaining crystals and solving a single crystal X-ray structure of an enzyme remains challenging due to the dimensions, concerning space and mass, of most enzymes.^[24] Enzyme modelling takes place in three steps.

1. The enzyme is simplified by reducing it to its active site including the metal core and the amino acids that are in close proximity to build a structural model.

This core is then built from metal salts and appropriate ligands resembling the amino acids.^[22] Histidine for example is often present around the enzyme core for deprotonation reactions, but more importantly for its coordinative properties. A bioinorganic substitute

would be imidazole, as the aromatic N-donor ring is the key component of histidine, but also other aromatic N-donors, such as pyridine or pyrazole, are often used.

2. Discovering and understanding the reaction mechanism of the enzyme.

Often theories have been postulated, based on the proven reaction products and a chemist's intuition. Verifying the mechanism however is a difficult and time consuming task. The reaction has to be quenched at different stages and intermediates have to be isolated and characterised.

3. The structural model is extended to a functional model, which in addition executes the same catalytic reactions as the enzyme.

While replicating the active site of an enzyme is relatively easy, having the model function as a true enzymatic model is much more difficult. Reactions in enzymes take place at the active site, but still the enzyme in general is much larger and has an amino acidic sheath around the metal centre, which plays an important part in the catalytic efficiency of enzymes.^[25]

1.3 Metalloxygenases and Metallooxidases

The selective oxidation of organic compounds is of great importance to the chemical industry.^[26,27] Thereby enzyme catalysed oxidation reactions are particularly interesting, since they make use of molecular oxygen as a cheap oxidising agent and offer high substrate specificity, as well as an excellent regio- and stereoselectivity. Moreover these reactions function under mild conditions. This type of enzyme may also facilitate the accessibility to reactions, synthetic chemists only have limited access to (e.g. the conversion of methane to methanol).^[26,28]

Concerning oxidation reactions, two types of enzymes have to be distinguished; oxygenases and oxidases. Oxygenases are enzymes that transfer oxygen onto their substrate. Therein NADP/NADPH is often used as a source of protons and electrons. Typical reactions catalysed by oxygenases are monohydroxylations of aromatics, epoxidations of C-C double bonds or the insertion of oxygen in a Baeyer-Villiger like reaction.^[29] Depending on whether oxygen atoms or molecules are transferred, mono- and dioxygenases have to be differentiated. A well-known example for monooxygenases is tyrosinase, whereas catecholoxidase acts as a dioxygenase.

Oxidases on the other hand are enzymes that catalyse a redox reaction. Here, molecular oxygen functions as an electron acceptor. Products of these reactions are water or hydrogen peroxide.^[30] The most prominent example is the cytochrome-c-oxidase.

1.4 Copper enzymes^[31]

A large amount of enzymes incorporate copper in their active centres. Depending on the structure of their active core, they can be divided into different categories. The most important for this work are copper enzymes of type I, II and III (Figure 1).

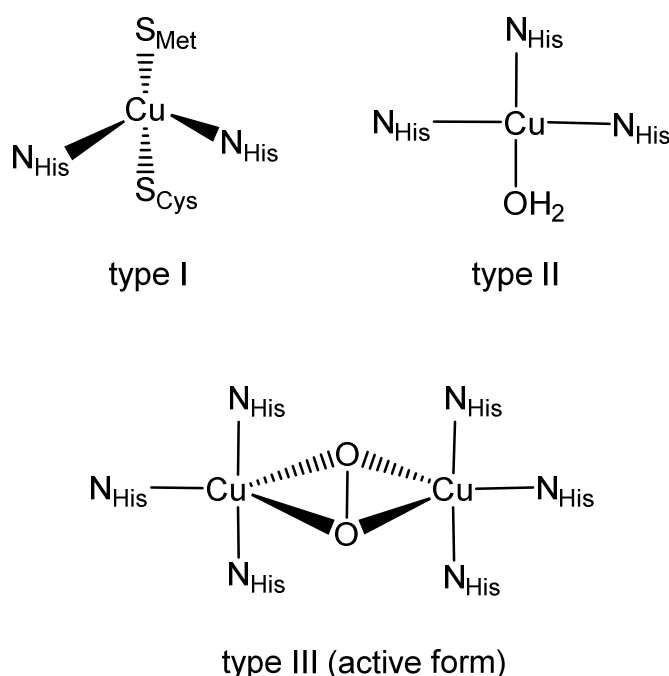


Figure 1. Structures of type I, II and III copper enzymes.

Type I and II are mononuclear complexes; type I enzymes are surrounded by two sulphur and two nitrogen atoms, more specifically two histidines, one methionine and one cysteine. Type I enzymes are referred to as “blue copper centres”, because of their strong UV absorption around 600 nm.^[32] Common examples are plastocyanin, azurin and nitrate reductase. The geometry around the copper centre is strongly distorted from a tetrahedral coordination (3+1 coordination). In type II the copper atom is surrounded by three histidine moieties and one aqua ligand. Type II enzymes are known as common “non-blue” copper centres. Examples include galactose-oxidase, (CuZn)-dismutase or the non-blue copper

centre in cytochrome-c-oxidase. The geometry is considered as planar with a weak additional coordination. Type III copper enzymes contain copper atoms which are surrounded by three histidine residues in their inactive form. To get to the active form, dioxygen is bound in a O-bridging ($\mu\text{-}\eta^2\text{:}\eta^2$)-mode. Common examples are tyrosinase and hemocyanin.^[33]

Type I copper enzymes are involved in reversible electron transfer, while type II enzymes activate oxygen in cooperation with organic co-factors. Type III enzymes are also involved in oxygen activation and additionally in oxygen transfer.

1.5 Tyrosinase, catechol oxidase and hemocyanin

Tyrosinase is a type III copper enzyme that is involved in the activation of oxygen in nature. The active site of tyrosinase consists of a ($\mu\text{-}\eta^2\text{:}\eta^2$)-peroxodicopper(II) core that was confirmed by Matoba *et al.* in 2006 by crystal structure analysis of *Streptomyces castaneoglobisporus* tyrosinase in combination with a caddie protein (Figure 2, A).^[34]

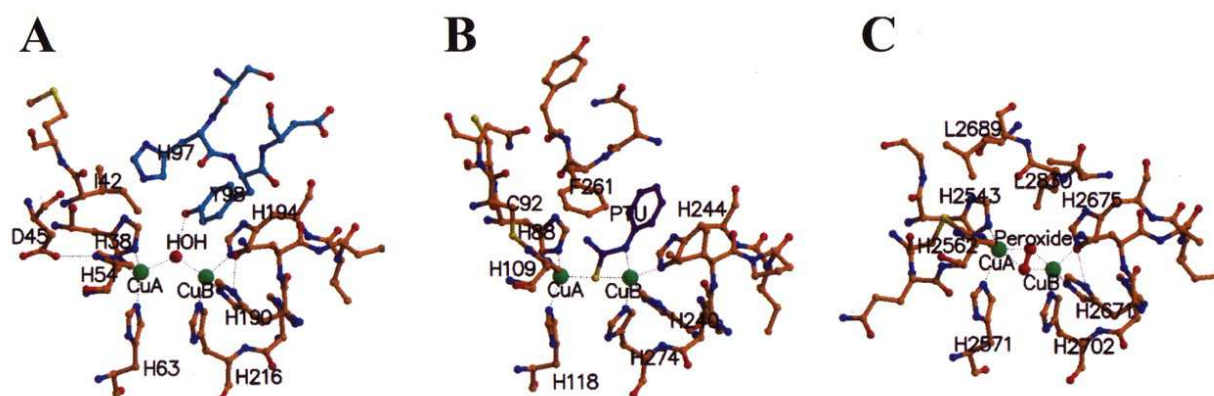


Figure 2. A, active centre of the met-form of tyrosinase complexed with ORF 378. B, active centre of the inhibitor-bound potato catechol oxidase. C, active centre of the oxy-form of octopus hemocyanin.^[34]

Tyrosinase displays phenolase and catecholase activity. It is involved in the first reaction step of the synthesis of melanin out of tyrosine. Melanin is a pigment found for example in the skin, hair and feathers of animals and in plants.^[35–38] Catechols are common structural motives in bioactive natural products and therefore important for the industry, e.g. in the production of pigments, the aroma of vanillin or photosensitive materials.^[39] Their efficient and ecological synthesis – e.g. by selectively oxidising phenols in the *ortho*-position – is highly interesting for synthetic chemistry. Until now, the transformation from phenol to

catechol was difficult to realise by transition metal catalysis, because multi-step synthesis and the use of expensive reagents in stoichiometric quantities were necessary.^[40,41]

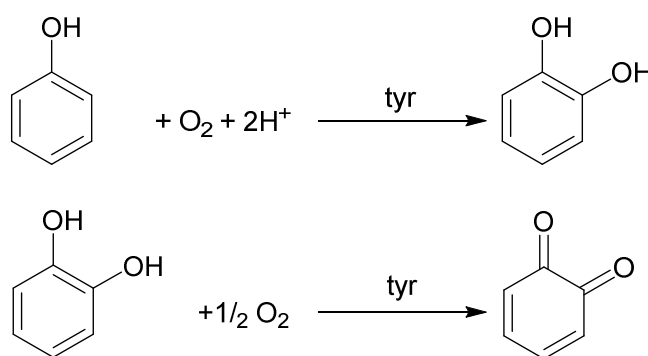
The fact that quinones are always coloured makes them to common components in naturally originated pigments, for example in bacteria, fungi or flowers. Moreover they are often found in antibiotics as they have antibacterial properties.^[42]

Catechol oxidase (Figure 2, **B**) is a ubiquitous plant enzyme, also belonging to type III copper enzymes that catalyses the oxidation of a broad range of catechols to the corresponding *o*-quinones.^[43] It differs from tyrosinase, which can catalyse both the monooxygenation of monophenols and the oxidation of catechols to quinones. Catechol oxidase can for instance be found in potatoes^[34] and also has antiseptic values. It is located in the cell cytoplasm, whereas catechol is present in the cell vacuoles, resulting in the generation of the natural antiseptic *o*-quinone, when plant tissue is damaged.^[44]

Hemocyanin (Figure 2, **C**) is the transporter of oxygen in the blue blood of molluscs and arthropods, like octopuses or crabs (e.g. horseshoe crab). It can consist of two (dimer), six (hexamer) or even ten (decamer) monomer subunits which can bind an oxygen molecule each in a Cu-peroxo binding mode. Remarkable is that – depending on the species – hemocyanin can be composed of up to eight hexamers (e.g. horseshoe crab) or two decamers (e.g. octopus). Because of its large size, hemocyanin usually floats free in the blood.^[45]

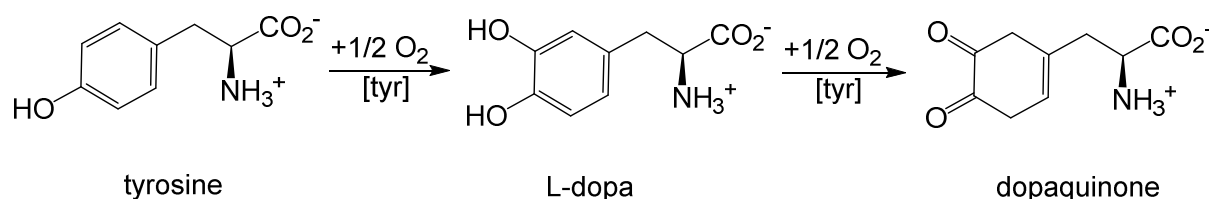
1.6 Reaction mechanism of tyrosinase

As mentioned before, tyrosinase exhibits monophenolase and diphenolase activity, which means that both the reaction of phenol to *o*-catechol and the subsequent reaction to *o*-quinone are catalysed (Scheme 1).^[46]



Scheme 1. Monophenolase and diphenolase reaction, catalysed by tyrosinase. adapted from [46]

Electron transfer for this reaction follows an inner-sphere mechanism.^[31] Tyrosinase is essential for the reaction of tyrosine to melanin. It hereby catalyses the first two reaction steps, from tyrosine to L-dopa and subsequently to dopaquinone (Scheme 2). Further reaction steps towards melanin include the oxidation of dopaquinone to dopachrome and several other reaction steps. Depending on the species, either tyrosinase itself can catalyse the reaction to melanin or the enzymes dopachrome tautomerase (DCT) and 5,6-dihydroxyindole-2-carboxylic-acid oxidase (DHIC-oxidase) are required.^[47,48]



Scheme 2. Reaction of tyrosinase to dopaquinone, catalysed by tyrosinase.^[49]

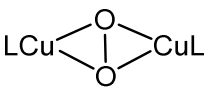
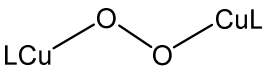
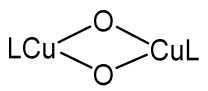
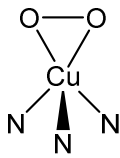
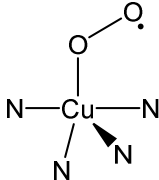
In the catalytic cycle of tyrosinase three different tyrosinase states occur. The passive state of tyrosinase is called *met*-form, where two copper ions are bridged by small bridging ligands such as water or hydroxide.^[34] In the *oxy*-form dioxygen is bound between two copper atoms and an O-O-bond is formed. Here the spin containing $d_{x^2-y^2}$ -orbitals of the copper atoms and the π^* -orbitals of the oxygen atoms show antiferromagnetic coupling, resulting in a diamagnetic complex. This effect was shown by Matoba *et al.* in 2006 by crystal structure analysis.^[34] In 1996 Solomon *et al.* postulated a reaction mechanism for the catalysis of tyrosinase which Itoh extended to the one shown in Scheme 3.^[31,50]

1.7 Oxygen activation

Besides iron, copper is one of the most frequent metals in the active centre of many enzymes, due to its naturally high occurrence and also its electrochemical nature with easily accessible redox potentials.^[19]

The reaction of oxygen with copper can result in a variety of different Cu-oxygen species (Table 1).^[55]

Table 1. Structural features of Cu₂O₂ and CuO₂ species.^[55]

					
Structure	side-on ($\mu\text{-}\eta^2\text{:}\eta^2$)-peroxo ^sP	end-on trans-($\mu\text{-}1,2$)-peroxo ^tP	bis($\mu\text{-oxo}$) O	Cu(III)- Peroxo ^MP	superoxo ^ES
Oxidation state	+II	+II	+III	+III	+II
Cu–Cu [Å]	3.51	4.36	2.80	–	–
Cu–O [Å]	1.92	1.85	1.82	1.85	1.84
O–O [Å]	1.42	1.43	2.32	1.44	1.28

All dinuclear copper cores shown in Table 1 are isoelectronic to each other. **^sP** and **^tP** both are peroxides with an O–O bond, while **O** incorporates a bis($\mu\text{-oxo}$) core. Because of the different binding modes, the copper oxidation states are different. Regarding Cu–Cu distances, the longest one can be found in the **^tP** species with 4.36 Å. The Cu–Cu distance in **^sP** with 3.51 Å is still long, while it is considerably shorter in the oxo species **O** (2.80 Å).

Two examples of mononuclear Cu–O₂ species are shown in Table 1 as well, referred to as **^MP** and **^ES**. The **^MP** core is another peroxo compound with Cu in the oxidation state of +III, while **^ES** is a superoxide radical with Cu in the oxidation state +II. The O–O bond length in **^MP** is in the same range as in **^sP** and **^tP** and therefore considerably shorter than the respective O–O distance in **O**, but longer than the one in **^ES**.

Considering thermodynamical investigations, the most important species are the side-on peroxo and bis($\mu\text{-oxo}$)-complexes.^[56] All in all, an important factor influencing the thermodynamic stability of such complexes is the nature of the ligands. More precisely it depends on the steric properties and mostly on the basicity, as well as the donor ability of

the used ligands, whether the $^{\text{S}}\text{P}$ or the O core is generated.^[57] A hybrid permethylated-amine-guanidine ligand for example only forms the O core^[58], which suggests that bidentate, sterically non-demanding strong σ -donors shift the equilibrium toward the O complex.^[55,59] Because of their spectroscopic properties, O and P species can easily be distinguished (Table 2) and therefore the binding situation of complexes can normally be determined *via* UV/Vis and resonance Raman spectroscopy.^[55]

Table 2. Spectroscopic features of $(\mu\text{-}\eta^2\text{:}\eta^2)$ - and bis($\mu\text{-oxo}$)-complexes.^[47,55]

	side-on $(\mu\text{-}\eta^2\text{:}\eta^2)$	bis($\mu\text{-oxo}$)
UV/Vis spectroscopy	350 nm ($\epsilon = 20000 \text{ Lmol}^{-1}\text{cm}^{-1}$) 550 nm ($\epsilon = 1000 \text{ Lmol}^{-1}\text{cm}^{-1}$)	300 nm ($\epsilon = 14000 \text{ Lmol}^{-1}\text{cm}^{-1}$) 400 nm ($\epsilon = 14000 \text{ Lmol}^{-1}\text{cm}^{-1}$)
Resonance Raman	750 cm^{-1} (O-O)	600 cm^{-1} (O-O) 100–200 cm^{-1} (Cu-Cu)

As listed in Table 2, side-on $(\mu\text{-}\eta^2\text{:}\eta^2)$ -peroxo complexes show UV/Vis absorption bands at around 350 and 550 nm with an intensity ratio of 20:1, as well as a characteristic resonance Raman valence vibration at 750 cm^{-1} ($\nu(\text{O-O})$). Bis($\mu\text{-oxo}$)-species on the contrary exhibit UV/Vis bands at 300 and 400 nm with equal intensities and two resonance Raman valence vibrations at 600 ($\nu(\text{O-O})$) and between 100 and 200 cm^{-1} ($\nu(\text{Cu-Cu})$). The origin of the UV/Vis bands is discussed in more detail in chapter 3.2.

1.8 State of research in oxygen activation

Over the last 20 years, interest in copper-dioxygen species as well as in their catalytic reactions has been continuously high, owing to their promising prospects for bioinspired oxidation and oxygenation catalysis.^[60] The crystal structures in Figure 3 depict O₂-derived metalloenzyme intermediates, showing that the metal-O₂ structure motives in Table 1 are in fact found in intermediate or activated structures in nature.

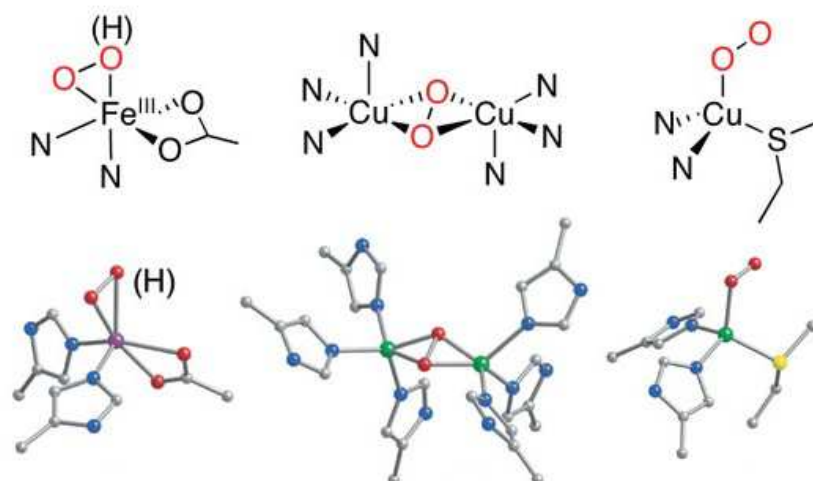


Figure 3. O₂-derived metalloenzyme intermediates, structurally characterised by X-ray crystallography.

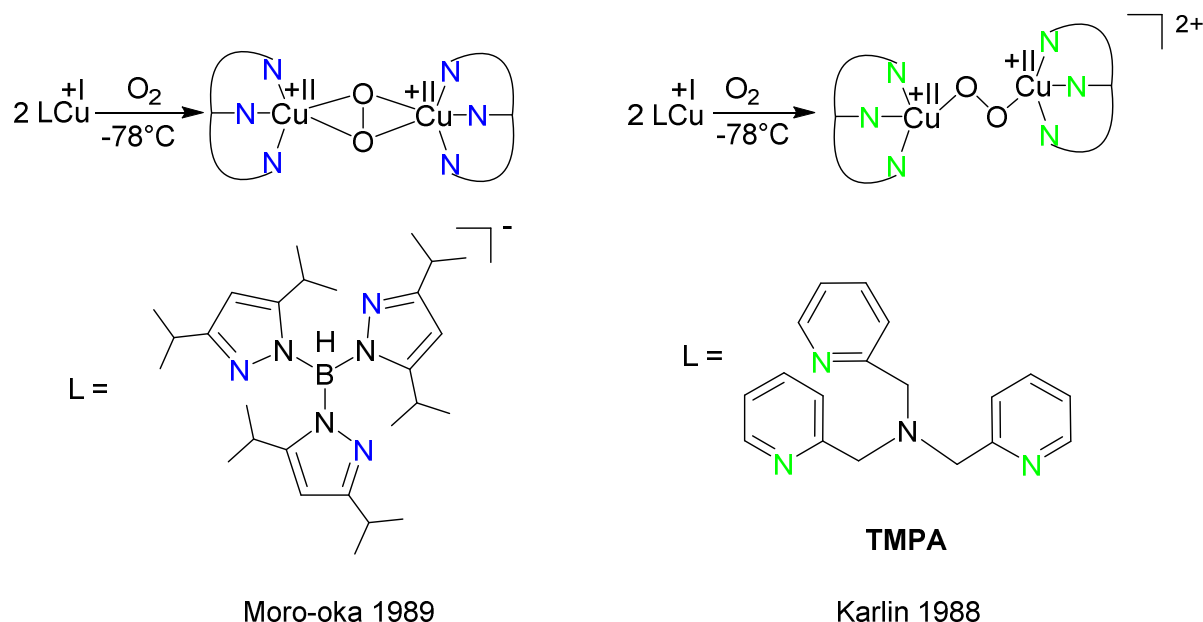
From left to right: oxygenated intermediate from naphthalene dioxygenase; (μ - η^2 : η^2 -peroxo)dicopper(II)core of oxy-tyrosinase; O₂ adduct identified in peptidylglycine α -hydroxylating monooxygenase.

For clarity, histidine imidazolyl donor ligands are indicated by N. Key oxygen atoms involved in these processes are shown in red. In the molecular models, carbon is shown in grey, oxygen in red, nitrogen in blue, copper in green, sulphur in yellow and iron in purple. ^{adapted from [19]}

Both copper-oxo and -peroxo complexes are popular research topics. As both species are in equilibrium due to their similar stabilisation energies, dependence of the generation of oxo vs. peroxo complex on the ligand is under continuous observation.^[57] Peroxo complexes are investigated as model systems for enzymes like tyrosinase or hemocyanin, while bis(μ -oxo) complexes now serve as models for enzymes such as particulate methane monooxygenase. Formerly however they were studied as tyrosinase models as well. Plenty of ligand families have been investigated, including tris(pyrazolyl)borates^[61], tris(pyrazolyl)methanes^[62], alkyl amines^[63], pyridines^[64], ketiminates^[65] and guanidines.^[66,67]

In 1989 Moro-oka *et al.* were the first to crystallise a (μ - η^2 : η^2)-peroxo core by using the tris(3,5-diisopropyl(pyrazolyl)borate ligand HB(3,5-*i*Pr₂Pz)₃ (Scheme 4).^[61] They obtained violet crystals by reduction of the solvent acetone under vacuum at -20°C followed by

cooling to -78°C . They also discovered two ways to generate the peroxo-complex, which is either by direct addition of O_2 to the copper(I) complex or by H_2O_2 treatment of the hydroxo dicopper(II) species. A copper-peroxo species was synthesised before by Karlin *et al.* in 1988 (Scheme 4), but it possessed trans- μ -1,2 coordination (end-on) and showed significantly different spectroscopic features than oxy-hemocyanin or oxy-tyrosinase.^[68]



Scheme 4. Left side: reaction of $[\text{Cu}(\text{HB}(3,5\text{-}i\text{Pr}_2\text{Pz})_3)]$ with oxygen; right side: reaction of $[\text{Cu}(\text{TMPA})]$ with oxygen.^[61,68]

Tolman and co-workers were the first who used β -ketiminate copper complexes of the type $[\text{LCuCl}]_n$ ($n = 1$ or 2) and $[\text{LCu}(\text{MeCN})]$ to determine structural differences of the copper complexes when steric properties of L were changed (Figure 4).^[65] Therefore several crystal structures of both types were analysed. Upon reaction of ketiminate Cu complexes with oxygen at -80°C the formation of a $(\mu\text{-oxo})\text{-Cu(III)}$ species was detectable via UV/Vis spectroscopy. Here the alternative route upon addition of H_2O_2 afforded the bis($\mu\text{-oxo}$) complex as well, but only when NEt_3 was added additionally.

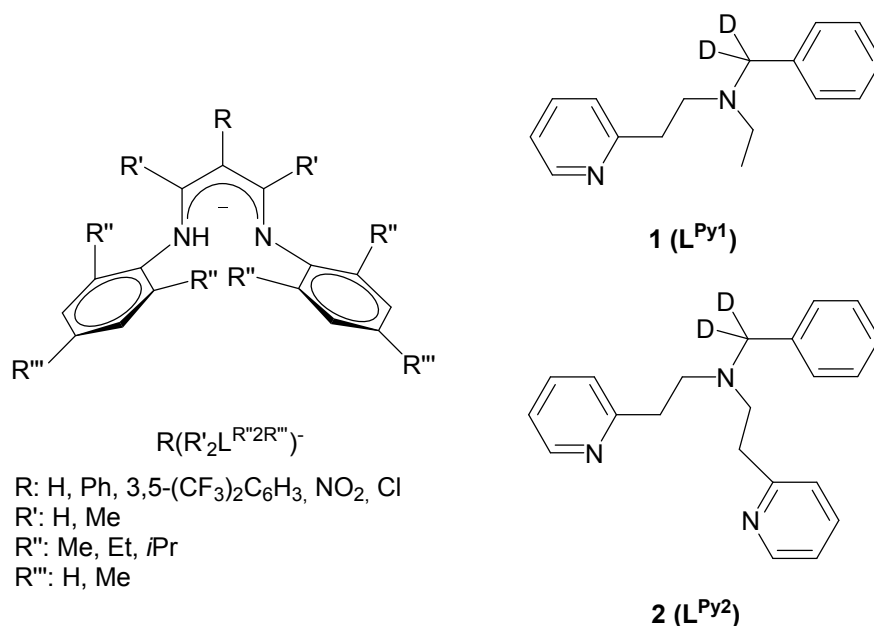


Figure 4. Left side: Structure of β -ketiminate ligands as used by Tolman.^[65]; right side: Structure of bidentate (**1**) and tridentate (**2**) 2-(2-pyridyl)ethylamin ligands as used by Itoh.^[64]

Pyridine substituted amine ligands were investigated in 2003 by Itoh *et al.* (Figure 4).^[64] Reacting the Cu(I) species of **2** with O₂ at -80°C afforded the (μ - η^2 : η^2)-peroxo complex, whereas the substitution of **2** with the sterically less demanding ligand **1** resulted in the bis(μ -oxo)-compound. The oxo-species was characterised by X-ray diffraction analysis, the peroxo species by UV/Vis and X-ray absorption spectroscopy (XAS). Both species are catalytically active, as has been shown by the reactions of ten different phenolic substrates. However keeping the reaction mechanism of tyrosinase in mind^[69], substrate reactions here always furnished C-C coupled products, which is in contrast to the inner-sphere electron transfer mechanism of tyrosinase.

Henkel and Herres-Pawlis established guanidine ligands and made progress in this field at the beginning of the 21st century.^[66,67] A family of new bis(guanidine)copper(I) compounds was introduced, containing [Cu₂(btmgp)₂][PF₆]₂, [Cu₂(DPipG₂p)₂][PF₆]₂, [Cu₂(DMPG₂p)₂][PF₆]₂ and [Cu₂(DMEG₂p)₂][PF₆]₂·2MeCN. Each species was characterised by X-ray diffraction analysis to show a twelve-membered heterocyclic Cu₂N₄C₆ ring. The first three species reacted with O₂ to afford the oxo-species [Cu₂O₂(btmgp)₂][PF₆]₂ and [Cu₂O₂(DPipG₂p)₂][PF₆]₂ and the peroxo-species [Cu₂O₂(DMPG₂p)₂][PF₆]₂. Similar to the data observed by Itoh, the sterically less demanding ligand generates the bis(μ -oxo) core.

Moreover, a few years later Henkel *et al.* were able to synthesise a room temperature stable bis(μ -oxo) complex containing a sterically demanding peralkylated bis(guanidine)-based ligand.^[67] On this complex structural studies were performed using EXAFS and resonance

Raman measurements. These analytic methods helped to gain insight into the electronic structure, concerning the ground and excited state of the bis(μ -oxo) species.

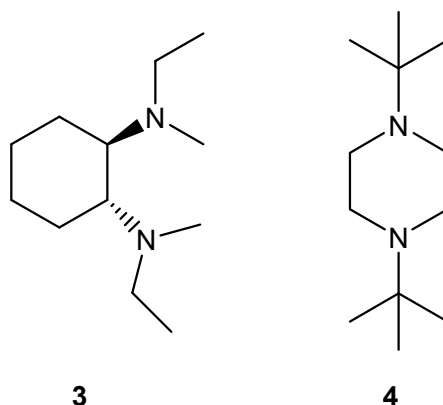


Figure 5. Structure of peralkylated diamine ligands (L^{PDA}) as used by Stack.^[63]

Stack *et al.* reported peralkylated diamines for the reaction with O_2 at low temperatures in aprotic solvents (Figure 5).^[63] Reactions were performed at $-73^\circ C$ with weakly or non-coordinating anions, such as ClO_4^- , SbF_6^- , BF_4^- or $CF_3SO_3^-$. Several crystal structures could be obtained that provided insight into the complexity of biological Cu_2O_2 reactions.

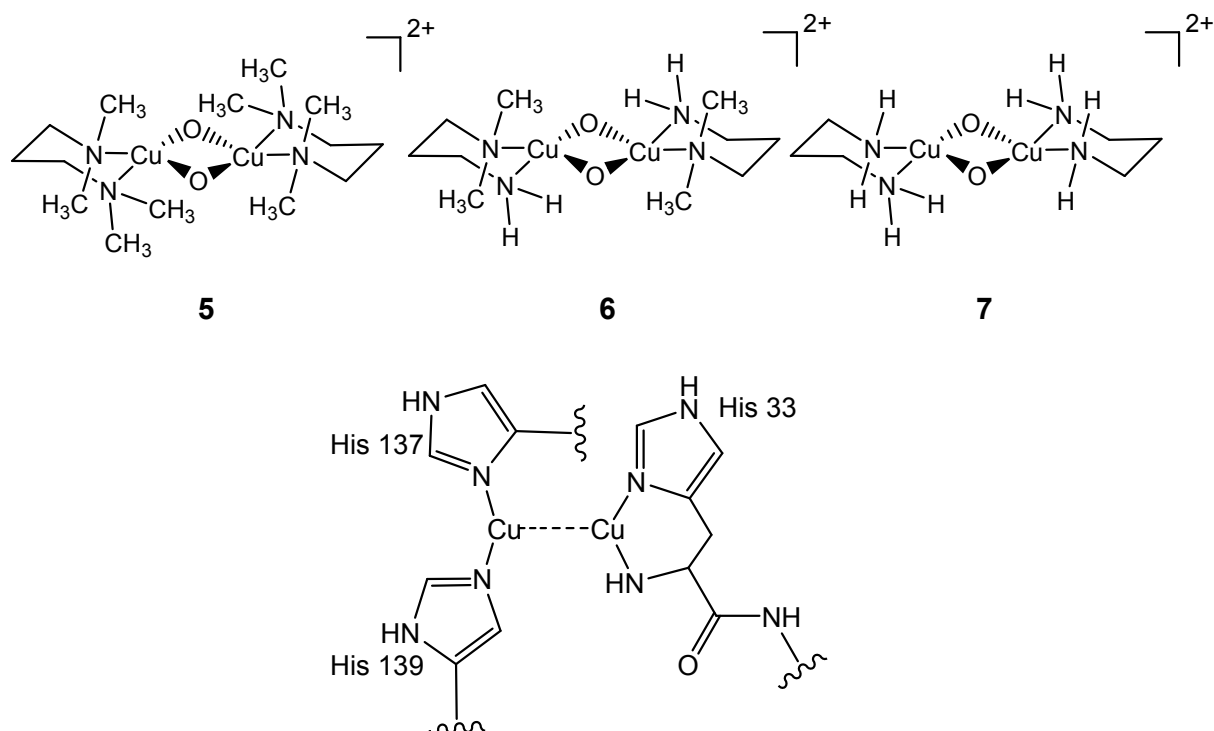


Figure 6. Top: Structure of bis- μ -oxo copper(III)-species with ligands TMPD, DMPD and PD.; bottom: active centre of particulate methane monooxygenase (pMMO).^[70]

For the stoichiometric ratio of $Cu(I)L:O_2 = 2:1$ – using **3** and **4** (Figure 5) – two different Cu_2O_2 -species were achieved. Using **3** in the conversion with O_2 afforded the $Cu(III)$ - μ -oxo-species, whereas the reaction of **4** with O_2 furnished a $(\mu-\eta^2:\eta^2)$ -peroxo complex. Therefore

Stack and co-workers could further proof the importance of the ligand in the reaction of Cu(I)-species with O₂.

Very recently, Stack *et al.* presented other simple primary amine ligands for the stabilisation of a dicopper(III)-bis(μ -oxo) complex, resembling the active centre of particulate methane monooxygenase (Figure 6).^[70]

Based on **5**, upon the addition of 2 eq of *N,N*-dimethylpropylenediamine (DMPD) at -125°C, **6** was achieved in a ligand exchange reaction. The same applies to the reaction of **5** with propylenediamine (PD), resulting in **7**. DFT calculations showed that **6** and **7** are energetically more stable. **5** and **6** did not show catalytic H-abstraction activity, which was explained by the sterically shielded Cu₂O₂ core, as shown descriptively with a space filling model.

In 1998 Casella reported a peroxo-complex, containing the very spacious ligand *N,N,N',N',N''*-pentakis[(1-methyl-2-benzimidazolyl)methyl]dipropylenetriamine (Figure 7).^[71] Using a simplified version of this ligand (**9**, Figure 7), Casella *et al.* were able to achieve the first monophenolase reaction using a Cu₂O₂-complex a few years later.^[72] They also showed oxidation of fluoro-phenols catalysed by tyrosinase^[73] and were the first ones to trap a ternary complex of tyrosinase/O₂/phenol at low temperatures.^[74] This experiment proofed that the (μ - η^2 : η^2)-form is the only active enzyme species of tyrosinase. In general the group has made significant contributions in the field of O₂ activation, especially concerning the elucidation of the catalytic cycle of tyrosinase.^[74,75]

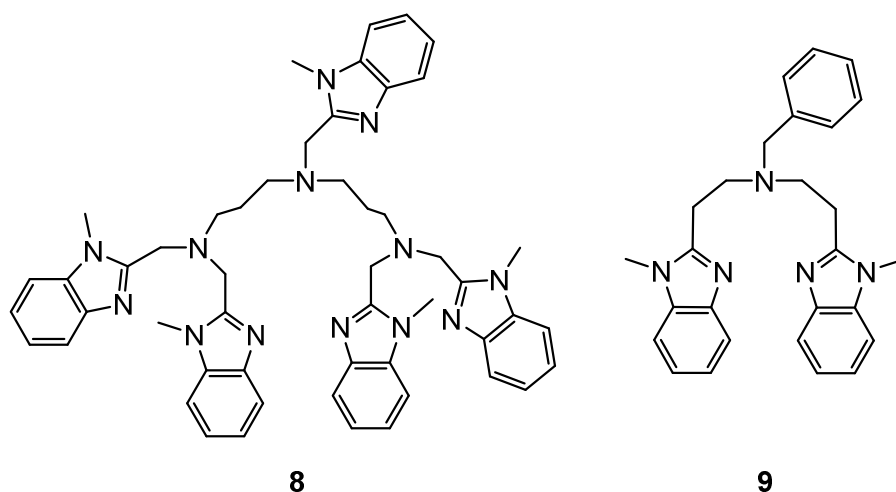


Figure 7. Structure of *N,N,N',N',N''*-pentakis[(1-methyl-2-benzimidazolyl)methyl] dipropylenetriamine (**8**) and *N,N*-bis(2-*N*-methylbenzimidazol-2-yl)ethyl)benzylamine (**9**) as used by Casella.^{[71][72]}

In 2006, Lehnert *et al.* described structural and electronic differences of copper(I) complexes with tris(pyrazolyl)methane and hydrotris(pyrazolyl)borate ligands.^[62] To understand reactivity differences of copper(I) acetonitrile complexes towards O₂, they started the investigation by varying certain parameters on Cu(I) complexes. Parameters included the solvent as a fourth ligand, the counterion, steric hindrance at the pyrazolyl substituent and overall charge of N3 type ligands. The ligands used in this study were tris(3,5-*isopropyl*(pyrazolyl))borate (HB(3,5-*iPrPz*)₃), tris((3-*tert*butyl,5-*isopropyl*)(pyrazolyl))borate (HB(3-*tBuPz*-5-*iPrPz*)₃), tris(3,5-*isopropyl*(pyrazolyl)methane (HC(3,5-*iPrPz*)₃) and tris((3-*tert*butyl,5-*isopropyl*)(pyrazolyl))methane (HC(3-*tBupz*-5-*iPrPz*)₃). Differences in the reactivity of their Cu(I) complexes were attributed to differences in the oxidation potentials, as determined by cyclic voltammetry. However the oxygen species containing these ligands took quite a long time to build and showed no catalytic activity.

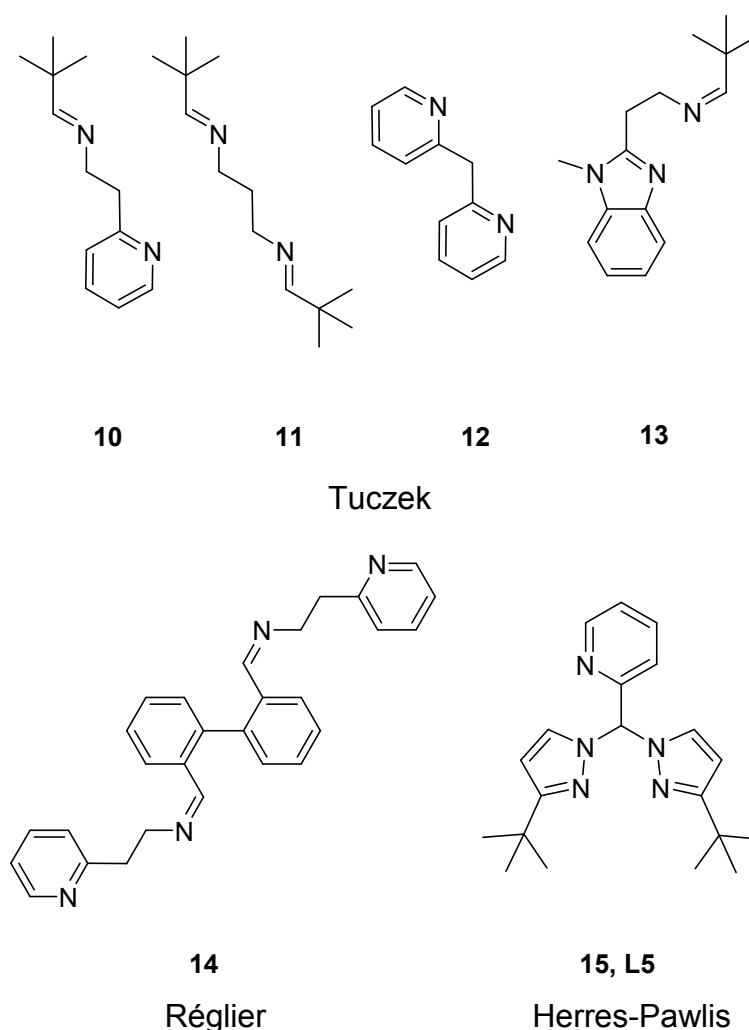


Figure 8. Structures of an imine/pyridine (10), a bis(imine) (11), a bis(pyridine) (12), a benzimidazole/imine (13), an imine/pyridine containing ligand with biphenyl spacer (14) and a bis(pyrazolyl)(pyridinyl)methane ligand (15,L5).^[18,77–79]

Changing the ligand class can result in the formation of another Cu_2O_2 -species, but one can also vary within a ligand class, for example by modifying one donating substituent. Herres-Pawlis *et al.* have investigated the donor competition between pyridinyl and pyrazolyl moieties in the $\text{HC}(3\text{-}t\text{BuPz})_2(\text{Py})$ ligand, showing that nucleophilicity, as well as basicity have to be taken into account and still the topic is not trivial.^[76]

Despite the intensive research in this field over the last decades, only few systems were able to achieve significant catalytic phenol hydroxylation so far. Firstly in 1990 Réglier *et al.* presented a model containing a biphenyl spacer (**14**, Figure 8).^[77] In 2010 Tuczek *et al.* followed with a mononuclear copper(I) complex consisting of pyridinyl and/or imine moieties as precursor (**10–12**, Figure 8).^[78]

To tie in with this achievement, Tuczek *et al.* prepared yet another $(\mu\text{-}\eta^2\text{:}\eta^2)$ -peroxo copper complex. This time a mixed benzimidazole/imine ligand was used (**13**, Figure 8). Investigations concerning the catalytic activity of $[\text{Cu}_2\text{O}_2\text{13}_2]$ with 2,4-di-*tert*-butyl-phenol (DTBP-H) showed a TON of 31 after 6.5 h. However besides the quinone, the C-C coupling product of DTBP-H was detected in large quantities as well.

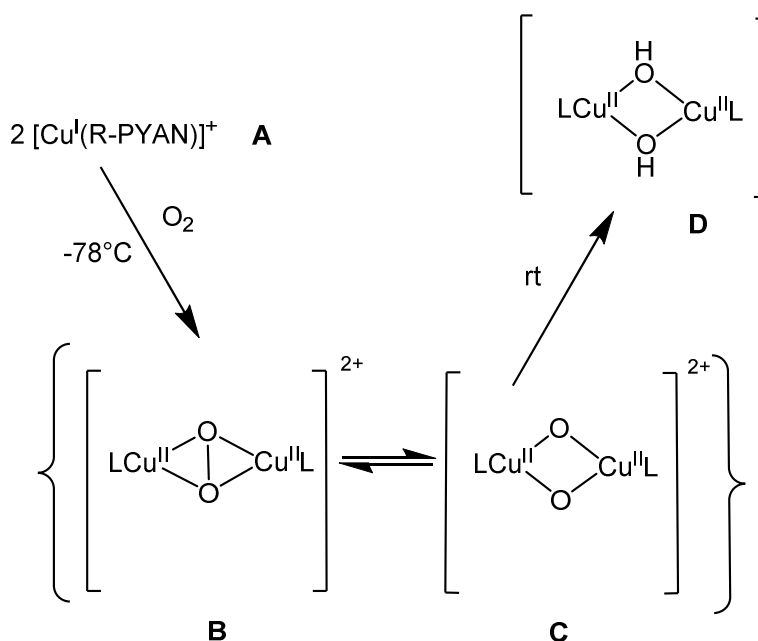
Recently, Herres-Pawlis *et al.* generated the first tyrosinase model consisting of bis(pyrazolyl)methanes (**15**, Figure 8), where the formation of quinones from different phenolic substrates without the formation of C-C coupling products was demonstrated.^[18]

Showing that tyrosinase models are still a "*hot topic*", Tuczek *et al.* recently published another catalytic system using ligands consisting of imine and benzimidazole or imine and pyrazolyl moieties respectively^[51,79], while Lumb *et al.* made use of catalytic copper-dioxygen chemistry to generate valuable organic products out of simple substituted phenols.^[80] Meyer *et al.* observed reversible O_2 -uptake using bis(oxazoline) (BOX) ligands.^[60] The resulting $(\mu\text{-}\eta^2\text{:}\eta^2)$ -peroxo dicopper(II)-species was isolated as a surprisingly stable solid and was subject to various analytic methods. First reactivity studies using 2,4-di-*tert*butylphenol however showed the formation of a C–C coupling product, while *ortho*-hydroxylation could not be observed.

1.9 (μ - η^2 : η^2)-peroxo dicopper(II) vs. bis(μ -oxo) dicopper(III)

Because of the small energy barrier between oxo- and peroxo-species, investigations to understand which influences contribute to the stabilisation of one or the other are of major interest.

Based on the ligands **1** and **2** (Figure 4), it seems that sterically less demanding ligands lead to the formation of the bis(μ -oxo) complex. This is often the case but steric properties are not the only important factor to consider. Concerning this subject Karlin *et al.* published an in depth study using the pyridinyl substituted amine derivative R-PYAN (N-[2-(4-R-pyridin-2-yl)-ethyl]-N,N',N'-trimethyl-propane-1,3-diamine, **16^R**, Table 3).^[57] The Cu(I)/Cu(II) redox potentials of copper(I)-complexes like [Cu(R-PYAN)(MeCN)_n](BCF₅)₄ (R = NMe₂, OMe, H, Cl) only differ in a small range, however, depending on R, oxygen reactivity is largely influenced. In general oxo- and peroxo-species are stable at low temperatures. When warming the reaction mixture to room temperature, the stable bis(μ -hydroxo) complex is formed (Scheme 5).

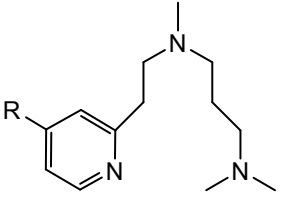


Scheme 5. Reaction of [Cu(I)(R-PYAN)] with oxygen.^[57]

Besides the electron donating or withdrawing properties of different moieties R, the solvent also has a strong influence on the Cu₂O₂-equilibrium. Table 3 displays an overview of substituent, as well as solvent effects which shows that the solvent effect plays a minor role, especially with the electron donating NMe₂ substituent, where the bis(μ -oxo) compound is built regardless of the solvent. In contrast, when the donating OMe-group is introduced into PYAN, mainly the peroxo-complex is formed. Regarding the likewise donating NMe₂-group,

the peroxo compound is built instead. Furthermore it was proven by resonance Raman spectra that better donating ligands lead to an O-O bond weakening. In summary this study shows that electronic ligand effects play a major role in the stabilisation of Cu₂O₂-species, while steric effects play a minor part. Solvents mostly play only a minor part as well, but in certain cases may lead to the generation of another product. In general coordinating solvents such as THF push the equilibrium towards the bis(μ -oxo) species.^[56,81,82]

Table 3. Overview of built species concerning the reaction of [Cu(I)(R-PYAN)] with oxygen. Reactions were performed at -78°C. Content in brackets symbolises minor product.^[57]

 R-PYAN (16^R)	CH ₂ Cl ₂	THF, acetone
R = H	peroxo	oxo + peroxo (1:1)
R = Cl	peroxo	peroxo + (oxo)
R = OMe	peroxo + (oxo)	oxo
R = NMe ₂	oxo	oxo

The last chapters focused mostly on oxygen activation, which will be an important part of this work, but the ligand model systems that were used are also in the focus for the activation of other small molecules, such as NO or N₂. In addition, besides copper complexes, complexes with cobalt as the central metal were found to be promising preliminary stages in the activation of nitrogen containing small molecules. Therefore the next chapter will concentrate on these subjects.

1.10 Cobalt complex chemistry^[83]

Cobalt is a transition metal and is found in nature mostly as ore in combination with arsenic or sulphur. It is much more oxidation resistant than iron. Technical applications of cobalt include alloys and it functions as pigment to blue glass or ceramics. Cobalt(II) and cobalt(III) are the most common oxidation states. They both show a high complex building tendency. Cobalt(III) has six d-electrons and builds complexes with neutral ligands, such as NH₃, H₂O and CO₂H.

Co(III) oxygen species are far less stable than Co(III) complexes with nitrogen ligands. Like copper, cobalt(II) also reacts with oxygen to generate different oxygen bound species. The difference however is that the reaction of Co(II) with oxygen results in a mononuclear η^1 -superoxo species and further reaction results in a dinuclear end-on trans-(μ -1,2)-peroxo-species (Figure 9), whereas Cu(II) more likely exhibits peroxo-complexes with the (μ - $\eta^2:\eta^2$)-coordination motive.

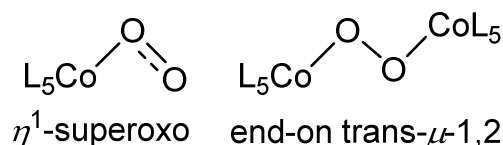


Figure 9. Coordination motives of the reaction of Co(II) species with oxygen.^[83]

In biochemistry, cobalt is of high importance as a micro-element, for example as part of the active centre of cobalamines.^[84] The most well-known example hereof is coenzyme B₁₂. Cobalamines are composed of a 15-membered planar macrocyclic corrin system with four N-donors and Co(III) in the centre, resembling the porphyrin ring of haemoglobin (Figure 10).^[85]

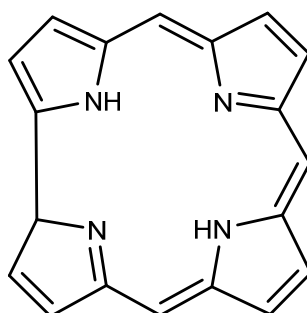


Figure 10. Structure of the corrin ring.

Mainly Co(III) complexes show an octahedral geometry with a low-spin arrangement, resulting in the highest ligand field splitting. Co(II) complexes have seven d-electrons and show a more diverse complex geometry, but primarily either octahedral high-spin or tetrahedral complexes with fully occupied e_g -orbitals are stabilised. An example for a Co complex with nitrogen donors is shown in Figure 11. Regarding the geometry, less polarisable ligands such as oxygen or nitrogen lead to octahedral (Figure 11) and polarisable ligands such as Cl^- , Br^- , I^- , SCN^- lead to tetrahedral complexes (Figure 11).

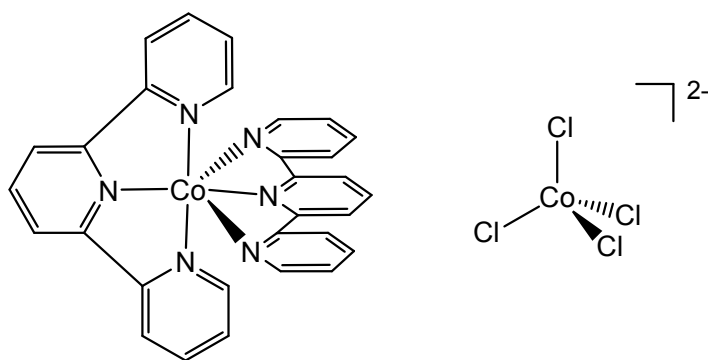
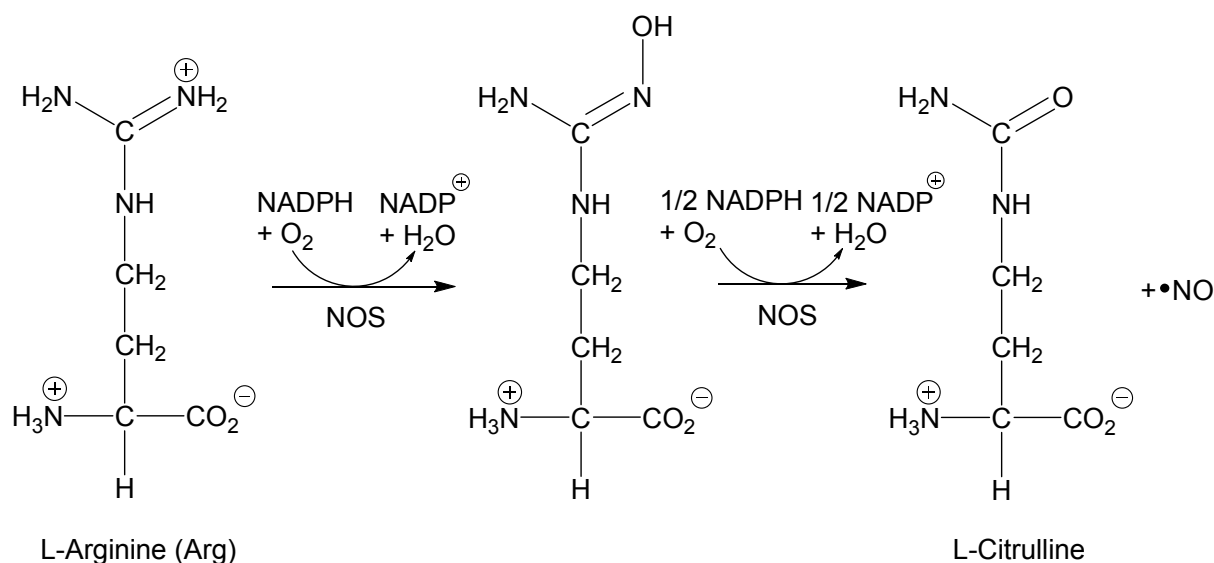


Figure 11. Structure of $\text{Co}(\text{tpy})_2$ and $[\text{CoCl}_4]^{2-}$.^[83]

1.11 NO in Bioinorganic Chemistry

For a long time nitric oxide has only been known as a colourless, poisonous gas. It is a free radical with eleven valence electrons. The single electron occupies an antibonding π^* -orbital, which explains the high reactivity of NO. Oxidation generates the nitrosyl cation NO^+ and reduction results in the nitroxyl anion NO^- .^[83] From a bioinorganic perspective, the complex formation of transition metals with NO is highly interesting. NO is a redoxactive ligand, which belongs to the group of “*non-innocent*” ligands. In complexes, NO’s redox activity makes it difficult to assign an oxidation state to it. Therefore Enemark and Feltham introduced a nomenclature that does not need to assign specific oxidation states to neither metal nor ligand.^[86] There, the metal ligand unit is written in curly brackets, for example $\{\text{CoNO}\}^{10}$. The number ten represents all d-electrons of the neutral metal plus all unpaired π^* -electrons of the ligand. Applying the neutral electron counting system, 10 is composed of 9 d-electrons for $\text{Co}(0)$ and 1 π^* d-electron for the NO radical.



Scheme 6. Reaction mechanism of NO-synthases.^[88]

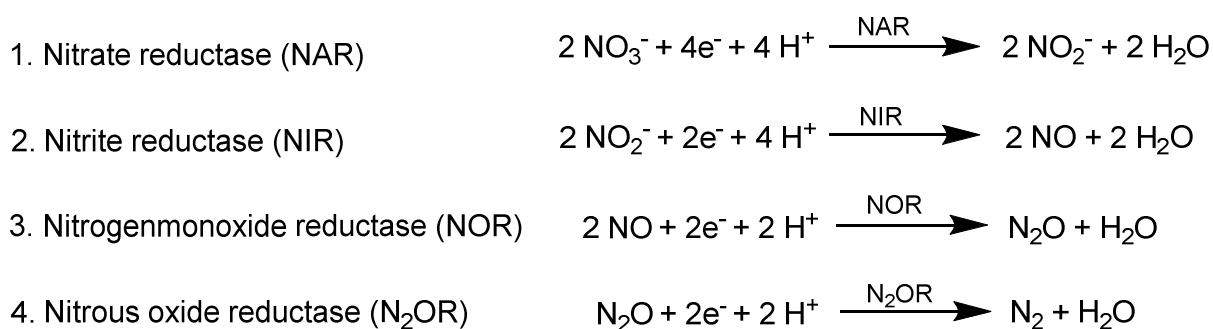
Furchgott and Ignarro recognised the physiological importance of NO and received the Nobel Prize in 1998 for their contribution to the finding that NO exhibits a vasodilatory effect and is important for the regulation of blood pressure.^[87]

NO is synthesised by NO-synthases (NOS). Here three different forms can be differentiated; endothelial- (eNOS), neuronal- (nNOS) and inducible-NOS (iNOS). They convert L-arginine *via* L-hydroxyarginine to L-citrulline and NO (Scheme 6).^[88]

Due to its small size and low polarity, NO can diffuse freely in the muscle layers, where it can activate the soluble guanylate cyclase (sGC), which most likely incorporates a low-spin Fe(II) haem centre.^[89] The binding of NO leads to a bond cleavage between Fe and a histidine, resulting in the active form of GC. Activation of GC in turn leads to an increase of the cGMP (cyclic guanosinemonophosphate) level. As a result of a higher cGMP level, the Ca^{2+} level is reduced, which results in a relaxation of the muscle septum. However the operation mode of GC is not understood in detail to this point.^[90] Based on its blood pressure reducing properties, NO releasing drugs are for example used in the treatment of heart diseases (e. g. angina pectoris).^[91] In order to understand systems like GC in detail and for the optimisation of medical treatments involving NO, it is of great importance to generate biomimetic systems and study their structure, as well as their electronic properties.

1.12 Microbial denitrification

Another biologically important nitrogen species is nitrate. It is the reactant of the microbial denitrification. This four step process is the energy source for certain bacteria, as well as archaea, fungi and yeasts.^[92] These reactions convert nitrate to nitrogen. Each reaction is catalysed by a different enzyme, which incorporate different metal atoms, such as Fe, Cu or Mo with different ligand environments.



Scheme 7. Reactions of the microbial denitrification.

Starting point is the reduction of nitrate to nitrite. This reaction is catalysed by nitrate reductase and is followed by three further reactions, in order to generate nitrogen.

Nitrate reductase is an oxido reductase that is composed of α -, β - and two γ -units, containing molybdenum in its active centre. It catalyses the reduction of nitrate to nitrite (Scheme 7).

There are two types of nitrite reductases: one is haem based and the other one contains copper. The iron based enzyme catalyses the reaction to various products whereas the copper containing ones specifically catalyse the reaction to NO (Scheme 7). Copper-containing nitrite reductases (CuNIRs) have at least one type I copper centre per protein, which are similar to azurin.^[93] Additionally type II copper centres can be found in NIRs, which are responsible for the binding and reduction of nitrite.^{[93][94]} In this case a Cys-His bridge is built, that connects a type I Cu-centre ligated Cys to a type II Cu-centre ligated His.^[95]

The nitrogenmonoxide reductase catalyses the reduction of NO to N₂O (Scheme 7). It has an iron based active centre.^[96] It also shows a co-regulation with nitrite reductase, which was demonstrated by mutation of the nitrite reductase gene.^[97]

The final reaction step to nitrogen is catalysed by nitrous oxide reductase (N₂OR) in combination with cytochrome-c (Scheme 7).^[98] Therefore N₂OR plays a crucial role in the conversion/reduction of the greenhouse gas nitrous oxide.^[99]

Overall studies with bacterial NO-binding enzymes and their model complexes provide structural, spectroscopic and mechanistic information and can therefore help in the investigation of other NO binding enzymes, such as guanylate cyclase.

1.13 Poly(pyrazolyl)methanes

As can be seen by the vast variety of Cu₂O₂-species, the spectrum of N-donating ligands suitable for tyrosinase modelling is huge. Keeping in mind the condition of mimicking the active centre of tyrosinase with histidine resembling, facially N-donating ligands that can be adjusted by varying their substituents and therefore the steric or electronic properties, we used bis(pyrazolyl)methane ligands.

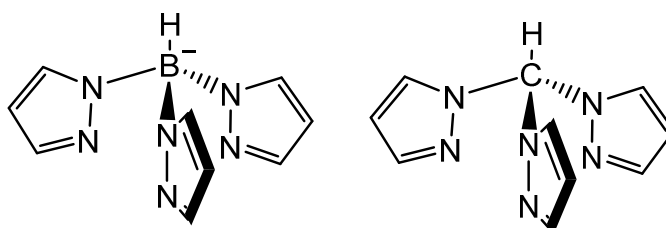
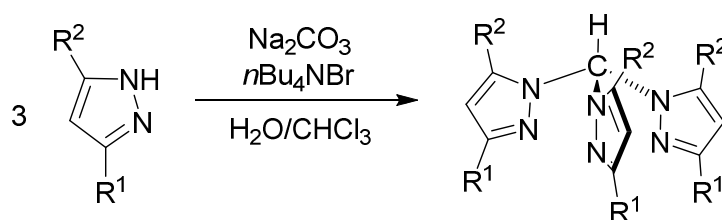


Figure 12. Structure of tris(pyrazolyl)borate and tris(pyrazolyl)methane.

Pioneering work in this field was done by Trofimenko in 1966, when he firstly reported tris(pyrazolyl)borates (Figure 12) as N-donating ligands and suggested them as good mimics for the histidine surrounding of copper centres.^[100] Tris(pyrazolyl)methanes belong to the class of scorpionate ligands owing it to their coordination mode, where two N-donors coordinate the metal from either side and the third one coordinates from the top, resembling the claws and sting of a scorpion.^[101] Despite their water sensitive B-N bond and their overall charge, they dominated the field of coordination chemistry compared to isoelectronic tris(pyrazolyl)methanes (Figure 12) for a long time, the reason being the easy accessibility of the borates. Besides methane derivatives, species containing different apical atoms, such as silicon^[102], nitrogen^[103], transition metals^[104], aluminium, indium, gallium^[105] or germanium^[106] are known. Originally tris(pyrazolyl)methanes were introduced to coordination chemistry by Hückel & Bretschneider in 1937.^[107] However their synthesis was not selective and byproducts such as mono- and disubstituted methanes with only one or two pyrazole functions were formed. For many years no efficient synthesis protocol was known.

Trofimenko synthesised the bis(pyrazolyl)methane $\text{H}_2\text{C}(\text{Pz})_2$ by the conversion of pyrazole with dibromomethane.^[108] Following the synthesis of pyrazole with dibromomethane at 150°C yielding 45% product, finally Trofimenko reacted pyrazole with 2,2-dimethoxypropane to obtain 75% of $\text{H}_2\text{C}(\text{Pz})_2$.^[108] After the successful synthesis of bis(pyrazolyl)methanes via the reaction of the potassium salt of the substituted pyrazoles with diiodomethane in a phase-transfer catalysis,^[109] attempts to synthesise substituted tris(pyrazolyl)methanes in that way failed. Progress in this area was made by Elguero *et al.* in 1984^[110] and finally by Reger *et al.*, who presented a synthesis of 3,5-substituted tris(pyrazolyl)methanes (Scheme 8).^[111] Thereby, 3 eq of a 3,5-disubstituted pyrazole are refluxed with an excess of sodium carbonate in a liquid-liquid phase transfer system (chloroform/water), followed by the reaction with *tert*-(*n*-butyl)ammoniumbromide. This reaction resulted in yields of about 60%. Because of their three identical donor functions they are also referred to as homoscorpionates. In contrast to that, bis(pyrazolyl)methanes (where one pyrazolyl substituent is switched to another donor function) are called heteroscorpionates.^[112] Scorpionate ligands with substituted pyrazole moieties are referred to as “second-generation” ligands.^[101]



Scheme 8. Reaction scheme of the synthesis of substituted tris(pyrazolyl)methanes.^[111]

In 1989 Canty *et al.* extended the research field of tris(pyrazolyl)methanes to bis(pyrazolyl)methanes, by synthesising bis(pyrazolyl)methanes that incorporate a pyridinyl rest.^[113] This reaction is based on a Peterson rearrangement.^[114] It proceeds in two steps: first, the generation of bis(pyrazolyl)methanone from the reaction of pyrazole with Et_3N and phosgene, and second the conversion of the ketone with an aldehyde that incorporates the third donor function. In this reaction the fleeting gas CO_2 is formed. Using this method Higgs and Carrano synthesised several bis(pyrazolyl)methanes with disubstituted pyrazolyl moieties and hydroxyphenol as the third donor.^[115]

An advantage compared to the tris(pyrazolyl)methanes is the possibility to vary and optimise the donor abilities through the variation of the third donor. Upon reaction with a transition metal, the preferred binding motive is a six-membered $\text{C}(\mu\text{-Pz})_2\text{M}$ ring in its boat conformation (Figure 13).^[101]

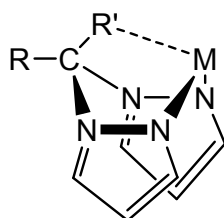
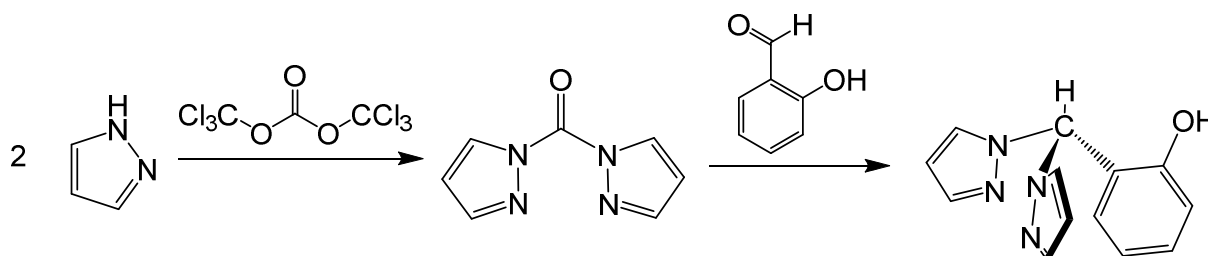


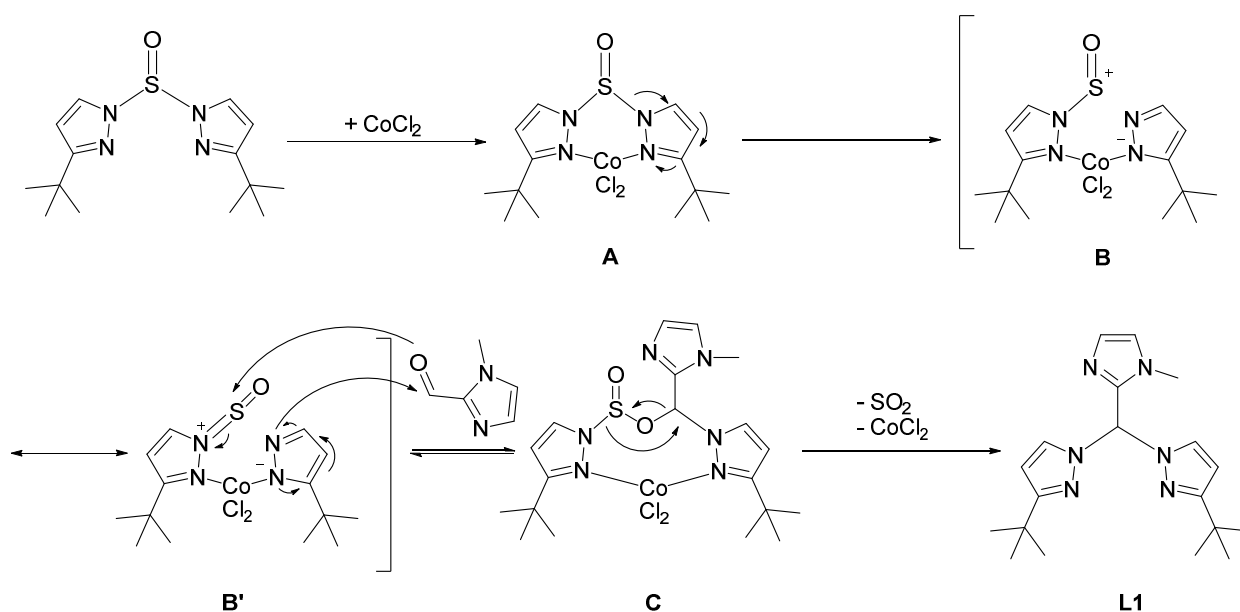
Figure 13. Boat conformation of a bis(pyrazolyl)methane complex.



Scheme 9. Reaction from pyrazole to bis(pyrazolyl)methane by using triphosgene and 2-hydroxybenzaldehyde.^[116]

Burzlauff *et al.* developed a cobalt catalysed synthesis for *N,N,O*-scorpionate ligands (Scheme 9) that are able to complexate transition metals.^[116]

Based on all these reactions, a unified synthesis for substituted bis(pyrazolyl)methane ligands was developed in 2010 by Herres-Pawlis *et al.*^[117] Following a modified Peterson rearrangement type reaction^[114], this cobalt catalysed reaction allows for the synthesis of a variety of bis(pyrazolyl)methane ligands in a one pot reaction in good to excellent yields. An additional advantage is the avoidance of the very toxic phosgene. A detailed reaction mechanism of the CoCl_2 -catalysed Peterson reaction is given in Scheme 10.



Scheme 10. Reaction mechanism of the Co-catalysed Peterson-like rearrangement.

Hereby cobalt is coordinated by two pyrazolyl nitrogens (**A**), followed by electron transfer to generate a separation of charge (**B**, **B'**). Nucleophilic attack of the free electron pair of a pyrazolyl nitrogen results in an O-S-bond formation (**C**). Rearrangement of this species leads to the ligand **L1**, with SO_2 being a byproduct and the Co-catalyst being regained.

Besides the common nitrogen donors and Burzlauff's *N,N,O*-systems, bis(pyrazolyl)methanes with sulfur-donors as the third moiety are known as well (Figure 14).^[118]

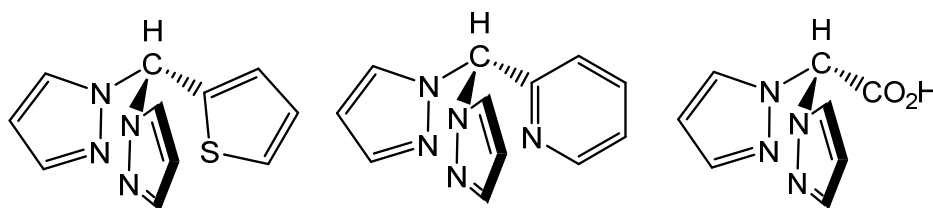


Figure 14. Structure of bis(pyrazolyl)methane ligands with *N,S*-, *N,N'*- and *N,O*-donors.

Additionally, Reger *et al.* introduced “third generation” ligands, which are multitopic ligands that possess several poly(pyrazolyl)methane units in one molecule (Figure 15). Reger’s group reported several self-assembled supramolecules using these ligands over the past decade.^[119–122] In general, functional groups’ specific sterical properties and non-covalent interactions can greatly influence the character of the ligands.^[123]

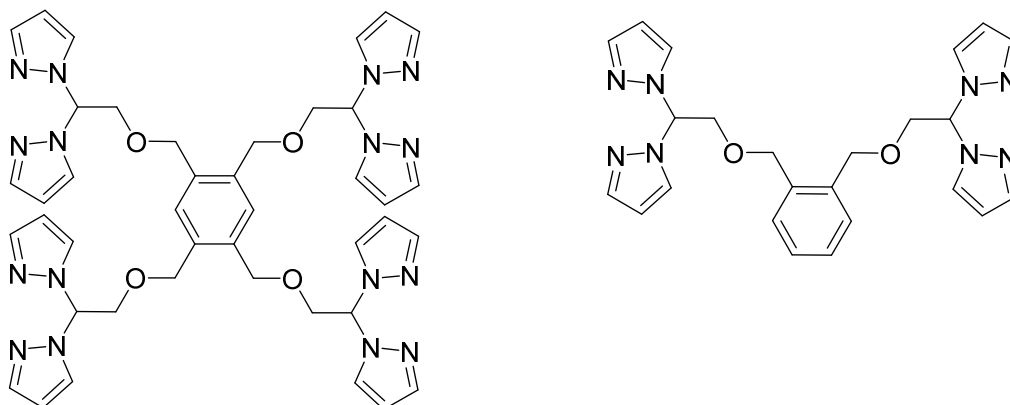


Figure 15. Structure of “third generation” scorpionate ligands.^[123]

Because of their excellent donor abilities poly(pyrazolyl)methanes can coordinate a variety of transition metals like iron, copper, cobalt and zinc.^[124] For the coordination mode not only the transition metal but mostly the steric properties of the ligand are important to consider. Unsubstituted poly(pyrazolyl)methanes generate bisfacial octahedral complexes with Cu(II) centres, while poly(pyrazolyl)methanes with sterically demanding substituents in the 3-position of the pyrazole form monofacial trigonal-bipyramidal or square-pyramidal complex geometries (Figure 16). With Cu(I) centres square-planar or tetrahedral coordination modes are created (Figure 16).^[125]

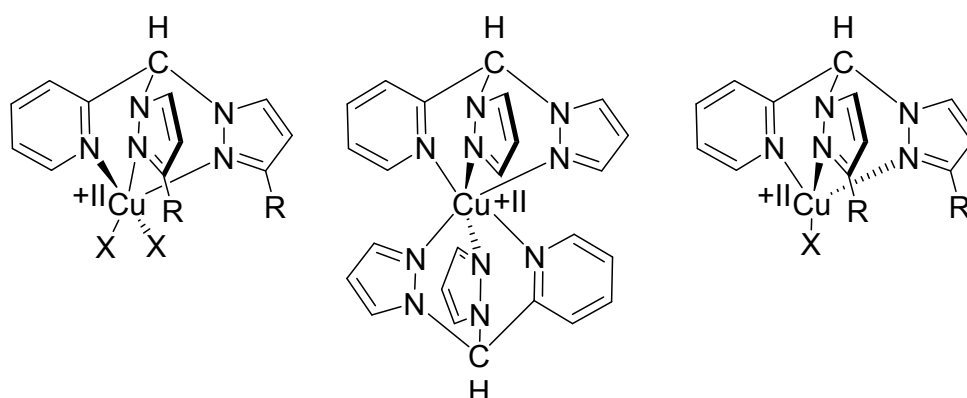


Figure 16. Possible coordination modes of Cu(I) and Cu(II) bis(pyrazolyl)methane complexes.

2 Objectives & Contents

2.1 Objectives

Catalysts are commonly used reagents in chemical synthesis, because they enable and speed up reactions, but do not influence them any further. As an example for biological catalysts, enzymes are biocompatible and highly selective as well as effective, but, due to their complex nature, a large amount of enzymes is not well understood.

The enzyme tyrosinase however has been characterised and X-ray diffraction analysis showed a Cu_2O_2 side-on $(\mu-\eta^2:\eta^2)$ -peroxo core, where each copper atom is surrounded by three histidine moieties.^[34] Tyrosinase catalyses the first reaction step in the biosynthesis of melanin which is a brown pigment found in the skin or feathers of animals and in plants.^[35–37] It shows monophenolase as well as diphenolase activity and therefore can convert phenols to catechols and subsequently catechols to quinones.^[126]

The main aim of this work is the development of a ligand that can activate oxygen, in order to build a $(\mu-\eta^2:\eta^2)$ -peroxo compound and, more importantly, this peroxo compound should ideally be catalytically active by executing the same reactions as tyrosinase itself. For this, the $(\mu-\eta^2:\eta^2)$ -peroxo Cu(II) species is treated with various phenolic substrates in order to determine whether and how much catechol or quinone are formed.

Requirements for the ligand are components that resemble the metal centre surrounding of the enzyme tyrosinase. The approach is to use bis(pyrazolyl)methane ligands, because their pyrazolyl moieties, which are aromatic nitrogen donors, resemble the histidines in tyrosinase. They are multidentate ligands that can be functionalised at the pyrazolyl units. In addition to the two pyrazolyls, a third donor function is present which can be varied as well. Precisely, the idea was to develop an imidazolyl containing bis(pyrazolyl)methane ligand that can activate oxygen as well as transfer it onto natural and non-biological substrates of tyrosinase.

Alongside, bis(pyrazolyl)methane complexes with different transition metal salts shall be synthesised. Their structural characterisation is supposed to give insight into the donor competition between pyrazolyl and pyridinyl, quinolinyl or imidazolyl units. Moreover binding modes and complex geometries shall be characterised. The evaluation of binding modes and the electronic structure also leans on density functional theory calculations.

Additionally, for the better understanding of the catalytic mechanism of tyrosinase, a nitrosobenzene bis(pyrazolyl)methane copper complex shall be synthesised, as a superoxide mimic. Such a superoxide species is supposed to be an intermediate during the activation of oxygen.

Besides the activation of oxygen, the activation of other small molecules like NO shall be studied by using NO gas and NO donor reagents.

2.2 Contents

The results of this thesis are discussed in chapters 3.1–3.6.

Chapter 3.1 explains the synthesis of the reactant 1-methylimidazolealdehyde and the bis(pyrazolyl)methane ligand HC(3-*t*BuPz)₂(1-Melm), which is later on used for oxygen activation and transfer. Structural aspects of the ligand's crystal structure are discussed alongside the crystal structure for a CuCl₂ complex of the same ligand.

The ligand introduced in chapter 3.1 plays a prominent role in the whole chapter 3.2. Here the oxygen activation with this ligand is investigated in depth by UV/Vis and X-ray absorption spectroscopy, UHR-ESI mass spectrometry and theoretical means such as NTO, NBO and TD-DFT calculations. This chapter includes the evaluation of the stoichiometric and catalytic activity of [Cu₂O₂{HC(3-*t*BuPz)₂(1-Melm)}₂][SbF₆]₂ (**P1**[SbF₆]₂), showing that **P1**[SbF₆]₂ is active in the hydroxylation catalysis and can convert natural and non-biological substrates of tyrosinase in good yields.

Three copper halide compounds are introduced at the beginning of chapter 3.3. Their molecular structures are discussed in detail including density functional theory. Furthermore the catalytic activity of another peroxo complex ([Cu₂O₂{HC(3-*t*BuPz)₂(Qu)}₂][SbF₆]₂, **P2**[SbF₆]₂) is shown in a self-assembly approach. Chapters 3.2 and 3.3 are round off with a comparison of the two peroxo species that were synthesised during this work.

In chapter 3.4 several transition metal nitrate complexes are presented. They provide important insight into the geometry of combined N and O ligand systems. A rare nitrate binding mode is shown and quantified.

In chapter 3.5 the formation of a superoxide mimic was attempted, as a superoxide is assumed to be an intermediate species in the building of the (μ-η²:η²)-peroxo compound and an active species in other copper enzymes.^[55] There, the copper(I) precursor [Cu(HC(3-*t*BuPz)₂(Py))][SbF₆] is reacted with nitrosobenzene. These reactions were optimised while

they were being followed UV/Vis spectroscopically. Moreover a couple of experiments were conducted in order to activate other small molecules besides O₂ such as NO. Preliminary tests with NO donor reagent diazald® and NO gas showed a possible NO activation.

Chapter 3.6 finally introduces further new bis(pyrazolyl)methane ligands containing *isopropyl* substituents at the pyrazolyl groups. Associated with their synthesis is the isomerisation effect of these *isopropyl* groups from the 3- to the 5-position of the pyrazolyl moiety. In the isomerised ligands steric pressure is avoided and a bisfacial bis(pyrazolyl)methane complex is formed. To conclude, structural features of two bisfacial cobalt complexes with unsubstituted pyrazolyl moieties at the ligand are discussed and compared to the *isopropyl* substituted ligand's complex.

3 Results & Discussion

3.1 Synthesis of a new bis(pyrazolyl)methane ligand and its copper(II) complex

On the basis of recent results published by Herres-Pawlis *et al.*^[18], a new bis(pyrazolyl)methane ligand was developed in order to further enhance the catalytic activity of its copper(II)-peroxo complex. Under retention of 3-*tert*butylpyrazole due to its bulky alkyl group preventing the formation of bisfacial complexes, pyridinyl was substituted by 1-methylimidazolyl, which is another aromatic nitrogen donor with different electronic properties. Using imidazole as an N-donating ligand is obvious, because it is the key building block of the amino acid histidine, which is present around the active centre of many enzymes.^[127] Keeping that in mind, it does not surprise that ligands containing imidazole moieties have already been used in the field of copper-oxygen chemistry (Figure 17). In 1995, Sorrell *et al.* used a substituted tris(imidazolyl)phosphine ligand to stabilise a peroxo dicopper(II) adduct.^[128] This was stable at -78°C for at least five days. Upon warming the solution to room temperature, the corresponding hydroxo complex was formed. Karlin and co-workers followed in 2009 with an imidazole containing TMPA-derivative (Figure 17)^[129], and in 2012 Limberg presented a tripodal ligand (**17**) (Figure 17) containing sterically demanding imidazole moieties for the stabilisation of Cu(I)- and Cu(II)-species, which showed an intramolecular tyrosinase-like reaction.^[130] Earlier this year a follow-up study of Limberg *et al.* concerning this ligand was published^[131]. There the ability of the Cu(I)**17** complex was tested for its catalytic ability in the reaction with the exogenous substrate *di**tert*butylphenol (DTBP). Following the reaction of Cu(I)**17** with O_2 UV/Vis spectroscopically did not show any evidence of a Cu_2O_2 species. Intermediate formation of this species however was assumed because of crystallographic evidence of $[\text{17Cu}(\text{OH})(\text{OTf})\text{Cu17}^{\text{ox}}](\text{OTf})$ (see [130]) and formation of the corresponding *di**tert*butylquinone upon addition of a large excess of DTBP and 2 eq. of NaDTBP to a solution of Cu(I)**17**, followed by treatment with O_2 . This reaction resulted in a high turnover number of 22 after 20 h, however equal amounts of the biphenol product were formed as well. In addition a second reaction was observed which presumably occurred after further reaction of $\text{Cu}_2\text{O}_2\text{17}_2$ with O_2 in combination with the quinone and NaDTBP, resulting in an ester consisting of DTBP and a furanone species. This reaction is a dioxygenation and resembles the reaction of flavanol-2,4-dioxygenase.

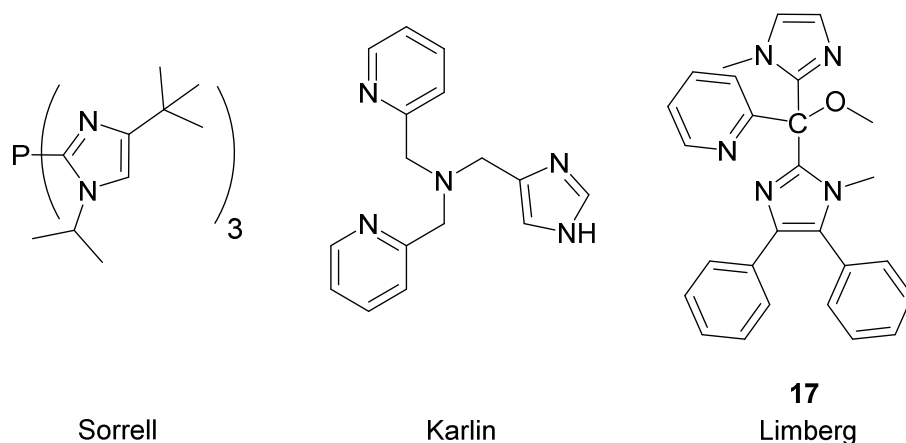


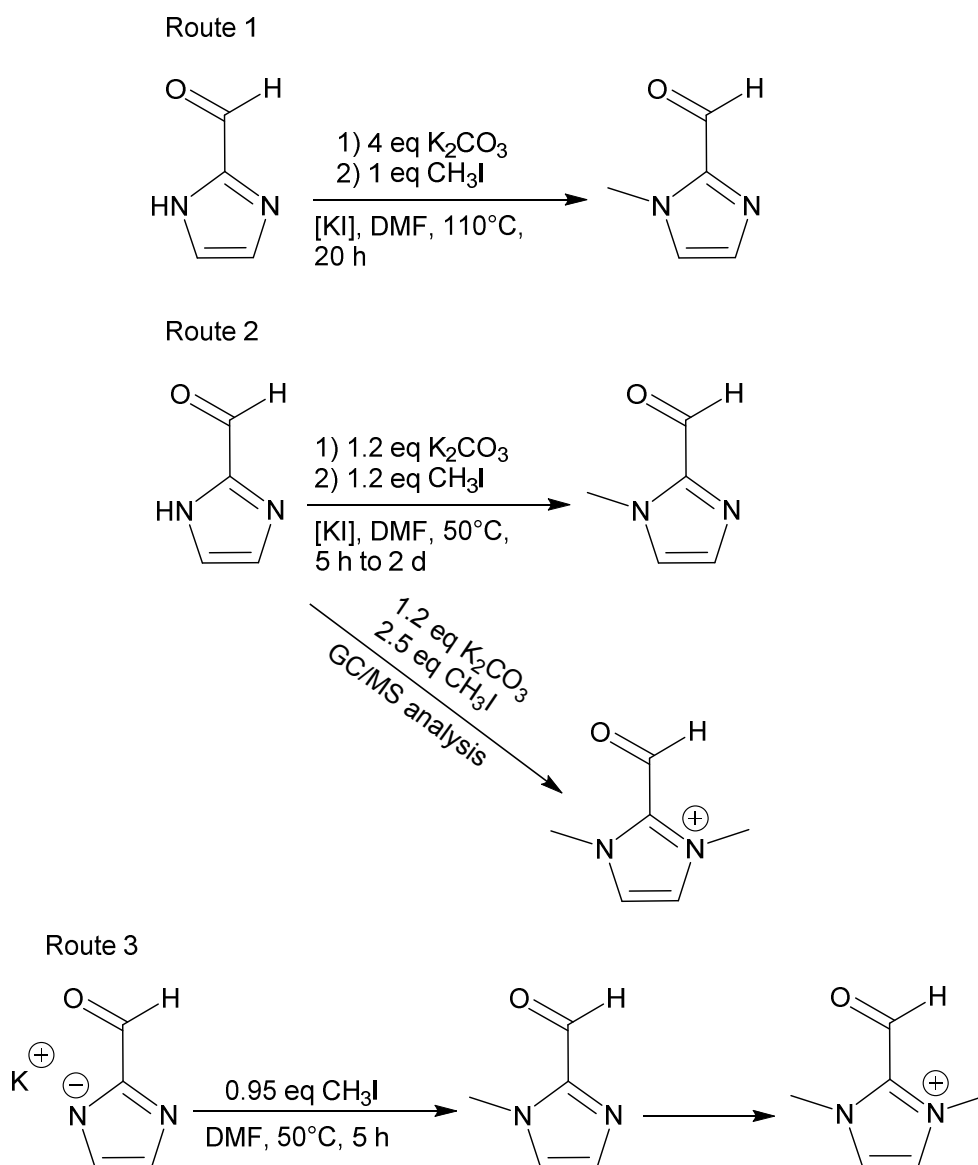
Figure 17. Imidazolyl containing ligands applied in the activation of oxygen. ^[128–130]

3.1.1 Optimisation of reaction conditions for the synthesis of 1-methyl-2-imidazolecarboxaldehyde

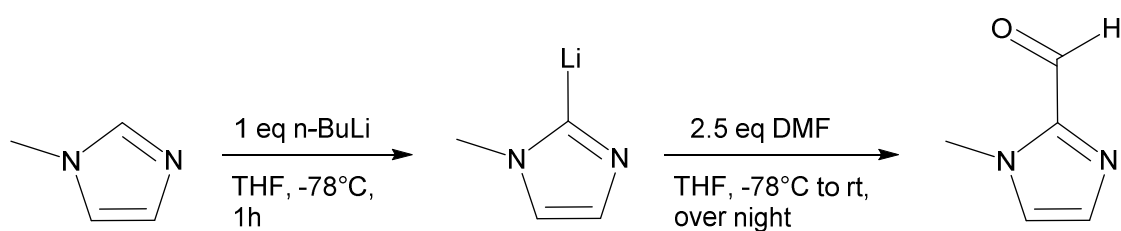
The ligand synthesis follows the route of Herres-Pawlis *et al.*,^[117] in which substituted pyrazoles are treated with sodium hydride and thionyl chloride, before the aldehyde component is added.

The preparation of desired aldehyde component 1-methylimidazole-2-carboxaldehyde was tried in three different ways (Scheme 11). To begin with, 2-imidazolecarboxaldehyde was alkylated with methyl iodide, following the synthesis of Babich *et al.*^[132] Thereby 2-imidazolecarboxaldehyde is dissolved in DMF and treated with an excess of potassium carbonate as a base, as well as catalytic amounts of potassium iodide and equimolar amounts of methyl iodide. The resulting mixture is heated to 110°C over night. Extraction of the product was tried with ethyl acetate, but resulted in extremely low yields. Another approach followed an advanced route, in which reaction conditions were different and adapted from [133]. Here, the reaction mixture was heated to only 50°C for 5 hours and the amount of added base was reduced, but resulted in low yields again. GC/MS spectroscopic analysis showed a nearly full conversion to the dimethylated product. Expansion of the reaction time to two days did not show any difference. Route 3 shows a modification of the reactant, which was the already deprotonated imidazolecarboxaldehyde. Here, reaction with a slight shortage of methyl iodide resulted in 45% of the desired product, but also showed a high amount of dimethylated product again.

In the light of these results, yet another approach was tried, where the starting compound was substituted by 1-methylimidazole. Applying the protocol of Brook^[134], 1-methylimidazole was deprotonated regioselectively with *n*-butyllithium, followed by the addition of an excess of DMF that functions as a synthetic equivalent of the carbonyl group, resulting in 60% yield (Scheme 12).



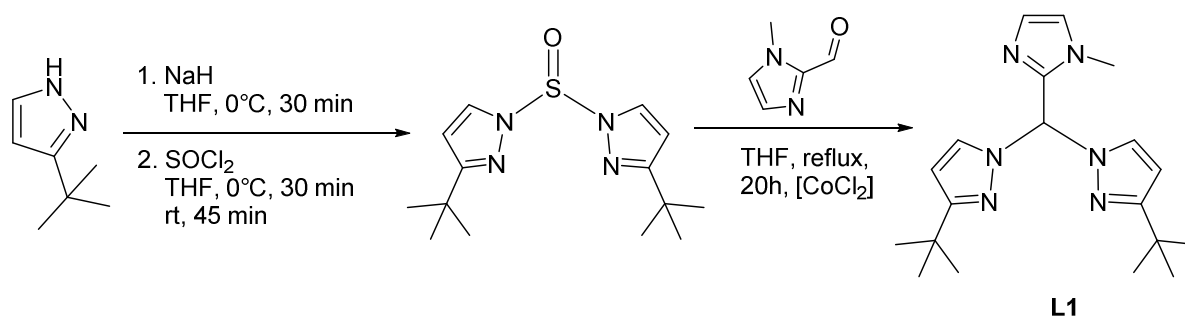
Scheme 11. Different routes for the synthesis of 1-methyl-2-imidazolecarboxaldehyde.



Scheme 12. Applied route for the synthesis of 1-methyl-2-imidazolecarboxaldehyde.

3.1.2 Structural characterisation of $\text{HC}(3\text{-}t\text{BuPz})_2(1\text{-MeIm})$ and $[\text{CuCl}_2\{\text{HC}(3\text{-}t\text{BuPz})_2(1\text{-MeIm})\}]$

Ligand **L1** was prepared like mentioned above, by treating the substituted pyrazolid with thionylchloride, resulting in the sulfoxide. Under reflux conditions and cobalt-catalysis, addition of 1-methyl-2-imidazolecarboxaldehyde yielded the bis(pyrazolyl)methane ligand $\text{HC}(3\text{-}t\text{BuPz})_2(1\text{-MeIm})$ (**L1**) as single crystals suitable for X-ray diffraction analysis (Scheme 13, Figure 18). A detailed mechanism for this reaction is shown in Scheme 10 in the introduction.



Scheme 13. Synthesis of $[\text{HC}(3\text{-}t\text{BuPz})_2(1\text{-MeIm})]$ (**L1**).

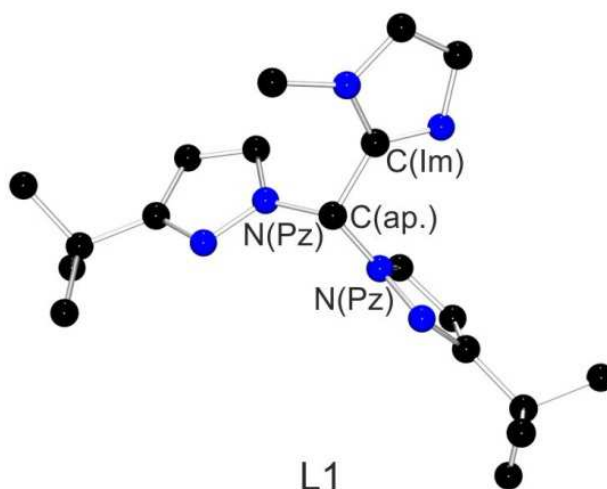


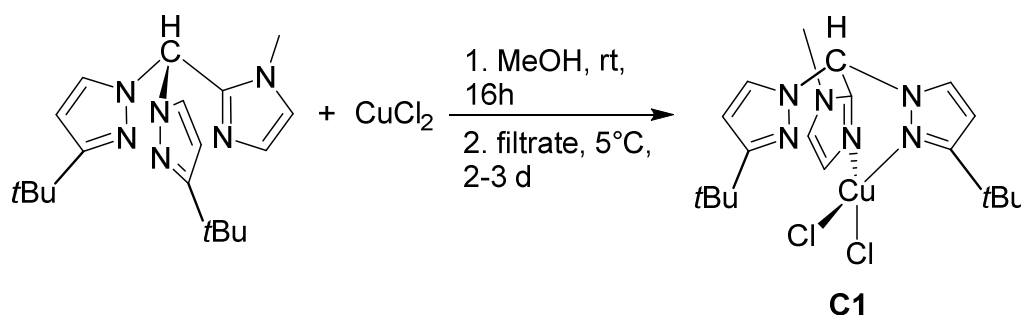
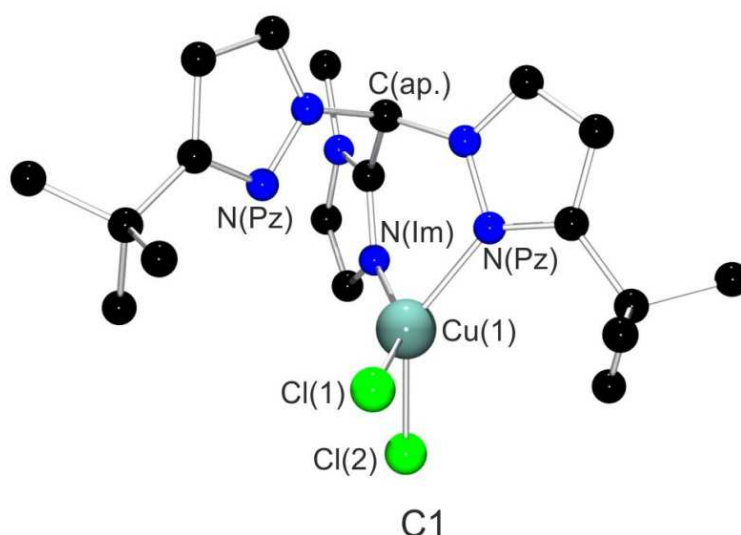
Figure 18. Molecular structure of **L1**.

L1 crystallises triclinically in the space group $P\bar{1}$ as clear, yellowish crystals. The apical C-atom is surrounded by two pyrazolyl nitrogens and one imidazole carbon in an almost perfect tetrahedral fashion (Table 4). Compared to other known bis(pyrazolyl)methanes, bond lengths are in the common range.^[117]

Table 4. Selected bond lengths and angles of **L1.**

Bond lengths [Å]		Bond angles [°]	
$C_{ap}-N_{Pz}$	1.450(2) 1.451(2)	$N_{Pz}-C_{ap}-N_{Pz}$	111.4(1)
$C_{ap}-C_{Im}$	1.507(2)		
$N_{Pz}-N_{Pz}$	1.358(2) 1.367(2)	$N_{Pz}-C_{ap}-C_{Im}$	109.9(1) 110.7(1)

Upon reaction of **L1** with $CuCl_2$ in methanol, single crystals of $[CuCl_2\{HC(3-*t*BuPz)_2(1-MeIm)\}]$ (**C1**) suitable for X-ray crystallography have been obtained from the reaction mixture. **C1** crystallises triclinically in the space group $P\bar{1}$ as dark green crystals, containing two units per elementary cell (Scheme 14, Figure 19). Table 5 lists important bond lengths and angles.

**Scheme 14. Synthesis of $[CuCl_2\{HC(3-*t*BuPz)_2(1-MeIm)\}]$ (**C1**).****Figure 19. Molecular structure of $[CuCl_2\{HC(3-*t*BuPz)_2(1-MeIm)\}]$ (**C1**).**

In **C1**, the Cu-atom is coordinated monofacially in a fourfold fashion by two chloride atoms and two nitrogen donors. One nitrogen donor belongs to the *tert*butylpyrazolyl-moiety and one to the imidazolyl-moiety. The second pyrazolyl moiety is in proximity, with a $Cu-N_{Pz}$

distance of 3.41 Å, but non-coordinating, leading to a four-coordinate neutral CuCl₂-complex.

Table 5. Selected bond lengths and angles for C1.

Bond lengths [Å]	Experimental	Calculated [Gaussian09, TPSSh, 6-31G(d)] ^{a[135]}
Cu-Cl(1)	2.225(1)	2.240
Cu-Cl(2)	2.251(1)	2.218
Cu-N _{Pz}	2.044(3)	2.000
Cu-N _{Im}	1.957(3)	1.961
C _{ap} -N _{Pz}	1.455(4)	1.457
	1.462(4)	1.459
C _{ap} -C _{Im}	1.502(5)	1.502
Bond angles [°]		
Cl(1)-Cu-Cl(2)	97.3(1)	103.3
Cl(1)-Cu-N _{Pz}	98.8(1)	95.5
Cl(1)-Cu-N _{Im}	150.8(1)	137.4
Cl(2)-Cu-N _{Pz}	141.7(1)	146.8
Cl(2)-Cu-N _{Im}	93.4(1)	94.8
N _{Pz} -Cu-N _{Im}	89.3(1)	89.3
τ ₄ ^[136]	0.479	0.54
[a] this combination was found to be the most accurate in the benchmarking of Cu ₂ O ₂ bis(pyrazolyl)methane complexes. ^[137]		

The Cu-N_{Im} bond is shorter than the Cu-N_{Pz} bond and also shorter than other common Cu-N_{donor} bonds (e.g. Cu-N_{Py}). This indicates a stronger donor-ability for the imidazole donor, which will be discussed later on. Bond angles around the copper atom vary from 90–150°, showing the distortion of the structure. Based on the crystal structure of **C1**, a theoretical structural optimisation was performed. The results are also displayed in Table 5. Comparing experimental and calculated bond lengths for **C1**, no significant deviation can be detected, because the only bond length predicted shorter, is the Cu-Cl(2) one. For bond angles, the calculations are not as accurate, but clearly show the same dispersion as in the molecular structure of **C1**. For example the N_{Pz}-Cu-N_{Im} and Cl(2)-Cu-N_{Im} angles are predicted almost correct, while all others deviate not more than 6°, excluding the Cl(1)-Cu-N_{Im} angle.

3.1.3 Definition of the τ -parameter

In order to compare coordination geometries of complexes, τ_4 - or τ_5 -values are calculated, depending on the number of direct bonding partners. Hereby the two largest bond angles around the central metal are determined and inserted into the according formula (equations **1** and **2**). Reedijk *et al.* defined the structural parameter τ_5 in 1984.^[138] Its values can range from 0 to 1, 0 representing a trigonal-bipyramidal coordination-sphere and 1 a square-pyramidal one. In 2007, Houser *et al.* invented a formula for a τ_4 -value that is based on equation **2**.^[136] τ_4 also ranges from 0 to 1, with 0 indicating a square-planar geometry and 1 being the result of a perfect tetrahedron.

$$\tau_5 = \frac{\beta - \alpha}{60} \quad (1)^{[138]}$$

$$\tau_4 = \frac{360^\circ - (\alpha + \beta)}{141^\circ} \quad (2)^{[136]}$$

The τ_4 -value calculated for **C1** is 0.48. Thus complex **C1** can only be referred to as distorted, as its geometry is located between tetrahedral and square-planar and cannot be assigned to one in particular. This is also reflected by the diverse bond angles in complex **C1**.

3.2 Efficient biomimetic hydroxylation catalysis with a bis(pyrazolyl)imidazolymethanecopper-peroxide complex

3.2.1 General Introduction

All Cu_2O_2 -compounds show very distinct spectroscopic features which are visible in UV/Vis- or resonance Raman spectroscopy, so that their differentiation is relatively easy. For bis(pyrazolyl)methane-peroxo complexes the first indicator of their formation is their colour, which is deep purple. Consistent with the colour, the UV/Vis spectrum shows two characteristic bands due to ligand to metal charge-transfer transitions (LMCTs). More precisely, electron density is shifted from occupied, antibonding π^* -orbitals of oxygen to $d_{x^2-y^2}$ orbitals of copper (Figure 20).^[31] For most Cu-peroxo complexes the two UV-bands are located at 350 nm and 550 nm with an intensity ratio of 20:1.^[55] The stronger band stems from a $\pi_{\sigma}^* \rightarrow d_{x^2-y^2}$ transition, which is symmetry allowed, in contrast to the $\pi_{\nu}^* \rightarrow d_{x^2-y^2}$ transition, where the orbitals have no overlap. The generally high extinction coefficients suggest a good σ -donor ability of the peroxide unit. Small O-O-bond frequencies that appear in resonance Raman spectra point to a weak O-O-bond, which can be explained by the partial occupation of the antibonding σ^* -orbital of the peroxide, resulting from a π -backbonding from Cu to the peroxide unit (Figure 20).^[31]

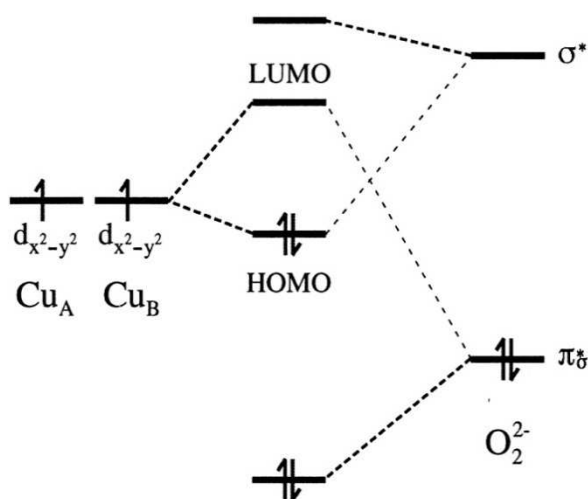
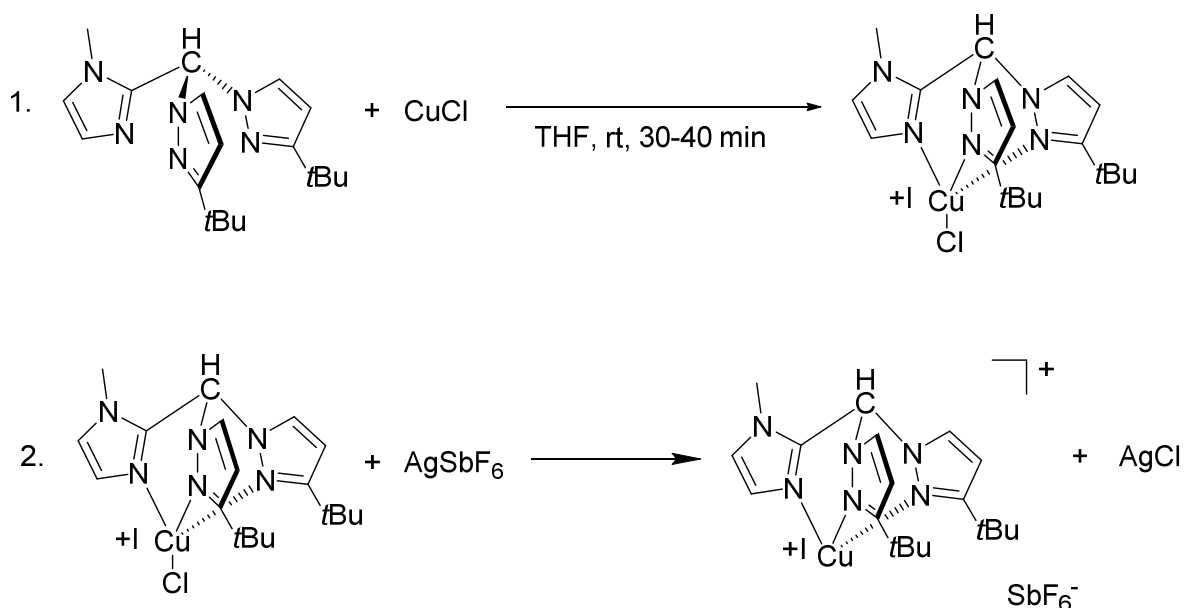


Figure 20. Electronic structure of the peroxide-Cu(II) bond in $(\mu\text{-}\eta^2\text{:}\eta^2)$ bridged species. ^{adapted from [31]}

3.2.2 Characterisation of $[\text{Cu}_2\text{O}_2\{\text{HC}(3\text{-}t\text{BuPz})_2(1\text{-MeIm})\}_2][\text{SbF}_6]_2$

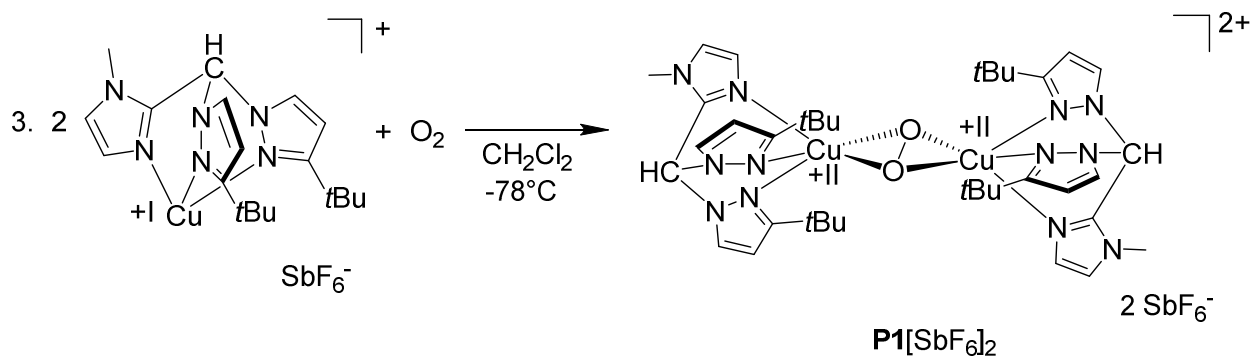
3.2.2.1 UV/Vis Spectroscopy

Analogous to the method that was introduced by Lehnert in 2006^[62], the peroxo species is generated *in situ* starting from the bis(pyrazolyl)methane ligand $\text{HC}(3\text{-}t\text{BuPz})_2(1\text{-MeIm})$, which is dissolved in THF and then combined with CuCl (Scheme 15). The suspension is stirred for 40 min to give the CuCl -complex, before it is treated with a solution of AgSbF_6 , in order to generate a free coordination site at the copper atom, due to the non-coordinating SbF_6^- -anion (Scheme 15).



Scheme 15. Synthesis of the precursor complex $[\text{Cu}\{\text{HC}(3\text{-}t\text{BuPz})_2(1\text{-MeIm})\}][\text{SbF}_6]$.

This precursor is then injected into an O_2 -saturated CH_2Cl_2 -solution at -78°C (Scheme 16), resulting in an immediate colour change of the solution to deep purple.



Scheme 16. Formation of $[\text{Cu}_2\text{O}_2\{\text{HC}(3\text{-}t\text{BuPz})_2(1\text{-MeIm})\}_2][\text{SbF}_6]_2$ (**P1** $[\text{SbF}_6]_2$).

The formation of the resulting peroxo complex $[\text{Cu}_2\text{O}_2\{\text{HC}(3\text{-}t\text{BuPz})_2(1\text{-MeIm})\}_2][\text{SbF}_6]_2$ (**P1** $[\text{SbF}_6]_2$) is monitored *via* UV/Vis spectroscopy (Figure 21).

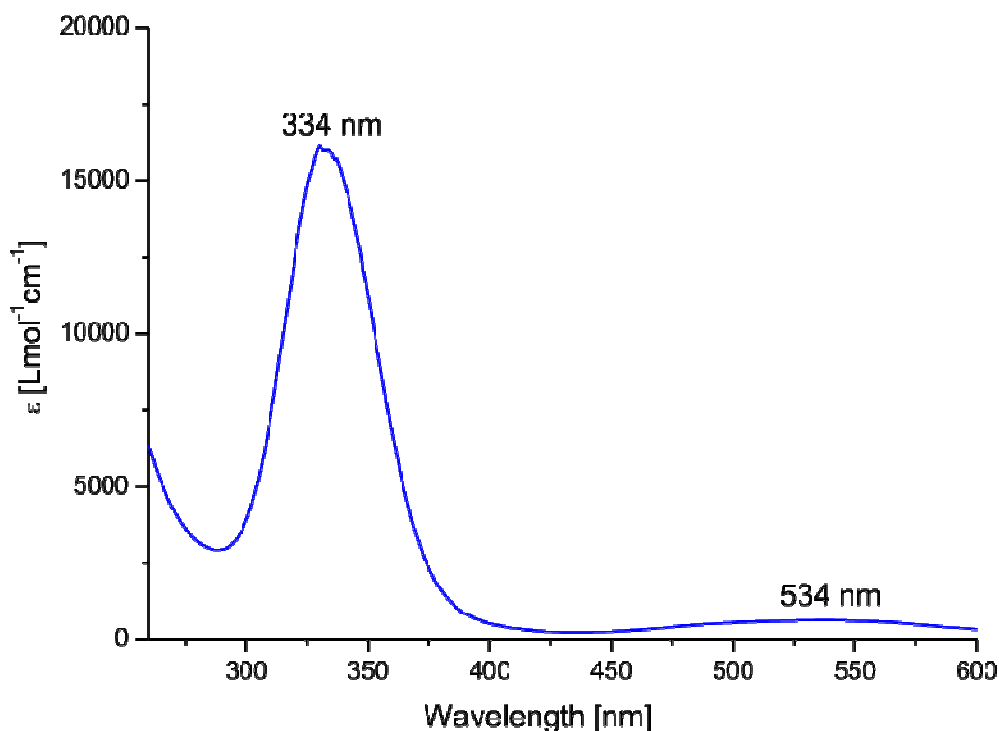


Figure 21. UV/Vis spectrum of $[\text{Cu}_2\text{O}_2\{\text{HC}(3\text{-}t\text{BuPz})_2(1\text{-MeIm})\}_2][\text{SbF}_6]_2$ (**P1** $[\text{SbF}_6]_2$).

The species **P1** $[\text{SbF}_6]_2$ could be generated to 85% at -78°C and is stable at that temperature for several days. The yield of the peroxo complex was calculated based on the extinction coefficient of $[\text{Cu}_2\text{O}_2\text{L5}_2][\text{SbF}_6]_2$.^[125] **P1** $[\text{SbF}_6]_2$ is built very fast, so that formation is completed in 10–15 min.

The decay was measured at 0°C ; at room temperature it is too fast. Decomposition of **P1** $[\text{SbF}_6]_2$ follows an exponential decay of the first order. This can be described with the following formula (3):

$$A(t) = A_0 \cdot e^{\left(\frac{-t}{\tau}\right)} \quad (3)$$

The half-life of a species can be calculated according to formula 4.

$$t_{\frac{1}{2}} = \ln 2 \cdot \tau \quad (4)$$

The half-life of **P1**[SbF₆]₂ was calculated to 3.8 min. The UV/Vis-spectrum shows two bands at 334 nm and at 534 nm. The deep violet colour of the solution and the existence of the UV-bands in this region, separated by 200 nm clearly show the formation of a peroxo complex. As it is known from other familiar copper(II)-peroxide complexes, their UV/Vis spectra exhibit intense oxygen to copper charge-transfer absorptions, which are consistent with the presence of highly covalent Cu-O-bonds.^[55] The enzymes oxyTy and oxyHc also show similar UV transitions.^[139,140]

3.2.2.2 Explanation of the UV/Vis band-shift

A striking difference however is the blue-shift of the UV/Vis bands compared to other known Cu₂O₂-peroxo species. In order to understand this phenomenon, theoretical calculations were performed, including second order perturbation theory calculations of **C1** and **P1** (Table 6).^[141] Table 6 shows for **C1** that N_{Im} has a greater donor ability, which is reflected in the shorter Cu-N_{Im} compared to the Cu-N_{Pz} bond length. This factor is assumed in **P1** as well. However, here NBO calculations show higher CT energies for pyrazolyl. This seems to be the case when the imidazolyl units are located at the axial positions. This conformer (Figure 22) was used nevertheless for all theoretical investigations, because it is the energetically favourable one (see also below). Reasons behind this are under current investigation by Herres-Pawlis *et al.*^[141]

Table 6. Charge-transfer energies for C1 and P1. (Gaussian09, TPSSH/6-31G(d) and NBO 6.0).^[135,137,142]

CT energies [kcal mol ⁻¹]		
	C1	P1 ^[141]
N _{Pz} → Cu	21.1	36.8/38.6
N _{Im} → Cu	22.4	23.7/23.9

Continuative theoretical investigations that were performed are TD-DFT calculations in order to predict the UV/Vis spectrum of **P1**[SbF₆]₂ and NTO analysis to show the molecular orbitals involved in UV transitions.

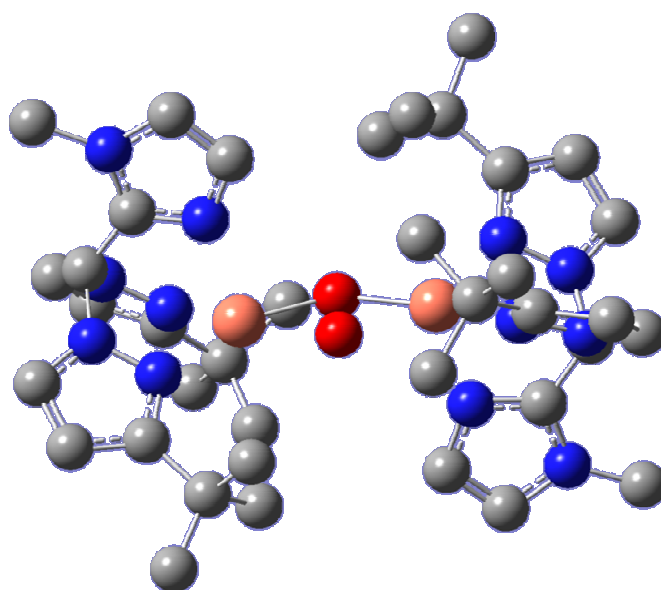


Figure 22. Theoretical model of $[\text{Cu}_2\text{O}_2\{\text{HC}(3\text{-tBuPz})_2(1\text{-Melm})\}_2]^{2+}$ (P1). (Gaussian09, TPSSh/6-31G(d). Hydrogen atoms are omitted for clarity).^[135,137,141]

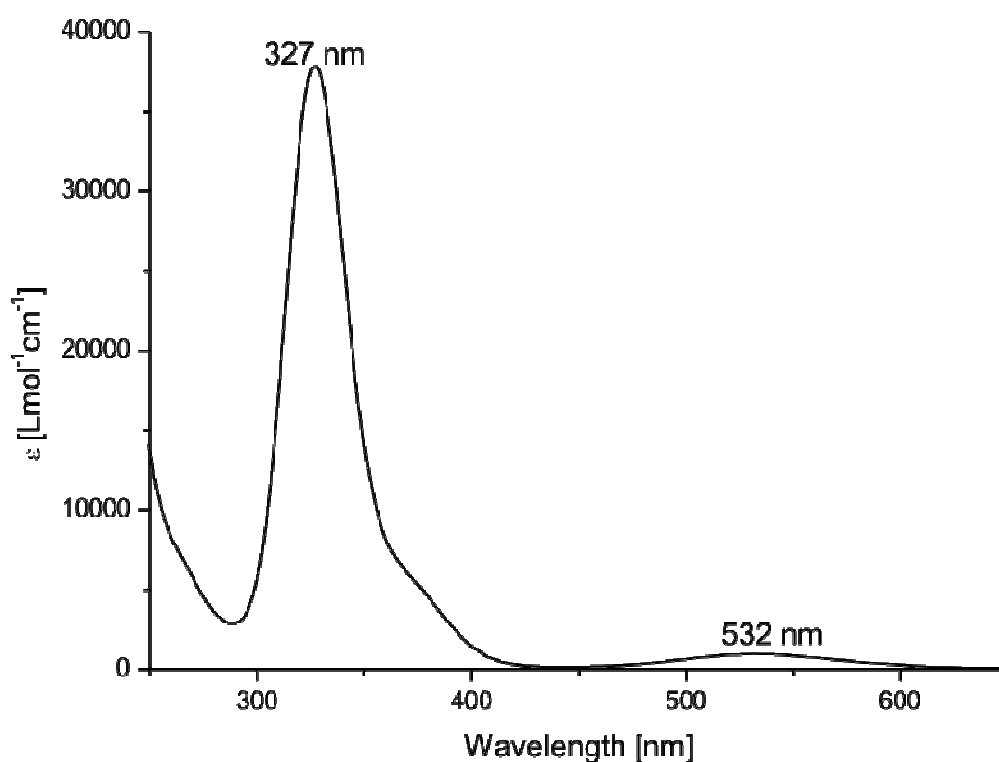


Figure 23. Calculated UV/Vis spectrum of $[\text{Cu}_2\text{O}_2\{\text{HC}(3\text{-tBuPz})_2(1\text{-Melm})\}_2][\text{SbF}_6]_2$ (P1[SbF₆]₂) (TD-DFT, Gaussian09, TPSSh, 6-31G(d)).^[135,137,141]

TD-DFT calculations were performed with the TPSSh/6-31G(d) combination.^[137] The resulting spectrum is shown in Figure 23. It is in excellent agreement with the experimental one (Figure 21) and also predicts the blue-shift of the UV/Vis bands. Even the intensity ratio is

well predicted. Figure 22 shows the model of $[\text{Cu}_2\text{O}_2\{\text{HC}(3\text{-tBuPz})_2(1\text{-Melm})\}_2][\text{SbF}_6]_2$, on which theoretical calculations were based. 1-Methylimidazolyl moieties reside on the axial position at the copper atoms, because this conformer is energetically more stable.

Key parameters deduced from Gaussian calculations amongst others are bond lengths and atom distances of the peroxo core of **P1** $[\text{SbF}_6]_2$ (Table 7).^[141]

Table 7. Calculated atom distances in P1 (Gaussian09, TPSSh, 6-31G(d)).^[135,137,141]

Distance [Å]	Broken-symmetry	Singlet
Cu --- Cu	3.572	3.530
O-O	1.471	1.451

Distances for the singlet state are slightly shorter than for broken-symmetry. Analysis of X-ray absorption spectra (see 3.2.2.5) shows an experimental Cu-Cu distance of 3.69(6) Å, which is closer to the theoretical value for broken-symmetry **P1**.

Energy comparison between the singlet $(\mu\text{-}\eta^2\text{:}\eta^2)$ -peroxo and bis(μ -oxo) compound indicates a 6.16 kcal/mol more stable peroxo complex, which is also the only species that is observed experimentally. The energy analysis of broken-symmetry $(\mu\text{-}\eta^2\text{:}\eta^2)$ -peroxo versus singlet $(\mu\text{-}\eta^2\text{:}\eta^2)$ -peroxo showed a 2.96 kcal mol⁻¹ more stable broken-symmetry state.^[141]

3.2.2.3 Natural transition orbital (NTO) analysis

In order to understand the band-shifting effect in more detail, a Natural Transition Orbital (NTO) analysis was performed as well^[141], which was introduced in 2003 by R. Martin.^[143] To understand the benefits of NTO analysis, other common methods to analyse optical excitations should be mentioned here as well.

In order to describe ground states of electronic systems, the *ab initio* approach (Hartree-Fock) often is too vague and therefore is combined with semi-empirical Hamiltonians. For the description of excited states a similar expansion can be used, called the random-phase approximation (RPA). Is it applied to reference states derived from density functional theory (DFT) and is referred to as time-dependent DFT (TD-DFT). This method is more precise than the analogous method, where RPA is used on Hartree-Fock reference states. Such calculations result in an excitation energy, paired with several coefficients, in order to

determine the contribution each particle-hole pair makes to the excited state excitation amplitudes. Evaluation of these calculations however is often difficult, as no dominant configuration can be found amongst the excitation amplitudes, making it impossible to determine the qualitative nature of an excited state.

Therefore Martin developed the natural transition orbital analysis, which results in a compact orbital representation for the electronic transition density matrix. Here a maximal correspondence is achieved for the excited particle and the empty hole.

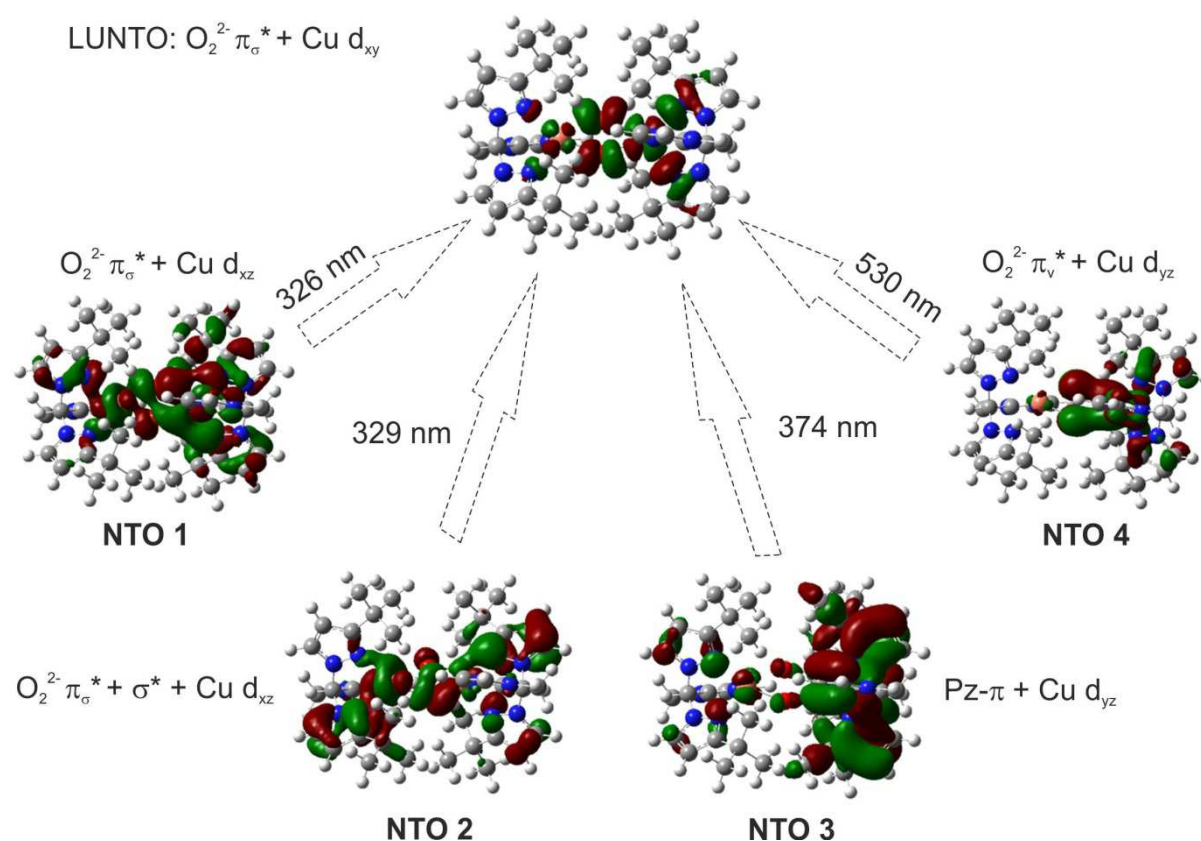


Figure 24. NTO-analysis of $[Cu_2O_2\{HC(3-tBuPz)_2(1-Melm)\}_2]^{2+}$ (P1).^[141]

Calculations on the geometry-optimised coordinates were performed with the TPSSh functional using the broken-symmetry approach, combined with the 6-31G(d) basis set.^[137]

Figure 24 shows the results of this calculation. LUNTO stands for “*Lowest Unoccupied Natural Transition Orbital*” and symbolises the orbital that accepts electrons in the transition process that is investigated. In our case these are both transitions visible in the UV/Vis spectrum. NTO-analysis provided four electronic transitions. The ones at 326, 329 and 374 nm unite to the transition at 334 nm in the experimental spectrum, which is pretty accurate as the arithmetic average of these three is 343 and therefore only 9 nm above the

experimental value. The second transition is predicted very well too, as the deviation to the experimental value is only 4 nm. Each NTO consists of fractions of several orbital types of copper and the oxygen-peroxide unit. The LUNTO for example is composed of π_{σ}^* orbital parts at the oxygen atoms and d_{xy} orbitals at the copper atoms. The less intensive transition at 534 nm originates from an NTO showing oxygen π_{ν}^* and Cu d_{xy} characteristics (**NTO 4**). For NTOs **1–3** it is not as easy to see the parts contributing to the transition orbital. **NTO 1** shows elements of π_{σ}^* at the oxygen atoms and of d_{xz} at copper. In **NTO 2** the same applies, with an additional O- σ^* fraction mixed in. **NTO 3** does not incorporate any O-orbital parts, but shows participation of the ligand. This π -contribution has been observed before and was assigned to a pyrazolyl/pyridinyl (in this case pyrazolyl/imidazolyl) $\pi^* \rightarrow d_{xy}$ transition.^[18,144]

3.2.2.4 Mass spectrometry

Further analyses of **P1**[SbF₆]₂ included cryo-UHR ESI mass spectrometry (Figure 24), which confirms the formation of a $(\mu-\eta^2:\eta^2)$ -copper(II)-peroxo core. These measurements have been performed at the FAU University of Erlangen-Nürnberg in collaboration with Prof. Dr. Ivana Ivanović-Burmazović.^[145]

Table 8 displays the main species contributing to the mass spectrum. The different isotopes of carbon, copper and antimony are taken into account.

Table 8. Most important isotopes of [Cu₂O₂{HC(3-*t*BuPz)₂(1-Melm)}₂][SbF₆]⁺.

Total formula	m/z (calculated)
C ₃₈ H ₅₆ ⁶³ Cu ₂ N ₁₂ O ₂ ¹²¹ SbF ₆	1073.2184
C ₃₇ ¹³ CH ₅₆ ⁶³ Cu ₂ N ₁₂ O ₂ ¹²¹ SbF ₆	1074.2217
C ₃₈ H ₅₆ ⁶³ Cu ⁶⁵ CuN ₁₂ O ₂ ¹²¹ SbF ₆	1075.2166
C ₃₈ H ₅₆ ⁶³ Cu ₂ N ₁₂ O ₂ ¹²³ SbF ₆	1075.2188
C ₃₇ ¹³ CH ₅₆ ⁶³ Cu ⁶⁵ CuN ₁₂ O ₂ ¹²¹ SbF ₆	1076.2199
C ₃₇ ¹³ CH ₅₆ ⁶³ Cu ₂ N ₁₂ O ₂ ¹²³ SbF ₆	1076.2221
C ₃₈ H ₅₆ ⁶³ Cu ⁶⁵ CuN ₁₂ O ₂ ¹²³ SbF ₆	1077.2170
C ₃₇ ¹³ CH ₅₆ ⁶³ Cu ⁶⁵ CuN ₁₂ O ₂ ¹²³ SbF ₆	1078.2203

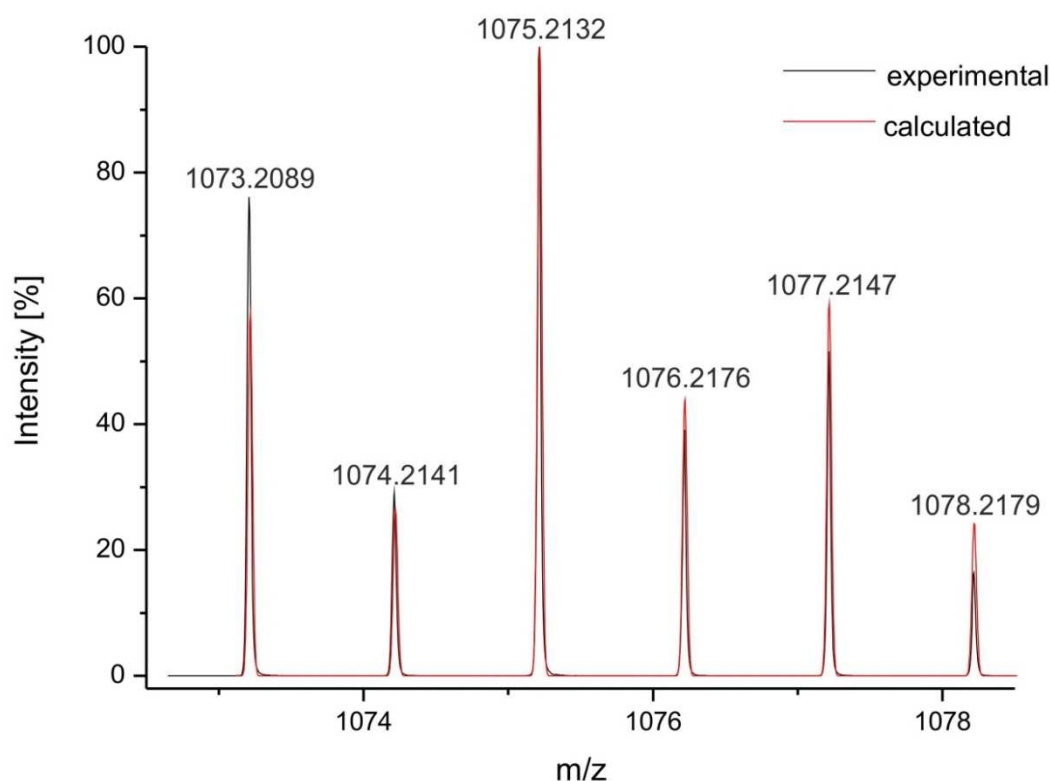


Figure 25. Cryo UHR-ESI mass spectrum of $[\text{Cu}_2\text{O}_2\{\text{HC}(\text{3-}t\text{BuPz})_2(\text{1-Melm})\}_2][\text{SbF}_6]^+$.^[145]

Figure 25 shows the excellent accordance of calculated and experimental ESI mass spectra.

3.2.2.5 X-ray absorption spectroscopy^[146,147]

Alongside the analytical methods mentioned above, X-ray absorption spectroscopy was performed on a 10 mM CH_2Cl_2 solution of $[\text{Cu}_2\text{O}_2\{\text{HC}(\text{3-}t\text{BuPz})_2(\text{1-Melm})\}_2][\text{SbF}_6]_2$ in collaboration with Prof. Dr. M. Bauer (University of Paderborn) at the beamline BM23 of the European Synchrotron Radiation Facility ESRF in Grenoble.^[148] Two different X-ray absorption modes (XANES and EXAFS) provide conclusive evidence concerning the oxidation state of copper, as well as atom distances in the peroxide complex.

XAS spectroscopy is element specific, because every element has its own distinct absorption edge. The absorption edge symbolises a drop in the transmitted X-ray energy, which arises, when the X-ray energy matches the binding energy of an electron of an atom in the sample, which at once increases the amount of absorbed X-rays.^[149]

Figure 26 shows the Cu K-edge XANES spectrum of sample **P1**. XANES stands for "**X-ray Absorption Near Edge Structure**", which analyses the X-ray absorption really close to the absorption edge.

The principle behind this measurement method is the absorption of an X-ray photon by the condensed matter of the sample, generating a core hole. This excited state has a very short life-time and the core hole is again filled with an electron from another level followed by emission of fluorescence or an Auger electron. Auger electrons are energetic electrons emitted from an excited atom after a series of internal relaxation events.

Figure 26 displays a signal at 8978 eV, which is of low intensity. This points to the dipole-forbidden 1s-3d quadrupole transition, which is characteristic of Cu(II).^[150–152] At 8937 eV only a weak shoulder is visible. This possible 1s→4p+LMCT shake-down transition^[153] would show a sharp signal for the oxidation state +3, which therefore is ruled out. Furthermore Solomon *et al.* and Meyer *et al.* have observed a similar white line morphology for dinuclear ($\mu\text{-}\eta^2\text{:}\eta^2$) side-on complexes.^[60,154] All in all the features of the XANES spectrum displayed in Figure 26 lead to the conclusion of an oxidation state for copper of +2.

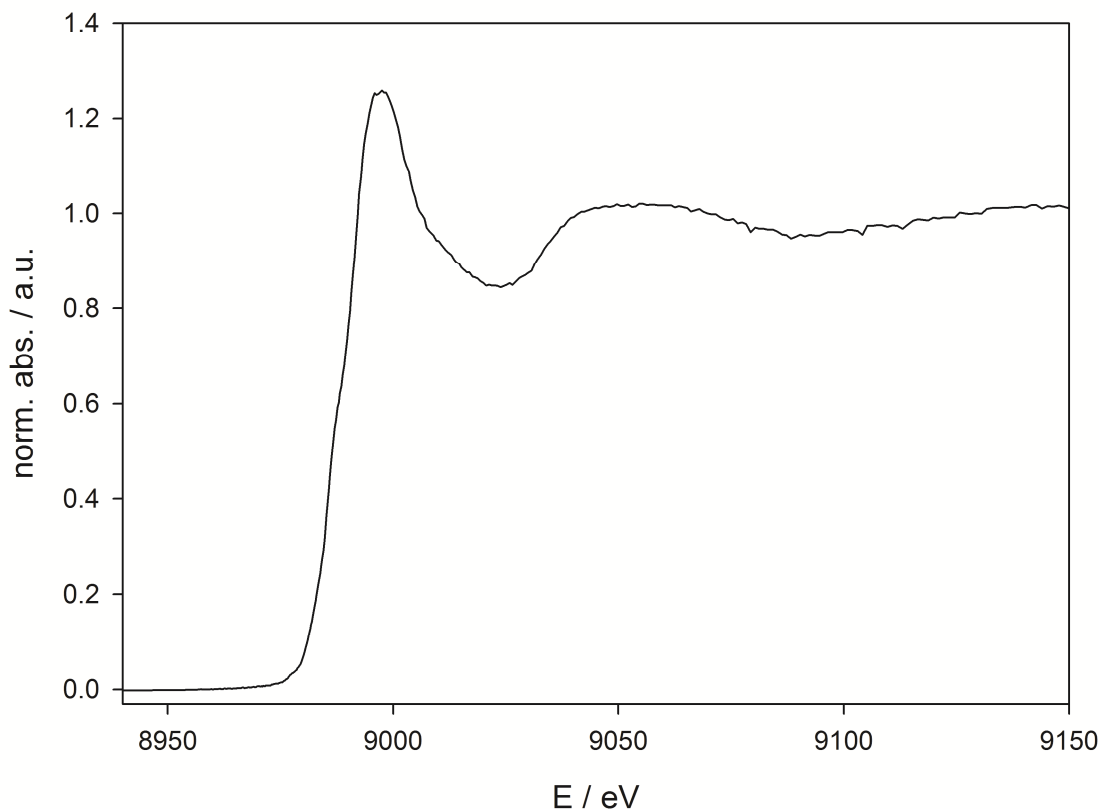


Figure 26. Cu K-edge XANES spectrum of **P1**[SbF₆]₂.^[148]

The EXAFS spectrum and the according Fourier transformed function of **P1** are given in Figure 27 and the extracted structural parameters are listed in Table 9. The abbreviation EXAFS stands for "*Extended X-Ray Absorption Fine Structure*", which analyses, as the name suggests, the edge-near fine structure. This method gives information about the number, type and distance of neighbouring atoms.

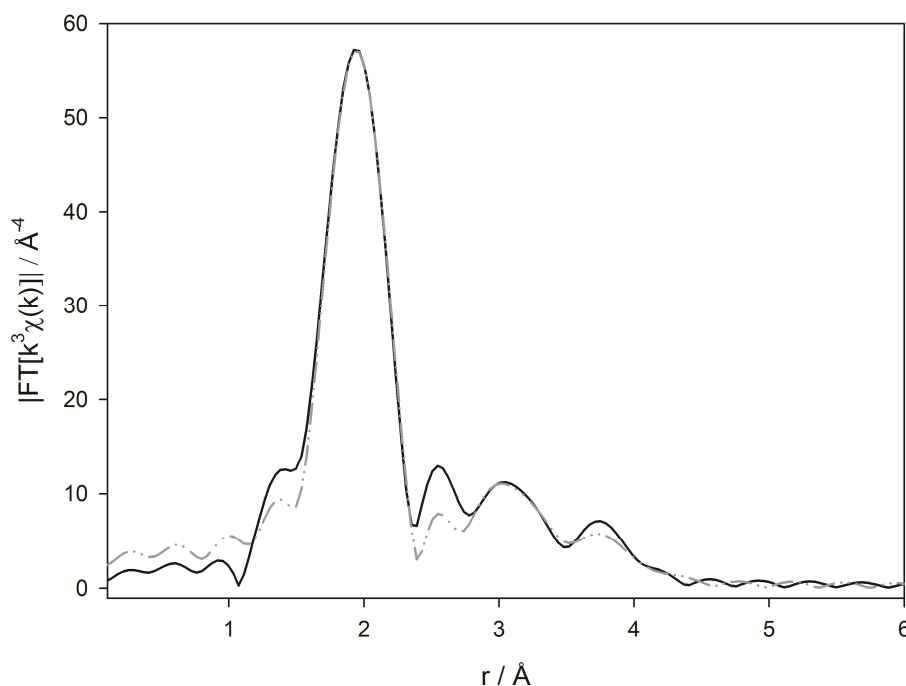


Figure 27. Filtered Fourier backtransformed Cu K-edge EXAFS spectrum (black solid line: experiment, grey dashed line: fitted function) of $\text{P1}[\text{SbF}_6]_2$.^[148]

In Figure 27 four peaks can be seen. At an average distance of 1.99 Å the oxygen atoms composing the peroxo core and the ligand's nitrogen atoms are located. At 2.92 and 3.37 Å two more combined ligand C/N shells give a signal in the *r*-space, which is in reasonable agreement with the calculated structure for **P1**. The dimeric structure of **P1** in solution is proven by a Cu-Cu distance of 3.69 Å. Higher distance multiple scattering shells were removed by Fourier filtering.^[152,154]

Table 9. Structural parameters obtained by fitting the experimental EXAFS functions with theoretical models.^[148]

	Abs-Bs ^a	N(Bs) ^b	r(Abs-Bs) ^c [Å]	σ ^d [Å]	R ^e [%]
P1 [SbF ₆] ₂	Cu-N/O	5.4 ± 0.5	1.99 ± 0.02	0.063 ± 0.006	15.05
	Cu-C/N	1.4 ± 0.2	2.92 ± 0.03	0.032 ± 0.003	
	Cu-C/N	4.6 ± 0.9	3.37 ± 0.03	0.112 ± 0.012	
	Cu-Cu	1.3 ± 0.4	3.69 ± 0.06	0.110 ± 0.033	
^a Abs=X-ray absorbing atom, Bs=backscattering atom (neighbour). ^b Number of neighbour atoms. ^c Distance between Abs and Bs. ^d Debye-Waller like factor to account for disorder. ^e Quality of fit.					

3.2.3 Catalytic studies on $\mathbf{P1[SbF_6]_2}$

Functional enzyme models not only need to incorporate a model of the active centre of the enzyme, but also be able to execute the catalytic reactions of those. Figure 28 shows the *o*-form of tyrosinase again, depicting the Cu_2 -peroxide-centre and three histidine moieties on each copper atom. Based on this structure, the model complex $\mathbf{P1[SbF_6]_2}$ was designed. A possible reaction mechanism for the transformation of *p*-substituted phenolic compounds by such complexes is shown in Scheme 17. In addition to the substrate, NEt_3 is added in order to deprotonate the substrate before its reaction with the Cu-peroxo core. The use of this auxiliary base has been established by Réglier *et al.*^[77] and Tuzcek *et al.*^[78]

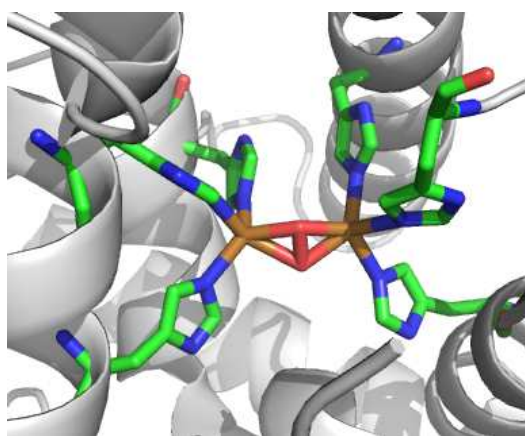
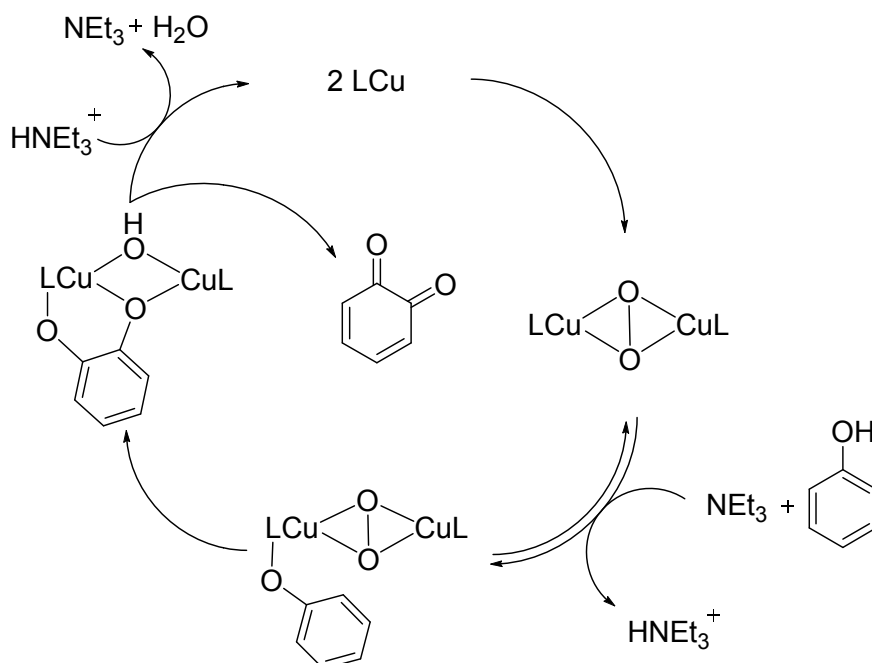


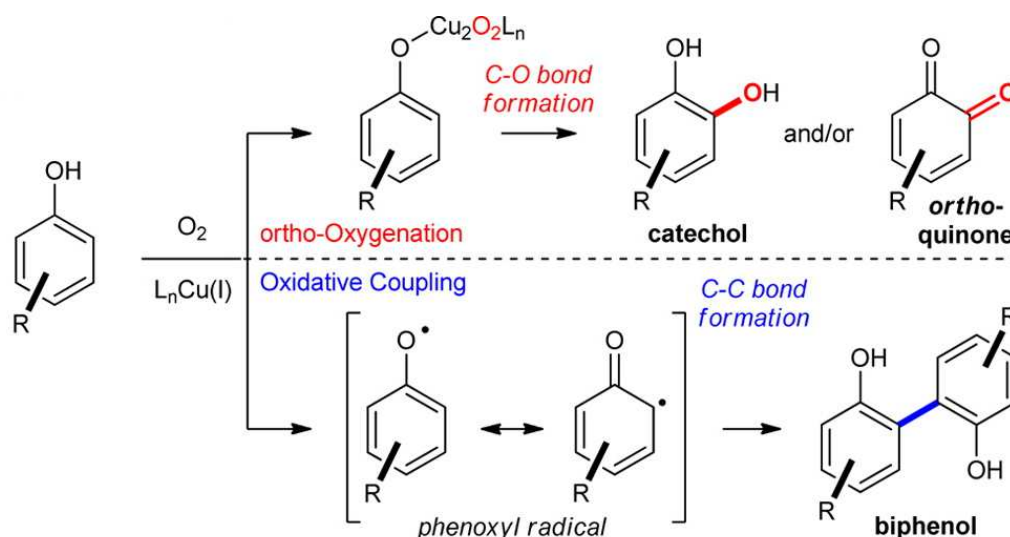
Figure 28. Structure of the active site of tyrosinase. Green: Carbon, blue: Nitrogen, orange: Copper, red: Oxygen.^[34]



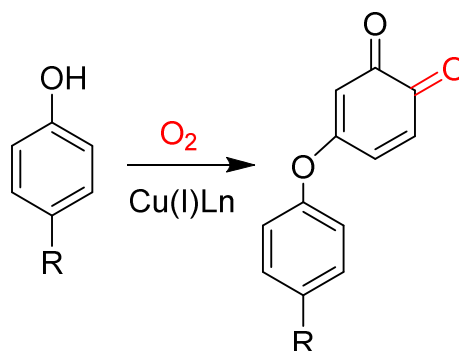
Scheme 17. Proposed reaction pathway for model complexes of tyrosinase. adapted from [46]

It was previously shown that an inner-sphere oxygen atom transfer (OAT) mechanism is present in the catalytic cycle of tyrosinase.^[31,46,53,155] Thereby, selective *ortho*-oxygenation of phenols is the result of an inner-sphere OAT between the $(\mu-\eta^2:\eta^2)$ -peroxodicopper(II) core and a phenolate. The other possible reaction way for OAT would be an outer-sphere pathway, which would generate free radicals leading to a C-C coupled product (Scheme 18) and neither to a catechol, nor a quinone. Therefore functional models for tyrosinase would have to be able to catalyse the reaction of phenols to quinones without the generation of C-C coupled byproducts.

Lumb *et al.* recently also studied catalytic reactions of substituted phenols with Cu(I)-iminopyridine ligand systems and O₂ as a tool for organic synthesis. They showed that in these reactions *para*-substituted phenols with moieties of different steric demands furnished *meta*-C-O-coupled quinones (Figure 29).^[80,156] These possible reaction products have to be taken into account in our studies as well.



Scheme 18. Competitive pathways in catalytic aerobic oxidations of phenols. ^{adapted from [156]}



Selection of moieties R: Et, *i*Pr, Cy, OMe, OBn

Figure 29. Reaction of *para*-substituted phenols with oxygen under Cu-catalysis. ^[80]

3.2.3.1 Catalytic oxidation of phenols to quinones

The ability to convert phenolic substrates into quinones was investigated by adding 25 eq of *p*-methoxyphenol and 50 eq of triethylamine.^[77,78,157] The formation of 1 eq of quinone in 45 min and 2 eq in 18h (Table 10) was detected.

This catalytic activity was calculated applying Lambert Beer's rule with an extinction coefficient for the quinone of $1700 \text{ Lmol}^{-1}\text{cm}^{-1}$.^[158] Formation of the quinone was followed by UV/Vis spectroscopy, due to the strong UV band of 4-methoxycyclohexa-3,5-diene-1,2-dione at 418 nm (Figure 30).

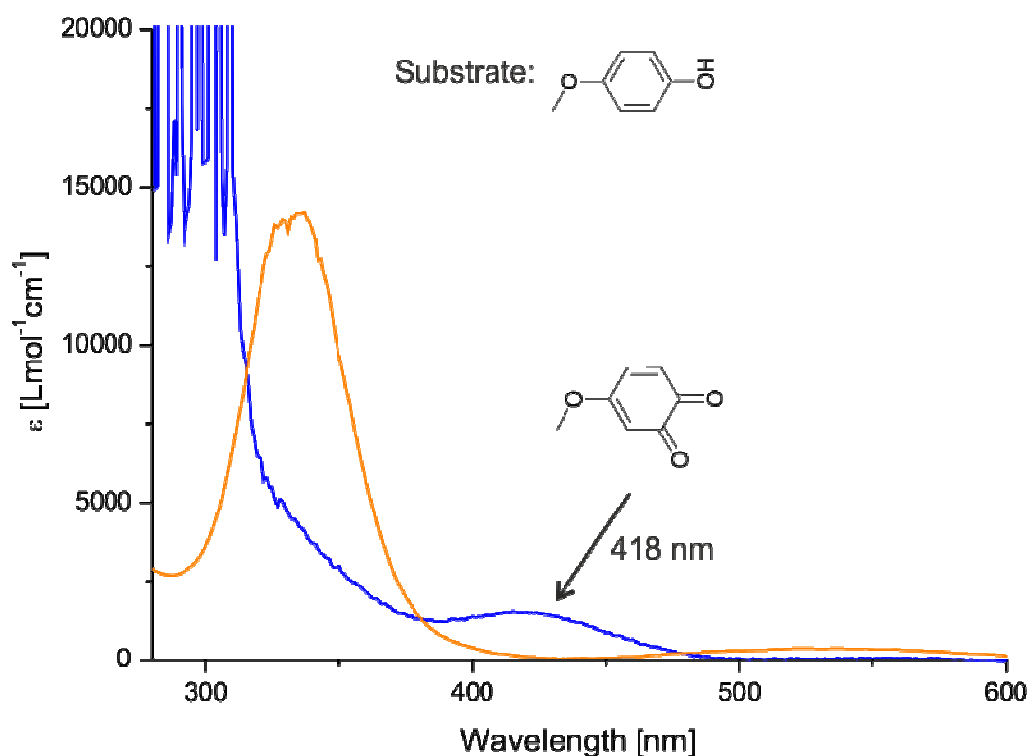


Figure 30. UV/Vis spectrum of the formation of $[\text{Cu}_2\text{O}_2\{\text{HC}(\text{3-}t\text{BuPz})_2(1\text{-MeIm})\}_2][\text{SbF}_6]_2$ (orange) and the formation of the quinone (blue). Between 260 and 310 nm the spectrum does not follow Lambert Beer's law due to high concentration.

Addition of 25 eq of 8-hydroxyquinoline and 50 eq of triethylamine under an oxygen pressure of 1 atm, leads to the formation of 14 eq of quinone in 20 min. Here as well, formation of the quinone naphthalene-1,2-dione with its strong band at 413 nm was followed UV/Vis spectroscopically (Figure 31). Catalytic activity was calculated applying Lambert Beer's rule with an extinction coefficient for the quinone of $1000 \text{ Lmol}^{-1}\text{cm}^{-1}$.^[159]

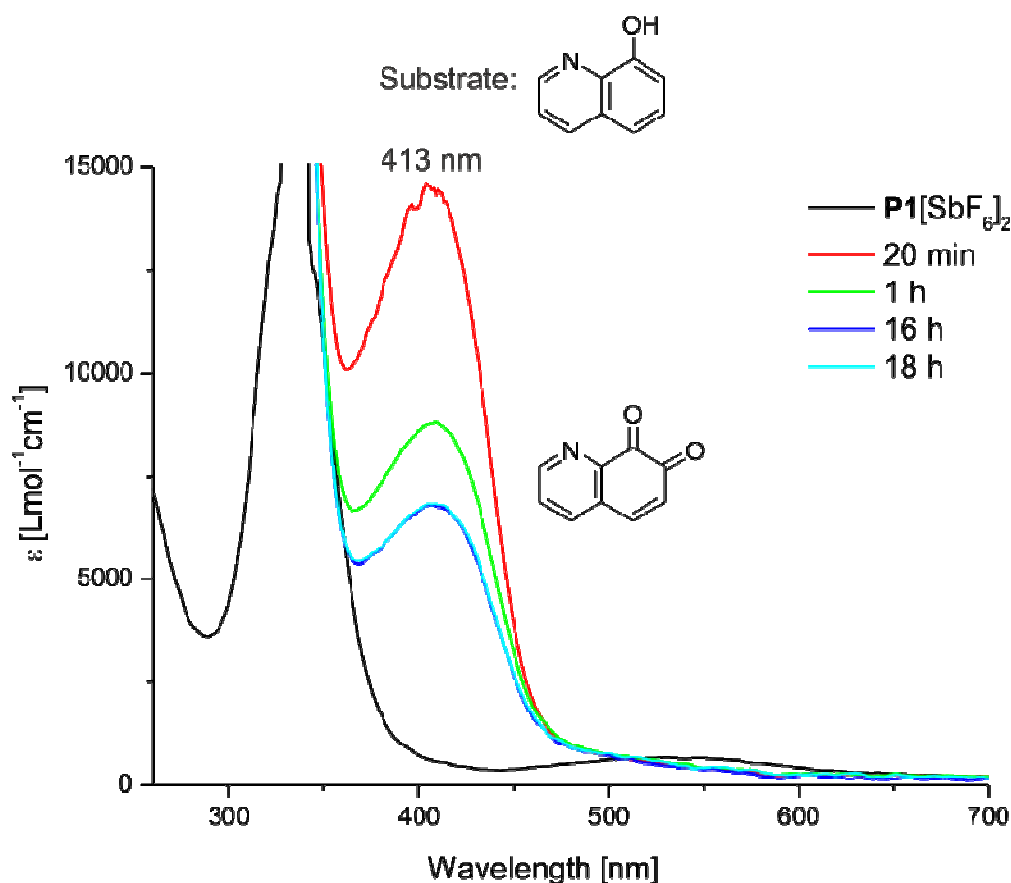


Figure 31. UV/Vis spectrum of the formation of $[\text{Cu}_2\text{O}_2\{\text{HC}(3\text{-}t\text{BuPz})_2(1\text{-MeIm})\}_2][\text{SbF}_6]_2$ (black) and the formation of the quinone (all colours).

Table 10. Catalytic efficiency of $[\text{Cu}_2\text{O}_2\{\text{HC}(3\text{-}t\text{BuPz})_2(1\text{-MeIm})\}_2][\text{SbF}_6]_2$ with phenolic substrates.

Substrate	Reaction time	Turnover numbers
<i>p</i> -Methoxyphenol	30 min	1
	18h	2
8-Hydroxyquinoline	20 min (max.)	14
	1h	9
	16h	7
	18h	7

Table 10 depicts an overview of the catalytic efficiency of **P1** $[\text{SbF}_6]_2$. It shows that 8-hydroxyquinoline is processed extremely fast with a remarkable TON of 14. This maximum is already reached after 20 min. Following the reaction for longer, a slow decrease in efficiency can be observed; after 1h the TON is at 9 and after 16h and 18h at 7.

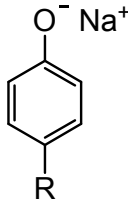
The substrate *p*-methoxyphenol however is converted much slower and only reaches a maximum TON of 2. Here a TON of 1 after 45 min and 2 after 18h is observed. Reasons for the low TON here and the over time decreasing TON of the conversion to naphthalene-1,2-

dione are most likely subsequent reactions of the highly reactive quinones. Concerning this, Lumb as well as Limberg showed some possible side reactions.^[80,131,156]

3.2.3.2 Stoichiometric catalysis investigations

For stoichiometric conversions with 5 eq of each substrate, the generation of the respective catechol was proven at -80°C (Table 11). An H-substituted substrate, as well as one containing an electron withdrawing substituent and one containing an electron donating substituent were tested. Evaluation of NMR data proves over 95% of formed catechol for the unsubstituted and the electron-donating OMe-substituted phenolate. For the NO_2 -substituted phenol 60% of catechol were obtained, which is also a good conversion, considering the electron-withdrawing effect of the nitro substituent. Neither stoichiometric substrate reaction showed signs of a C-C coupling product, so that a reaction mechanism analogous to tyrosinase can be anticipated.

Table 11. Yield of catechol after treatment of $[\text{Cu}_2\text{O}_2\{\text{HC}(3\text{-}t\text{BuPz})_2(1\text{-MeIm})\}_2][\text{SbF}_6]_2$ with stoichiometric amounts of *para*-substituted phenol.

	R	Equivalents	Reaction time	% Catechol
	H	5	5 min	> 95
	OMe	5	5 min	> 95
	NO_2	5	60 min	60

3.2.4 Summary

The new bis(pyrazolyl)methane ligand **L1** was synthesised and reaction of **L1** with CuCl₂ gave the distorted tetrahedral complex **C1**. This coordination is unusual for monofacial bis(pyrazolyl)methane complexes, which are usually five-coordinate. In **C1** one pyrazolyl moiety is pushed away from the central metal and does not coordinate, which is seen as a first indicator for the strong donor ability of imidazole. DFT calculations of bond lengths in **C1** confirmed this and an additional second order perturbation NBO analysis proved a larger charge-transfer energy for N_{im}→Cu compared to N_{pz}→Cu as well.

The according Cu(I) complex of **C1** was used as a precursor for the activation of oxygen. Hereby AgSbF₆ was added to the *in-situ* formed Cu(I) compound, which was then treated with oxygen. UV/Vis spectroscopic analysis showed two characteristic LMCT bands at 334 and 534 nm, indicating the formation of a (μ-η²:η²)-peroxo compound (**P1**[SbF₆]₂). It is fully generated in 10–15 min and has a half-life at 0°C of 3.8 min. Additional analytic methods, such as XAS spectroscopy and cryo-ESI spectrometry verified the existence of a (μ-η²:η²)-Cu₂O₂ core.

TD-DFT and NTO calculations predicted the experimentally measured UV/Vis bands well. In comparison to other known copper peroxo species, these bands are blue-shifted about 15 nm. This effect was explained by the stronger N_{im} donation, which leads to an increase of the LUMO orbital, resulting in an energetically larger LMCT transition.^[70]

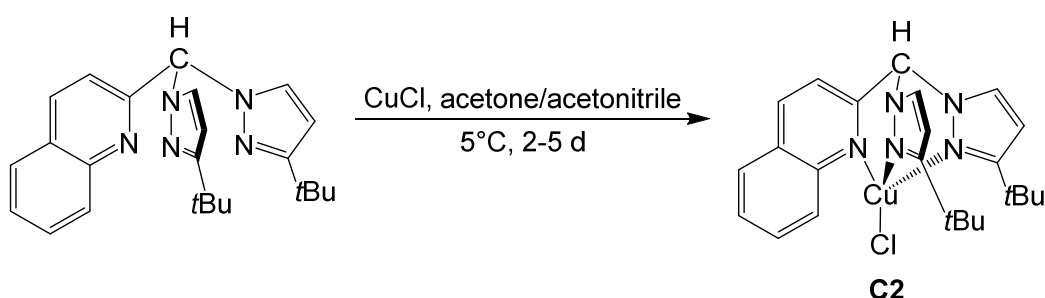
Based on the formation of the peroxo complex, this compound was treated with phenolic substrates in order to investigate its catalytic capacity in analogy to tyrosinase. At –80°C stoichiometric (5 eq) amounts of nitrophenolate, 4-methoxyphenolate and phenolate were reacted with **P1**[SbF₆]₂ and the amount of generated catechol was determined by NMR analysis. Here, for activated and unsubstituted phenolates a yield of over 90% of catechol was found and for the deactivated phenolate 60%. The absence of NMR signals indicating a C-C coupling product proved a reaction mechanism analogous to tyrosinase. In addition catalytic amounts of 4-methoxyphenol and 8-hydroxyquinoline together with the auxiliary base NEt₃ were added to **P1**[SbF₆]₂ at room temperature and UV/Vis spectra showed the formation of the according quinones. Catalytic conversion with 8-hydroxyquinoline was quick and efficient with a maximum TON of 14, but showed a slow decay over time, while conversion with 4-methoxyphenol was much slower.

3.3 Biomimetic hydroxylation catalysis through self-assembly of a bis(pyrazolyl)methanecopper-peroxo complex^[160]

3.3.1 Structural characterisation of bis(pyrazolyl)methanecopper complexes

It was mentioned in the introduction that heteroscorpionate ligands can generate different coordination modes, depending on the nature of the ligand (mostly concerning its steric demands) and the oxidation state of the metal (Figure 16). Concerning this subject, experiments with the bis(pyrazolyl)methane ligands HC(3-*t*BuPz)₂(Py) (**L5**) and HC(3-*t*BuPz)₂(Qu) (**L2**) and Cu(I) as well as Cu(II) salts were performed. **L2** and **L5** were resynthesised according to Herres-Pawlis *et al.*^[117] The crystal structures of the resulting complexes **C2–C4** will be discussed in the following.

Independent dissolving of CuCl and **L2**, followed by their combination affords [CuCl{HC(3-*t*BuPz)₂(Qu)}] as crystals suitable for X-ray diffraction analysis (**C2**, Scheme 19, Figure 32).



Scheme 19. Synthesis of [CuCl{HC(3-*t*BuPz)₂(Qu)}] (**C2**).

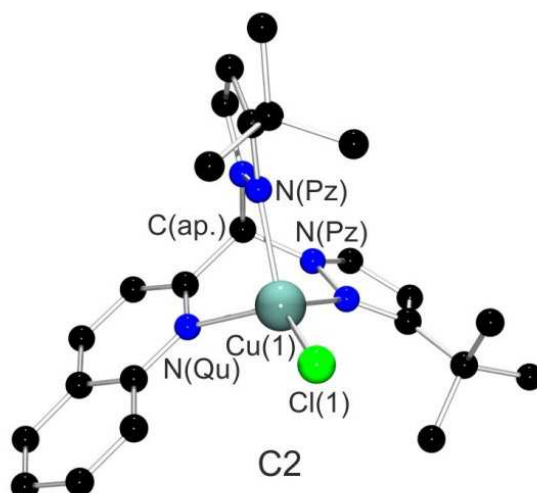


Figure 32. Molecular structure of [CuCl{HC(3-*t*BuPz)₂(Qu)}] (**C2**).

C2 crystallises in the orthorhombic space group *Pnma* as red crystals in which the central atom is coordinated in a fourfold fashion by two pyrazolyl nitrogen atoms and one quinolinyl nitrogen atom (Figure 32). Further coordination aspects will be discussed later on (see Tables 12/13).

Conversion of the bis(pyrazolyl)pyridinylmethane ligand $\text{HC}(3\text{-}t\text{BuPz})_2(\text{Py})$ (**L5**) with CuCl furnished the product **C3** (Scheme 20, Figure 33) as yellow crystals.

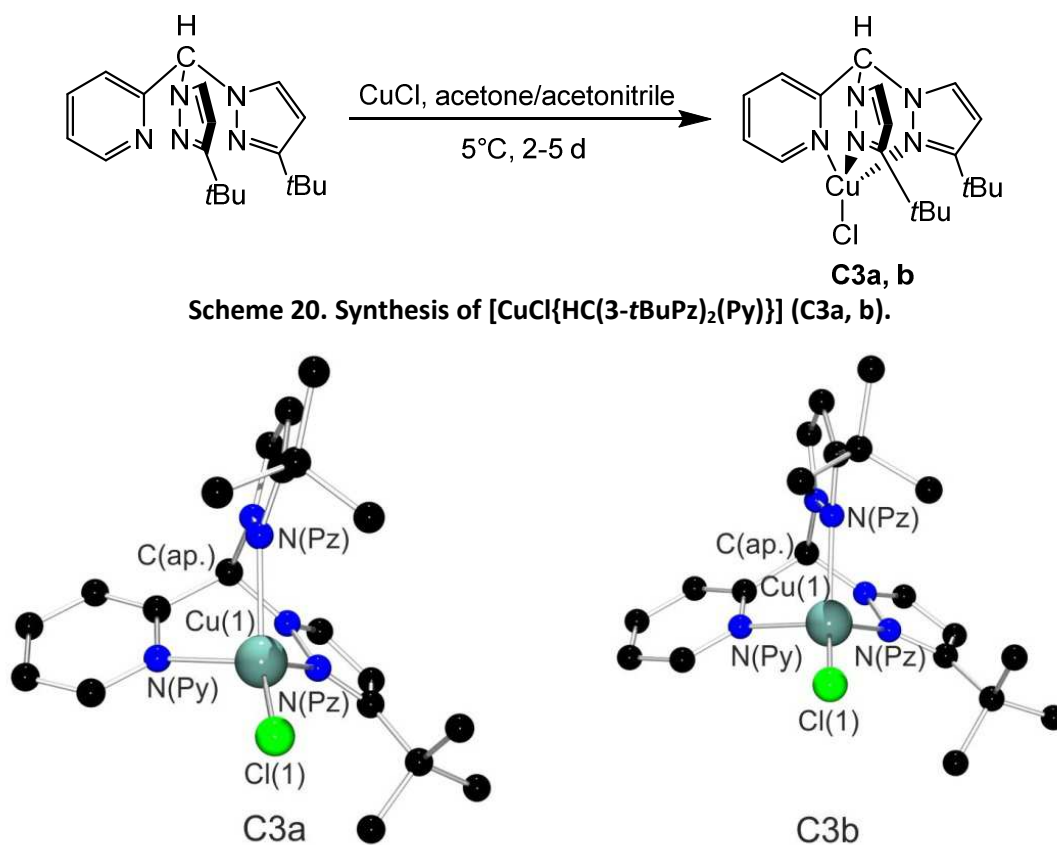
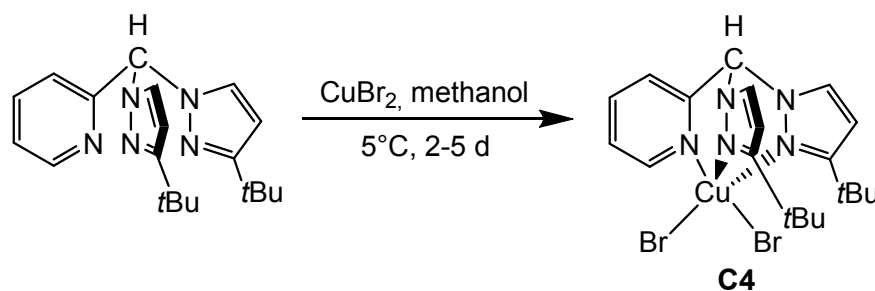


Figure 33. Molecular structures of $[\text{CuCl}\{\text{HC}(3\text{-}t\text{BuPz})_2(\text{Py})\}]$ (C3a, b**).**

C3 crystallises in the monoclinic space group $P2_1/c$ with two slightly different conformers in the elemental cell, referred to as **C3a** and **C3b**. Similar to **C2** the copper atom is coordinated four-fold, this time by two pyrazolyl nitrogen atoms and the pyridinyl nitrogen atom. Selected bond lengths and angles are listed in Tables 10 and 11.



The Cu(II) salt CuBr_2 affords $[\text{CuBr}_2\{\text{HC}(3\text{-}t\text{BuPz})_2(\text{Py})\}]$ (**C4**) (Scheme 21, Figure 34), when treated with **L5** in methanol.

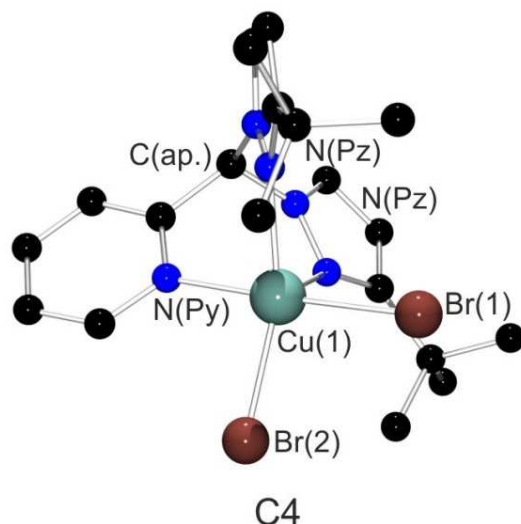


Figure 34. Molecular structure of $[\text{CuBr}_2\{\text{HC}(3\text{-}t\text{BuPz})_2(\text{Py})\}]$ (**C4**).

C4 also crystallises in the monoclinic space group $P2_1/c$ as dark green crystals. In **C4** the copper atom is surrounded by five ligands, three of which belong to the bis(pyrazolyl)methane ligand (one pyridinyl nitrogen atom and two pyrazolyl nitrogen atoms) and the two bromide anions of the Cu(II) salt. Selected bond lengths and angles are listed in Tables 12 and 13.

Figure 35 shows the molecular structure of $[\text{CuCl}_2\{\text{HC}(3\text{-}t\text{BuPz})_2(\text{Py})\}]$ (comparing complex **CC4**), which was synthesised by A. Hoffmann from CuCl_2 and $\text{HC}(3\text{-}t\text{BuPz})_2(\text{Py})$ (**L5**).^[125]

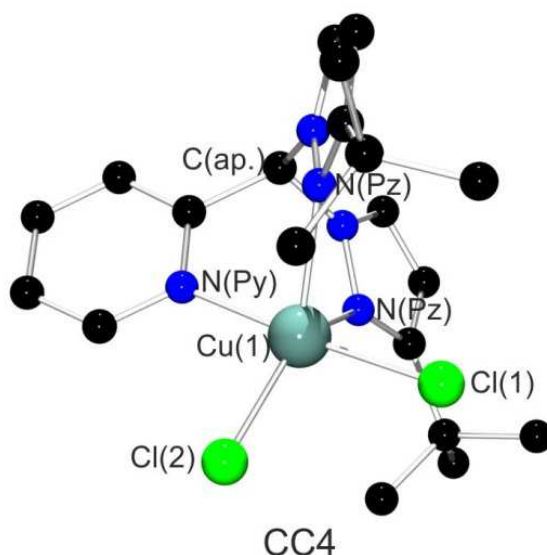


Figure 35. Molecular structure of **CC4**.^[125]

Table 12. Selected bond lengths [Å] of **C2**–**C4** and **CC4**.

Bond lengths [Å]	C2 ^a	C3a ^a	C3b ^a	C4 ^b	CC4 ^a
Cu-N _{Pz}	2.124(2)	2.106(2) 2.183(2)	2.082(2) 2.120(2)	2.117(6) 2.421(6)	2.233(3)
Cu-N _{Py} Cu-N _{Qu} [*]	2.149(2)*	2.120(2)	2.132(2)	2.051(6)	2.058(4)
Cu-X	2.215(1)	2.199(1)	2.187(1)	2.388(1) 2.409(1)	2.225(2) 2.267(1)
C _{ap} -N _{Pz}	1.456(2)	1.449(3) 1.449(3)	1.450(3) 1.460(3)	1.441(9) 1.458(9)	1.448(3)
C _{ap} -C _{Py} C _{ap} -C _{Qu} [*]	1.511(4)*	1.519(4)	1.507(3)	1.503(10)	1.515(6)
[a] X = Cl, [b] X = Br					

All four complexes are coordinated by only one heteroscorpionate ligand, due to steric shielding of alkyl groups in the 3-position of the pyrazolyls.^[112,161]

Table 13 includes the τ -value, that provides an easy determination of the coordination mode around the metal centre and was explained earlier.^[136,138] All relevant crystallographic data are collected in Table 30 and Table 31 in the appendix.

In **C2** and **C3** the metal ion is four-coordinate, displaying a distorted tetrahedral geometry (Figure 32, Figure 33), with nearly identical τ -values. Bond angles deviate more from the ideal tetrahedral angle in **C2**. In both complexes **C2** and **C3b**, Cu-N_{Pz} bond lengths are shorter than the corresponding Cu-N_{Py} or Cu-N_{Qu} bond lengths, which is in contrast to **C3a**, **C4** and **CC4**. In general bis(pyrazolyl)methane complexes show a donor competition between their N-donors which appears here again.^[76,162] This effect is discussed in more detail in the next paragraph. As for the Cu-Cl bond length, it is shorter in **C3** than in **C2**.

In **C4** and **CC4** the metal ion is five-coordinate, resulting in a distorted square pyramidal geometry for **C4** and a distorted trigonal-bipyramidal one for **CC4** (Figure 34, Figure 35). Both in **C4** and in **CC4**, Cu-N_{Py} bond lengths are shorter than the corresponding Cu-N_{Pz} ones. It is difficult to determine, which nitrogen is the stronger donor, as basicity and nucleophilicity have to be taken into account. Normally the donor-competition is won by pyrazolyl (see **C2** and **C3** with distorted tetrahedral environment), but in **C4** and **CC4** with fivefold coordination it is the other way round. The sterically demanding *tert*butyl groups may hinder the pyrazolyl

unit on getting closer to the metal ion. The Cu-Cl bond length in **CC4** is naturally shorter than the Cu-Br bond length in **C4**, which is in agreement with common Cu-X bond lengths. The N_{Pz} -Cu-Cl(1)/ N_{Pz} -Cu-Br(1) and N_{Pz} -Cu-Cl(2)/ N_{Pz} -Cu-Br(2) bond angles reflect, (as already suggested by the τ -values) that **C4** is distorted and cannot be assigned to a specific geometry and that **CC4** is of distorted trigonal-bipyramidal geometry. For **CC4** the pyridinyl N-donor and Cl(2) reside at the axial positions, whereas the two pyrazolyl N-donors and Cl(1) form the equatorial positions. $C_{apical}-N_{Pz}$ bond lengths are equal for **C4** and **CC4**.

Table 13. Selected bond angles [°] of **C2–C4** and **CC4** and according τ -values.

Bond angles [°]	C2^a	C3a^a	C3b^a	C4^b	CC4^a
N_{Pz} -Cu-X(1)	124.2(1)	130.0(1)	130.9(1)	115.2(2)	133.6(1)
	124.2(1)	127.2(1)	129.3(1)	151.7(2)	133.6(1)
N_{Pz} -Cu-X(2)	/	/	/	93.5(2)	93.5(2)
				95.2(2)	93.5(1)
N_{Py} -Cu-X(1)	129.2(1)*	121.5(1)	118.1(1)	92.2(2)	93.3(1)
N_{Qu} -Cu-X(1)*					
N_{Py} -Cu-X(2)	/	/	/	176.6(2)	175.9(1)
N_{Qu} -Cu-X(2)*					
N_{Pz} -Cu- N_{Pz}	89.1(1)	90.5(1)	86.6(1)	92.1(2)	92.2(2)
N_{Pz} -Cu- N_{Py}	89.1(1)*	88.5(1)	90.8(1)	83.2(2)	83.8(1)
N_{Pz} -Cu- N_{Qu} *	89.1(1)*	86.0(1)	88.7(1)	83.7(2)	93.8(1)
X(1)-Cu-X(2)	/	/	/	90.6(1)	90.8(1)
$\tau_4^{[136]}$, $\tau_5^{*[138]}$	0.76	0.73	0.71	0.42*	0.71*
[a] X = Cl, [b] X = Br					

In addition to structural investigations, density functional theory calculations were performed in order to analyse the coordination of all four complexes. The TPSSh functional in combination with the double-zeta basis set 6-31G(d) was used, since this combination yielded good results in the benchmarking of Cu_2O_2 complexes.^[137] Key geometric parameters of the theoretical calculations of **C2–C4** and **CC4** are listed in Tables 12 and 13. These data show that another conformer was found for **C3**, which is reflected by the significantly smaller N_{Qu} -Cu-Cl angle, so that these data are not discussed in this section. All attempts to find the other conformer failed. However the experimental structure of **C2** is in good agreement with the theoretical values for bond lengths and angles. Only the Cu- N_{Qu} bond

length is predicted a bit too short. The N_{Pz} -Cu- N_{Pz} and N_{Qu} -Cu- N_{Pz} angles are predicted about 4° too large. Moreover the N_{Qu} -Cu-Cl(1) bond angle is predicted too small, but the N_{Pz} -Cu-Cl(1) angle is in good agreement with the experimental data. For the five-coordinate complexes **C4** and **CC4** it can be seen, that the theoretical data are in accordance with the experimental data as well. In complex **C4** all relevant bond lengths are predicted well. The mirror plane in **CC4** is also found for the ground state calculation. In **CC4**, with the exception of the Cu- N_{Pz} bond length, which is predicted too short, all other bond lengths conform to the experimental data. Looking at the bond angles in complexes **C4** and **CC4**, it strikes, that the N_{Pz} -Cu-Cl(1) and N_{Pz} -Cu-Cl(2) angles in **CC4** are predicted quite well, whereas the corresponding angles in **C4** are predicted either too large or too small. With the exception of the N_{Py} -Cu-Cl(2) angle, which is predicted too small, the remaining bond angles are predicted 3 – 8° too large with the one other exception of the N_{Pz} -Cu- N_{Py} angle in **C4**.

Table 14. Calculated key bond lengths [Å] of **C2**–**C4** and **CC4** (Gaussian09, TPSSH/6-31G(d)).^[135,137]

Bond lengths [Å]	C2 ^a	C3 ^a	C4 ^a	CC4 ^a
Cu- N_{Pz}	2.011	1.982	2.071 2.397	2.161
Cu- N_{Py} / Cu- N_{Qu} *	1.975*	2.009	2.056	2.060
Cu-X	2.262	2.243	2.342 2.352	2.274 2.264
C_{apical} - N_{Pz}	1.458	1.460	1.459 1.449	1.453
C_{apical} - C_{Py} / C_{apical} - C_{Qu} *	1.522*	1.524	1.521	1.520
[a] X = Cl, [b] X = Br				

Table 15. Calculated key bond angles [°] of C2–C4 and CC4 (Gaussian09, TPSSh/6-31G(d)).^[135,137]

Bond angles [°]	C2^a	C3^a	C4^a	CC4^a
N _{Pz} -Cu-X(1)	122.7	130.0	121.6 138.9	130.2
N _{Pz} -Cu-X(2)	/	/	87.4 90.7	90.4
N _{PY} -Cu-X(1)/ N _{Qu} -Cu-X(1)*	122.4*	106.3	163.2	168.6
N _{PY} -Cu-X(2)/ N _{Qu} -Cu-X(2)*	/	/	95.8	93.0
N _{Pz} -Cu-N _{Pz}	93.7	94.1	98.6	98.2
N _{Pz} -Cu-N _{PY} / N _{Pz} -Cu-N _{Qu} *	93.8*	92.2	77.7 84.0	82.1
X(1)-Cu-X(2)	/	/	98.6	98.4
τ_4 , τ_5 *	0.81	0.88	0.41*	0.64*
[a] X = Cl, [b] X = Br				

Regarding τ -values, predicted and experimental ones coincide well. For **C4** experimental and calculated τ -values match almost exactly. For **C3a** a comparison would not make sense, as different conformers were found. The geometry of **C2** is predicted a bit more distorted tetrahedral as observed experimentally. For **CC4** the calculated τ_5 -value identifies a slightly less distorted trigonal-bipyramidal geometry than the experimental data suggests. Additionally, NBO analyses were performed of the optimised structures of **C2–C4** and **CC4** (Table 16).^[142,163,164] The second order perturbation theory yields the charge-transfer energies for the donation from the pyrazolyl or pyridinyl units to copper.

Table 16. Charge-transfer energies [kcal mol⁻¹] for C2–C4, as well as CC4 and P2 (Gaussian09, TPSSh/6-31G(d) and NBO 6.0).^[135,137,142]

CT energies	C2	C3a^a	C4	CC4	P2
N _{Pz} →Cu	32.4	29.7	17.9	14.4	39.2
N _{Pz} →Cu	32.4	27.0	8.5	14.4	32.2
N _{PY} /N _{Qu} *→Cu	32.5*	24.2	18.4	17.4	17.2*
[a] data obtained directly from crystal structure (unoptimised)					

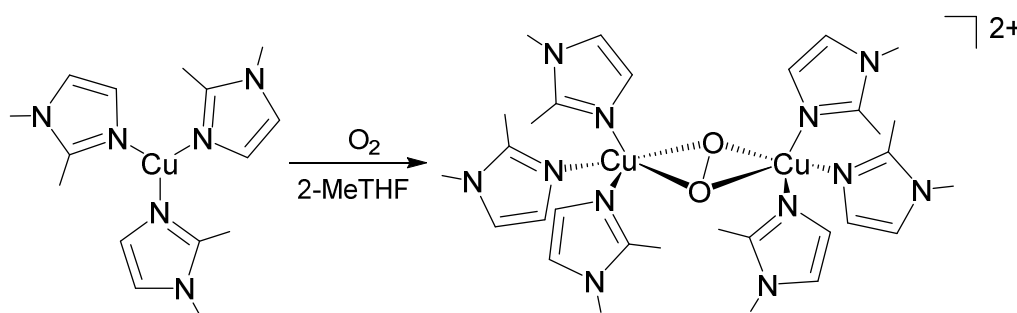
At a glance it can be seen that the charge-transfer energies mostly correlate with the M-N bond lengths. Both four coordinate complexes [CuCl{HC(3-*t*BuPz)₂(Qu)}] (**C2**) and [CuCl{HC(3-

$t\text{BuPz}_2(\text{Py})\}$ (**C3a**) show similar charge-transfer energy values. Additionally, in **C2** the bond lengths for the Cu-N_{Pz} and Cu-N_{Qu} bond are similar, which is also reflected in the similar values for the charge-transfer energies. Different charge-transfer energies concerning the $\text{N}_{\text{Pz}}\text{-M}$ bond are represented by different $\text{N}_{\text{Pz}}\text{-M}$ bond lengths. In **C3a** the charge-transfer energy of pyridinyl to copper is smaller than the respective energy for pyrazolyl. This does not correlate with the medium-long Cu-N_{Py} bond. A better correlation is found in $[\text{CuBr}_2\{\text{HC}(3\text{-}t\text{BuPz})_2(\text{Qu})\}]$ (**C4**) and $[\text{CuCl}_2\{\text{HC}(3\text{-}t\text{BuPz})_2(\text{Qu})\}]$ (**CC4**). Charge-transfer energies for $\text{N}_{\text{Pz}}\text{-Cu}$ are different in **C4**, which is in accordance with different Cu-N_{Pz} bond lengths. The donor ability is predicted slightly higher for pyridinyl, therefore the Cu-N_{Py} bond length should be shorter than the Cu-N_{Pz} bond length, as found experimentally. In **CC4** the charge-transfer energies are exactly the same for both pyrazolyl-M interactions. Theoretical calculations showed equal Cu-N_{Pz} bond lengths due to the mirror plane in **CC4**, so the values for the charge-transfer energy tie in with that. Moreover the charge-transfer energy for pyridinyl is slightly larger than for pyrazolyl, which again reflects in the shorter Cu-N_{Py} bond length. To sum it up, the NBO analysis shows that for the five-coordinate complexes $[\text{CuBr}_2\{\text{HC}(3\text{-}t\text{BuPz})_2(\text{Qu})\}]$ (**C4**) and $[\text{CuCl}_2\{\text{HC}(3\text{-}t\text{BuPz})_2(\text{Qu})\}]$ (**CC4**), the pyridinyl units donate slightly more than the pyrazolyl units, but exactly the opposite applies for $[\text{CuCl}\{\text{HC}(3\text{-}t\text{BuPz})_2(\text{Py})\}]$ (**C3a**). Therefore, here the donor rivalry between pyrazolyl and pyridinyl/quinolinyl that has been observed before can be seen clearly.^[162]

3.3.2 Biomimetic hydroxylation catalysis through self-assembly of

$[\text{Cu}_2\text{O}_2\{\text{HC}(3\text{-}t\text{BuPz})_2(\text{Qu})\}_2][\text{SbF}_6]_2$

Self-assembly is a principle that can for example be found in the field of chemistry, biochemistry or material science. The term stands for the autonomous organisation of an unordered system without human intervention.



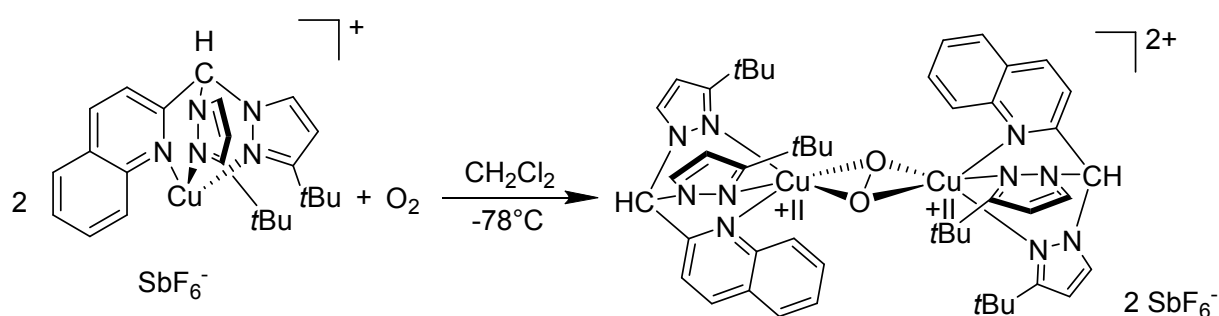
Scheme 22. Oxygenation of Cu(I)-tris(1,2-dimethyl-1H-imidazole) in 2-MeTHF.^[144]

Common examples in biochemistry are the aggregation of micelles and lipid bilayers or the formation of double-stranded DNA. These systems elegantly show the balance of enthalpy and entropy in living systems.^[144,165]

An illustrative model for the concept of self-assembly in biochemistry is the tobacco mosaic virus (TMV).^[166] It is a helical virus particle that is composed of 2130 identical subunits, each containing 158 amino acids, which form a helical sheath around an RNA strand.^[167] The remarkable thing about the TMV system is that the assembling of the complete structure may be coded for in a gene of 500 bp length, which is only 8% of the overall virus genome, showing the economical aspect of self-assembly.

As Whitesides mentioned in 2002, the term of self-assembly has been stretched and overused for many different processes over the years. Here, we will focus on systems that comply with his definition for self-assembly (“...,we limit the term to processes that involve pre-existing components (separate or distinct parts of a disordered structure), are reversible, and can be controlled by proper design of the components”^[165]). Whiteside also states that self-assembly reflects information such as shape or surface properties in individual components, which determine the interactions amongst them. Therefore it is important for chemists to design components that organise themselves into desired patterns and functions. In 2012, concerning the goal of building a model complex for tyrosinase Stack *et al.* introduced the term self-assembly using very simple monodentate imidazole ligands, Cu(I) and O₂ at –125°C, resulting in a (μ - η^2 : η^2)-peroxo species (independent on the order of component addition) that was also able to hydroxylate different phenolic substrates (Scheme 22).^[144] The phenolic substrate however had to be added after the self-assembly of the peroxo compound in an extra step.

Based on the formation of complex **C2**, catalytic studies were performed with the ligand HC(3-*t*Bupz)₂(Qu) (**L2**).



Scheme 23. Synthesis of [Cu₂O₂{HC(3-*t*BuPz)₂(Qu)}₂][SbF₆]₂ (**P2**[SbF₆]₂).

C2 was used as a building block for the precursor in the activation of oxygen. However, due to its insolubility, **C2** could not be used directly, but had to be generated *in-situ* from the starting compounds. The resulting species was hence treated with AgSbF_6 immediately and the precursor $[\text{Cu}\{\text{HC}(3\text{-}t\text{BuPz})_2(\text{Qu})\}][\text{SbF}_6]$ could be obtained. This precursor was then injected into an O_2 -saturated CH_2Cl_2 -solution at -78°C (Scheme 23).

Following injection of the corresponding Cu(I) precursor, the peroxo species $[\text{Cu}_2\text{O}_2\{\text{HC}(3\text{-}t\text{BuPz})_2(\text{Qu})\}_2][\text{SbF}_6]_2$ (**P2** $[\text{SbF}_6]_2$) was allowed to build at -80°C for several hours.

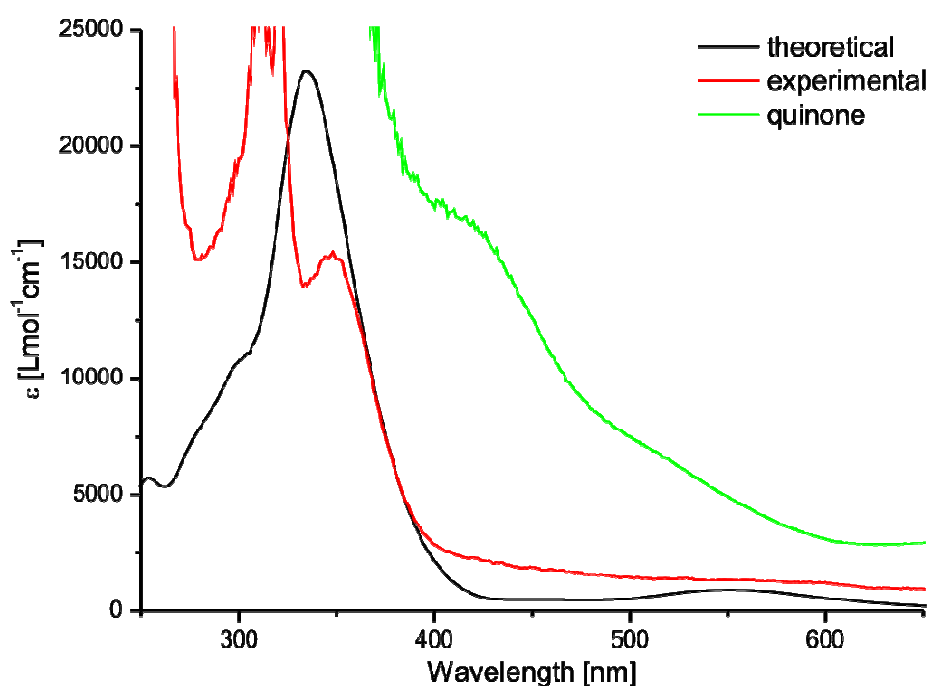


Figure 36. UV/Vis spectrum of $[\text{Cu}_2\text{O}_2\{\text{HC}(3\text{-}t\text{Bupz})_2(\text{Qu})\}_2][\text{SbF}_6]_2$ (**P2** $[\text{SbF}_6]_2$) (red: experimental, black: theoretical^[141]) and the final UV/Vis spectrum of the formation of the quinone in the self-assembly mode (green)^[168].

After UV/Vis spectroscopical analysis it was observed that the reaction is very slow, so that the peroxo species was only formed to 80% after 8 h. Longer reaction times however lead to the decay of **P2** $[\text{SbF}_6]_2$. The spectrum shows a band at 345 nm and an almost not identifiable one at 550 nm (due to the low peroxo concentration). These two bands stem from LMCT transitions. They are in good analogy with the UV/Vis-bands found for oxy-tyrosinase and oxy-hemocyanin.^[139] Additional bands in the area of 305–320 nm originate from intra-ligand transitions.

Further analyses involved the determination of the kinetics for the formation of the peroxo compound. It could be shown that for the first 250 minutes the reaction follows a pseudo first-order-kinetics with a reaction rate of $k = 5.4 \times 10^{-3} \text{ s}^{-1}$ (Figure 37). It is assumed that the

speed-limiting step is the attachment of the oxygen to one copper core, resulting in a superoxide intermediate species, before the peroxo complex is built. After formation, the **P2** core already decays at -78°C with $t_{1/2}$ of 1.46 min at 0°C .

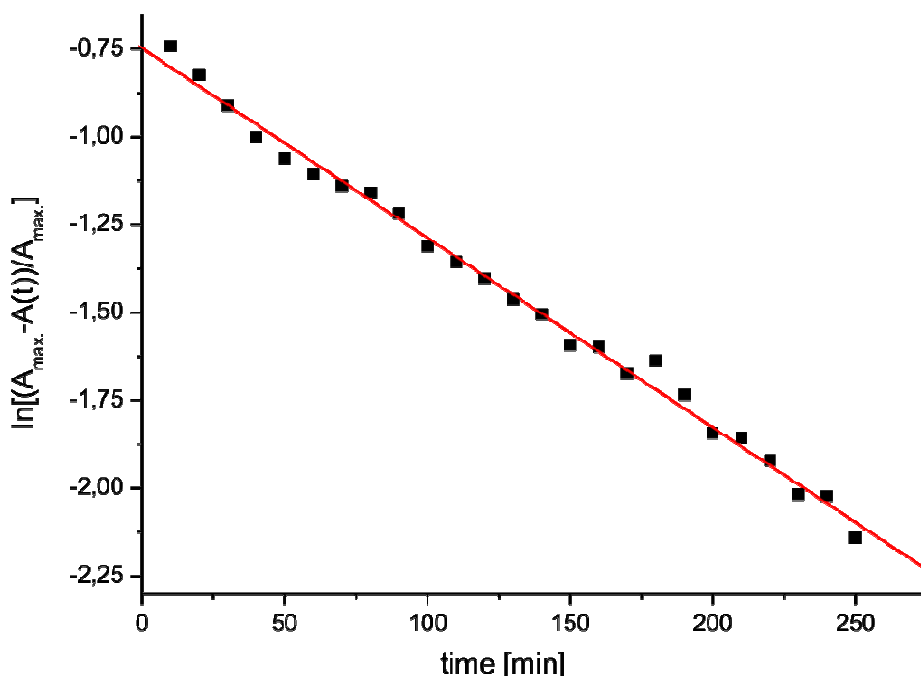


Figure 37. Pseudo-first order plot for the determination of the rate constant of the formation of **P1**. Red: linear fit ($R = 0.997$)

By using the self-assembly approach, an astonishing catalytic activity in the *ortho*-hydroxylation of the substrate *para*-methoxyphenol and subsequent oxidation to the quinone using the new $[\text{Cu}_2\text{O}_2\{\text{HC}(3\text{-}t\text{BuPz})_2(\text{Qu})\}_2][\text{SbF}_6]_2$ system was observed.^[168]

In spite of the low stability of the **P2** species, when all components were combined (i.e. copper(I) precursor, 25 eq. of 4-methoxyphenol, 50 eq. of triethylamine) and subsequent addition of oxygen, following the protocol of Tucek *et al.*^[78] the hydroxylation and subsequent oxidation yields the biomimetic quinone product, which can be observed by UV/Vis spectroscopy owing to its intense absorption at 418 nm. Hereby, a turnover of 10 in 1h could be monitored. This shows that the **P2** species has formed as a reactive intermediate during oxygenation. The direct capture of the species **P2** at room temperature was not possible. However, the formation of **P2** $[\text{SbF}_6]_2$ and phenol hydroxylation is fast enough to compete with the decay. This result shows that bis(pyrazolyl)pyridinylmethane copper complexes possess a large potential for further catalytic hydroxylation applications in synthetic organic chemistry.

3.3.3 Theoretical investigations

Moreover natural bond orbital (NBO), TD-DFT (Figure 36) and natural transition orbital (NTO) calculations were carried out for the peroxo complex, in order to understand the bonding situation in this species, and furthermore to gain insight into the electron transitions that generate the UV/Vis bands.

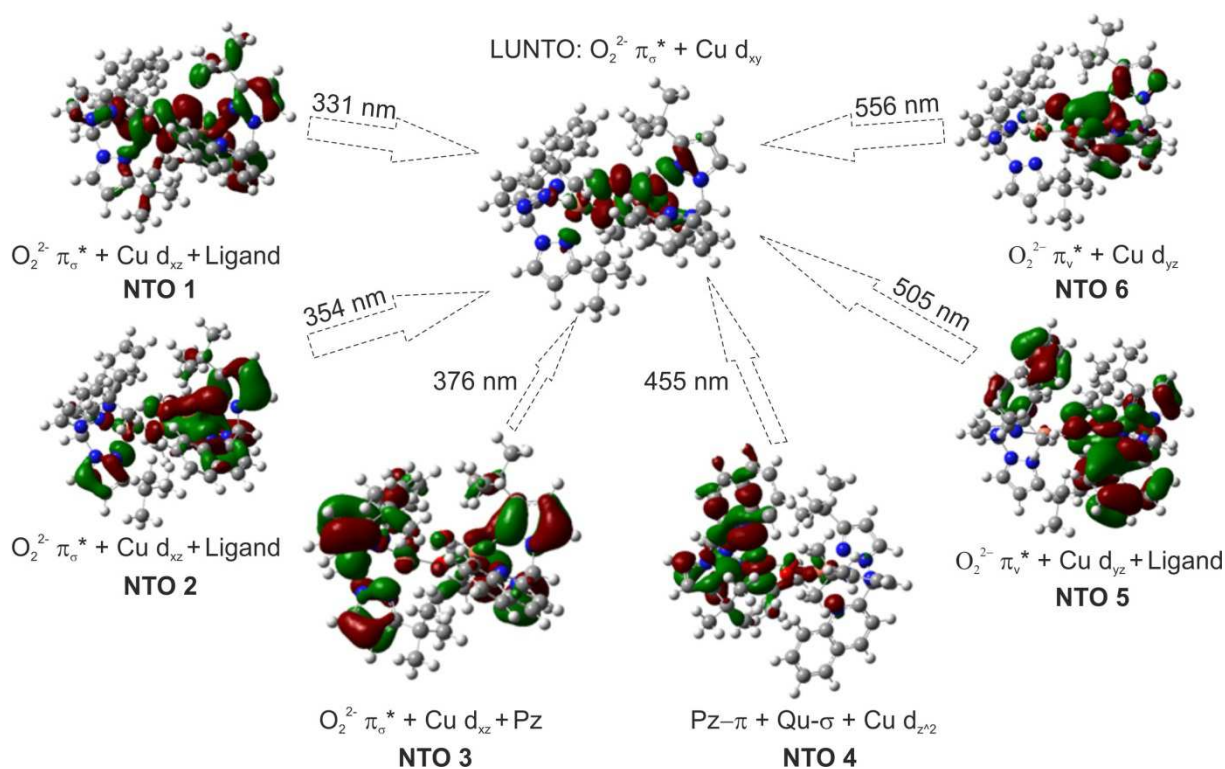


Figure 38. NTO-analysis of $[Cu_2O_2\{HC(3-tBuPz)_2(Qu)\}_2]^{2+}$ (**P2**).^[141]

NTO analysis^[169] of the UV/Vis transitions (Figure 38) obtained by time-dependent DFT (TD-DFT, TPSSH/6-31G(d))^[135,137] reveals the visible transition at 550 nm as the classical out-of-plane $\pi_v^* \rightarrow d_{xy}$ LMCT with its lower intensity. With regard to symmetry and composition it is in accordance with the classical Cu_2O_2 theory.^[31] The broad shoulder stems from a transition originating from pyrazolyl π - and quinolynyl σ -donating orbitals into the same LUNTO. This is in accordance with the NTO analysis performed for the original pyridinyl peroxo system.^[18] In comparison to the NTO analysis of **P1** $[SbF_6]_2$ (Figure 24) more NTOs contribute to the transition of the smaller wavelength, which is due to the quinolynyl moiety. So in this case **NTOs 1–3** combine to the transition at 350 nm and **NTOs 4–6** result in the transition at 550 nm. **NTOs 1–3** all have $O_2^{2-}-\pi_\sigma^*$ and $Cu-d_{xz}$ character, while **NTOs 5–6** have $Cu-d_{yz}$ and $O_2^{2-}-\pi_v^*$ character in common. **NTO 4** however shows $Pz-\pi$, $Qu-\sigma$ and $Cu-d_{z^2}$ properties.

The UV transitions all have mixed character, being transitions between the in-plane π_{σ}^* orbital and the ligands into the d_{xy} copper orbital. In **P2**, the pyrazolyl units donate stronger to copper than the quinolinyl units (Table 14).

3.3.4 Summary

Three new bis(pyrazolyl)methane copper(I) and copper(II) complexes, containing the ligands $\text{HC}(3\text{-}t\text{BuPz})_2(\text{Py})$ (**L5**) and $\text{HC}(3\text{-}t\text{BuPz})_2(\text{Qu})$ (**L2**) were synthesised (**C2–C4**). All four complexes are coordinated by only one heteroscorpionate ligand, due to steric shielding of alkyl groups in the 3-position of the pyrazolyls.^[112,161] **C2** and **C3** have distorted tetrahedral geometry and **C4** has a distorted square-pyramidal one. Bond lengths and angles were calculated too, with τ -values being predicted well.

The donor situation was studied by NBO analysis, but no clear picture was found. Depending on the coordinative situation, both pyrazolyl and pyridinyl units can function as the stronger donor.

In situ generated **C2** serves as part of a precursor that can be used for the activation of oxygen in the modelling of the enzyme tyrosinase by formation of the peroxide species **P2** $[\text{SbF}_6]_2$. A self-assembly approach was tested successfully, showing catalytic hydroxylation catalysis by **P2** $[\text{SbF}_6]_2$ of phenols, resulting in a TON of 10 after 1h.

Comparison of $[\text{Cu}_2\text{O}_2\{\text{HC}(3\text{-}t\text{BuPz})_2(1\text{-Melm})\}_2][\text{SbF}_6]_2$ (**P1** $[\text{SbF}_6]_2$) and $[\text{Cu}_2\text{O}_2\{\text{HC}(3\text{-}t\text{BuPz})_2(\text{Qu})\}_2][\text{SbF}_6]_2$ (**P2** $[\text{SbF}_6]_2$):

Looking back at the last two chapters, several differences between the two copper(II) peroxo species that were characterised (**P1** $[\text{SbF}_6]_2$ and **P2** $[\text{SbF}_6]_2$) can be determined. In the following the two are compared concerning their properties.

The first and most prominent difference to notice is the blue-shift in the UV/Vis bands of **P1** $[\text{SbF}_6]_2$ compared to **P2** $[\text{SbF}_6]_2$. In general, $(\mu\text{-}\eta^2\text{:}\eta^2)$ -peroxo complexes show LMCT-transitions at 350 and 550 nm, which is the case for **P2** $[\text{SbF}_6]_2$ and also for the already mentioned $[\text{Cu}_2\text{O}_2\{\text{HC}(3\text{-}t\text{BuPz})_2(\text{Py})\}_2][\text{SbF}_6]_2$ ($[\text{Cu}_2\text{O}_2(\text{L5})_2][\text{SbF}_6]_2$).^[18,139] Because of that it can be deduced that the pyridinyl and quinolinyl moieties have similar electronic properties, due to a similar electronic structure of the ligands $\text{HC}(3\text{-}t\text{BuPz})_2(\text{Py})$ (**L5**) and $\text{HC}(3\text{-}t\text{BuPz})_2(\text{Qu})$ (**L2**). The 1-methylimidazolyl moiety in **L1** however increases the electron

density at this ligand, which was proven by NBO analysis (see 3.2.2.3). The stronger donor ability of the imidazolyl nitrogen atom was therefore defined as the reason for the shorter Cu-N_{im} bond length in the complex **C1**.

In addition to the shifted UV/Vis transitions, differences can also be detected concerning the building velocity of **P1**[SbF₆]₂ and **P2**[SbF₆]₂. While **P1**[SbF₆]₂ is built completely in 10–15 minutes, **P2**[SbF₆]₂ takes at least 8 hours to form completely, which is due to the quinolinyl moiety in **P2**.

Concerning the stability of **P1**[SbF₆]₂ and **P2**[SbF₆]₂, **P1**[SbF₆]₂ is more stable at –78°C than **P2**[SbF₆]₂. While **P2**[SbF₆]₂ already partly decays whilst forming, the imidazolyl moiety containing peroxo compound is stable at –78°C for several days. Half-times of **P1**[SbF₆]₂ and **P2**[SbF₆]₂ at 0°C are 3.8 min and 1.5 min. The parent species [Cu₂O₂(**L5**)₂][SbF₆]₂ is formed fast as well and is stable at –78°C for weeks.

Herres-Pawlis *et al.* could prove a diverse catalytic activity for [Cu₂O₂(**L5**)₂][SbF₆]₂ concerning a variety of different substrates (with different electronic properties).^[18] **P1**[SbF₆]₂ shows a similar catalytic activity, but with a much faster reaction for the 8-hydroxyquinoline substrate (TON of 14 after 10 minutes compared to 8 after 16 h). Stoichiometric experiments resulted in a quantitative catechol conversion for unsubstituted phenolate salts and for fluoride substituted ones, similar to [Cu₂O₂(**L5**)₂][SbF₆]₂, while nitro-substituted phenolates yielded 60% catechol, which is less compared to >90% conversion with this substrate for [Cu₂O₂(**L5**)₂][SbF₆]₂.

First kinetic experiments showed a faster hydroxylation of phenols for **P1**[SbF₆]₂ compared to [Cu₂O₂(**L5**)₂][SbF₆]₂.^[170] For **P2**[SbF₆]₂ with its slow building velocity, no stoichiometric conversions were performed, whereas a self-assembly approach has only been tested for **P2**[SbF₆]₂. The *isopropyl* substituted ligand HC(3-*i*PrPz)₂(Py) (**L3**) did not show any signs of a peroxo complex formation.

3.4 Analysis and Characterisation of bis(pyrazolyl)methane nitrate complexes

3.4.1 Introduction

The activation of small molecules, like O₂, NO or CO₂ is a research field that earned large interest over decades and has significant impact in biology, medicine and industrial catalysis.^[171] Its importance has grown due to climate change and the greenhouse effect. Taking the example of processing toxic gases, a possible area of application might be the cleaning of exhaust gases. In exhaust fumes various toxic gases containing nitrogen are present, including NO, NO₂ and N₂O.^[172]

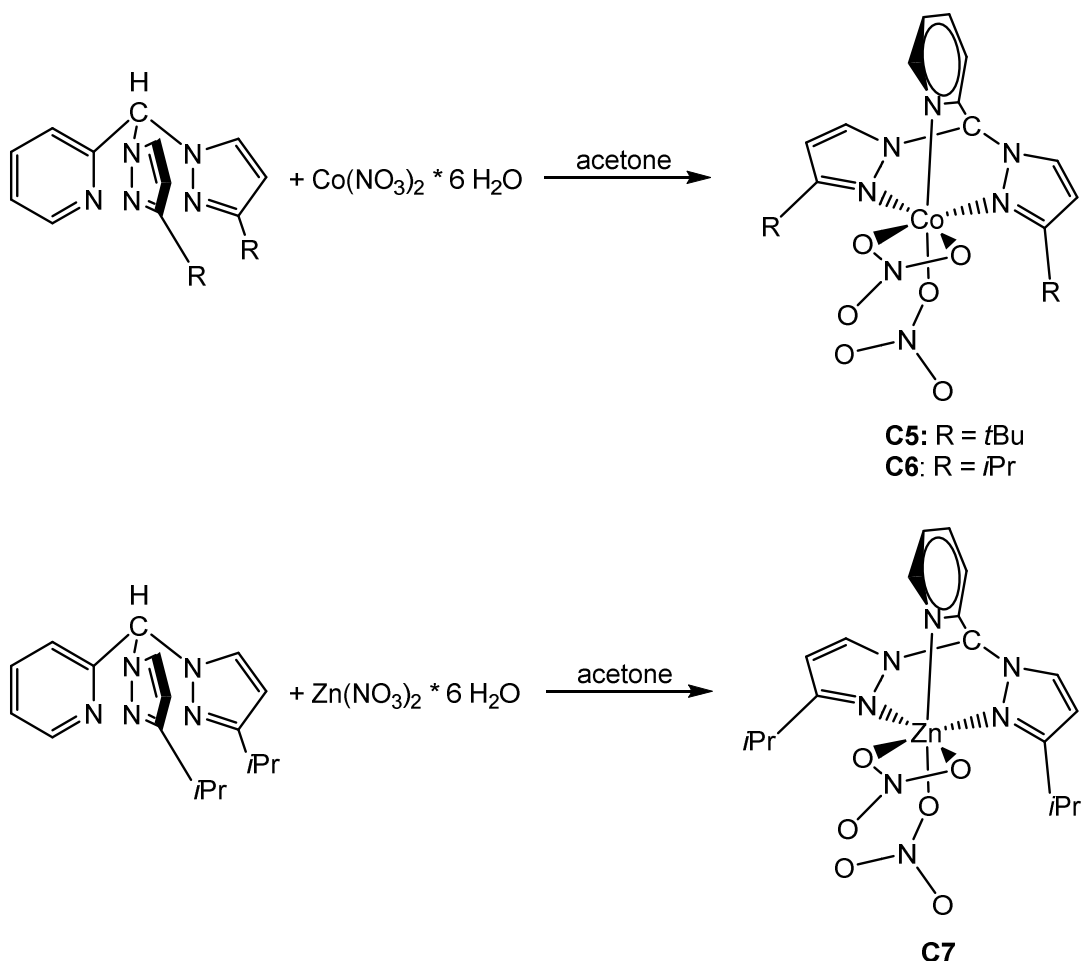
Another example of the processing of small molecules containing nitrogen, in order to obtain molecular nitrogen is the biosynthetic pathway of denitrification.^[92] As was mentioned in the introduction, this multi-step process generates nitrogen from nitrate, with nitrite, nitrogen monoxide and nitrous oxide being intermediates.

Analysing the crystal structures of bis(pyrazolyl)methane complexes concerning their coordination sphere and binding modes provides important insight into the influence of donor functions on the coordination sphere. Until now, monofacial bis(pyrazolyl)methane complexes are only known with the halides chloride and bromide in combination with the transition metals Co, Cu, Fe and Zn.^[125] Chloride can be abstracted by the addition of a silver salt, resulting in a free coordination site. This free coordination site can be used for the reaction with oxygen (see 3.2.2, 3.3.2). Moreover in chapter 3.5.3 the reaction of a bis(pyrazolyl)methane complex with NO gas and NO transferring agents is described.

In this thesis, it was possible to obtain X-ray structural data for bis(pyrazolyl)methane complexes using transition metal nitrate salts. These were found to favour a different coordination mode compared to all previously shown structures of **C1–C7**.

3.4.2 Structural characterisation of bis(pyrazolyl)methane nitrate complexes

Reaction of the Co(II)-nitrate salt with HC(3-*t*BuPz)₂(Py) (**L5**) affords magenta coloured crystals, which crystallise monoclinically in the space group *P2₁/c* (**C5**, Figure 39), containing four units per elementary cell.



Scheme 24. Synthesis of $[\text{Co}(\text{NO}_3-\kappa\text{O})(\text{NO}_3-\kappa^2\text{OO}')\{\text{HC}(3-\text{tBuPz})_2(\text{Py})\}]$ (C5), $[\text{Co}(\text{NO}_3-\kappa\text{O})(\text{NO}_3-\kappa^2\text{OO}')\{\text{HC}(3-\text{iPrPz})_2(\text{Py})\}]$ (C6) and $[\text{Zn}(\text{NO}_3-\kappa\text{O})(\text{NO}_3-\kappa^2\text{OO}')\{\text{HC}(3-\text{iPrPz})_2(\text{Py})\}]$ (C7).

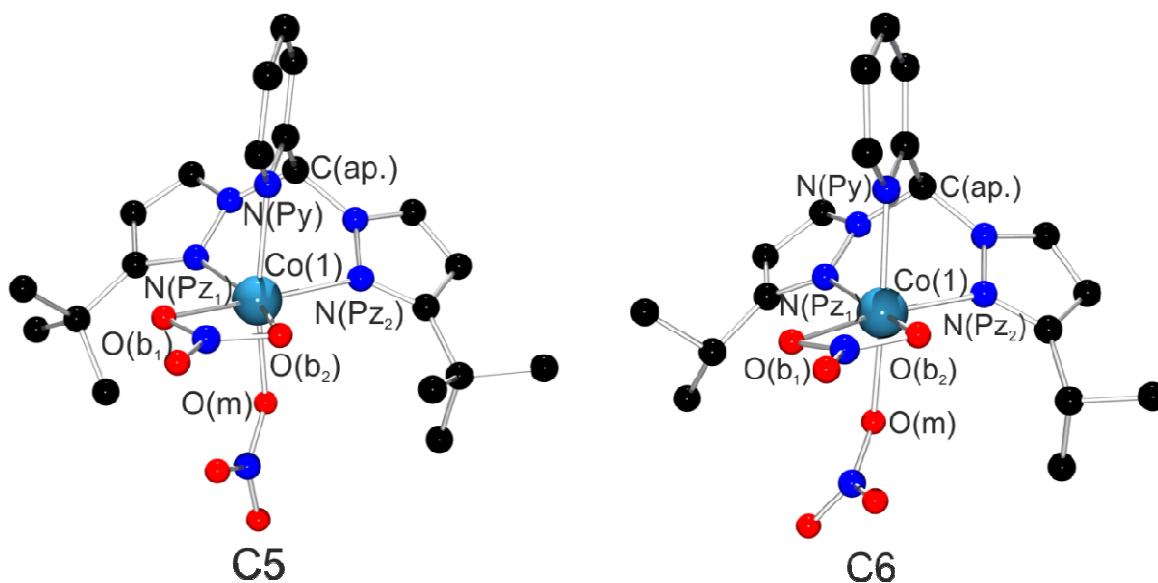


Figure 39. Molecular structures of $[\text{Co}(\text{NO}_3-\kappa\text{O})(\text{NO}_3-\kappa^2\text{OO}')\{\text{HC}(3-\text{tBuPz})_2(\text{Py})\}]$ (C5) and $[\text{Co}(\text{NO}_3-\kappa\text{O})(\text{NO}_3-\kappa^2\text{OO}')\{\text{HC}(3-\text{iPrPz})_2(\text{Py})\}]$ (C6).

In **C5** the cobalt atom is coordinated six-fold by the three coordination sites of the bis(pyrazolyl)methane ligand and monodentately as well as bidentately by the two nitrate groups of the cobalt salt. **C6** is the analogous complex to **C5** with the bis(pyrazolyl)methane ligand $\text{HC}(3\text{-iPrPz})_2(\text{Py})$ (**L3**) (Figure 39), while **C7** refers to the corresponding zinc complex, which also is coordinated by **L3** (Figure 40).

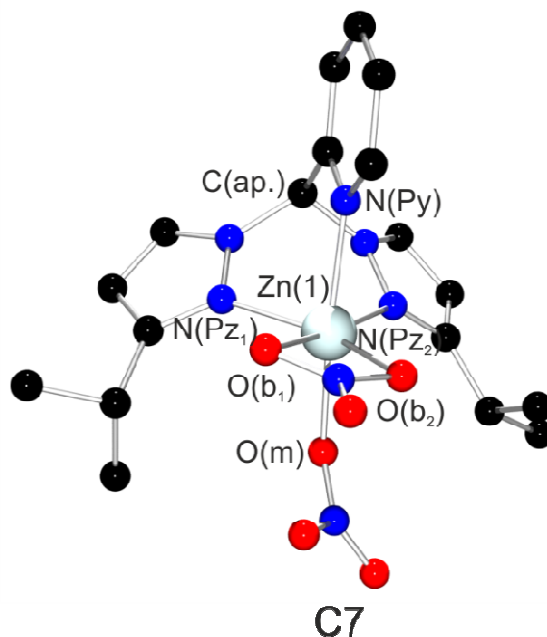


Figure 40. Molecular structure of $[\text{Co}(\text{NO}_3\text{-}\kappa\text{O})(\text{NO}_3\text{-}\kappa^2\text{OO}')\{\text{HC}(3\text{-iPrPz})_2(\text{Py})\}]$ (**C6**).

C6 contains one molecular unit per elementary cell, while **C7** contains two units per elementary cell. **C6** and **C7** crystallise in the triclinic space group $P\bar{1}$. Complexes **C5**, **C6** and **C7** possess the same coordination geometry, which is distorted octahedral in each case. Table 17 lists the bond lengths and Table 18 the bond angles of **C5**, **C6** and **C7**.

Table 17. Selected bond lengths for **C5**, **C6** and **C7**.

Bond lengths [Å]	C5 (M = Co)	C6 (M = Co)	C7 (M = Zn)
Co-N _{Pz1}	2.159(1)	2.076(3)	2.061(2)
Co-N _{Pz2}	2.174(1)	2.100(3)	2.124(2)
Co-N _{Py}	2.156(1)	2.166(3)	2.169(2)
Co-O _m	2.044(1)	2.060(3)	2.096(1)
Co-O _{b1}	2.207(1)	2.166(3)	2.297(2)
Co-O _{b2}	2.134(1)	2.118(3)	2.091(2)

Table 18. Selected bond angles for C5, C6 and C7.

Bond angles [°]	C5 (M = Co)	C6 (M = Co)	C7 (M = Zn)
Co-O _m -N	128.2(1)	127.0(2)	126.4(1)
Co-O _{b1} -N	90.7(1)	93.0(2)	88.2(1)
Co-O _{b2} -N	94.0(1)	91.0(2)	96.8(1)

All three monofacial complexes have two different M-N_{Pz} (M = metal) bond lengths, which means that no mirror plane exists in either structure.

Analysing the metal-nitrogen and metal-oxygen bond lengths listed in Table 17, it strikes that M-N_{Py} bond lengths are in general longer in the complexes with the *isopropyl* substituted ligand (**C6**, **C7**) than in **C5** with the *tertbutyl* substituted one. For M-N_{Pz} bond lengths, the opposite is the case. Comparing the M-N_{Py} and M-N_{Pz} distances in **C6** and **C7**, the latter are shorter. **C5** shows a mixed picture concerning this investigation, as one Co-N_{Pz} and the Co-N_{Py} distance are almost similar. Concerning the M-O distances a commonality can be found amongst all three nitrate complexes. Each M-O_m bond length is shorter than the corresponding M-O_b ones.

The M-O_m-N angles are all similar. Each bidentate nitrate group is bound distorted, resulting in two different M-O_b-N angles, with **C7** showing the largest distortion.

Table 19. Selected octahedron angles of C5–C7.

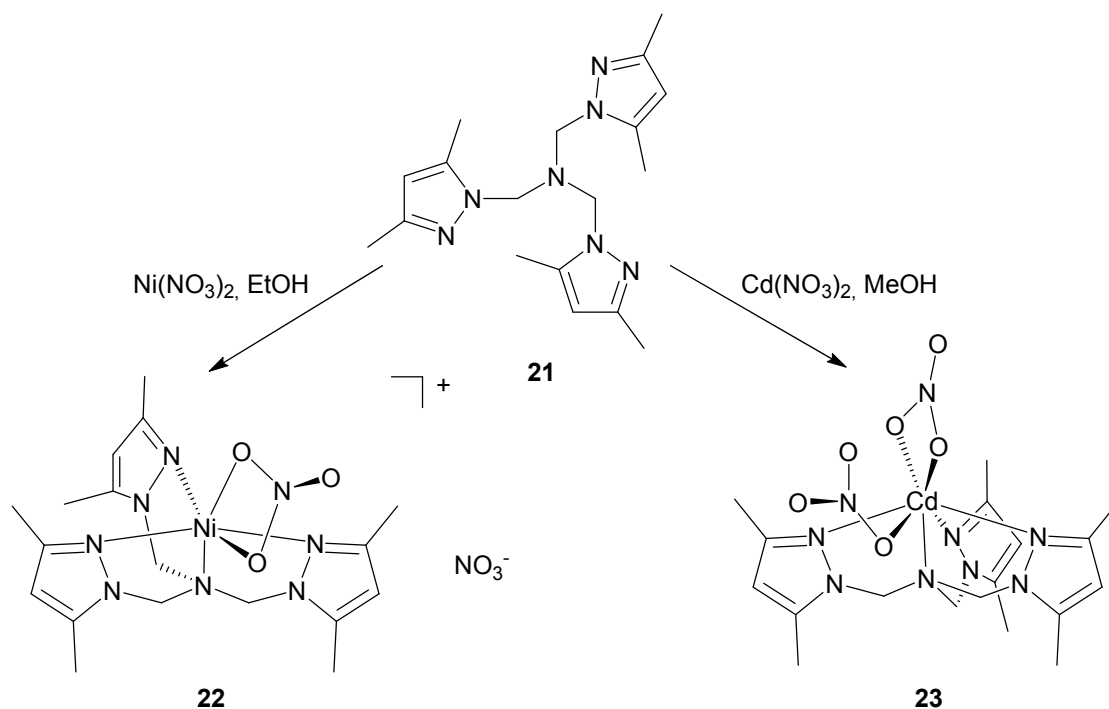
Bond angles [°]	C5 (M = Co)	C6 (M = Co)	C7 (M = Zn)
O _{b1} -M-O _{b2}	59.3(1)	60.4(1)	58.6(1)
N _{Pz} -M-N _{Pz}	92.4(1)	89.9(1)	90.7(1)
N _{Py} -M-O _m	169.5(1)	171.0(1)	169.9(1)
O _m -M-N _{Pz1}	94.4(1)	88.3(1)	93.1(1)
O _m -M-N _{Pz2}	85.9(1)	93.2(1)	86.0(1)
O _{b1} -M-O _m	100.1(1)	88.7(1)	101.3(1)
O _{b2} -M-O _m	96.2(1)	100.9(1)	90.4(1)

From Table 19 it can be seen that all three octahedral complexes **C5**, **C6** and **C7** are distorted. The O_{b1}-M-O_{b2} angle is around 60° for all three complexes and is therefore much smaller than the anticipated 90° angle. However considering that O_{b1} and O_{b2} are part of the bidentately bound nitrate anion, it is evident that this angle cannot be stretched to up to

90°. The N_{pz} -M- N_{pz} angle however is close to 90° for all three complexes. Accordingly, the corresponding N_{pz} -M- O_b angles are larger than 90°. The octahedron axis is defined by the atoms N_{py} , M and O_m ; the angle between those atoms should ideally be 180°. In reality the N_{py} -M- O_m angle is about 170°. Therefore the axis is tilted towards the bis(pyrazolyl)methane ligand and away from the nitrate oxygen atoms. O_m -M- N_{pz2} and O_{b1} -M- O_m have similar values for **C5** and **C7**, while values for the corresponding angle in **C6** are different.

3.4.3 Calculation of the binding mode

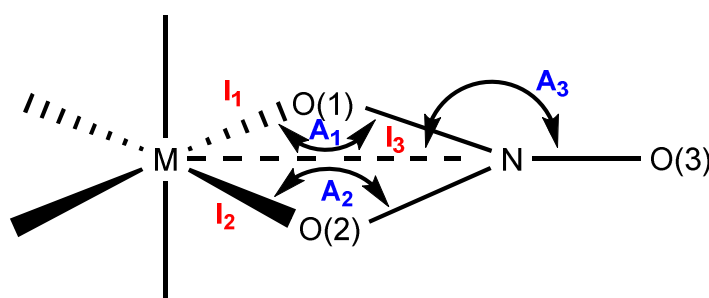
That nitrate can bind on metals in two different coordination modes has been known for a long time.^[173] In 1965 Curtis & Curtis conducted a study regarding nitrate-amine nickel(II) compounds with monodentate and bidentate nitrate ions.^[173] They investigated the compounds $[Ni(en)_2(NO_3)_2]$ (**18**), $[Ni(en)_2NO_3]X$ (**19**) ($X = BF_4^-$, ClO_4^- , I^-) and $Ni(dien(NO_3)_2)$ (**20**) by means of infrared spectroscopy. For species **18** the following infrared bands were found: 708, 728, 818, 1305 and 1420 cm^{-1} . These were assigned to monodentately bound nitrates. Complex **19** showed infrared vibrations at 695, 743, 807, 1290 and 1475 cm^{-1} , which is typical for bidentately bound nitrate. Analogously, **20** showed vibrations indicative of both mono- and bidentately bound nitrate, which led to the conclusion that both binding modes are present there. **20** is one of the few known examples, where a rather simple transition metal nitrate complex exhibits both binding modes in one complex.



Scheme 25. Structure of tris(3,5-dimethyl(pyrazolyl))methylamine (**21**) and synthesis of $[Ni(21)(O_2NO)][NO_3]$ (**22**) and $[Cd(21)(O_2NO)(ONO_2)]$.^{adapted from [174,175]}

In 1985 Reedijk *et al.* conducted experiments with transition metal nitrate salts and the pyrazolyl ligand tris(3,5-dimethyl(pyrazolyl))methylamine (**21**).^[174] Scheme 25 depicts the structure of the according nickel (**22**) and cadmium (**23**) compound^[175] based on X-ray diffraction analyses. **21** hereby acts as a tripodal quadridentate ligand. The coordination geometry of **22** is distorted octahedral and for **23** distorted bicapped octahedral. The nickel complex is a cation in which one nitrate group is coordinated bidentately and the second nitrate is the counterion. In **23** both nitrate groups are bound on the central metal, once unisobidentately and once monodentately.

In order to determine the binding mode concerning the nitrate groups, the calculation according to Figure 41, which was introduced by Reedijk *et al.*^[175], was applied for each of the three complexes **C5–C7**. Hereby the atom distances l_1 , l_2 and l_3 are defined, as well as the bond angles A_1 , A_2 and A_3 . Determination of l_2-l_1 , A_1-A_2 , l_3-l_2 and A_3 results in values that can be assigned to one of three binding modes, which are monodentate, anisobidentate and bidentate (Table 20).



binding mode	monodentate	anisobidentate	bidentate
l_2-l_1	>0.6	$0.3-0.6$	<0.3
A_1-A_2	>28	$14-28$	<14
l_3-l_2	<0.1	$0.1-0.2$	>0.2
A_3	<162	$162-168$	>168

Figure 41. Quantification of the binding mode for the nitrate groups.^[175]

Table 20 proves one monodentately and one bidentately bound nitrate group per complex, which is in accord with the image of the molecular structures.

Table 20. Binding modes for nitrate groups of C5, C6 and C7.

	C1		C2		C3	
	1	2	1	2	1	2
l_2-l_1	1.162	0.0734	1.285	0.022	1.257	0.206
A_1-A_2	92.2	3.34	32	2	61.98	8.66
l_3-l_2	-0.19	0.351	-0.337	0.342	-0.32	0.287
A_3	150	176.4	138	178.5	139.01	172.86
	monodentate	bidentate	monodentate	bidentate	monodentate	bidentate

The complex geometry of Co(II) complexes is diverse and relies strongly on the surrounding ligands. Co(II)-O complexes often are not stable, unless for example polydentate O-donors, such as acetylacetonate or oxalate are applied. Common examples for such complexes are $[\text{Co}(\text{acac})_3]$ and $[\text{Co}(\text{ox})_3]^{3-}$. These complexes show an octahedral geometry. Moreover less polarizable ligands, containing O and N atoms favour the formation of octahedral complexes.^[83] So overall it does not surprise that complexes **C5** and **C6** have a distorted octahedral geometry, considering the polydentate bis(pyrazolyl)methane ligand and nitrate anions. With the octahedral geometry being the most stable option, it is not unusual that one nitrate anion is coordinated bidentately, in order to complete the octahedron.

Zinc almost exclusively exists in the oxidative state +II in compounds. Because of its 10 d-electrons no crystal field stabilisation energy can be gained and therefore Zn(II) complexes can generate any geometry. Which one is present, mostly depends on the steric demands of the ligands.

Applying the formulas from Figure 41, a consistent determination of the binding mode of nitrate or similar anions through geometric parameters is possible. This method is more precise than the infrared spectroscopic one from Curtis, but it is obviously only possible when crystallographic data is present.

3.4.4 Evaluation of NBO calculations

In order to investigate the donor situation between competing N- and O-donors in **C5–C7** natural bond orbital calculations were performed. Second order perturbation theory calculations applying the BP86 functional and 6-31G(d) basis set^[162] resulted in charge-transfer energies concerning all binding partners of the central metal (Table 21).

Table 21. Charge-transfer energies [kcal mol⁻¹] for C5–C7 (Gaussian09, BP86/6-31G(d) and NBO 6.0).^[135,142,162]

CT energies [kcal mol ⁻¹]	C5 (M = Co)	C6 (M = Co)	C7 (M = Zn)
O _{b1} →M	17.89	19.40	42.45
O _{b2} →M	17.72	20.26	48.81
O _m →M	26.44	25.92	65.08
N _{Pz1} →M	12.24	14.44	34.83
N _{Pz2} →M	11.74	14.34	33.91
N _{Py} →M	11.70	9.95	27.49

Regarding the M-N bonds of **C6** and **C7**, charge-transfer energies for N_{Pz}→Co/Zn are larger than for the corresponding N_{Py} bonds, which is in accord with the bond lengths from Table 17, where M-N_{Pz} bonds are shorter. This is evidence for the stronger donor force of pyrazolyl moieties. Looking at the nitrate groups, CT energies for O_m→Co/Zn are larger than the values for the bidentate nitrate groups. Here as well CT energy values tie in with the corresponding bond lengths, resulting in overall shorter O_m→Co/Zn bonds.

Table 22. NBO charge distribution in C5, C6 and C7 (Gaussian09, BP86/6-31G(d) and NBO 6.0).^[135,142,162]

	C5 (M = Co)	C6 (M = Co)	C7 (M = Zn)
M	+1.058	+1.027	+1.171
O _{b1}	-0.496	-0.483	-0.511
O _{b2}	-0.496	-0.491	-0.543
O _{b3}	-0.343	-0.346	-0.343
N _b	+0.700	+0.695	+0.700
O _m	-0.589	-0.580	-0.652
O _{m2}	-0.392	-0.403	-0.411
O _{m3}	-0.396	-0.395	-0.394
N _m	+0.695	+0.695	+0.697
N _{Pz1}	-0.344	-0.345	-0.369
N _{Pz2}	-0.335	-0.342	-0.361
N _{Py}	-0.483	-0.465	-0.490

In addition to charge-transfer energies, NBO charges were investigated. Table 22 lists the values for the central metal, the donating bis(pyrazolyl)methane nitrogen atoms and all elements belonging to the nitrate groups. The metal has the highest positive partial charge, followed by N_b and N_m . All remaining atoms possess partial negative NBO charges.

The study of NBO charges gives an idea of the electronic effects in the complexes, however they do not represent absolute charges. Starting with a comparison of N_{pz} and N_{py} , the NBO charge is more negative at the pyridinyl nitrogen atom (hence more basic). However, the CT energy for $N_{pz} \rightarrow M$ is higher, making the pyrazolyl moiety the stronger donor (more nucleophilic), resulting in a shorter N_{pz} -M bond length as well. Consulting the basicity of pyridine and pyrazole, pyridine is the stronger base with a pK_B value of 8.8, compared to 11.5 for pyrazole^[176], so if only basicity is considered, the N_{py} -M bond should be the shorter one. However several effects play a role in the determination of a donor-acceptor bond. Not only basicity, but also nucleophilicity, spin state, Jahn-Teller distortion and steric effects have to be considered. The complex donor competition between pyrazolyl and pyridinyl moieties in bis(pyrazolyl)methane complexes has been observed and reviewed by Herres-Pawlis *et al.*^[160,162], but it remains complex and case specific.

In general, charge distribution within **C5**, **C6** and **C7** is very similar. Comparing the three, **C7** has the highest positive charge at the central atom and overall the largest negative values on all atoms which form bonds to the central metal. All atoms, which do not contribute to the N/O \rightarrow M bonds (marked in green) have similar NBO charge values, when **C5**, **C6** and **C7** are compared.

3.4.5 Summary

Three new bis(pyrazolyl)methane cobalt and zinc complexes (**C5–C7**) were synthesised by reacting the ligands HC(3-*t*BuPz)₂(Py) (**L5**) and HC(3-*i*PrPz)₂(Py) (**L3**) with the according nitrate salts. An infrequent coordination geometry resulted, showing one monodentately and one bidentately bound nitrate group, resulting in distorted octahedral complex geometries for all three complexes. The coordination mode of nitrate was calculated in each case, applying the formula of Reedijk *et al.*^[175], which results in a consistent determination through the application of geometric parameters.

NBO calculations showed a larger CT energy for the $N_{p_z} \rightarrow M$ bond, which is in accord with the shorter N_{p_z} -M in comparison to the N_{p_y} -M bond length. Evaluation of NBO charges showed similar charge distributions for all three complexes.

3.5 Investigations towards a copper(II)-superoxide mimic and NO activation with bis(pyrazolyl)methanes

3.5.1 Introduction

In the physiological context the NO molecule plays an important role because of its blood pressure lowering properties as well as its function in signal transduction.^[177,178] In addition, NO is also an interesting ligand for coordination chemistry, as it is redox active and can bind on metals neutrally, as a cation or anion.^[179] It is possible to introduce NO as ligand to a complex species in different ways. Besides the reaction with NO gas directly, NO can be generated *in situ via* the reaction of sodiumnitrite with concentrated sulphuric acid in a two phase reaction.^[180,181] Another method is the addition of NO⁺ salts, such as NOBF₄ or NOSbF₆, which additionally provide bulky anions which facilitate crystallisation. Furthermore several compounds can transfer NO directly, such as diazald® or tritylthionitrite (TTN, Figure 42).^[182,183]

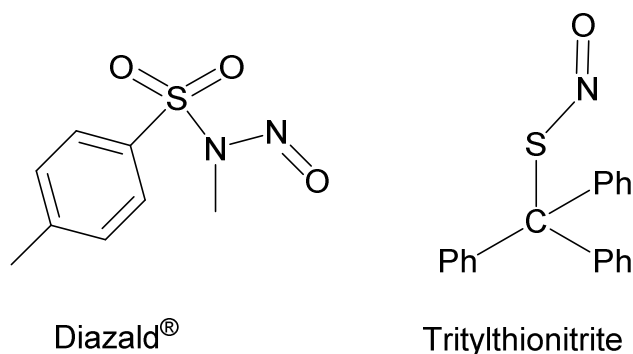
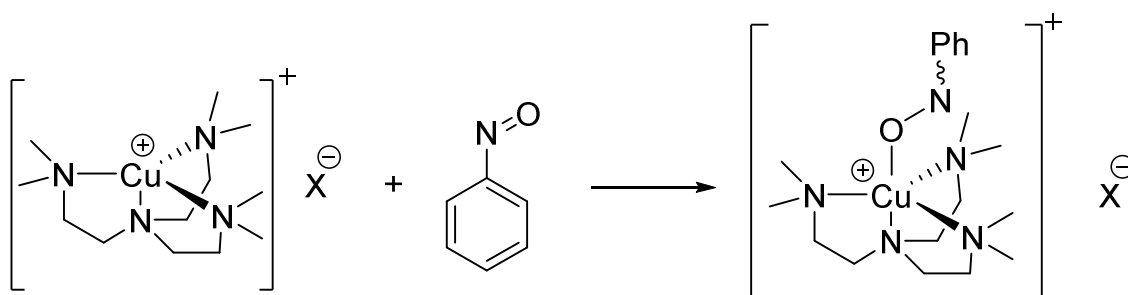


Figure 42. Structure of NO transferring reagents diazald® and tritylthionitrite (TTN).

Nitrosobenzene on the other hand is a compound, which acts as a superoxide mimic. In nature such Cu(II) end-on superoxide structures are discussed as intermediates in the catalytic cycle of the monooxygenase dopamine-hydroxylase and others. Ottenwaelder *et al.* were able to crystallise nitrosobenzene Cu(I) species including nitrogen donors as superoxide mimics (Scheme 26).^[184]



Scheme 26. Synthesis of [Me₆trenCu(PhNO-κO)]⁺ adapted from [184].

3.5.2 Copper nitrosobenzene species as superoxide mimics

As a superoxide is supposed to be an intermediate in the catalytic cycle of tyrosinase as well, experiments with a Cu(I) bis(pyrazolyl)methane precursor and nitrosobenzene were performed.^[185] The copper(I) precursor was synthesised exactly like the one that was used for the reaction with oxygen (see 3.2). Conditions for nitrosobenzene reactions were screened with a variety of solvents, reaction temperatures and amounts of nitrosobenzene. As soon as nitrosobenzene was added to the precursor solution, an immediate colour change to deep-red was observed.

Table 23. Overview of extinction coefficients of the reaction of $[\text{Cu}\{\text{HC}(3\text{-}t\text{BuPz})_2(\text{Py})\}]^+$ with nitrosobenzene at $\lambda = 454$ and $\lambda = 558$ nm.

Solvent	CH_2Cl_2			THF			CHCl_3		
Temperature [°C]	rt	-30	-78	-78			-60		
Equivalents	2	2	2	1	2	4	1	2	4
$\epsilon_{\lambda = 454 \text{ nm}} [\text{Lmol}^{-1}\text{cm}^{-1}]$	1940	1690	2500	/	1230	1430	2875	4383	1973
$\epsilon_{\lambda = 558 \text{ nm}} [\text{Lmol}^{-1}\text{cm}^{-1}]$	1620	1490	2250	/	1160	1260	2561	3889	1706

It was determined that reactions in chloroform at low temperatures with 2 eq of nitrosobenzene yielded the highest conversions. The lowest absorption was observed with THF at any temperature, which might be due to coordination of the solvent to the copper precursor.

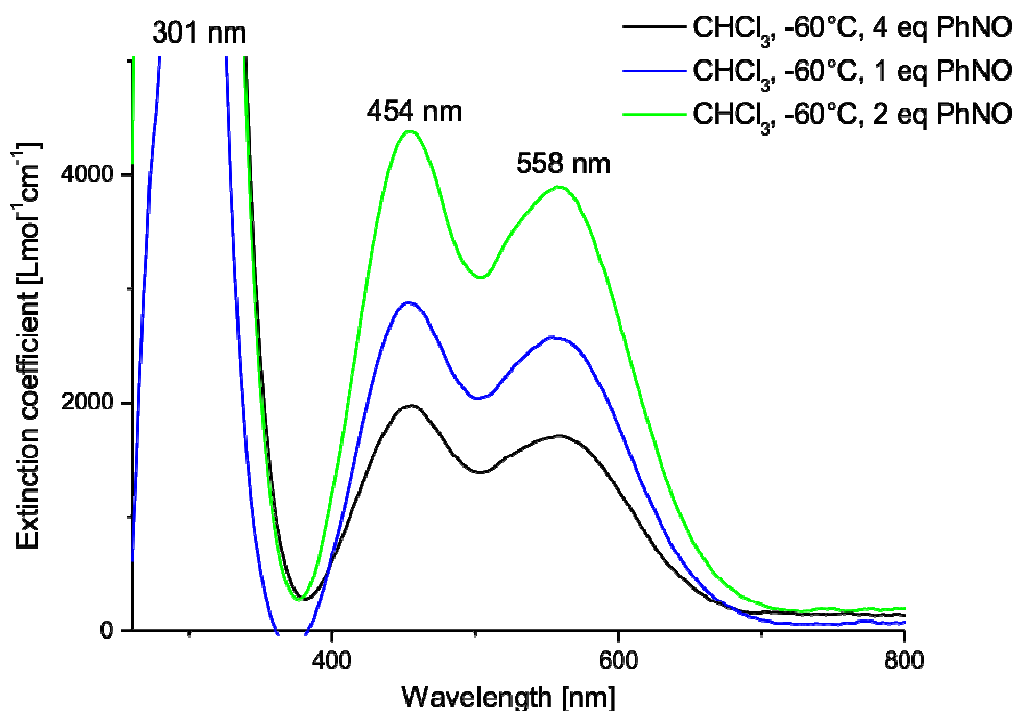


Figure 43. Experimental UV/Vis spectra of the reaction of $[\text{Cu}\{\text{HC}(3\text{-}t\text{BuPz})_2(\text{Py})\}]^+$ with nitrosobenzene.

The UV/Vis spectra of the reactions performed under the conditions displayed in column three are shown in Figure 43.

As it was not possible to obtain crystals for structural analysis of the nitrosobenzene species, structural optimisation and TD-DFT calculations of the singlet and triplet compound were performed. When comparing the stabilisation energies it shows that the singlet species is favoured over the triplet state, no matter which coordination mode is investigated. ($-3.44 \text{ kcal mol}^{-1}$ for κN and $-1.67 \text{ kcal mol}^{-1}$ for κO). Comparisons within the isomers indicated a preference for the κN binding mode each. In Figure 44 the structural optimisation of both the κO - and κN -compound of the singlet state are pictured. An energy barrier in favour of the κN -isomer of $2.4 \text{ kcal mol}^{-1}$ was calculated.

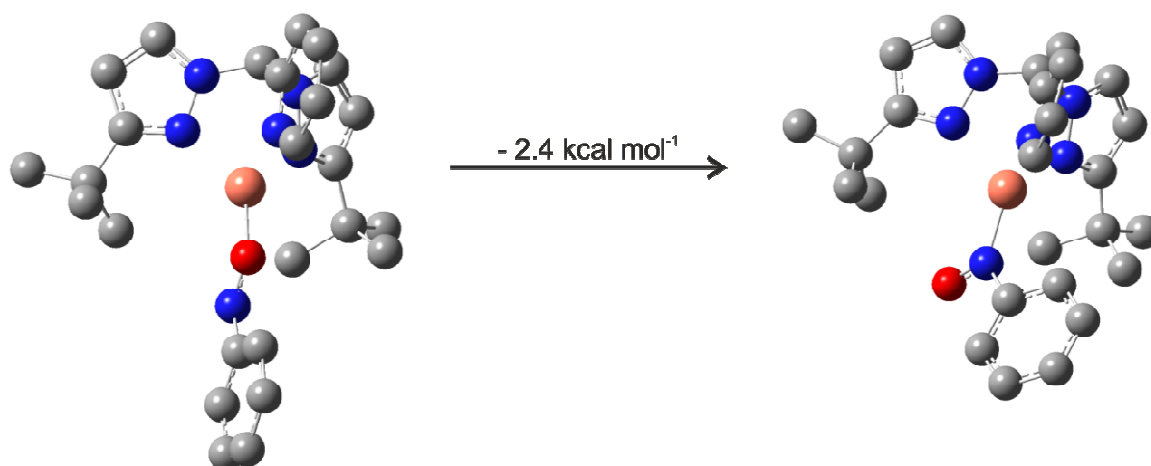


Figure 44. Structural optimisation of singlet $[\text{Cu}\{\text{HC}(3\text{-tBuPz})_2(\text{Py})\}\{\text{PhNO-}\kappa\text{O}\}]^+$ and $[\text{Cu}\{\text{HC}(3\text{-tBuPz})_2(\text{Py})\}\{\text{PhNO-}\kappa\text{N}\}]^+$ (B3LYP, 6-31G(d), Gaussian09).^[186]

Comparison of the calculated UV/Vis spectra of the singlet and triplet κN -compounds (comparison between the according κN - and κO -species only shows minor differences) indicated a better agreement of the calculated singlet state to the experimental data.^[186] For a more accurate determination whether the singlet κN - or κO -complex was built, Table 24 lists their according calculated absorption maxima.

Table 24. TD-DFT calculated UV/Vis absorption maxima for singlet $[\text{Cu}\{\text{HC}(3\text{-}t\text{BuPz})_2(\text{Py})\}\{\text{PhNO-}\kappa\text{O}\}]^+$ and $[\text{Cu}\{\text{HC}(3\text{-}t\text{BuPz})_2(\text{Py})\}\{\text{PhNO-}\kappa\text{N}\}]^+$ (B3LYP, 6-31G(d), Gaussian09) in comparison to experimental values.^[186]

	κO -species	κN -species	Exp.
$\lambda_{\text{max.1}}$ [nm]	195	190	301
$\lambda_{\text{max.2}}$ [nm]	287	295	454
$\lambda_{\text{max.3}}$ [nm]	488	406	558
$\lambda_{\text{max.2}} - \lambda_{\text{max.1}}$ [nm]	92	105	153
$\lambda_{\text{max.3}} - \lambda_{\text{max.2}}$ [nm]	201	111	104

The number of three predicted absorption maxima $\lambda_{\text{max.1}}$, $\lambda_{\text{max.2}}$ and $\lambda_{\text{max.3}}$ is in accord with the experimental spectra, but their position is off. Considering however the distance between the maxima, the κN -species seems more likely to have been built. This would also coincide with the calculated stabilisation energy. More theoretical analyses using broken-symmetry DFT should be performed here.

Only few compounds of copper with nitrosobenzene are known and structurally characterised. Besides Ottenwaelder's $[\text{Me}_6\text{trenCu}(\text{PhNO-}\kappa\text{O})]^+$ species, $[\text{Cu}(\text{iPrPhNO-}\kappa\text{N})_3]^+$ has been crystallised as an example for an N-bound nitrosobenzene complex, but considering its three substituted nitrosobenzene units and no nitrogen donor involved, this complex cannot serve for a comparison.^[187,188]

3.5.3 Diazald and TTN as NO transferring agents

The reaction of $[\text{Cu}\{\text{HC}(3\text{-}t\text{BuPz})_2(\text{Py})\}]^+$ with TTN did not give any conclusive evidence of NO-donating properties, as multiple products were built according to UV/Vis measurements that could not be characterised yet.

Furthermore two separate experiments were performed in which $[\text{Cu}\{\text{HC}(3\text{-}t\text{BuPz})_2(\text{Py})\}]^+$ was reacted once with a solution of diazald® at rt and once with NO gas in a secluded gas injection system at -60°C . Figure 45 displays the UV/Vis spectra of both experiments. Here the NO transferring property of the reagent diazald® is clearly visible, as both spectra resemble each other largely and only differ in their absorption, which is evident, as NO gas was present in an extreme excess and diazald® only in 0.5 eq. Importantly, the reaction with diazald® does not indicate any minor products. Attempts to yield crystals of the expected product (Figure 46) failed so far.

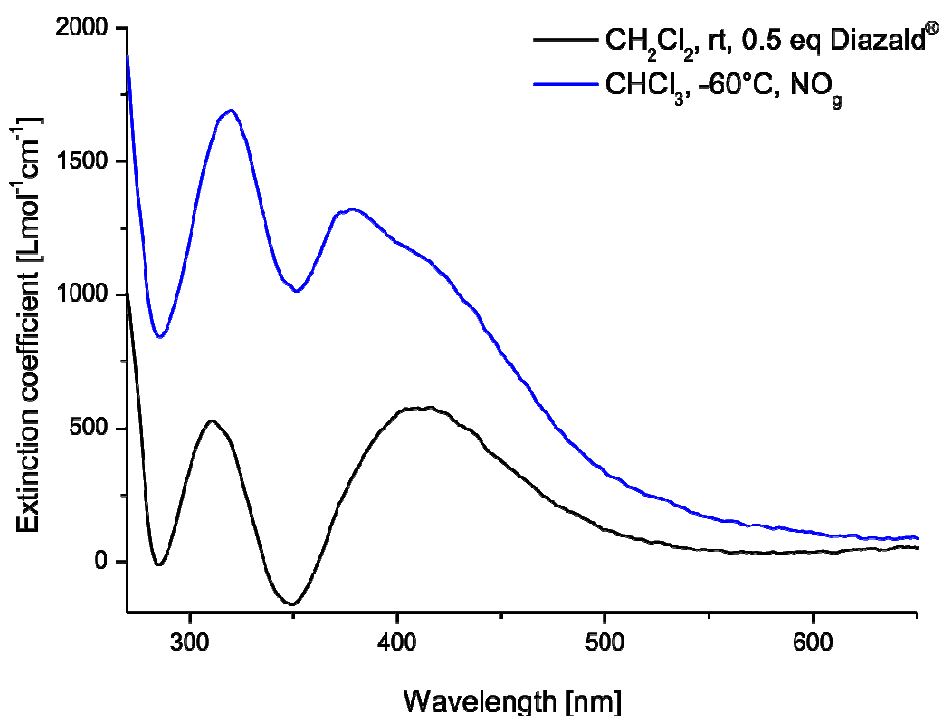


Figure 45. UV/Vis spectra of the reaction of $[\text{Cu}\{\text{HC}(3\text{-}t\text{BuPz})_2(\text{Py})\}]^+$ with diazald® (black) and NO gas (blue).

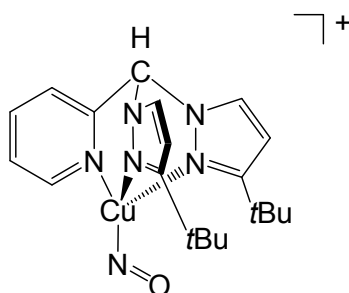


Figure 46. Expected reaction product of the reaction of $[\text{Cu}\{\text{HC}(3\text{-}t\text{BuPz})_2(\text{Py})\}]^+$ with NO donor agents.

3.5.4 Summary

In summary, experiments were conducted in order to firstly generate a superoxide mimic for the enzyme tyrosinase and secondly with NO transferring agents, as well as NO gas to activate NO.

Initially reaction conditions were optimised. The experiments with nitrosobenzene clearly showed a reaction with the Cu(I) precursor, generating a room temperature stable deep red species. The reaction was followed by UV/Vis spectroscopy, but it was not possible to determine definitely whether the κN - or κO -complex was built. Comparison with TD-DFT investigations indicated the formation of the κN -species.

The experiments with TTN did not give conclusive results, because several species were built that could not be characterised.

Comparing the reaction of the Cu(I) precursor with NO gas and with diazald® proofed the NO transferring ability of diazald®, however the resulting product could not be characterised yet.

3.6 Basic studies on bis(pyrazolyl)methane ligands and their complexation behaviour

3.6.1 Isomerisation and structural properties

As mentioned in the introduction (1.13), the ligand class of bis(pyrazolyl)methanes is large, because of the wide variability of substituents at the pyrazolyl units, as well as the flexible third donor function. Figure 47 shows an overview of all the bis(pyrazolyl)methane ligands that were used in this thesis. **L2** and **L5–L7** were resynthesised according to the protocol established by Herres-Pawlis *et al.*^[117] **L3'** and **L4'** represent the isomerised counterparts of **L3** and **L4**. Scheme 27 depicts the synthesis of **L3** and a mixture of **L4** and **L4'** with **L4'** being part of the bisfacial cobalt complex **C10**.

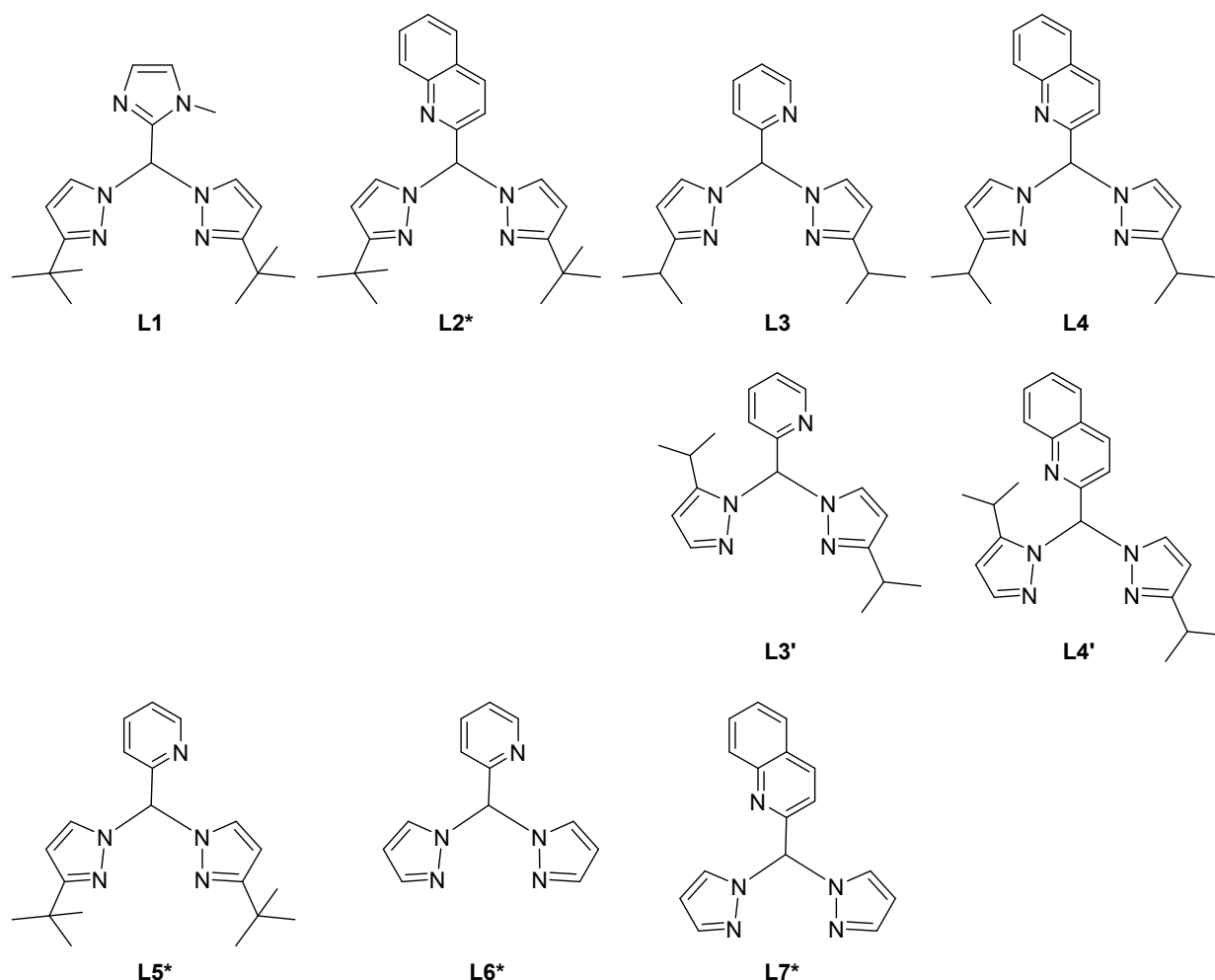
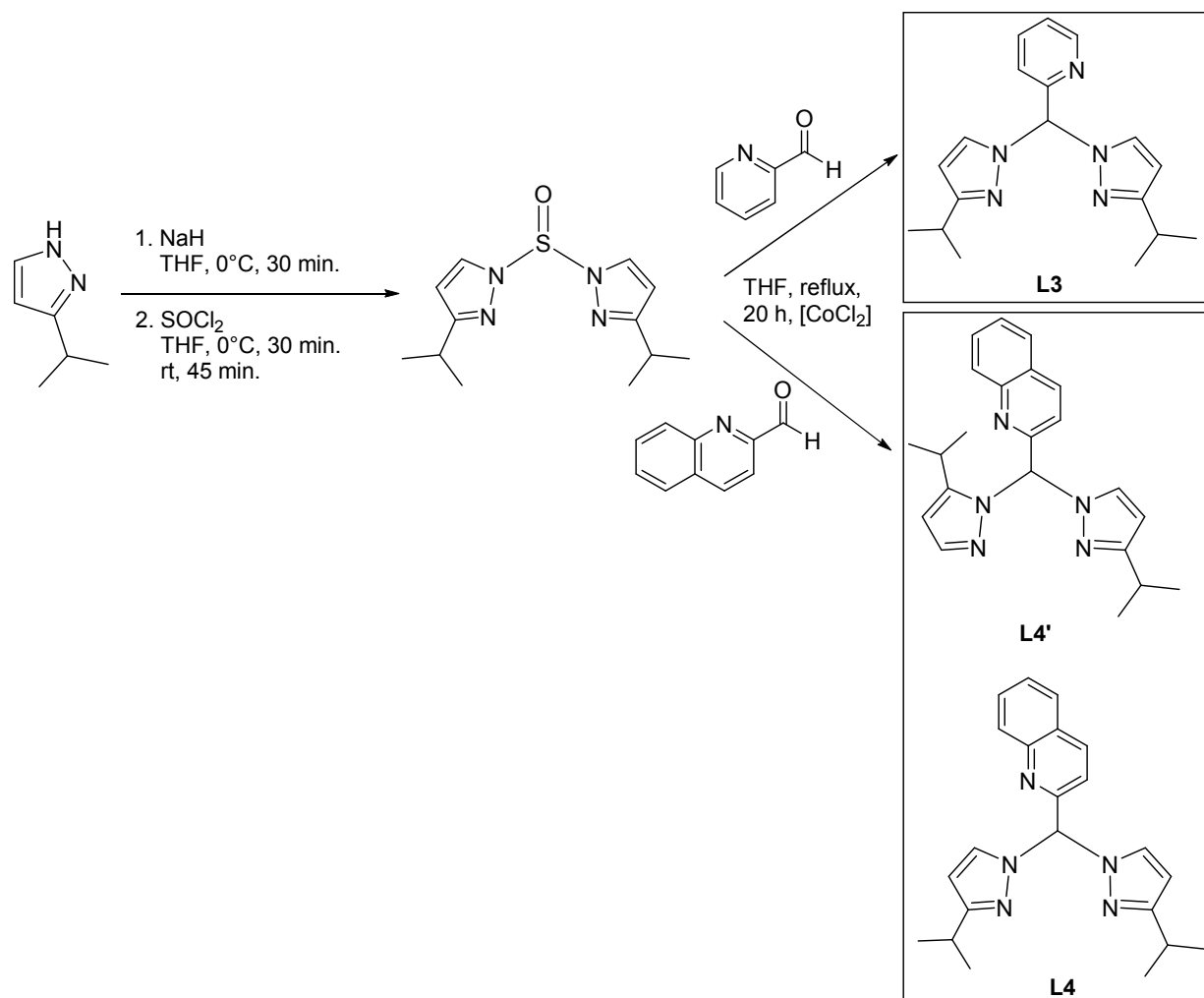


Figure 47. Structures of ligands L1–L7 as well as L3' and L4'. With * marked ligands were resynthesised according to [117].

An often occurring side-effect concerning the synthesis of substituted bis(pyrazolyl)methane ligands is the rearrangement of the ligand moiety in the 3-position, resulting in mixed species with substituents in the 3- and 5-position.^[189,190] This isomerisation can occur due to too much thermal energy during the distillation of the ligand or by Lewis acid catalysis during the reaction of the ligand with metal salts.



Scheme 27. Synthesis of HC(3-*i*PrPz)₂(Py) (**L3**) and a mixture of HC(3-*i*PrPz)₂(Qu) (**L4**) and HC(3-*i*PrPz)(5-*i*PrPz)(Qu) (**L4'**).

Figure 48 shows the molecular structures of the known bis(pyrazolyl)methane ligand HC(3-*t*BuPz)₂(Qu) (**L2**)^[117] and the new ligand HC(3-*i*PrPz)(5-*i*PrPz)(Py) (**L3'**). Both have a distorted tetrahedral geometry at the apical C-atom.

L2 crystallises in the triclinic space group $P\bar{1}$ with two molecular units per elementary cell and **L3'** crystallises in the triclinic space group $P\bar{1}$ as well, with four units per elementary cell. Table 25 displays key bond lengths and angles in **L2** and **L3'**.

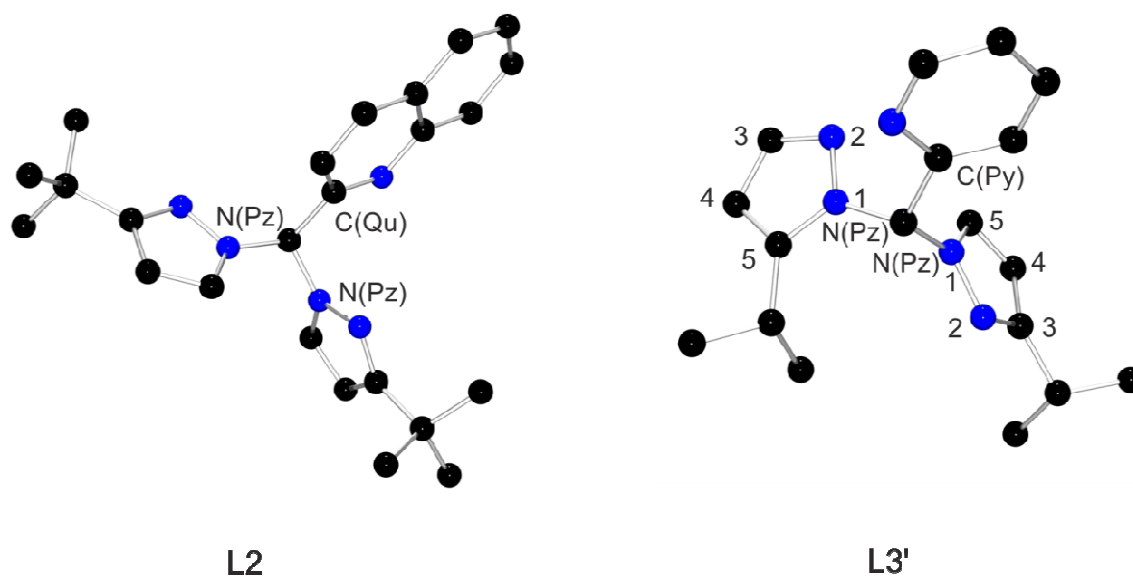


Figure 48. Molecular structures of HC(3-*t*BuPz)₂(Qu) (L2) and HC(3-*i*PrPz)(5-*i*PrPz)(Py) (L3').

The molecular structure of **L3'** shows an isomerised ligand. As this is a common effect, a protocol for the reisomerisation of 3/5-substituted compounds was established in this thesis, which is based on the reisomerisation of tris(pyrazolyl)methanes.^[111,191,192] Hereby, the isomerised ligand is refluxed with catalytic amounts of *p*-toluenesulfonic acid in toluene, resulting in the thermodynamically favoured 3/3 product.^[111,193]

The Lewis acid catalysed isomerisation has been investigated by Herres-Pawlis *et al.* recently. Hereby the 3/3 substituted version of ligand **L3'** was reacted with various iron(II) salts in an attempt to generate monofacial iron complexes. However upon reaction isomerisation occurred and complexes of the type [Fe{HC(3-*i*PrPz)(5-*i*PrPz)(Py)}₂]²⁺ were achieved. It seems that these systems attempt to avoid steric pressure. Theoretical studies proved a 20 kcal mol⁻¹ more stable [Fe{HC(3-*i*PrPz)(5-*i*PrPz)(Py)}₂]²⁺ complex.^[190]

Table 25. Key bond lengths [Å] and angles [°] in L2 and L3'.

Bond lengths [Å]	L2*	L3'
C _{ap} -N _{Pz}	1.437(4)	1.456(2)
	1.448(4)	1.451(2)
C _{ap} -C _{Qu*/Py}	1.524(5)	1.519(3)
N _{Pz} -N _{Pz}	1.373(4)	1.362(2)
	1.347(4)	1.365(2)
Bond angles [°]		
N _{Pz} -C _{ap} -N _{Pz}	111.4(3)	109.3(2)
N _{Pz} -C _{ap} -C _{Qu*/Py}	112.8(3)	112.2(2)
	111.6(3)	113.4(2)

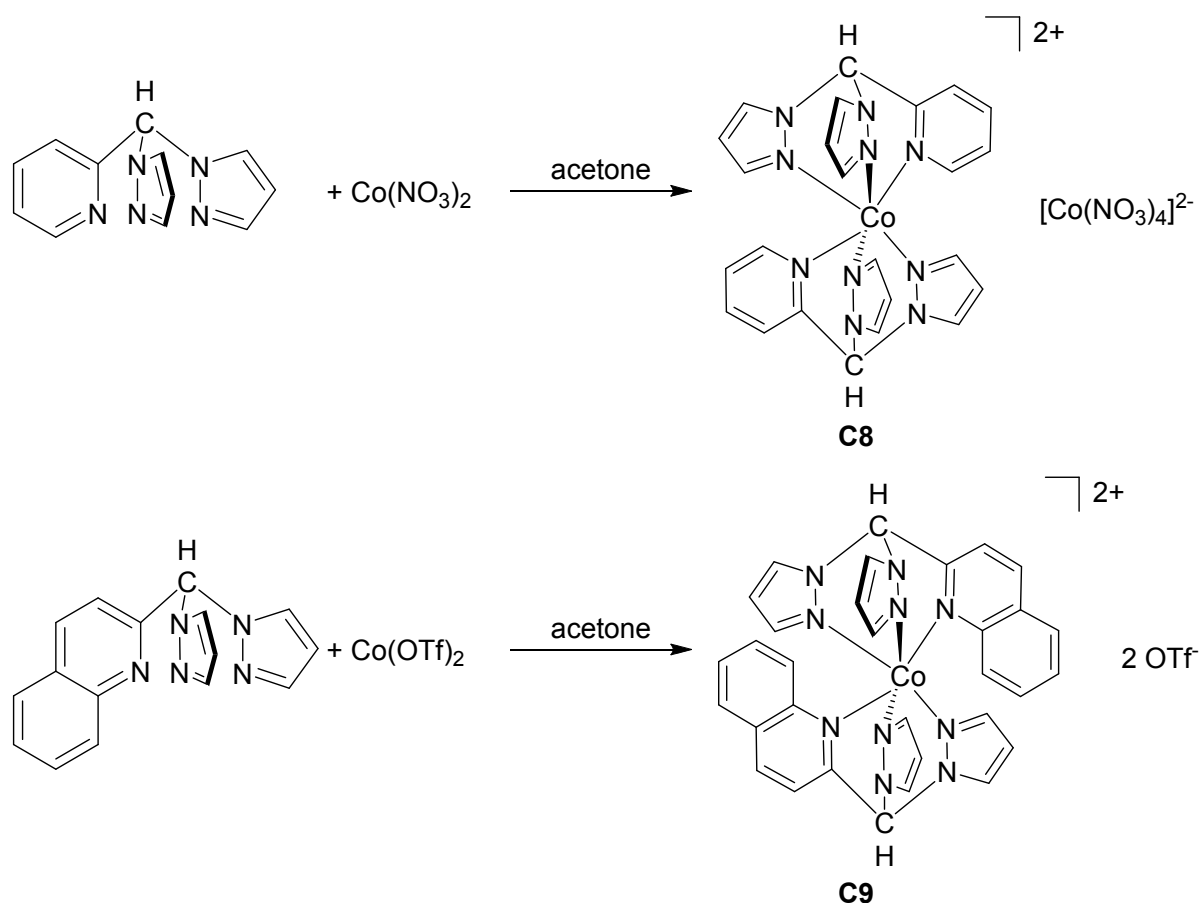
The bond lengths in **L2** and **L3'** are very similar. In general the $C_{ap}-N_{Pz}$ bond length is shorter than the $C_{ap}-C_{Qu}$ or $C_{ap}-C_{Py}$ one. Bond angles confirm the slight distortedness of both structures compared to an ideal tetrahedron.

3.6.2 Structural studies on cobalt bis(pyrazolyl)methane complexes

In fundamental studies on the complexation behaviour of bis(pyrazolyl)methane ligands, we investigated several bisfacial complexes. Reaction of $Co(NO_3)_2$ with $HC(Pz)_2(Py)$ (**L6**)^[117] afforded the bisfacial Co complex $[Co\{HC(Pz)_2(Py)\}_2][Co(NO_3)_4]$ (**C8**) and reaction of $Co(OTf)_2$ with $HC(Pz)_2(Qu)$ (**L7**)^[117] furnished $[Co\{HC(Pz)_2(Qu)\}_2][(OTf)_2]$ (**C9**) (Scheme 28, Figure 49).

The molecular structure of the **C8** cation, **C8**²⁺, has been known since 1991.^[162,194]

It was synthesised by Astley *et al.* by adding a solution of **L6** in acetone to a solution of the aqueous cobalt nitrate salt in acetone. Vapour diffusion of diethyl ether into an acetonitrile-methanol (1:1) solution of the cobalt complex resulted in yellow crystals.



Scheme 28. Synthesis of $[Co\{HC(Pz)_2(Py)\}_2][Co(NO_3)_4]$ (**C8**) and $[Co\{HC(Pz)_2(Qu)\}_2][(OTf)_2]$ (**C9**).

The difference between C8^{2+} and Astley's structure (CC8^{2+}) solely is the counterion. C8^{2+} has the $[\text{Co}(\text{NO}_3)_4]^{2-}$ anion as counterpart and CC8^{2+} single nitrate anions.

Table 26 lists various bond lengths and angles in C8^{2+} , CC8^{2+} and C9^{2+} . C8^{2+} and C9^{2+} both have a mirror plane, so that there is only one value for Co- N_{Pz} and Co- N_{Py} bond lengths.

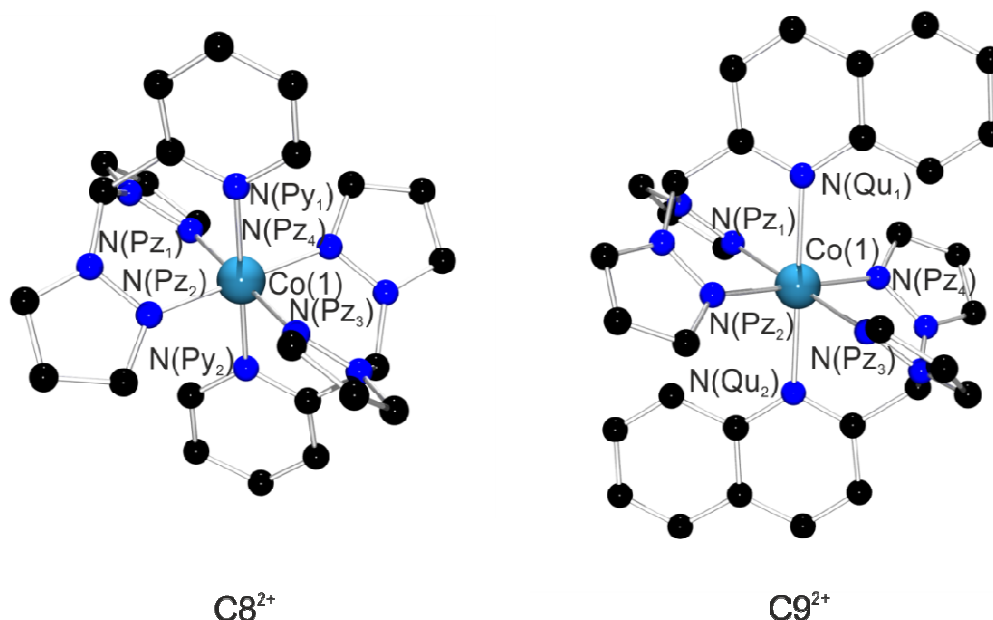


Figure 49. Molecular structure of $[\text{Co}\{\text{HC}(\text{Pz})_2(\text{Py})\}_2]^{2+}$ (C8^{2+}) in crystals of $[\text{Co}\{\text{HC}(\text{Pz})_2(\text{Py})\}_2][\text{Co}(\text{NO}_3)_4]$ (C8) and of $[\text{Co}\{\text{HC}(\text{Pz})_2(\text{Qu})\}_2]^{2+}$ (C9^{2+}) in crystals of $[\text{Co}\{\text{HC}(\text{Pz})_2(\text{Qu})\}_2][(\text{OTf})_2]$ (C9). In C8 pyrazolyl and pyridinyl moieties are disordered. Here only one isomer is shown for clarity.

Table 26. Key bond lengths [\AA] and angles [$^\circ$] in C8^{2+} , CC8^{2+} and C9^{2+} .

Bond lengths [\AA]	C8^{2+}	CC8^{2+} ^[194]	C9^{2+} *
Co- $\text{N}_{\text{Pz1/3}}$	1.913(11)	2.106(4)	2.095(16)
Co- $\text{N}_{\text{Pz2/4}}$	1.922(3)	2.130(5)	2.090(2)
Co- $\text{N}_{\text{Py}}/\text{N}_{\text{Qu}}$	1.972(11)	2.118(4)	2.238(2)
Bond angles [$^\circ$]			
$\text{N}_{\text{Pz1}}\text{-Co-}\text{N}_{\text{Pz3}}$	180.0(7)	180.0	180.0
$\text{N}_{\text{Pz3}}\text{-Co-}\text{N}_{\text{Pz4}}$	91.1(3)	86.4(2)	89.73(6)
$\text{N}_{\text{Pz3}}\text{-Co-}\text{N}_{\text{Pz2}}$	88.9(3)	/	90.27(6)
$\text{N}_{\text{Pz4}}\text{-Co-}\text{N}_{\text{Pz2}}$	180.0(1)	180.0	180.0
$\text{N}_{\text{Pz4}}\text{-Co-}\text{N}_{\text{Py2}}/\text{N}_{\text{Qu2}}$ *	90.8(5)	84.5(2)	83.2(6)
$\text{N}_{\text{Pz3}}\text{-Co-}\text{N}_{\text{Py2}}/\text{N}_{\text{Qu2}}$ *	86.8(5)	83.9(2)	82.72(6)

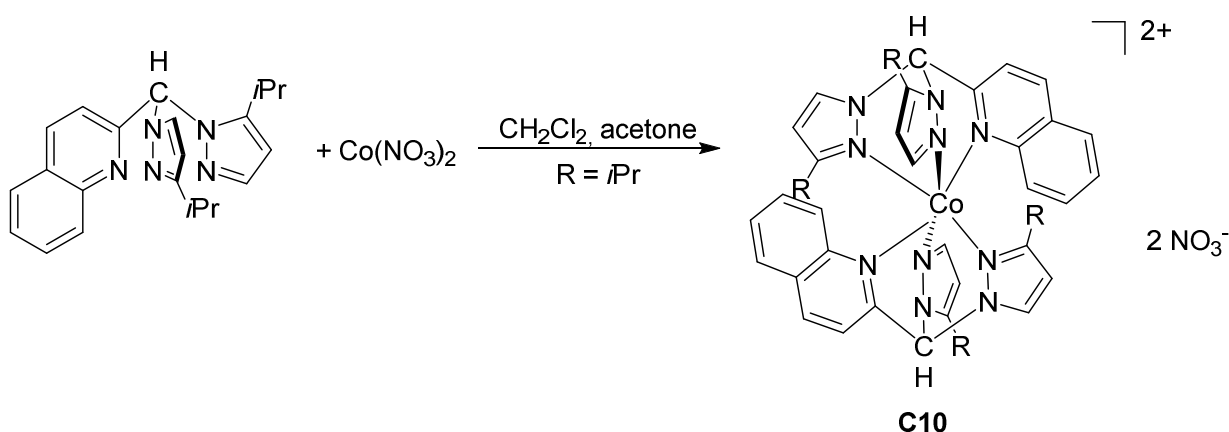
Comparing C8^{2+} and CC8^{2+} , bond lengths in CC8^{2+} are generally longer and range from 2.106(4) \AA to 2.130(5) \AA . In CC8^{2+} one Co- N_{Pz} bond length is the longest of the M-N bonds,

whereas in **C8**²⁺ the Co-N_{Py} bond length is the longest one. Bis(pyrazolyl)methane bite angles in **CC8**²⁺ lie between 83.9(2) and 86.4(2)°. In **C8**²⁺, those have values between 86.8(5) and 91.1(3)°, which makes the geometry of **C8**²⁺ slightly more distorted than **CC8**²⁺.

Bond lengths in **C9**²⁺ are significantly longer than in **C8**²⁺. Both have in common that the Co-N_{Py}, as well as the Co-N_{Qu} bond lengths are longer than the Co-N_{Pz} ones. Bite angles in **C9**²⁺ vary from 82.7(1) to 89.7(1)° which lie more in the area of **CC8**²⁺.

For the study of catalytic activity, metal complexes with free coordination sites are required, or ones with weakly coordinating or easily abstractable anions. These requirements are met for example by bis(pyrazolyl)methane ligands of the second generation, which were introduced by Trofimenko a while ago.^[101] With their alkyl substituents at the pyrazolyl moiety of the bis(pyrazolyl)methane ligand, a bisfacial coordination mode should be ruled out whereas ligands with unsubstituted pyrazolyls coordinate bisfacially at a central atom (see **C8**, **C9**).

Reaction of a mixture of HC(3-*i*PrPz)₂(Qu) **L4** and its isomerised counterpart HC(3-*i*PrPz)(5-*i*PrPz)(Qu) (**L4'**) with Co(NO₃)₂ (Scheme 29) yielded red crystals, the molecular structure of the cationic unit of which is displayed in Figure 50.



Scheme 29. Synthesis of [Co{HC(3-*i*PrPz)(5-*i*PrPz)(Qu)}₂][(NO₃)₂] (**C10**).

Complex **C10** is bisfacial as well, because the isomerisation of the *isopropyl* groups reduces steric pressure.

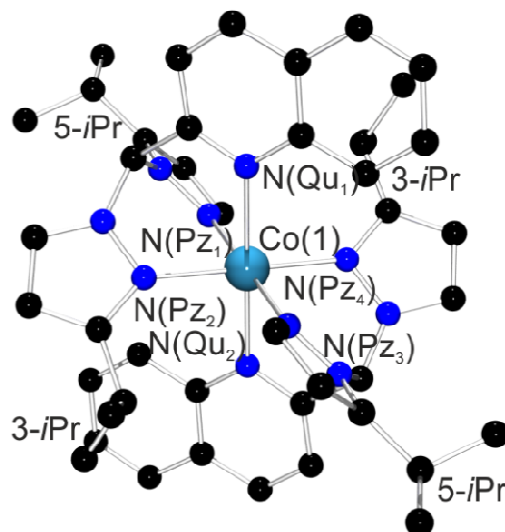
**C10²⁺**

Figure 50. Molecular structure of $\{[HC(3\text{-}iPrPz)(5\text{-}iPrPz)(Qu)]_2Co\}^{2+}$ (**C10²⁺**) in crystals of $[Co\{HC(3\text{-}iPrPz)(5\text{-}iPrPz)(Qu)\}_2][NO_3]_2$ (**C10**).

Table 27 lists key bond lengths and angles of **C10²⁺**. N_{Pz1} and N_{Pz3} represent 3-isopropyl substituted pyrazolyl moieties, whereas N_{Pz2} and N_{Pz4} belong to 5-isopropyl substituted pyrazolyls.

Table 27. Key bond lengths [\AA] and angles [$^\circ$] in **C10²⁺**.

Bond lengths [\AA]	C10²⁺
Co- $N_{Pz1/3}$	2.122(1)
Co- $N_{Pz2/4}$	2.074(1)
Co- N_{Qu}	2.230(1)
Bond angles [$^\circ$]	
$N_{Pz1}\text{-Co-}N_{Pz3}$	180.0(1)
$N_{Pz3}\text{-Co-}N_{Pz4}$	88.3(1)
$N_{Pz3}\text{-Co-}N_{Pz2}$	91.7(1)
$N_{Pz4}\text{-Co-}N_{Pz2}$	180.0(1)
$N_{Pz4}\text{-Co-}N_{Qu2}$	95.8(1)
$N_{Pz3}\text{-Co-}N_{Qu2}$	95.0(1)

Here, just like in **C8²⁺** and **C9²⁺**, the Co- N_{Qu} bond length is longer than the Co- N_{Pz} one. In addition it strikes that Co- $N_{Pz1/3}$ in comparison to Co- $N_{Pz2/4}$ show a clear difference in length. This is due to the isomerised isopropyl groups, resulting in different Co- N_{Pz} bond lengths for the 3- and 5-isomer. The Co- N_{Pz} bond length to the 3-isomer is longer in this case.

Astley found for his systems^[194] that metal-ligand bond lengths are significantly shorter in bisfacial complexes than in their monofacial counterparts. This observation cannot be confirmed for **C10** (see for example **C11** in comparison to **C10**).

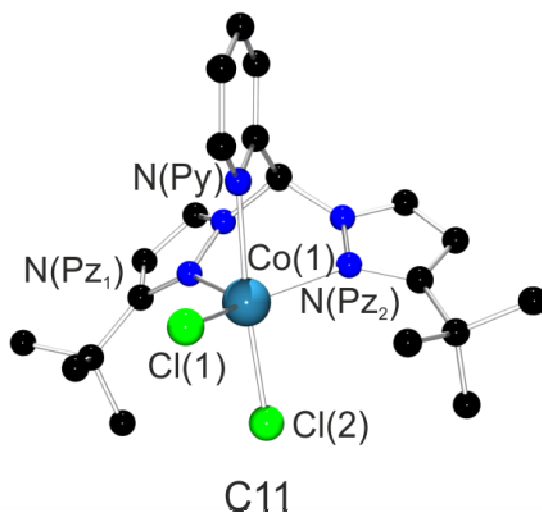
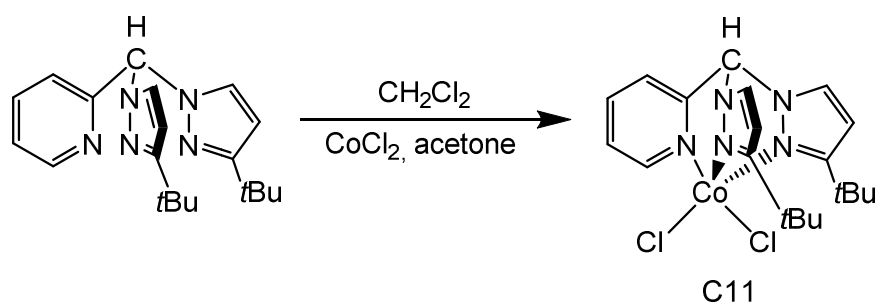


Figure 51. Molecular structure of $[\text{CoCl}_2\{\text{HC}(3\text{-}t\text{BuPz})_2(\text{Py})\}]$ (**C11**).

Figure 51 displays the molecular structure of **C11**. This complex has already been characterised by A. Hoffmann as a different isomer (**CC11**) in another space group.^[125] **C11** crystallises in the triclinic space group $P2_1/c$ with four units per elementary cell and was resynthesised the same way as **CC11** was originally prepared (Scheme 30). Single crystals were obtained by dissolving the solid of **C11** in methanol and diffusion of THF.



Scheme 30. Synthesis of $[\text{CoCl}_2\{\text{HC}(3\text{-}t\text{BuPz})_2(\text{Py})\}]$ (**C11**).^[125]

In **C11** the cobalt atom is surrounded five-fold by the three nitrogen donors of the bis(pyrazolyl)methane ligand and by two chlorido ligands. Table 28 lists important bond lengths and angles in **C11** and **CC11**, as well as the τ_5 -value that was calculated for both.^[195]

Table 28. Key bond lengths [\AA] and angles [$^\circ$] in **C11** and **CC11**^[125] and τ_5 -values of both.

	C11	CC11
Bond lengths [\AA]		
Co-N _{Pz}	2.130(3) 2.146(3)	2.106(7) 2.131(6)
Co-N _{Py}	2.220(3)	2.224(6)
Co-Cl(2)	2.331(1)	2.309(2)
Co-Cl(1)	2.309(1)	2.358(2)
C _{ap} -N _{Pz}	1.466(4) 1.445(4)	1.441(9) 1.444(9)
C _{ap} -C _{Py}	1.523(5)	1.481(9)
Bond angles [$^\circ$]		
N _{Pz} -Co-Cl(2)	97.5(1) 95.6(1)	97.2(1) 95.3(2)
N _{Pz} -Co-Cl(1)	123.5(1) 137.0(1)	129.2(2) 131.0(2)
N _{Py} -Co-Cl(1)	89.2(1)	89.4(2)
N _{Py} -Co-Cl(2)	174.2(1)	174.9(2)
N _{Pz} -Co-N _{Pz}	95.9(1)	96.5(2)
N _{Pz} -Co-N _{Py}	83.0(1) 78.6(1)	81.6(2) 80.0(2)
Cl(1)-Co-Cl(2)	95.3(1)	95.0(1)
τ_5 ^[195]	0.619	0.731

Inspection of the τ_5 -value clearly shows the two different isomers of **C11**. Hereby **CC11** is distorted more towards a trigonal bipyramid than **C11**. Furthermore Co-N_{Pz} bond lengths are more alike in **C11**, while Co-N_{Py} bonds are longer than Co-N_{Pz} bonds in both, which is normal for such complexes. Co-Cl and C_{ap}-N_{Pz} bond lengths are similar within **C11** as well as in **CC11**. Lastly the C_{ap}-C_{Py} bond is longer in **C11** than in **CC11**.

3.6.3 Summary

In this chapter two more molecular structures of bis(pyrazolyl)methane ligands were presented and the effect of isomerisation of alkyl substituents at the pyrazolyl moieties was discussed. Furthermore three bisfacial Co complexes were introduced. **C8** and **C9** incorporate the HC(Pz)₂(Qu) ligand, for which no other coordination geometry than bisfacial is expected.

C10 includes the isomerised ligand **L4'** and shows the bisfacial coordination mode as well. Moreover, due to the 3/5-isomerisation Co-N_{pz} bond lengths now differ. It shall be pointed out that the unisomerised HC(3-*i*PrPz)₂(Py) ligand did not favour a bisfacial geometry (**C6**, see chapter 3.4) and isomerisation there did also not occur upon reaction with the cobalt salt. At last the two isomers of the Co(II) complexes **C11** and **CC11** were compared in order to find a larger distortion towards a trigonal bipyramidal geometry in **CC11**.

4 Conclusion & Outlook

4.1 Conclusion

The central aim of this thesis was the development of a new biomimetic tyrosinase model with efficient catalytic hydroxylation activity. Therefore, a synthetic route towards a new bis(pyrazolyl)methane ligand that can be applied in the activation of small molecules, had to be explored. Furthermore density functional theory investigations and the analysis of single crystal structural data of bis(pyrazolyl)methane transition metal complexes should shed more light on the complex donor competition between the different aromatic N-donor moieties.

Bis(pyrazolyl)methanes (BPM) represent a versatile ligand class, that has been known for a long time and has been accessible through a one pot synthesis for a couple of years now^[117], which allows for the simplified synthesis of a large variety of differently substituted ligands. Three new ligands of this class were synthesised in the course of this thesis (Figure 52).

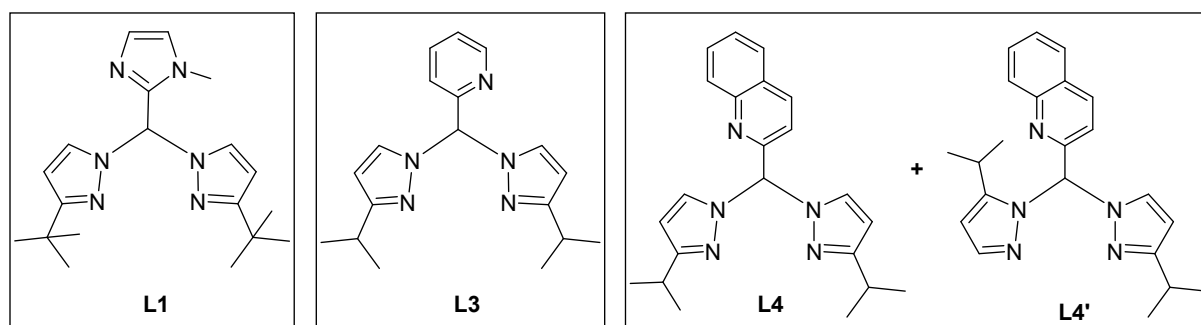


Figure 52. Structures of newly synthesised bis(pyrazolyl)methane ligands L1, L3 and L4/L4'.

Complex synthesis with the new ligand **L1** afforded the CuCl₂ complex [CuCl₂{HC(3-*t*BuPz)₂(1-Melm)}] (**C1**). Characterisation of **C1** showed a shorter Cu-N_{Im} bond length in comparison to the Cu-N_{Pz} bond, which is also shorter than other common Cu-N_{donor} bonds (e.g. Cu-N_{Py}). According charge-transfer energy investigations indicated a stronger donor-ability for the imidazolyl donor compared to the pyrazolyl donors.

Formation of the (μ-η²:η²)-peroxo compound ([Cu₂O₂{HC(3-*t*BuPz)₂(1-Melm)}]₂)[SbF₆]₂, **P1**[SbF₆]₂) at -78°C was proven by UV/Vis spectroscopy, cryo-UHR ESI mass spectrometry and X-Ray absorption spectroscopy (XAS) and was completed in 10–15 minutes. UV/Vis spectroscopic analysis showed two characteristic LMCT bands at 334 and 534 nm. The blue-

shift of these bands in comparison to the UV/Vis absorption bands of other tyrosinase model complexes, which lie at 350 and 550 nm^[47,55], was investigated by theoretical means. All in all the blue-shift was traced back to the stronger N_{im}-donation, which leads to an increase of the LUMO, resulting in an energetically larger LMCT transition.

By treating **P1**[SbF₆]₂ with phenolic substrates, catalytic activity according to tyrosinase could be observed. Formation of the corresponding quinones was followed by UV/Vis spectroscopy. Hereby catalytic conversion with the non-biological substrate 8-hydroxyquinoline showed to be rapid and efficient with a TON of 14 after 20 min and treatment with the second substrate 4-methoxyphenol resulted in a TON of 2 after 18 h. In a second experiment, after addition of stoichiometric amounts of phenolic substrates, the reaction was stopped at low temperatures on the level of the catechol, amount of which was determined by NMR analysis and did not show any signs of a C-C coupling product. This fact suggests a reaction mechanism following an inner-sphere oxygen atom transfer analogous to tyrosinase.

Besides **P1**[SbF₆]₂, the new copper(I) complex with the ligand HC(3-*t*BuPz)₂(Qu) (**L2**) was treated with oxygen at low temperatures. Here as well a (μ - η^2 : η^2)-peroxo compound ([Cu₂O₂{HC(3-*t*BuPz)₂(Qu)}₂][SbF₆]₂, **P2**[SbF₆]₂) was verified by UV/Vis spectroscopy. The time until the complete formation of **P2**[SbF₆]₂ amounted to 8h. The position of the UV/Vis bands at 350 and 550 nm was similar to those of oxy-tyrosinase.^[139] In a catalytic self-assembly approach, the addition of all components to the reaction mixture at once (precursor, phenol, NEt₃, O₂) led to the formation of the according quinone, which was proven by UV/Vis spectroscopy.^[160]

Both **P1**[SbF₆]₂ and **P2**[SbF₆]₂ contain similar bis(pyrazolyl)methanes, but show different properties. While **P2**[SbF₆]₂ already partly decays whilst forming, the imidazolyl moiety containing peroxo compound is stable at -78°C for several days.

Against the background of understanding the reaction mechanism of tyrosinase in more detail, experiments were conducted in order to generate a copper superoxide mimic for the enzyme tyrosinase, as such a superoxide is believed to be an intermediate state in the catalytic cycle of tyrosinase. Treatment of [Cu{HC(3-*t*BuPz)₂(Py)}]⁺ with nitrosobenzene showed a reaction, generating a room temperature stable deep red species. Supported by theoretical calculations, formation of the singlet κ N-nitrosobenzene species was suspected.

Regarding the activation of NO, the reaction of $[\text{Cu}\{\text{HC}(3\text{-}t\text{BuPz})_2(\text{Py})\}]^+$ with NO gas and with diazald[®] resulted in the same species as could be proven by UV/Vis spectroscopy, which confirms that diazald[®] is able to deliver NO onto copper-BPM complexes.

With the already characterised BPM ligand $\text{HC}(3\text{-}t\text{BuPz})_2(\text{Py})$ ^[117] (**L5**) and **L2** four bis(pyrazolyl)methane copper complexes (with copper in the oxidation states I and II) were synthesised and characterised (Figure 53). These complexes displayed coordination geometries from distorted tetrahedral to distorted square-pyramidal and distorted trigonal-bipyramidal. The donor situation of all four complexes was studied by NBO analysis, but a mixed picture was found: depending on the coordinative situation both pyrazolyl and pyridinyl units can win this competition.

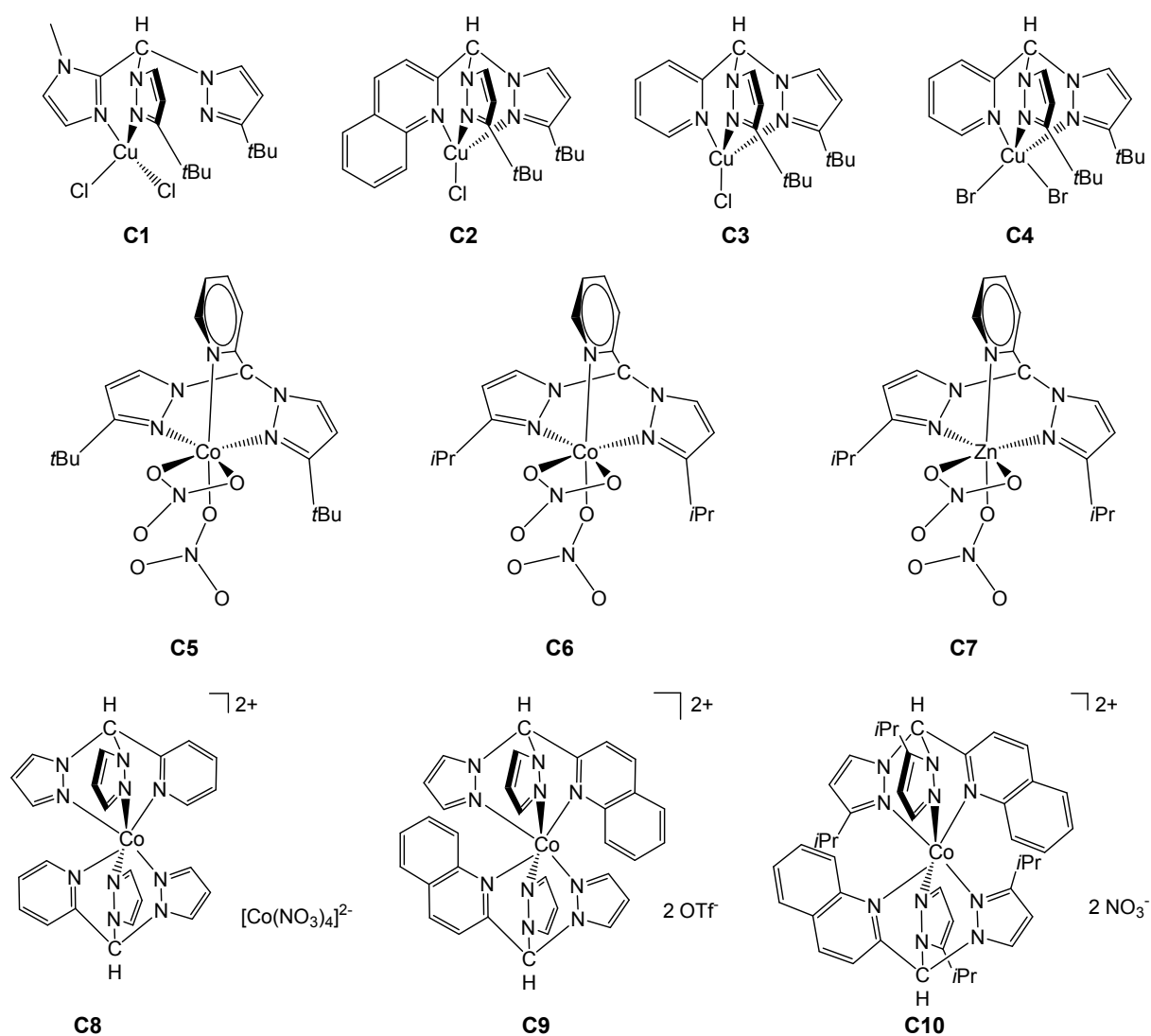


Figure 53. Structures of newly synthesised transition metal bis(pyrazolyl)methane complexes **C1–C10**.

A couple of transition metal nitrate complexes with the ligands HC(3-*t*BuPz)₂(Py) (**L5**) and HC(3-*i*PrPz)₂(Py) (**L3**) were presented as well (Figure 53), because they provide important insight into the geometry of combined N and O ligand systems. Here a rare nitrate binding mode, which consists of mono- and bidentately bound nitrate groups, could be shown and quantified. The geometry of all monofacial nitrate complexes is distorted octahedral.

In order to understand the substituent effect of the ligands in more detail, bisfacial cobalt complexes with unsubstituted BMP ligands as well as a bisfacial complex incorporating an *isopropyl* unit at the pyrazolyl moieties of the ligand were investigated (Figure 53). Here the 3/5-isomerisation effect of pyrazolyl was observed, which for example already occurred during the synthesis of **L4/L4'**. Normally BPM ligands of the second generation would not form bisfacial complexes; however, with one *isopropyl* group in the 3- and one in the 5-position of the pyrazolyl moiety, steric hindrance is overcome and a bisfacial coordination mode is generated. All bisfacial cobalt complexes point towards the pyrazolyl N-donor to be the stronger donor in comparison to pyridine, although pyridine is the more basic one. In addition the monofacial cobalt complex [CoCl₂{HC(3-*t*BuPz)₂(Py)}] (**C11**) was synthesised and compared to its isomer (which has been characterised before^[125]), showing a stronger distortion towards a trigonal bipyramidal geometry.

During this thesis both the efficient stoichiometric oxidation of phenolates to catecholates at -80°C and catalytic oxidation of phenols to quinones at room temperature, through a reaction pathway consistent with the generally accepted enzymatic mechanism of tyrosinase could be shown applying the new HC(3-*t*BuPz)₂(1-Melm) ligand. With HC(3-*t*BuPz)₂(Qu) the catalytic activity of the according (μ - η^2 : η^2)-copper(II) species was shown *via* a self-assembly approach.^[160] These results show that bis(pyrazolyl)methane copper complexes possess a large potential for further catalytic hydroxylation applications in synthetic organic chemistry.

4.2 Outlook

In order to understand the reaction mechanism concerning the formation as well as the subsequent catalytic reactions of ([Cu₂O₂{HC(3-*t*BuPz)₂(1-Melm)}₂)[SbF₆]₂ in more detail, stopped-flow measurements as well as Hammett correlations would be reasonable next steps. Additionally more different substrates should be tested concerning the transfer of

oxygen. Single crystals of both peroxo species would help in the further characterisation and the understanding of such complexes.

Continuative experiments could also include the development of further bis(pyrazolyl)methane ligands for use in the activation of oxygen. While three bis(pyrazolyl)methane copper peroxo complexes have been characterised so far (two in this thesis and one by A. Hoffmann in 2011^[18]), each of them can be optimised concerning for example their stability, effectivity or reaction time. So in order to avoid certain drawbacks, new bis(pyrazolyl)methane ligands could incorporate different third donor functions. Furthermore the analysis of more structural data of monofacial complexes containing the HC(3-*t*BuPz)₂(1-Melm) ligand would be helpful in the deeper understanding of the electronic structure of such complexes as well as the donor force of imidazolyl and its role in the band-shift of the according UV/Vis bands.

For continuative investigations concerning the superoxide mimic species, the detailed characterisation of reaction products as well as single crystals would be helpful.

Another field to further investigate would be the activation of small molecules like NO or CO₂ based on first results that were presented here. Hereby not only copper complexes but also those with other transition metals like cobalt, iron and zinc could be explored.

5 Experimental Section

5.1 General

All experiments involving moisture- and air-sensitive compounds were carried out by using standard Schlenk techniques. The solvents used were dried by standard literature procedures.^[196] Nitrogen was obtained from the house supply and predried with sicapent and porous ceramics.

5.2 Physical Methods

Mass spectrometry

HR-cryo-ESI: In cooperation with Prof. Dr. I. Ivanović-Burmazović at the FAU Erlangen-Nürnberg, cryospray-ionisation MS (CSI-MS) measurements were performed on a UHR-TOF Bruker Daltonik (Bremen, Germany) maXis plus 5G, an ESI-ToF MS capable of resolution of at least 60,000 FWHM, which was coupled to a Bruker Daltonik Cryospray unit. Detection was in positive-ion mode and the source voltage was 4.5 kV. The flow rates were 250 μ L/hour. The drying gas (N_2), to aid solvent removal, was held at -75°C and the spray gas was held at -80°C . The machine was calibrated prior to every experiment *via* direct infusion of the Agilent ESI-TOF low concentration tuning mixture, which provided an m/z range of singly charged peaks up to 2700 Da in both ion modes.

FAB: Fast-atom bombardment (FAB) mass spectra were obtained with a Thermo Finnigan MAT 95 or a Jeol MStation sectorfield mass spectrometer. Ionisation was achieved with accelerated xenon atoms (8 kV) in a glycerin or 2-nitrobenzylalcohol matrix on a copper target. For low resolution measurements, the resolution was at about 1000 and for high resolution at about 5000. Depending on the method, areas between 40 and 3040 u were recorded.

ESI: Electrospray ionisation (ESI) mass spectra were obtained from a Thermo Finnigan LTQ Ultra Fourier Transform Ion Cyclotron Resonance Mass Spectrometer. Resolution was adjusted to 100,000 at $m/z = 400$. Depending on the method areas between 50 and 2000 u were recorded. ESI measurements were performed at an IonMax ionic source with ESI-head. The source voltage was 4 kV with a spray capillary temperature of 250°C , a sheathgas flowrate of 25 and a sweepgas flowrate of 5 units.

X-Ray absorption spectroscopy

X-Ray absorption spectroscopy measurements were performed by Prof. Dr. M. Bauer and coworkers of the University of Paderborn.

Measurements at the Cu K-edge were carried out at the beamline BM23 of the European Synchrotron Radiation Facility ESRF (Grenoble, France) in fluorescence mode making use of a hyperpure solid state Ge detector. The sample was measured in frozen solution at liquid nitrogen temperature using CH₂Cl₂ as matrix. Due to the low concentration of 0.01 mol L⁻¹ several scans were conducted and averaged to increase the signal to noise ratio. Data reduction followed standard procedures.^[151] Due to the high residual noise Fourier filtering was applied in the range $\Delta r = 3\text{--}11.5 \text{ \AA}$.

NMR spectroscopy

For the measurement of ¹H- and ¹³C-spectra, a Jeol EX-400 or Jeol EX-270 nuclear resonance spectrometer was used and spectra were recorded at 25°C. Assignment of NMR signals was done with the help of additional 2D experiments (DEPT-135, COSY, HMBC, HMQC). Deuterated chloroform was used as solvent and functioned as internal standard (CDCl₃: 7.26 ppm). Chemical shifts refer to the δ -scale and are listed in ppm. Spin-spin coupling constants (ⁿJ) are given in Hertz (Hz) with n being the number of bonds between coupling nucleuses. The multiplicity of signals is described as follows: s = singlet, d = doublet, t = triplet, sept = septet, m = multiplet.

Elemental analysis

Elemental analyses were performed with a Vario EL or Vario MICRO CHNS analyser.

UV/Vis spectroscopy

UV/Vis spectra were recorded with a Varian Cary 60 spectrophotometer from Agilent Technologies in combination with a fibre-optic quartz glass immersion probe (Hellma, 1 mm) in a customised Schlenk measurement-cell.

Infrared spectroscopy

Infrared spectra were recorded with a Jasco FTIR 460 spectrophotometer in the range of 650–3500 cm⁻¹. Measurements took place at room temperature in the ATR measurement mode.

X-ray diffraction analysis

The crystal data for **L1**, **L2** and **L3'** as well as **C1–C10** are presented in Tables 30–36.

The data was collected either with a KappaCCD (Bruker 396 AXS BV) (**C2**), a Bruker D8 Quest (**C3**, **C5–C7**, **C9**), a Bruker D8 Venture (**C1**, **C4**, **C8**) or an Oxford KM4 XCalibur2 (**L1**, **L2**, **L3'**, **C10**, **C11**) diffractometer with graphite-monochromated Mo-K α radiation ($\lambda = 0.71073 \text{ \AA}$).

Data reduction and absorption correction was performed with HKL Denzo and Scalepack (**C2**)^[197], with SAINT and SADABS (**C1** and **C3–C9**)^[198] or with the programs CRYSLIS (Oxford, UK, 2008) and CRYSLIS RED (Oxford, UK, 2008) (**L1–L3'**, **C10**, **C11**).

The structures were solved by direct and conventional Fourier methods and all non-hydrogen atoms were refined anisotropically with full-matrix least-squares cycles based on F^2 (XPREP,^[199] SHELXS^[200] and ShelXle^[201]). Hydrogen atoms were derived from difference Fourier maps and placed at idealised positions, riding on their parent C atoms, with isotropic displacement parameters $U_{\text{iso}}(\text{H}) = 1.2 U_{\text{eq}}(\text{C})$ and $1.5 U_{\text{eq}}(\text{C methyl})$. All methyl groups were allowed to rotate but not to tip. For refinement fullmatrix least-squares methods were applied (SHELXL97).^[202]

5.3 Computational details

DFT calculations were performed with the Gaussian09 program suite.^[135] The geometries of **C1–C4** were optimised using the nonlocal hybrid meta GGA TPSSh functional^[203] and the double- ζ basis set 6-31G(d) as implemented in Gaussian on all atoms. The starting geometries for complexes **C1–C4** were generated from the molecular structures. Frequency calculations did not show imaginary values. NBO calculations for the complexes were accomplished by using the NBO 6.0 program suite.^[142,163,164]

Geometry optimisation and TD-DFT calculations of the singlet nitrosobenzene species was done by using the BP86 functional^[204–206] and the double- ζ basis set 6-31G(d) as implemented in Gaussian on all atoms.^[186]

For the geometry optimisation of **C5–C7** on which NBO analysis was based, the BP86 functional and the double- ζ basis set 6-31G(d) as implemented in Gaussian was used on all atoms on the basis of the molecular structures.

The geometries of the peroxo species were optimised by A. Hoffmann using the nonlocal hybrid meta GGA TPSSh functional^[203] and the double- ζ basis set 6-31G(d) as implemented in

Gaussian on all atoms. Continuous spectra were plotted with the AOMix program by A. Hoffmann as well.^[207,208]

5.4 Chemicals

The following chemicals were purchased and used as received without further purification, except from the oily suspension of sodium hydride, which was washed with dry pentane several times before use.

n-Butyllithium (2.5M solution in hexane, Sigma-Aldrich), 1-methylimidazole (99%, Sigma-Aldrich), cobalt(II) chloride (p.a., anhydrous, Sigma-Aldrich), deuterated chloroform (99.8% D, H₂O < 0.01%, euriso-top), magnesiumsulphate (99%, Grüssing), sodiumchloride (≥ 99%, Bernd Kraft), sodiumhydride (57–63%, oily dispersion, Alfa-Aesar), sodiumsulphate (p.a., Riedel-de-Haën), thionylchloride (>99.5%, Acros Organics), pyridine-2-carboxaldehyde (99%, ABCR), *p*-toluenesulfonic acid monohydrate (99%, ABCR), sodiumcarbonate (waterfree, VWR), copper(II)chloride dehydrate (99%, Applichem), copper(II)bromide (98%, Fluka), cobalt(II)nitrate hexahydrate (99.9%, Sigma-Aldrich), zincnitrate hexahydrate (98%, Applichem), silverhexafluoroantimonate (98%, ABCR), nitrosobenzene (≥ 97%, Sigma-Aldrich), 8-hydroxyquinoline (98%, ABCR), 4-Methoxyphenol (≥ 98%, Alfa-Aesar), NEt₃ (99%, Acros Organics), acetophenone (for synthesis, Merck)

5.5 Syntheses

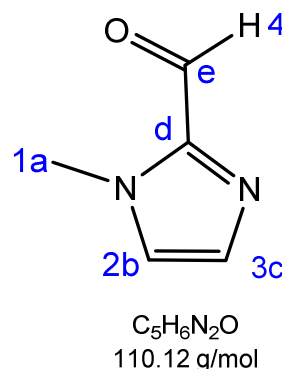
5.5.1 Synthesis of starting materials

The starting materials *isopropylpyrazole*^[209], *tertbutylpyrazole*^[161], *pyrazole*^[210], *quinolone-2-carboxaldehyde*^[211], CuCl^[212] were synthesised according to literature. Co(OTf)₂ was available in the group and had been synthesised according to Funahashi *et al.*^[213]

The substituted phenolates 4-nitrophenolate, 4-methoxyphenolate, as well as phenolate were synthesised according to Casella *et al.*^[214]

5.5.2 Synthesis of 1-methyl-2-imidazolealdehyde adapted from [215]

At -78°C under nitrogen, *n*-BuLi (48.2 mL, 0.12 mol, 2.5 M solution in hexane, 1 eq) is added dropwise to a solution of 1-methylimidazole (9.89 g, 0.12 mol, 1 eq) dissolved in 100 mL of dry THF. The solution is stirred at -78°C for 1h, before DMF (23.2 mL, 0.30 mol, 2.5 eq) is added. The formation of a colourless precipitate can be observed. Following stirring for an additional hour at -78°C , the reaction mixture is warmed to room temperature and stirred overnight. The reaction is quenched by the addition of 150 mL of water, resulting in the dissolution of the colourless solid. The aqueous phase is extracted with CH_2Cl_2 (5×100 mL). The combined organic phases are washed with water (75 mL) and brine (75 mL) and dried over Na_2SO_4 . The solvent is reduced under vacuum and the product is purified by vacuum distillation (44°C , 6.2×10^{-2} mbar), yielding 1-methyl-2-imidazolealdehyde as a colourless wax (7.97 g, 72.4 mmol, 60%).



$^1\text{H-NMR}$ (400 MHz, CDCl_3 , 25°C): δ [ppm] = 3.98 (s, 3H, 1-H), 7.07 (d, $^3J_{\text{HH}} = 0.8$ Hz, 1H, 2-H), 7.23 (d, $^3J_{\text{HH}} = 0.8$ Hz, 1H, 3-H), 9.77 (s, 1H, 4-H).

$^{13}\text{C-NMR}$ (100 MHz, CDCl_3 , 25°C): δ [ppm] = 35.0 (C-a), 127.4 (C-b), 131.6 (C-c), 143.8 (C-d), 182.2 (C-e).

HR-EI $^+$ -MS (m/z (%)): 110.048 $[\text{M}]^+$, (m/z calcd. for $\text{C}_5\text{H}_6\text{N}_2\text{O} = 110.056$).

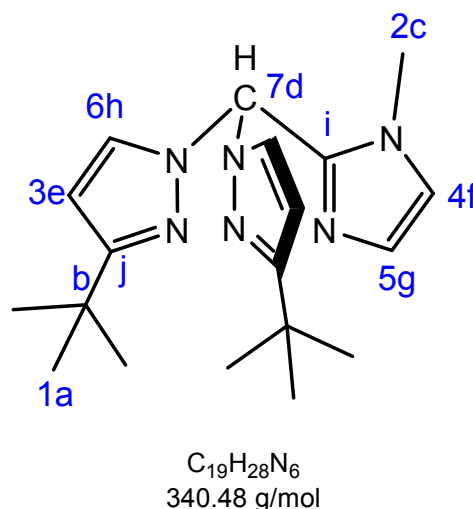
Analytic data is in accord with the corresponding literature data.^[215]

5.5.3 Synthesis of ligands L2, L5, L6 and L7

The ligands $\text{HC}(3\text{-}t\text{BuPz})_2(\text{Qu})$ (**L2**), $\text{HC}(3\text{-}t\text{BuPz})_2(\text{Py})$ (**L5**), $\text{HC}(\text{Pz})_2(\text{Py})$ (**L6**) and $\text{HC}(\text{Pz})_2(\text{Qu})$ (**L7**) were synthesised according to literature.^[117]

5.5.3.1 Synthesis of 2-(1-methylimidazolyl)bis(3-tertbutylpyrazolyl)methane HC(3-*t*BuPz)₂(1-Melm) (L1)

3-*tert*butylpyrazole (5.00 g, 0.40 mol, 2 eq) is added in small portions to a slurry of NaH (1.00 g, 0.42 mol, 2.1 eq) in 50 mL of freshly distilled, dry THF at 0°C under vigorous stirring, until no more gas evolution is visible. Next, thionylchloride (1.50 mL, 0.20 mol, 1 eq) is added dropwise to the yellow suspension at 0°C and stirred firstly at 0°C for 30 min and afterwards at room temperature for another 45 min. 1-Methylimidazole-2-carboxaldehyde (2.20 g, 0.20 mol, 1 eq) and catalytic amounts of CoCl₂ (0.05 g) are added, before the mixture



is refluxed overnight and the evolution of SO₂ gas is visible. The solution changes colour to red-orange. After cooling the reaction mixture to room temperature, water (50 mL) and diethyl ether (50 mL) are added, followed by 2h of stirring. Lastly, the combined organic phases are extracted with diethyl ether (3 × 45 mL) and washed with water (2 × 50 mL) and brine (2 × 50 mL). The combined organic phases are dried over Na₂SO₄ and the solvent is reduced *in vacuo*. The product is gained by vacuum distillation (40°C, 1.4 × 10⁻² bar) in the second fraction as single crystals in good yield (4.7 g, 0.14 mol, 69%). The crystals were characterised via X-ray diffraction analysis.

¹H-NMR (400 MHz, CDCl₃, 25°C): δ [ppm] = 1.26 (s, 18H, 1-H), 3.45 (s, 3H, 2-H), 6.15 (d, ³J_{HH} = 2.5 Hz, 2H, 3-H), 6.87 (d, ³J_{HH} = 1.2 Hz, 1H, 4-H), 7.04 (d, ³J_{HH} = 1.2 Hz, 1H, 5-H), 7.44 (d, ³J_{HH} = 2.5 Hz, 2H, 6-H), 7.64 (s, 1H, 7-H).

¹³C-NMR (100 MHz, CDCl₃, 25°C): δ [ppm] = 30.6 (C-a), 32.2 (C-b), 33.1 (C-c), 71.5 (C-d), 103.5 (C-e), 122.8 (C-f), 128.0 (C-g), 129.4 (C-h), 142.0 (C-i), 163.1 (C-j).

ATR-IR: $\tilde{\nu}$ [cm⁻¹] = 2959 [w, (v, CH_{aliph})], 2928 [w, (v, CH_{aliph})], 2902 [w, (v, CH_{aliph})], 2866 [vw, (v, CH_{aliph})], 1531 (w), 1519 (m), 1501 (w), 1478 (w), 1461 (w), 1400 (w), 1362 (w), 1335 (m), 1317 (w), 1281 (w), 1244 (m), 1225 (w), 1206 (w), 1189 (w), 1153 (m), 1135 (w), 1046 (m), 1022 (w), 993 (w), 927 (w), 852 (w), 818 (m), 805 (s), 762 (vs), 724 (m), 698 (m), 664 (w).

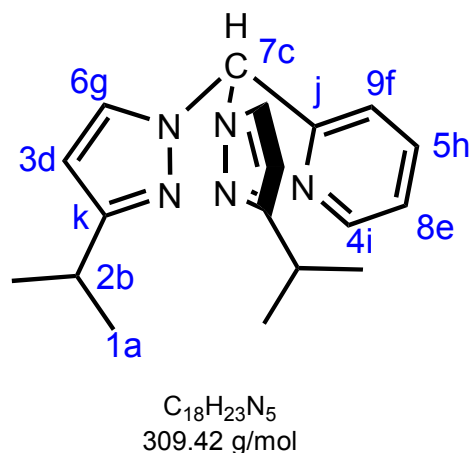
ESI⁺-MS (acetone) (m/z (%)): 364 (17) [(HC(3-*t*BuPz)₂(1-Melm)], +H, +Na]⁺, 363 (100) [(HC(3-*t*BuPz)₂(1-Melm)], +Na]⁺, 341 (42) [(HC(3-*t*BuPz)₂(1-Melm)], +H]⁺, 218 (10) [C₁₀H₁₉N₄, +Na]⁺, 217 (96) [C₁₂H₁₇N₄]⁺, 214 (1) [C₁₃H₁₆N₃]⁺.

HR-ESI⁺-MS (acetone) (m/z (%)): 363.227 [M+Na]⁺ (m/z calcd. for C₁₉H₂₈N₆Na = 363.46).

EA: C₁₉H₂₈N₆ (340.48 g/mol): calcd. C 67.0, H 8.3, N 24.7; found C 67.1, H 8.3, N 24.3.

5.5.3.2 Synthesis of 2-(Pyridinyl)bis(3-isopropylpyrazolyl)methane HC(3-*i*PrPz)₂(Py) (L3)

3-Isopropylpyrazole (11.02 g, 0.10 mol, 2 eq) is added in small portions to a slurry of NaH (2.88 g, 0.12 mol, 2.2 eq) in 100 mL of freshly distilled, dry THF at 0°C under vigorous stirring, followed by continuous stirring at 0°C, until no more gas evolution is visible. Next, thionylchloride (3.70 mL, 0.05 mol, 1 eq) is added dropwise to the yellow suspension. It follows stirring at 0°C for 30 min and afterwards at room temperature for another 45 min. Pyridin-2-carboxaldehyde (5.40 g,



0.05 mol, 1 eq) and catalytic amounts of CoCl₂ (0.17 g) are added, before the mixture is refluxed overnight and the evolution of SO₂ gas is visible. After cooling the reaction mixture to room temperature, water (70 mL) and diethyl ether (70 mL) are added, followed by 2 h of stirring. Lastly, the combined organic phases are extracted with diethyl ether (3 × 60 mL) and washed with water (70 mL). The combined organic phases are dried over Na₂SO₄ and the solvent is reduced *in vacuo*. The raw product mixture of the isomerised HC(3-*i*PrPz)(5-*i*PrPz)(Py) and HC(3-*i*PrPz)₂(Py) is obtained by vacuum distillation (130°C, 3 × 10⁻³ bar) as the second fraction (8.26 g, 26.0 mmol, 53%).

For the reisomerisation of HC(3-*i*PrPz)(5-*i*PrPz)(Py), the mixture is dissolved in 75 mL of toluene and catalytic amounts of *p*-toluenesulfonic acid (0.38 g, 2.00 mmol) are added. The mixture is heated to reflux for 24 h. After cooling to room temperature, a solution of Na₂CO₃ (5%, 150 mL) is added for neutralisation. The organic phase is separated, washed with water (3 × 30 mL) and dried over MgSO₄. At last the solvent is reduced *in vacuo*. The product is obtained by vacuum distillation as a yellow viscous oil (130°C, 2 × 10⁻³ bar, 6.84 g, 22.1 mmol, 85%).

¹H-NMR (400 MHz, CDCl₃, 25°C): δ [ppm] = 1.23 (d, ³J_{HH} = 10.0 Hz, 12H, 1-H), 2.98 (sept., ³J_{HH} = 10.0 Hz, 2H, 2-H), 6.12 (d, ³J_{HH} = 3.6 Hz, 2H, 3-H), 6.93 (d, ³J_{HH} = 11.8 Hz, ⁴J_{HH} = 0.8 Hz, 1H, 4-H), 7.21–7.26 (m, 1H, 5-H), 7.41 (d, ³J_{HH} = 3.6 Hz, 2H, 6-H), 7.58 (s, 1H, 7-H), 7.66 (td, ³J_{HH} = 11.8 Hz, ⁴J_{HH} = 2.8 Hz, 1H, 8-H), 8.59–8.62 (m, 1H, 9-H).

^{13}C -NMR (100 MHz, CDCl_3 , 25°C): δ [ppm] = 22.9 (C-a), 27.9 (C-b), 78.4 (C-c), 103.2 (C-d), 122.2 (C-e), 123.7 (C-f), 130.1 (C-g), 137.1 (C-h), 149.7 (C-i), 155.5 (C-j), 160.5 (C-k).

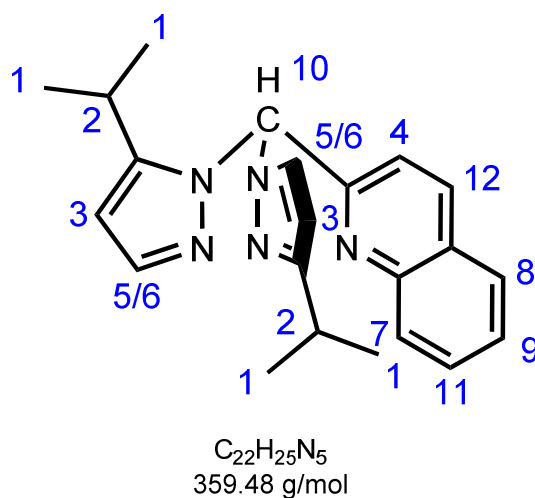
ATR-IR: $\tilde{\nu}$ [cm^{-1}] = 2961 [w, (v, CH_{aliph})], 2930 [w, (v, CH_{aliph})], 2870 [w, (v, CH_{aliph})], 1589 (w), 1573 (w), 1522 (m), 1471 (m), 1457 (w), 1436 (m), 1402 (w), 1380 (w), 1362 (w), 1326 (w), 1288 (m), 1264 (w), 1215 (m), 1150 (w), 1094 (w), 1068 (m), 1048 (m), 996 (m), 926 (w), 870 (w), 839 (w), 808 (m), 751 (vs), 719 (m), 673 (m).

ESI $^+$ -MS (acetone) (m/z (%)): 333 (4) [(HC(3-*i*PrPz) $_2$ (Py), +H, +Na] $^+$, 332 (21) [(HC(3-*i*PrPz) $_2$ (Py), +Na] $^+$, 201 (9) [$\text{C}_{10}\text{H}_{16}\text{N}_3$, +Na] $^+$, 200 (100) [$\text{C}_{12}\text{H}_{14}\text{N}_3$] $^+$, 158 (<1) [$\text{C}_9\text{H}_8\text{N}_3$] $^+$.

HR-ESI $^+$ -MS (acetone) (m/z (%)): 333.189 (10) [HC(3-*i*PrPz) $_2$ (Py), +H, +Na] $^+$, 332.185 (50) [HC(3-*i*PrPz) $_2$ (Py), +Na] $^+$, 310.203 (16) [HC(3-*i*PrPz) $_2$ (Py), +H] $^+$. (m/z calcd. for $\text{C}_{18}\text{H}_{24}\text{N}_5\text{Na}$ = 333.19, $\text{C}_{18}\text{H}_{23}\text{N}_5\text{Na}$ = 332.19, $\text{C}_{18}\text{H}_{24}\text{N}_5$ = 310.20)

5.5.3.3 Synthesis of a mixture containing 2-(Quinolinyl)(3-isopropylpyrazolyl) (5-isopropylpyrazolyl)methane HC(3-*i*PrPz)(5-*i*PrPz)(Qu) (*L4'*) and 2-(Quinolinyl)bis(3-isopropylpyrazolyl)methane HC(3-*i*PrPz) $_2$ (Qu) (*L4*)

3-Isopropylpyrazole (18.40 g, 0.17 mol, 2.0 eq) is added in small portions to a slurry of NaH (4.00 g, 0.12 mol, 2.0 eq) in 130 mL of freshly distilled, dry THF at 0°C under vigorous stirring, followed by continuous stirring at 0°C , until no more gas evolution is visible. Next, thionylchloride (6.50 mL, 0.09 mol, 1 eq) is added dropwise to the yellow suspension. It follows stirring at 0°C for 30 min and afterwards at room temperature



for another 45 min. Quinoline-2-carboxaldehyde (13.1 g, 0.09 mol, 1 eq) and catalytic amounts of CoCl_2 (0.30 g) are added, before the mixture is refluxed overnight and the evolution of SO_2 gas is visible. After cooling the reaction mixture to room temperature, water (160 mL) and diethyl ether (80 mL) are added, followed by 2 h of stirring. Lastly, the combined organic phases are extracted with diethyl ether (3×80 mL) and washed with water (80 mL). The combined organic phases are dried over Na_2SO_4 and the solvent is reduced *in vacuo*. A mixture of the products HC(3-*i*PrPz)(5-*i*PrPz)(Qu) and HC(3-*i*PrPz) $_2$ (Qu) is obtained by vacuum distillation (170°C , 8×10^{-2} bar) as the second fraction. Attempts to

reisoimerise the product failed, as the following distillation led to isomerisation and a mixture of $\text{HC}(3\text{-}i\text{PrPz})(5\text{-}i\text{PrPz})(\text{Qu})$ and $\text{HC}(3\text{-}i\text{PrPz})_2(\text{Qu})$ was obtained again.

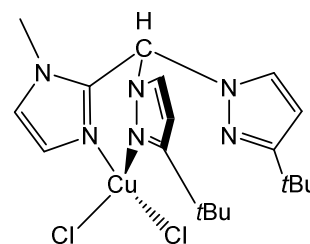
$^1\text{H-NMR}$ (270 MHz, CDCl_3 , 25°C): δ [ppm] = 1.19–1.41 (m, 12H, 1-H), 2.92–3.42 (m, 2H, 2-H), 6.13–6.17 (m, 2H, 3-H), 7.14–7.21 (m, 1H, 4-H), 7.48 (d, $^3J_{\text{HH}} = 2.4$ Hz, 1H, 5-H), 7.50 (d, $^3J_{\text{HH}} = 2.7$ Hz, 1H, 6-H), 7.52–7.58 (m, 1H, 7-H), 7.64–7.71 (m, 1H, 8-H), 7.77–7.83 (m, 1H, 9-H), 7.84 (s, 1H, 10-H), 8.05 (t, $^3J_{\text{HH}} = 9.5$ Hz, 1H, 11-H), 8.15 (dd, $^3J_{\text{HH}} = 8.4$ Hz, $^5J_{\text{HH}} = 4.6$ Hz, 1H, 12-H).

The presence of $\text{HC}(3\text{-}i\text{PrPz})_2(\text{Qu})$ and $\text{HC}(3\text{-}i\text{PrPz})(5\text{-}i\text{PrPz})(\text{Qu})$ leads to signal overlaps in the NMR spectrum. Due to this and the formation of byproducts, a more detailed characterisation is not possible.

5.5.4 Synthesis of transition metal complexes

5.5.4.1 Synthesis of (2-(1-Methylimidazolyl))bis(3-tertbutylpyrazolyl)methanedichloridocopper(II) [$\text{CuCl}_2\{\text{HC}(3\text{-}t\text{BuPz})_2(1\text{-MeIm})\}$] (C1)

Copper(II)chloride (0.17 g, 1.00 mmol) is suspended in 5 mL of methanol, resulting in a green-brown slurry. A solution of $\text{HC}(3\text{-}t\text{BuPz})_2(1\text{-MeIm})$ (0.34 g, 1.00 mmol) dissolved in 5 mL of methanol is added dropwise to the copper-salt mixture and after stirring for 16h at room temperature a deep green solid precipitates. Storage of the mixture at room temperature resulted in single-crystals suitable for X-ray diffraction analysis (0.14 g, 0.29 mmol, 30%).



$\text{C}_{19}\text{H}_{28}\text{Cl}_2\text{CuN}_6$
474.92 g/mol

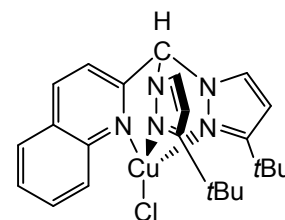
ATR-IR: $\tilde{\nu}$ [cm^{-1}] = 3100 [vw, (v, CH_{arom})], 2902 [w, (v, CH_{aliph})], 2865 [w, (v, CH_{aliph})], 1518 (m), 1474 (w), 1459 (w), 1417 (w), 1350 (m), 1229 (m), 1204 (w), 1152 (w), 1081 (w), 1054 (w), 970 (w), 861 (m), 831 (w), 811 (m), 803 (vs), 782 (vs), 770 (vs), 756 (m), 728 (w), 699 (m), 669 (w), 634 (w), 627 (w), 614 (m), 603 (m).

FAB⁺-MS (m/z (%)): 440 (16) [$\text{Cu}^{37}\text{Cl}\{(\text{HC}(3\text{-}t\text{BuPz})_2(1\text{-MeIm}))\}^+$, 438 (20) [$\text{Cu}^{35}\text{Cl}\{(\text{HC}(3\text{-}t\text{BuPz})_2(1\text{-MeIm}))\}^+$, 403 (40) [$\text{Cu}\{(\text{HC}(3\text{-}t\text{BuPz})_2(1\text{-MeIm}))\}^+$, 342 (15) [$\text{HC}(3\text{-}t\text{BuPz})_2(1\text{-MeIm})\}^+$, 217 (100) [$\text{HC}(3\text{-}t\text{BuPz})(1\text{-MeIm})\}^+$, (m/z calcd. for $\text{C}_{19}\text{H}_{28}\text{ClCuN}_6^+ = 438.1$).

EA: $\text{C}_{19}\text{H}_{28}\text{Cl}_2\text{CuN}_6$ (474.92 g/mol): calcd. C 48.1, H 5.9, N 17.7; found C 47.9, H 6.0, N 17.7.

5.5.4.2 Synthesis of Bis(3-tertbutylpyrazolyl)(2-quinolinyl)methanechloridocopper(I) [CuCl{HC(3-tBuPz)₂(Qu)}] (C2)

A yellow solution of HC(3-tBuPz)₂(Qu) (0.39 g, 1.00 mmol) dissolved in 5 mL of acetone, is added dropwise to a colourless solution of CuCl (0.10 g, 1.00 mmol) dissolved in 20 mL of acetonitrile. The solution turns orange and after 18h a red solid precipitates. After filtering off the solid matter, red crystals are obtained from the filtrate at 5°C after several days (0.32 g, 0.66 mmol, 66%). The crystals are characterised *via* X-ray diffraction analysis.



C₂₄H₂₉ClCuN₅
486.53 g/mol

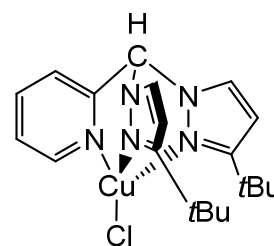
ATR-IR: $\tilde{\nu}$ [cm⁻¹] = 3106 [vw (v, CH_{arom})], 2960 [w, (v, CH_{aliph})], 2904 [vw, (v, CH_{aliph})], 2862 [vw, (v, CH_{aliph})], 1619 (vw), 1596 (w), 1572 (vw), 1556 (vw), 1518 (m), 1480 (w), 1456 (w), 1439 (w), 1420 (w), 1392 (vw), 1378 (w), 1363 (w), 1352 (w), 1335 (w), 1307 (vw), 1236 (m), 1186 (vw), 1157 (w), 1124 (vw), 1057 (m), 977 (w), 930 (w), 873 (vw), 842 (w), 827 (w), 806 (m), 790 (m), 775 (vs), 746 (w), 727 (w), 687 (vw), 668 (w), 653 (vw).

FAB⁺-MS (*m/z* (%)): 487 (2) [Cu³⁷Cl{HC(3-tBuPz)₂(Qu)}]⁺, 485 (2) [Cu³⁵Cl{HC(3-tBuPz)₂(Qu)}]⁺, 450 (26) [Cu{HC(3-tBuPz)₂(Qu)}]⁺, 389 (9) [{HC(3-tBuPz)₂(Qu)}+H]⁺, 275 (7) [{HC(Pz)₂(Qu)}]⁺, (*m/z* calcd. for C₂₄H₂₉ClCuN₅ = 485.1).

EA: C₂₄H₂₉ClCuN₅ (486.53 g/mol): calcd. C 59.3, H 6.0, N 14.4; found C 59.2, H 6.0, N 14.3.

5.5.4.3 Synthesis of (2-Pyridinyl)bis(3-tertbutylpyrazolyl)methanechloridocopper(I) [CuCl{HC(3-tBuPz)₂(Py)}] (C3)

A yellow solution of HC(3-tBuPz)₂(Py) (0.34 g, 1.00 mmol) dissolved in 5 mL of acetone, is added dropwise to a colourless solution of CuCl (0.10 g, 1.00 mmol) dissolved in 20 mL of acetonitrile. The solution turns yellow and is stored at 5°C over night, where the solution turns light-green. Concentration of the solvent until a solid precipitates and storage of the filtrate at 5°C results in yellow crystals (0.11 g, 0.25 mmol, 25%). The crystals are characterised *via* X-ray diffraction analysis.



C₂₀H₂₇ClCuN₅
436.47 g/mol

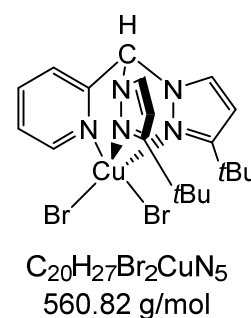
ATR-IR: $\tilde{\nu}$ [cm⁻¹] = 3107 [vw (v, CH_{arom})], 2957 [w, (v, CH_{aliph})], 2904 [w, (v, CH_{aliph})], 2862 [w, (v, CH_{aliph})], 1597 (w), 1574 (vw), 1519 (m), 1478 (w), 1443 (w), 1415 (w), 1392 (vw), 1362 (w), 1348 (w), 1335 (w), 1271 (w), 1236 (m), 1158 (w), 1053 (m), 1013 (w), 1004 (w), 879 (w), 869 (w), 843 (m), 823 (w), 776 (s), 757 (vs), 737 (m), 728 (m), 675 (m), 656 (w).

FAB⁺-MS (*m/z* (%)): 437 (30) [Cu³⁷Cl{HC(3-*t*BuPz)₂(Py)}]⁺, 435 (40) [Cu³⁵Cl{HC(3-*t*BuPz)₂(Py)}]⁺, 400 (100) [Cu{HC(3-*t*BuPz)₂(Py)}]⁺, 337 (<1) [HC(3-*t*BuPz)₂(Py)]⁺ (*m/z* calcd. for C₂₀H₂₇ClCuN₅ = 435.1).

EA: C₂₀H₂₇ClCuN₅ (436.47 g/mol): calcd. C 55.0, H 6.2, N 16.1; found C 54.9, H 6.3, N 16.1.

5.5.4.4 Synthesis of (2-Pyridinyl)bis(3-tertbutylpyrazolyl)methanedibromidocopper(II) [CuBr₂{HC(3-*t*BuPz)₂(Py)}] (C4)

A yellow solution of HC(3-*t*BuPz)₂(Py) (0.34 g, 1.00 mmol) dissolved in 5 mL of methanol, is added dropwise to a suspension of CuBr₂ (0.22 g, 1.00 mmol) in 7 mL of methanol. The mixture is stirred for 20h. During this time the solution turns dark green and a violet solid precipitates. Dark red crystals could be obtained by filtration and storage of the filtrate at 5°C for several days. The crystals are characterised *via* X-ray diffraction analysis (0.11 g, 0.20 mmol, 20%).



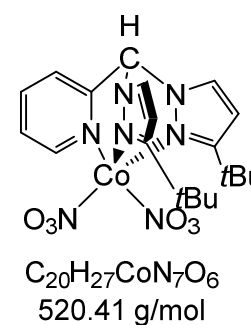
ATR-IR: $\tilde{\nu}$ [cm⁻¹] = 3106 [w (v, CH_{arom})], 3068 [vw (v, CH_{arom})], 2958 [w, (v, CH_{aliph})], 2920 [w, (v, CH_{aliph})], 2868 [vw, (v, CH_{aliph})], 1604 (w), 1522 (m), 1475 (w), 1468 (w), 1447 (m), 1435 (w), 1417 (w), 1393 (vw), 1362 (w), 1343 (w), 1302 (w), 1267 (m), 1236 (s), 1207 (m), 1163 (m), 1111 (w), 1065 (m), 1022 (m), 1000 (w), 928 (vw), 880 (m), 838 (m), 819 (m), 770 (vs), 739 (m), 727 (m), 677 (m), 643 (m), 608 (m).

FAB⁺-MS (*m/z* (%)): 481 (53) [Cu⁸¹Br{HC(3-*t*BuPz)₂(Py)}]⁺, 479 (47) [Cu⁷⁹Br{HC(3-*t*BuPz)₂(Py)}]⁺, 401 (100) [Cu{HC(3-*t*BuPz)₂(Py)}]⁺, 337 (3) [HC(3-*t*BuPz)₂(Py)]⁺, 214 (98) [HC(3-*t*BuPz)(Py)]⁺, (*m/z* calcd. for C₂₀H₂₇BrCuN₅ = 479.1).

EA: C₂₀H₂₇Br₂CuN₅ (560.82 g/mol): calcd. C 42.8, H 4.9, N 12.5; found C 42.5, H 4.9, N 12.4.

5.5.4.5 Synthesis of (2-Pyridinyl)bis(3-tertbutylpyrazolyl)methanedinitratocobalt(II) [Co(NO₃)₂{HC(3-*t*BuPz)₂(Py)}]·CH₂Cl₂ (C5)

A solution of HC(3-*t*BuPz)₂(Py) (0.34 g, 1.00 mmol) dissolved in 5 mL of acetone is added dropwise to a solution of Co(NO₃)₂ · 6 H₂O (0.29 g, 1.00 mmol) dissolved in 5 mL of acetone as well. The solution turns dark magenta and a solid precipitates. The suspension is filtered and dried *in vacuo*. Dissolution of the solid in acetonitrile and diffusion of CH₂Cl₂ results in magenta crystals (0.40 g, 0.66 mmol, 66%), which are



characterised by single-crystal X-ray diffraction analysis.

ATR-IR: $\tilde{\nu}$ [cm^{-1}] = 3142 [vw (v, CH_{arom})], 3127 [vw (v, CH_{arom})], 3112 [vw (v, CH_{arom})], 3078 [vw (v, CH_{arom})], 2970 [w, (v, CH_{aliph})], 2871 [vw, (v, CH_{aliph})], 1739 (m), 1603 [w, (v, NO)], 1526 (w), 1507 (w), 1480 (w), 1446 (m), 1429 (m), 1412 (m), 1386 (m), 1339 [vs, (v, NO)], 1321 (vs), 1294 (m), 1271 (m), 1233 (m), 1216 (m), 1157 (w), 1102 (w), 1077 (m), 1053 (m), 1036 (m), 1019 (w), 952 (w), 878 (m), 844 (m), 828 (m), 766 [s, (v, NO)], 741 (m), 698 (w), 676 (m).

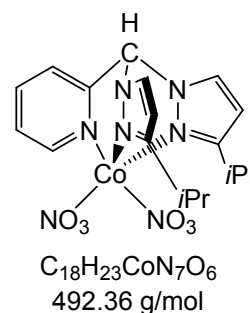
FAB⁺-MS (m/z (%)): 458 (100) [$\text{Co}(\text{NO}_3)\{\text{HC}(3\text{-}t\text{BuPz})_2(\text{Py})\}^+$, 338 (10) [$\text{C}_{20}\text{H}_{28}\text{N}_5^+$], (m/z calcd. for $\text{C}_{20}\text{H}_{27}\text{CoN}_6\text{O}_3 = 458.2$).

FAB⁻-MS (m/z (%)): 62 (20) [NO_3^-].

EA: $\text{C}_{20}\text{H}_{27}\text{CoN}_7\text{O}_6 \cdot \text{CH}_2\text{Cl}_2$ (605.34 g/mol): calcd. C 41.67, H 4.83, N 16.20; found C 41.73, H 4.77, N 16.28.

5.5.4.6 Synthesis of ((2-Pyridinyl)bis(3-isopropylpyrazolyl)methanedinitratocobalt(II) [$\text{Co}(\text{NO}_3)_2\{\text{HC}(3\text{-}i\text{PrPz})_2(\text{Py})\} \cdot \text{MeOH}$ (C6)

A solution of $\text{HC}(3\text{-}i\text{PrPz})_2(\text{Py})$ (0.31 g, 1.00 mmol) dissolved in 5 mL of acetone is added dropwise to a solution of $\text{Co}(\text{NO}_3)_2 \cdot 6 \text{H}_2\text{O}$ (0.13 g, 1.00 mmol) dissolved in 5 mL of acetone as well. Storage at 5°C results in the precipitation of magenta needles (0.11 g, 0.21 mmol, 21%), which are characterised by single-crystal X-ray diffraction analysis.



ATR-IR: $\tilde{\nu}$ [cm^{-1}] = 3112 [vw (v, CH_{arom})], 3078 [vw (v, CH_{arom})], 2970 [w, (v, CH_{aliph})], 2871 [vw, (v, CH_{aliph})], 1739 (m), 1603 [w, (v, NO)], 1526 (w), 1507 (w), 1480 (w), 1446 (m), 1429 (m), 1412 (m), 1386 (m), 1339 [vs, (v, NO)], 1321 (vs), 1294 (m), 1271 (m), 1233 (m), 1216 (m), 1157 (w), 1102 (w), 1077 (m), 1053 (m), 1036 (m), 1019 (w), 952 (w), 878 (m), 844 (m), 828 (m), 766 [s, (v, NO)], 741 (m), 698 (w), 676 (m).

ESI⁺-MS (CH_3OH): 200 (100) [$\text{C}_{10}\text{H}_{10}\text{N}_5^+$] (decomposition).

EA: $\text{C}_{18}\text{H}_{23}\text{CoN}_7\text{O}_6 \cdot \text{MeOH}$ (524.40 g/mol): calcd. C 44.92, H 5.03, N 18.81; found C 44.87, H 4.86, N 19.46.

5.5.4.7 Synthesis of ((2-Pyridinyl)bis(3-isopropylpyrazolyl)methanedinitratozinc(II)) [Zn(NO₃)₂{HC(3-*i*PrPz)₂(Py)}] (C7)

A solution of HC(3-*i*PrPz)₂(Py) (0.16 g, 0.5 mmol) dissolved in 2.4 mL of acetone is added dropwise to a solution of Zn(NO₃)₂ · 6 H₂O (0.15 g, 0.5 mmol) dissolved in 5 mL of acetone. Slow evaporation results in colourless crystals (0.46 g, 0.93 mmol, 93%), which are characterised by single-crystal X-ray diffraction analysis.

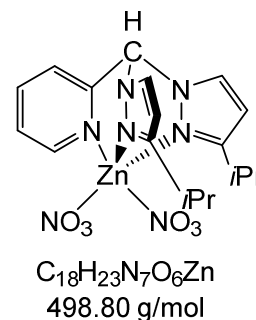
ATR-IR: $\tilde{\nu}$ [cm⁻¹] = 3146 [vw (v, CH_{arom})], 3129 [vw (v, CH_{arom})],

2990 [w, (v, CH_{aliph})], 2965 [w, (v, CH_{aliph})], 2932 [vw, (v, CH_{aliph})], 2871 [vw, (v, CH_{aliph})], 1602 (w), 1523 (w), 1495 (m), 1462 (m), 1447 (m), 1415 (m), 1391 (m), 1366 (w), 1348 (w), 1321 (m), 1301 [s, (v, NO)], 1273 (vs), 1236 (m), 1199 (m), 1065 (m), 1050 (m), 1041 (m), 1016 (m), 969 (w), 875 (m), 838 (m), 825 (m), 810 (w), 783 [s, (v, NO)], 761 (s), 735 (m), 723 (m), 674 (m), 639 (m), 626 (w).

FAB⁺-MS (*m/z* (%)): 437 (60) [⁶⁶Zn(NO₃)₂{HC(3-*i*PrPz)₂(Py)}]⁺, 435 (100) [⁶⁴Zn(NO₃)₂{HC(3-*i*PrPz)₂(Py)}]⁺, 309 (<1) [HC(3-*i*PrPz)₂(Py)]⁺ (*m/z* calc. for C₁₈H₂₃ZnN₆O₃ = 435.1).

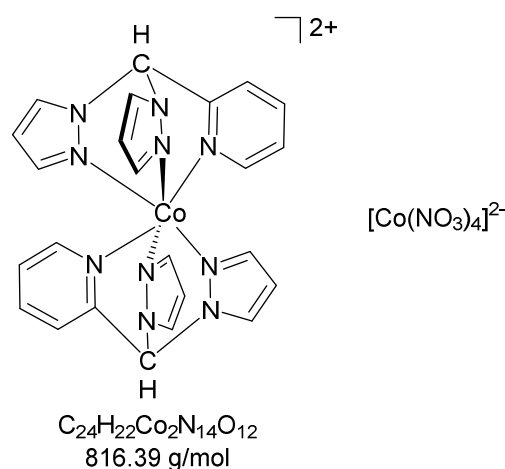
FAB⁻-MS (*m/z* (%)): 496 (5) [M-H]⁻, 62(89) [NO₃]⁻.

EA: C₁₈H₂₃N₇O₆Zn (498.80 g/mol): calcd. C 43.34, H 4.65, N 19.66; found C 43.34, H 4.85, N 19.63.



5.5.4.8 Synthesis of Bis((2-pyridinyl)bis(pyrazolyl)methane)cobalt(II) Tetranitratocobaltat [Co{HC(Pz)₂(Py)}₂][Co(NO₃)₄] · 2C₃H₆O (C8)

A light yellow solution of HC(Pz)₂(Py) (0.23 g, 1.00 mmol) dissolved in 2.5 mL of acetone is added dropwise to a solution of Co(NO₃)₂ · 6 H₂O (0.29 g, 1.00 mmol) dissolved in 2 mL of acetone. The solution turns dark and after several minutes the formation of a precipitate is noticeable. The solid is filtered off and the filtrate is stored at 5°C. After several days red crystals are obtained (0.2 g, 0.21 mmol, 21%), which are characterised by single-crystal X-ray diffraction analysis.



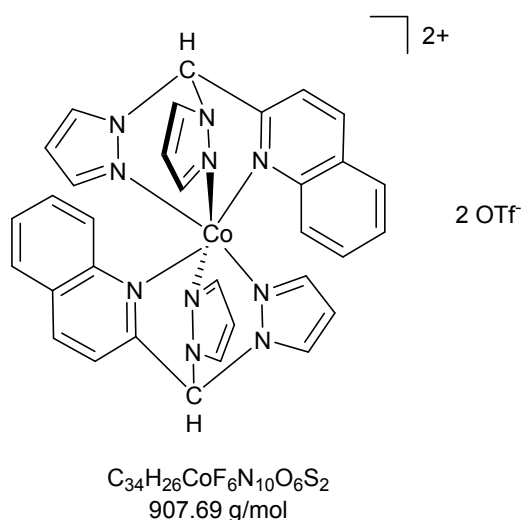
ATR-IR: $\tilde{\nu}$ [cm^{-1}] = 3123 [w (v, CH_{arom})], 3077 [w (v, CH_{arom})], 3008 [w (v, CH_{arom})], 1738 (w), 1703 (m), 1614 (vw), 1456 (s), 1414 (m), 1362 (s), 1315 (vs), 1281 (vs), 1262 (vs), 1227 (s), 1106 (w), 1071 (m), 1024 (m), 916(w), 876 (w), 840 (w), 828 (w), 812 (m), 763 (s), 726 (m), 681 (m), 661 (w), 634 (w).

FAB⁺-MS (m/z (%)): 571 (22) $[\text{Co}(\text{NO}_3)\{\text{HC}(\text{Pz})_2(\text{Py})\}_2]^+$, 509 (13) $[\text{Co}\{\text{HC}(\text{Pz})_2(\text{Py})\}_2]^+$, 225 (<1) $[\text{HC}(\text{Pz})_2(\text{Py})]_2^+$, (m/z calc. for $\text{C}_{24}\text{H}_{22}\text{CoN}_{10}$ = 509.1)

FAB⁻-MS (m/z (%)): 62(31) $[\text{NO}_3^-]$.

5.5.4.9 Synthesis of Bis(bis(pyrazolyl)(2-quinolinyl) methane)cobalt(II) ditriflate $[\text{Co}\{\text{HC}(\text{Pz})_2(\text{Qu})\}_2][\text{OTf}]_2$ (C9)

An orange solution of $\text{HC}(\text{Pz})_2(\text{Qu})$ (0.28 g, 1.00 mmol) dissolved in 5 mL of acetone is added dropwise to a solution of $\text{Co}(\text{OTf})_2$ (0.36 g, 1.00 mmol) dissolved in 5 mL of acetone. The solution turns red-brown and a beige solid starts to precipitate after several minutes. The precipitate is dissolved in methanol and diffusion of diethyl ether results in yellow crystals (0.23 g, 0.25 mmol, 25%), which are characterised by single-crystal X-ray diffraction analysis.



ATR-IR: $\tilde{\nu}$ [cm^{-1}] = 3141 [vw (v, CH_{arom})], 3127 [w (v, CH_{arom})], 3102 (vw, (v, CH_{arom})), 1597 (w), 1513 (m), 1460 (w), 1446 (w), 1436 (w), 1407 (m), 1380 (w), 1286 [s, (v, CF_3)], 1241 [s, (v, CF_3)], 1221 (m), 1163 (s), 1097 (m), 1078 (m), 1066 (m), 1028 [m, (v, SO_3)], 995 (m), 978 (m), 930 (m), 920 (m), 876 (w), 850 (w), 839 (m), 807 (m), 792 (m), 772 (vs), 681 (w), 667 (w), 637 (s), 631 (s), 607 (m).

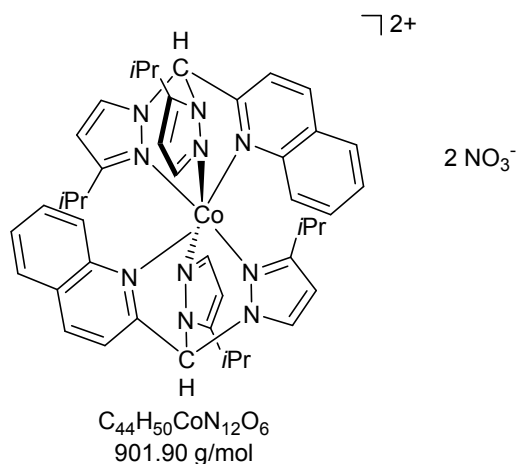
FAB⁺-MS (m/z (%)): 758 (15) $[\text{Co}\{\text{HC}(\text{Pz})_2(\text{Qu})\}_2(\text{OTf})]^+$, 609 (11) $[\text{Co}\{\text{HC}(\text{Pz})_2(\text{Qu})\}_2]^+$, 333 (11) $[\text{C}_{16}\text{H}_{12}\text{CoN}_5]^+$, 275 (<1) $[\text{HC}(\text{Pz})_2(\text{Qu})]^+$, (m/z calc. for $\text{C}_{33}\text{H}_{26}\text{CoN}_{10}\text{SF}_3\text{O}_3$ = 758.1).

FAB⁻-MS (m/z (%)): 149 (79) $[\text{CF}_3\text{SO}_3^-]$.

EA: $\text{C}_{34}\text{H}_{26}\text{CoF}_6\text{N}_{10}\text{O}_6\text{S}_2$ (907.07 g/mol): calcd. C 44.99, H 2.89, N 15.43, S 7.07; found C 44.51, H 3.07, N 14.99, S 6.98.

5.5.4.10 Synthesis of Bis((3-isopropylpyrazolyl)(5-isopropylpyrazolyl)(2-quinoliny))methanecobalt(II) dinitrate
[Co{HC(3-*i*PrPz)(5-*i*PrPz)(Qu)}₂][NO₃]₂·2MeOH (C10)

A yellow solution of a mixture of HC(3-*i*PrPz)(5-*i*PrPz)(Qu) and HC(3-*i*PrPz)₂(Qu) (0.36 g, 1.00 mmol) dissolved in 5 mL of acetone is added dropwise to a magenta solution of Co(NO₃)₂·6 H₂O (0.29 g, 1.00 mmol) dissolved in 5 mL of acetone, resulting in a red solution, which is stored at 5°C. After several days a light orange solid precipitates. The solid is filtered off and dried. Dissolving the solid in methanol and diffusion of diethyl ether



yields orange crystals (0.23 g, 0.25 mmol, 25%), which are characterised by single-crystal X-ray diffraction analysis.

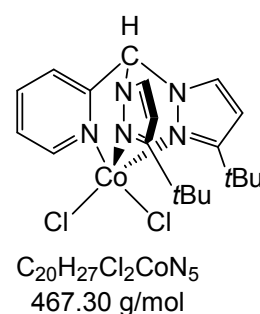
ATR-IR: $\tilde{\nu}$ [cm⁻¹] = 3106 [vw (v, CH_{arom})], 2967 [w (v, CH_{aliph})], 1619 (vw), 1594 (w), 1529 (w), 1510 (w), 1433 (s), 1415 (m), 1366 (m), 1310 (s), 1291 (vs), 1255 (m), 1242 (m), 1215 (m), 1198 (w), 1146 (w), 1095 (w), 1070 (w), 1048 (w), 1028 (m), 978 (w), 951 (w), 930 (m), 884 (w), 846 (m), 809 (m), 783 (vs), 734 (w), 695 (w), 679 (w), 647 (w), 631 (w), 622 (m).

FAB⁺-MS (*m/z* (%)): 417 (3) [C₂₂H₂₄CoN₅]⁺, (*m/z* calc. for C₂₂H₂₄CoN₅ = 417.1).

FAB⁻-MS (*m/z* (%)): 62 (55) [NO₃⁻].

5.5.4.11 Resynthesis of (2-Pyridinyl)(3-*tert*butylpyrazolyl)methanedichloridocobalt(II)
[CoCl₂{HC(3-*t*BuPz)₂(Py)}]·THF^[125] (C11)

A light yellow solution of HC(3-*t*BuPz)₂(Py) (1.69 g, 5.00 mmol) dissolved in 50 mL of CH₂Cl₂ is added dropwise to a deep blue solution of CoCl₂ (0.65 g, 5.00 mmol) dissolved in 25 mL of acetone. The solution turns violet and is stirred at room temperature for 90 min. The solvent is reduced *in vacuo*, yielding a violet solid. The solid is dissolved in methanol and diffusion of THF results in violet needles (1.31 g, 2.8 mmol, 86%), which are characterised by single-crystal X-ray diffraction analysis.



ATR-IR: $\tilde{\nu}$ [cm⁻¹] = 3117 [w (v, CH_{arom})], 3069 [vw (v, CH_{arom})], 3049 [vw (v, CH_{arom})], 2963 (w), 2908 [w (v, CH_{aliph})], 2869 [vw (v, CH_{aliph})], 2162 (vw), 2032 (vw), 1743 (vw), 1603 (w), 1574 (vw), 1521 (m), 1488 (w), 1471 (w), 1459 (w), 1446 (m), 1393 (vw), 1362 (w), 1346 (w),

1303 (vw), 1270 (w), 1237 (m), 1206 (m), 1162 (w), 1106 (vw), 1066 (m), 1028 (w), 1017 (m), 1009 (w), 984 (vw), 928 (vw), 882 (w), 840 (m), 821 (w), 775 (vs), 731 (m), 702 (w), 678 (m).

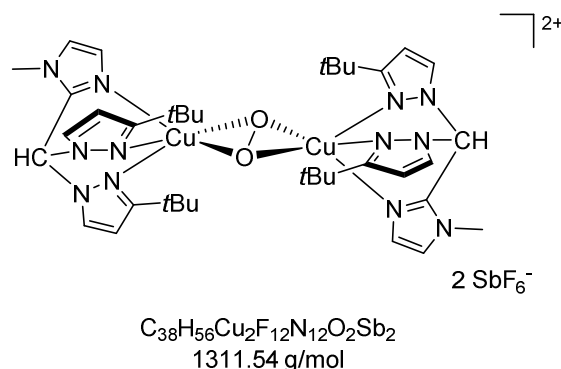
The analytical data is in accord with the literature.^[125]

5.5.5 Synthesis of Bis(2-(1-Methylimidazolyl))bis(3-*tert*butylpyrazolyl)methane)-copper(II)peroxide dihexafluoroantimonate [Cu₂O₂{HC(3-*t*BuPz)₂(1-Melm)}₂][SbF₆]₂ (P1[SbF₆]₂)

A solution of HC(3-*t*BuPz)₂(1-Melm) (0.54 g, 0.16 mmol) dissolved in 5 mL of THF, is added in one portion to CuCl (0.17 g, 0.17 mmol). The resulting suspension is stirred for 45 min to 1h.

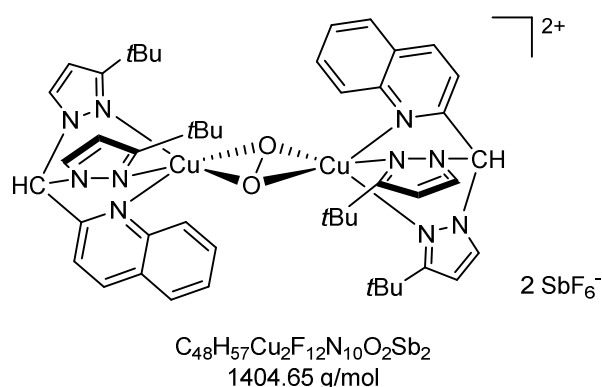
While vigorously shaking, a solution of AgSbF₆ (0.61 g, 0.17 mmol) dissolved in 250 µL of THF is added and AgCl precipitates, generating the precursor solution.

In a UV/Vis measurement cell 9 mL of CH₂Cl₂ are provided and cooled to -80°C. Oxygen is bubbled through the solvent for 5 min to generate an oxygen-saturated liquid. It follows the addition of 1 mL of the precursor solution, resulting in an immediate colour change to deep violet. Formation of the peroxide complex is followed UV/Vis-spectroscopically (see 3.2.2.1). The concentration of the peroxo complex in solution is 1.5 × 10⁻³ mol L⁻¹.



5.5.6 Synthesis of Bis(bis(3-*tert*-butylpyrazolyl)(2-Quinoliny))methanecopper(II)-peroxide dihexafluoroantimonate [Cu₂O₂{HC(3-*t*BuPz)₂(Qu)}₂][SbF₆]₂ (P2[SbF₆]₂)

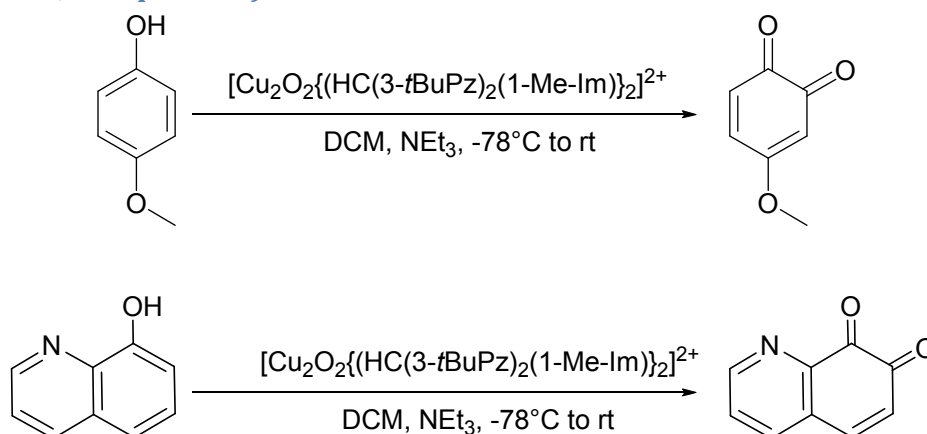
A solution of HC(3-*t*BuPz)₂(Qu) (0.62 g, 0.16 mmol) dissolved in 5 mL of CH₂Cl₂ is added in one portion to CuCl (0.17 g, 0.17 mmol). The resulting suspension is stirred for 45 min to 1h. While vigorously shaking, a solution of AgSbF₆ (0.61 g, 0.17 mmol) dissolved in 250 µL of THF is added and AgCl precipitates, generating the precursor solution.



In a UV/Vis measurement

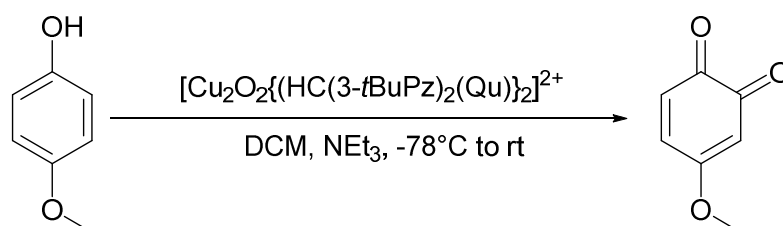
cell 9 mL of CH_2Cl_2 are provided and cooled to -80°C . Oxygen is bubbled through the solvent for 5 min to generate an oxygen-saturated liquid. It follows the addition of 1 mL of the precursor solution, and the solution is kept at -80° . A slow colour change to violet is visible and after 8h the formation of the peroxide complex is proven by UV/Vis spectroscopy (see 3.3.2). The concentration of the peroxo complex in solution is $1.5 \times 10^{-3} \text{ mol L}^{-1}$.

5.5.7 Oxidation of catalytic amounts of exogenous substrate with ($\text{P1}[\text{SbF}_6]_2$) (25 eq of phenol, 50 eq. of NEt_3)



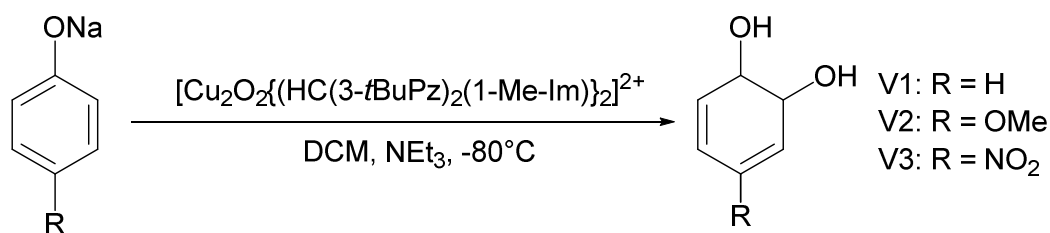
$\text{P1}[\text{SbF}_6]_2$ is prepared as described above (see 5.5.5) and its development is followed by UV/Vis-spectroscopy. After stabilisation of the optical spectrum, 200 μL of a CH_2Cl_2 solution containing 25eq. of phenol and 50 eq of NEt_3 are added. The reaction solution is warmed to room temperature and stirred overnight. After 16–18h the reaction is quenched with 3 mL of 0.5M HCl . The aqueous solution is extracted with CH_2Cl_2 ($3 \times 3 \text{ mL}$) and the combined organic phases are dried over MgSO_4 . The solvent is reduced *in vacuo*, followed by NMR spectroscopic characterisation. Turnover numbers are determined by dividing the concentration of the built quinone (which was determined from UV/Vis spectroscopical data) by the concentration of the peroxo complex.

5.5.8 Oxidation of catalytic amounts of exogenous substrate with ($\text{P2}[\text{SbF}_6]_2$) (25 eq of phenol, 50 eq. of NEt_3)^[160,168]



This experiment was performed by A. Hoffmann. A solution of 4-methoxyphenol (25 eq.) and triethylamine (50 eq.) in CH_2Cl_2 (200 μL) was added to the solution of $[\text{Cu}\{\text{HC}(3\text{-}t\text{BuPz})_2(\text{Qu})\}]\text{SbF}_6$ in CH_2Cl_2 at -78°C and with a fine needle O_2 was bubbled through this solution. The reaction was monitored by means of UV/Vis spectroscopy. Upon bubbling through O_2 , an intense 418 nm feature developed owing to the formation of the 4-methoxy-1,2-benzoquinone. The quantity of the quinone formed was determined from the extinction coefficient of the quinone minus the residual extinction coefficient of thermally decayed $\text{P}[\text{SbF}_6]_2$, thus yielding ten turnovers per dinuclear copper peroxide species after 1h. Turnover numbers are determined by dividing the concentration of the built quinone by the concentration of the peroxo complex.

5.5.9 Oxidation of stoichiometric amounts (5 eq) of exogenous substrate with $\text{P1}(\text{SbF}_6)_2$



The precursor is prepared according to 5.5.5.

In a centrifuge tube that is closed with a septum, 5 mL of CH_2Cl_2 are cooled to -80°C , followed by saturation of the solvent with O_2 . 500 μL of the precursor solution is added and an instant colour change to deep violet can be observed. After 15–20 min excess O_2 is removed by five cycles of vacuum/ N_2 purging and at least 5 min of purging the cell with N_2 . Next 250 μL of either a THF (R = H, OMe) or MeOH (R = NO₂) stock solution containing 5 eq of substrate are added, starting the reaction time, which amounts to 5 min for the unsubstituted phenolate and 60 min for both the substituted phenolates. The colour of the solution changes hereby to black. Reactions are stopped by the addition of 3 mL of 0.5M HCl to the solution at -80°C . The aqueous phase freezes and is light yellow, while the organic phase turns slightly turquoise. After equilibration to room temperature, a known quantity of acetophenone is added to the solution as an internal standard. Following the removal of volatiles under vacuum, the residue is extracted with CH_2Cl_2 (3×5 mL) and the combined organic phases are passed through a column of MgSO_4 , before reduction of the solvent *in*

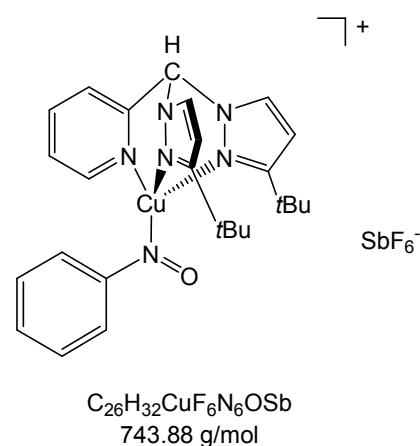
vacuo. The residue is dissolved in CDCl_3 for ^1H -NMR spectroscopical characterisation. Quantification of the products is done by comparing the amount of product *p*-catechols and the unreacted *p*-phenolates against the acetophenone standard.

Preparation of the stock solution:

	Sodium phenolate M = 116.09 g/mol	Sodium 4-methoxyphenolate M = 146.12 g/mol	Sodium nitrophenolate M = 161.09 g/mol
n [mmol]	5	5	5
m [mg]	58	73	81
Solvent	THF (3 mL)	THF (3 mL)	MeOH (3 mL)

5.5.10 Conversion of $[\text{Cu}\{\text{HC}(3\text{-}t\text{BuPz})_2(\text{Py})\}][\text{SbF}_6]$ with nitrosobenzene

$\text{HC}(3\text{-}t\text{BuPz})_2(\text{Py})$ (0.51 g, 0.15 mmol) is dissolved in 2.5 mL of the according solvent in which the measurement is performed (CH_2Cl_2 , THF or CHCl_3). The resulting solution is added to CuCl (0.17 g, 0.17 mmol) and the mixture is stirred at room temperature for 1h. While vigorously shaking, a solution of AgSbF_6 (0.61 g, 0.17 mmol), dissolved in 250 μL of THF, is added and AgCl precipitates, generating the precursor solution. In a UV/Vis measurement cell 10 mL of the according solvent are provided and cooled to -78°C for CH_2Cl_2 and THF and to -60°C for CHCl_3 .

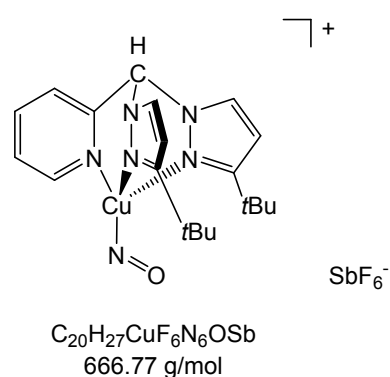


A stock solution containing 0.34 mmol nitrosobenzene in 2.5 mL of solvent (again CH_2Cl_2 , THF or CHCl_3) is prepared. The according equivalents which are added to the peroxo complex are varied by the amount of the injected stock solution. After addition of nitrosobenzene the reaction solution turns deep red.

Depending on the reaction temperature, now the solution is either kept cold or warmed up to the desired temperature. Reaction progress is followed by UV/Vis spectroscopy.

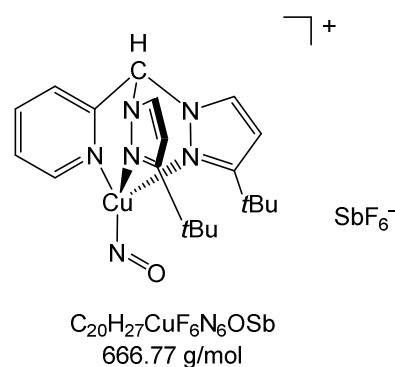
5.5.11 Conversion of $[\text{Cu}\{\text{HC}(\text{3-}t\text{BuPz})_2(\text{Py})\}][\text{SbF}_6]$ with NO gas

The precursor solution of $[\text{Cu}\{\text{HC}(\text{3-}t\text{BuPz})_2(\text{Py})\}][\text{SbF}_6]$ is prepared in CHCl_3 according to 5.5.10. At -60°C NO gas is bubbled through the precursor solution for 15 min. Hereby the solution turns from light green to light brown. For UV/Vis measurements, 10 mL of CHCl_3 are provided in a UV/Vis measurement cell and cooled to -60°C , followed by the addition of 500 μL of the precursor solution after NO addition.



5.5.12 Conversion of $[\text{Cu}\{\text{HC}(\text{3-}t\text{BuPz})_2(\text{Py})\}][\text{SbF}_6]$ with diazald®

The precursor solution of $[\text{Cu}\{\text{HC}(\text{3-}t\text{BuPz})_2(\text{Py})\}][\text{SbF}_6]$ is prepared in CH_2Cl_2 according to 5.5.10. For UV/Vis measurements, 10 mL of CH_2Cl_2 are provided in a UV/Vis measurement cell at room temperature, followed by the addition of 500 μL of the precursor solution. Finally 0.5 eq of diazald® dissolved in CH_2Cl_2 are added.



6 References

- [1] R. Noyori, *Asymmetric Catalysis in Organic Synthesis*, Wiley, New York, **1994**.
- [2] A. Pfaltz, H. Yamamoto, *Comprehensive Asymmetric Catalysis*, Springer, Berlin, **1999**.
- [3] I. Ojima, *Catalytic Asymmetric Synthesis*, Wiley-VCH, New York, **2000**.
- [4] M. Beller, C. Bolm, *Transition Metals for Organic Synthesis*, Wiley-VCH, Weinheim, **2004**.
- [5] M. Schmidt, H. Griengl, *Top. Curr. Chem.* **1999**, 193–226.
- [6] S. M. Roberts, *Biocatalysts for Fine Chemicals Synthesis*, Wiley-VCH, New York, **1999**.
- [7] R. A. Copeland, *Enzymes: A Practical Introduction to Structure, Mechanism and Data Analysis*, Wiley-VCH, Weinheim, **2000**.
- [8] K. Drauz, H. Waldmann, *Enzyme Catalysis in Organic Synthesis*, Wiley-VCH, Weinheim, **2002**.
- [9] A. S. Bommarius, B. R. Riebel, *Biocatalysis*, Wiley-VCH, Weinheim, **2004**.
- [10] A. Schellenberger, *Enzymkatalyse: Einführung in Die Chemie, Biochemie Und Technologie Der Enzyme*, Gustav Fischer Verlag, Jena, **1989**.
- [11] A. Dondoni, A. Massi, *Angew. Chem. Int. Ed. Engl.* **2008**, 47, 4638–4660; *Angew. Chem.* **2008**, 120, 4716–4739.
- [12] D. W. C. MacMillan, *Nature* **2008**, 455, 304–308.
- [13] P.-F. Xu, W. Wang, Eds., *Catalytic Cascade Reactions*, John Wiley & Sons Inc., Hoboken, New Jersey, **2014**.
- [14] V. Andrushko, N. Andrushko, Eds., *Stereoselective Synthesis of Drugs and Natural Products*, John Wiley & Sons Inc., Hoboken, New Jersey, **2013**.
- [15] D. Steinborn, *Grundlagen Der Metallorganischen Komplexkatalyse*, Vieweg Und Teubner Verlag, **2010**.
- [16] *Oxford Dictionary of Biochemistry & Molecular Biology*, Oxford University Press, Oxford, **2008**.
- [17] R. Garrett, C. M. Grisham, *Biochemistry*, Saunders College Pub., Philadelphia, **1995**.

- [18] A. Hoffmann, C. Citek, S. Binder, A. Goos, M. Rübhausen, O. Troeppner, I. Ivanović-Burmazović, E. C. Wasinger, T. D. P. Stack, S. Herres-Pawlis, *Angew. Chem. Int. Ed. Engl.* **2013**, 52, 5398–5401; *Angew. Chem.* **2013**, 125, 5508–5512.
- [19] L. Que Jr., W. B. Tolman, *Nature* **2008**, 455, 333–340.
- [20] A. D. Mc Naught, A. Wilkinson, *IUPAC. Compendium of Chemical Terminology (the “Gold Book”)*, Blackwell Scientific Publications, Oxford, **1997**.
- [21] K. Faber, *Biotransformations in Organic Chemistry*, Springer, **2011**.
- [22] J.-N. Rebilly, B. Colasson, O. Bistri, D. Over, O. Reinaud, *Chem. Soc. Rev.* **2014**, 44, 467–489.
- [23] R. H. Holm, E. I. Solomon, *Chem. Rev.* **2004**, 347–348.
- [24] E. P. Carpenter, K. Beis, A. D. Cameron, S. Iwata, *Curr. Opin. Struct. Biol.* **2008**, 18, 581–586.
- [25] D. A. Kraut, K. S. Carroll, D. Herschlag, *Annu. Rev. Biochem.* **2003**, 72, 517–571.
- [26] H. Arakawa, M. Aresta, J. N. Armor, M. A. Barteau, E. J. Beckman, A. T. Bell, J. E. Bercaw, C. Creutz, E. Dinjus, D. a. Dixon, K. Domen, D. L. DuBois, J. Eckert, E. Fujita, D. H. Gibson, W. a. Goddard, D. W. Goodman, J. Keller, G. J. Kubas, H. H. Kung, J. E. Lyons, L. E. Manzer, T. J. Marks, K. Morokuma, K. M. Nicholas, R. Periana, L. Que, J. Rostrup-Nielson, W. M. H. Sachtler, L. D. Schmidt, A. Sen, G. a. Somorjai, P. C. Stair, B. R. Stults, W. Tumas, *Chem. Rev.* **2001**, 101, 953–996.
- [27] T. Punniyamurthy, S. Velusamy, J. Iqbal, *Chem. Rev.* **2005**, 105, 2329–2363.
- [28] W. B. Tolman, *Activation of Small Molecules: Organometallic and Bioinorganic Perspectives*, Wiley-VCH, **2006**.
- [29] D. J. Leak, R. A. Sheldon, J. M. Woodley, P. Adlercreutz, *Biocatal. Biotransform.* **2009**, 27, 1–26.
- [30] F. K. P. Kerman, M. Salehifar, M. Mirzaei, *Eur. J. Exp. Biol.* **2014**, 4, 716–721.
- [31] R. H. Holm, P. Kennepohl, E. I. Solomon, *Chem. Rev.* **1996**, 96, 2239–2314.
- [32] P. M. Colman, H. C. Freeman, J. M. Guss, M. Murata, V. A. Norris, J. A. M. Ramshaw, M. P. Venkatappa, *Nature* **1978**, 272, 319–324.
- [33] E. A. Lewis, W. B. Tolman, *Chem. Rev.* **2004**, 104, 1047–1076.
- [34] Y. Matoba, T. Kumagai, A. Yamamoto, H. Yoshitsu, M. Sugiyama, *J. Biol. Chem.* **2006**, 281, 8981–8990.
- [35] R. Rox Anderson, J. A. Parrish, *J. Invest. Dermatol.* **1981**, 77, 13–19.

- [36] K. J. McGraw, R. J. Safran, K. Wakamatsu, *Funct. Ecol.* **2005**, *19*, 816–821.
- [37] J. B. Pridham, R. S. Andrews, *Phytochemistry* **1967**, *6*, 13–18.
- [38] R. A. Nicolaus, M. Piattelli, *Rend. Accad. Sci. Fis. Mat.* **1965**, *32*, 83–97.
- [39] H. Fiege, H.-W. Voges, T. Hamamoto, S. Umemura, T. Iwata, H. Miki, Y. Fujita, H.-J. Buysch, D. Garbe, W. Paulus, *Ullmann's Encyclopedia of Industrial Chemistry*, Wiley-VCH, **2000**.
- [40] E. A. Karakhanov, A. L. Maximov, Y. S. Kardasheva, V. A. Skorkin, S. V. Kardashev, E. A. Ivanova, E. Lurie-Luke, J. A. Seeley, S. L. Cron, *Ind. Eng. Chem. Res.* **2010**, *49*, 4607–4613.
- [41] C. Huang, N. Ghavtadze, B. Chattopadhyay, V. Gevorgyan, *J. Am. Chem. Soc.* **2011**, *133*, 17630–17633.
- [42] S. Ignacimuthu, M. Pavunraj, V. Duraipandiyan, N. Raja, C. Muthu, *Asian J. Trad. Med.* **2009**, *4*, 36–40.
- [43] C. Gerdemann, C. Eicken, B. Krebs, *Acc. Chem. Res.* **2002**, *35*, 183–191.
- [44] S. Petersen, W. Gauss, E. Urbschat, *Angew. Chemie* **1955**, 217–231.
- [45] L. Waxman, *J. Biol. Chem.* **1975**, *250*, 3796–3806.
- [46] M. Rolff, J. Schottenheim, H. Decker, F. Tucek, *Chem. Soc. Rev.* **2011**, *40*, 4077–4098.
- [47] E. I. Solomon, D. E. Heppner, E. M. Johnston, J. W. Ginsbach, J. Cirera, M. Qayyum, M. T. Kieber-Emmons, C. H. Kjaergaard, R. G. Hadt, L. Tian, *Chem. Rev.* **2014**, *114*, 3659–3853.
- [48] C. Olivares, C. Jiménez-Cervantes, J. A. Lozano, F. Solano, J. C. García-Borrón, *Biochem. J.* **2001**, *139*, 131–139.
- [49] I. Braasch, M. Scharl, J.-N. Volff, *BMC Evol. Biol.* **2007**, *7*, 74–91.
- [50] S. Itoh, S. Fukuzumi, *Acc. Chem. Res.* **2007**, *40*, 592–600.
- [51] J. N. Hamann, F. Tucek, *Chem. Commun.* **2014**, *50*, 2298–2300.
- [52] P. E. M. Siegbahn, *J. Biol. Inorg. Chem.* **2003**, *8*, 567–576.
- [53] L. M. Mirica, M. Vance, D. J. Rudd, B. Hedman, K. O. Hodgson, E. I. Solomon, T. D. P. Stack, *Science* **2005**, *308*, 1890–1892.
- [54] T. Inoue, Y. Shiota, K. Yoshizawa, *J. Am. Chem. Soc.* **2008**, 16890–16897.
- [55] L. M. Mirica, X. Ottenwaelde, T. D. P. Stack, *Chem. Rev.* **2004**, *104*, 1013–1045.

- [56] H.-C. Liang, M. J. Henson, L. Q. Hatcher, M. A. Vance, C. X. Zhang, D. Lahti, S. Kaderli, R. D. Sommer, A. L. Rheingold, A. D. Zuberbühler, E. I. Solomon, K. D. Karlin, *Inorg. Chem.* **2004**, *43*, 4115–4117.
- [57] L. Q. Hatcher, M. A. Vance, A. A. Narducci Sarjeant, E. I. Solomon, K. D. Karlin, *Inorg. Chem.* **2006**, *45*, 3004–3013.
- [58] S. Herres-Pawlis, P. Verma, R. Haase, P. Kang, C. T. Lyons, E. C. Wasinger, U. Flörke, G. Henkel, T. D. P. Stack, *J. Am. Chem. Soc.* **2009**, *131*, 1154–1169.
- [59] L. Q. Hatcher, K. D. Karlin, *Adv. Inorg. Chem.* **2006**, *58*, 131–184.
- [60] A. Walli, S. Dechert, M. Bauer, S. Demeshko, F. Meyer, *Eur. J. Inorg. Chem.* **2014**, 4660–4676.
- [61] N. Kitajima, K. Fujisawa, Y. Moro-oka, K. Toriumi, *J. Am. Chem. Soc.* **1989**, *111*, 8975–8976.
- [62] K. Fujisawa, T. Ono, Y. Ishikawa, N. Amir, Y. Miyashita, K. Okamoto, N. Lehnert, *Inorg. Chem.* **2006**, *45*, 1698–1713.
- [63] T. D. P. Stack, *Dalton Trans.* **2003**, *34*, 1881–1889.
- [64] T. Osako, K. Ohkubo, M. Taki, Y. Tachi, S. Fukuzumi, S. Itoh, *J. Am. Chem. Soc.* **2003**, *125*, 11027–11033.
- [65] D. J. E. Spencer, A. M. Reynolds, P. L. Holland, B. A. Jazdzewski, C. Duboc-Toia, L. Le Pape, S. Yokota, Y. Tachi, S. Itoh, W. B. Tolman, *Inorg. Chem.* **2002**, *41*, 6307–6321.
- [66] S. Herres-Pawlis, U. Flörke, G. Henkel, *Eur. J. Inorg. Chem.* **2005**, *2005*, 3815–3824.
- [67] S. Herres-Pawlis, S. Binder, A. Eich, R. Haase, B. Schulz, G. Wellenreuther, G. Henkel, M. Rübhausen, W. Meyer-Klaucke, *Chem. Eur. J.* **2009**, *15*, 8678–8682.
- [68] R. R. Jacobson, Z. Tyeklar, A. Farooq, K. D. Karlin, S. Liu, J. Zubieta, *J. Am. Chem. Soc.* **1988**, *110*, 3690–3692.
- [69] A. Granata, E. Monzani, L. Casella, *J. Biol. Inorg. Chem.* **2004**, *9*, 903–913.
- [70] C. Citek, B.-L. Lin, T. E. Phelps, E. C. Wasinger, T. D. P. Stack, *J. Am. Chem. Soc.* **2014**, *136*, 14405–14408.
- [71] E. Monzani, L. Quinti, A. Perotti, L. Casella, M. Gullotti, L. Randaccio, S. Geremia, G. Nardin, P. Faleschini, G. Tabbi, *Inorg. Chem.* **1998**, *37*, 553–562.
- [72] G. Battaini, M. De Carolis, E. Monzani, F. Tuczek, L. Casella, *Chem. Commun.* **2003**, 726–727.

- [73] G. Battaini, E. Monzani, L. Casella, E. Lonardi, A. W. J. W. Tepper, G. W. Canters, L. Bubacco, *J. Biol. Chem.* **2002**, 277, 44606–44612.
- [74] A. Spada, S. Palavicini, E. Monzani, L. Bubacco, L. Casella, *Dalton Trans.* **2009**, 6468–6471.
- [75] S. Palavicini, A. Granata, E. Monzani, L. Casella, *J. Am. Chem. Soc.* **2005**, 127, 18031–18036.
- [76] A. Hoffmann, S. Herres-Pawlis, *Z. Anorg. Allg. Chem.* **2013**, 639, 1426–1432.
- [77] M. Réglér, C. Jorand, B. Waegell, *J. Chem. Soc., Chem. Commun.* **1990**, 24, 1752–1755.
- [78] M. Rolff, J. Schottenheim, G. Peters, F. Tuczek, *Angew. Chem. Int. Ed. Engl.* **2010**, 49, 6438–6442; *Angew. Chem.* **2010**, 122, 6583–6587.
- [79] J. Schottenheim, N. Fateeva, W. Thimm, J. Krahmer, F. Tuczek, *Z. Anorg. Allg. Chem.* **2013**, 639, 1491–1497.
- [80] K. V. N. Esguerra, Y. Fall, J.-P. Lumb, *Angew. Chemie Int. Ed.* **2014**, 53, 5877–5881; *Angew. Chem.* **2014**, 126, 5987–5991.
- [81] J. Cahoy, P. L. Holland, W. B. Tolman, *Inorg. Chem.* **1999**, 38, 2161–2168.
- [82] V. Mahadevan, M. J. Henson, E. I. Solomon, T. D. P. Stack, *J. Am. Chem. Soc.* **2000**, 122, 10249–10250.
- [83] A. F. Hollemann, E. Wiberg, N. Wiberg, *Lehrbuch Der Anorganischen Chemie*, Walter De Gruyter, Berlin, New York, **2007**.
- [84] B. M. Babier, *Cobalamin: Biochemistry & Pathophysiology*, John Wiley & Sons Inc., **1975**.
- [85] D. L. Nelson, M. M. Cox, *Lehninger, Principles of Biochemistry*, Palgrave Mcmillan, W. H. Freeman, **2013**.
- [86] J. H. Enemark, R. D. Feltham, *Coord. Chem. Rev.* **1974**, 13, 339–406.
- [87] L. J. Ignarro, *Angew. Chem. Int. Ed. Engl.* **1999**, 38, 1882–1892; *Angew. Chem.* **1999**, 111, 2002–2013.
- [88] R. G. Knowles, S. Moncada, *Biochem. J.* **1994**, 258, 249–258.
- [89] D. Voet, J. G. Voet, C. W. Pratt, *Lehrbuch Der Biochemie*, Wiley-VCH Verlag GmbH, Weinheim, **2002**.
- [90] M. Follmann, N. Griebenow, M. G. Hahn, I. Hartung, F.-J. Mais, J. Mittendorf, M. Schäfer, H. Schirok, J.-P. Stasch, F. Stoll, A. Straub, *Angew. Chem. Int. Ed. Engl.* **2013**, 52, 9442–9462; *Angew. Chem.* 2013, **125**, 9618–9639.

- [91] K. E. Broderick, L. Alvarez, M. Balasubramanian, D. D. Belke, A. Makino, A. Chan, V. L. Woods, W. H. Dillmann, V. S. Sharma, R. B. Pilz, T. D. Bigby, G. R. Boss, *Exp. Biol. Med.* (Maywood, N.J., U.S.) **2007**, 232, 1432–1440.
- [92] I. M. Wasser, S. De Vries, P. Moënné-Loccoz, I. Schröder, K. D. Karlin, *Chem. Rev.* **2002**, 102, 1201–1234.
- [93] J. H. van Wonderen, D. N. Kostrz, C. Dennison, F. MacMillan, *Angew. Chem. Int. Ed. Engl.* **2013**, 52, 1990–1993; *Angew. Chem.* **2013**, 125, 2044–2047.
- [94] M. E. P. Murphy, S. Turley, E. T. Adman, *J. Biol. Chem.* **1997**, 272, 28455–28460.
- [95] W.-Z. Lee, W. B. Tolman, *Inorg. Chem.* **2002**, 41, 5656–5658.
- [96] W. J. Lennarz, M. D. Lane, *Encyclopedia of Biological Chemistry*, Academic Press, Elsevier, **2013**.
- [97] I. E. Tosques, A. V Kwiatkowski, J. Shi, J. P. Shapleigh, *J. Bacteriol.* **1997**, 179, 1090–1095.
- [98] B. C. Berks, S. J. Ferguson, J. W. B. Moir, D. J. Richardson, *Biochim. Biophys. Acta - Bioenerg.* **1995**, 1232, 97–173.
- [99] Environmental Protection Agency, *Revisions to the Greenhouse Gas Reporting Rule and Final Confidentiality Determinations for New or Substantially Revised Data Elements*, **2013**.
- [100] S. Trofimenko, *J. Am. Chem. Soc.* **1966**, 88, 1842–1844.
- [101] S. Trofimenko, *Scorpionates: The Coordination Chemistry of Polypyrazolylborate Ligands*, Imperial College Press, **1999**.
- [102] L. M. Richburg, J. A. Farouq, C. D. Incarvito, A. L. Rheingold, D. Rabinovich, *Polyhedron* **2000**, 19, 1815–1820.
- [103] K.-B. Shiu, C.-J. Chang, Y. Wang, M.-C. Cheng, *J. Organomet. Chem.* **1991**, 406, 363–369.
- [104] A. L. Bandini, G. Banditelli, G. Minghetti, F. Bonati, *Can. J. Chem.* **1979**, 57, 3237–3242.
- [105] K. R. Breakell, D. J. Patmore, A. Storr, *J. Chem. Soc., Dalt. Trans.* **1975**, 749–754.
- [106] A. Steiner, D. Stalke, *Inorg. Chem.* **1995**, 34, 4846–4853.
- [107] W. Hüchel, H. Bretschneider, *Chem. Ber.* **1937**, 103, 2024–2026.
- [108] S. Trofimenko, *J. Am. Chem. Soc.* **1970**, 69, 5118–5126.

- [109] S. Juliá, P. Sala, J. del Mazo, M. Sancho, C. Ochoa, J. Elguero, J.-P. Fayet, M.-C. Vertut, *J. Heterocycl. Chem.* **1982**, *19*, 1141–1145.
- [110] S. Juliá, J. M. del Mazo, L. Avila, J. Elguero, *Org. Prep. Proced. Int.* **1984**, *16*, 299–307.
- [111] D. L. Reger, T. C. Grattan, K. J. Brown, C. A. Little, J. J. S. Lamba, A. L. Rheingold, R. D. Sommer, *J. Organomet. Chem.* **2000**, *607*, 120–128.
- [112] A. Otero, J. Fernández-Baeza, A. Antiñolo, J. Tejeda, A. Lara-Sánchez, *Dalton Trans.* **2004**, 1499–1510.
- [113] P. K. Byers, A. J. Canty, R. T. Honeyman, *J. Organomet. Chem.* **1990**, *385*, 417–427.
- [114] L. K. Peterson, E. Kiehlmann, A. R. Sanger, K. I. Thé, *Can. J. Chem.* **1974**, *52*, 2367–2374.
- [115] T. C. Higgs, C. J. Carrano, *Inorg. Chem.* **1997**, *36*, 291–297.
- [116] J. Elflein, F. Platzmann, N. Burzlaff, *Eur. J. Inorg. Chem.* **2007**, 5173–5176.
- [117] A. Hoffmann, U. Flörke, M. Schürmann, S. Herres-Pawlis, *Eur. J. Org. Chem.* **2010**, 4136–4144.
- [118] P. Ballesteros, R. M. Claramunt, M. C. López, J. Elguero, G. Gómez-Alarcón, *Chem. Pharm. Bull.* **1988**, *36*, 2036–2041.
- [119] D. L. Reger, A. E. Pascui, M. D. Smith, *Eur. J. Inorg. Chem.* **2012**, 4593–4604.
- [120] D. L. Reger, R. Watson, M. D. Smith, *Inorg. Chem.* **2006**, *45*, 10077–10087.
- [121] D. L. Reger, R. P. Watson, J. R. Gardinier, M. D. Smith, P. J. Pellechia, *Inorg. Chem.* **2006**, *45*, 10088–10097.
- [122] D. L. Reger, E. A. Foley, R. P. Watson, P. J. Pellechia, M. D. Smith, F. Grandjean, G. J. Long, *Inorg. Chem.* **2009**, *48*, 10658–10669.
- [123] D. L. Reger, E. A. Foley, M. D. Smith, *Inorg. Chem.* **2010**, *49*, 234–242.
- [124] C. Pettinari, R. Pettinari, *Coord. Chem. Rev.* **2005**, *249*, 663–691.
- [125] A. Hoffmann, Poly(pyrazolyl)methanliganden in Der Koordinationschemie Der Späten 3d-Metalle Und in Der Bioanorganischen Chemie Und Katalyse, Dissertation and der Fakultät für Chemie der Technischen Universität Dortmund, **2011**.
- [126] J. L. Muñoz-Muñoz, F. Garcia-Molina, R. Varon, P. A. Garcia-Ruiz, J. Tudela, F. Garcia-Cánovas, J. N. Rodríguez-López, *IUBMB Life* **2010**, *62*, 539–547.
- [127] T. N. Sorrell, *Tetrahedron* **1989**, *45*, 3–68.

- [128] T. N. Sorrell, W. E. Allen, P. S. White, *Inorg. Chem.* **1995**, *34*, 952–960.
- [129] Y. Lee, G. Y. Park, H. R. Lucas, P. L. Vajda, K. Kamaraj, M. A. Vance, A. E. Milligan, J. S. Woertink, M. A. Siegler, A. A. Narducci Sarjeant, L. N. Zakharov, A. L. Rheingold, E. I. Solomon, K. D. Karlin, *Inorg. Chem.* **2009**, *48*, 11297–11309.
- [130] A. Arnold, C. Limberg, R. Metzinger, *Inorg. Chem.* **2012**, *51*, 12210–12217.
- [131] A. Arnold, R. Metzinger, C. Limberg, *Chem. Eur. J.* **2015**, *21*, 1198–1207.
- [132] K. P. Maresca, J. C. Marquis, S. M. Hillier, G. Lu, F. J. Femia, C. N. Zimmerman, W. C. Eckelman, J. L. Joyal, J. W. Babich, *Bioconjug. Chem.* **2010**, *21*, 1032–1042.
- [133] Y. Long, B. Cao, X. Xie, W. Wei, *Imidazopyridines as CXCR4 Antagonists and Their Preparation, Pharmaceutical Compositions and Use in the Treatment of Diseases*, **2012**, CN 102675305.
- [134] F. J. LaRonde, M. A. Brook, *Inorg. Chim. Acta* **1999**, *296*, 208–221.
- [135] M. J. Frisch, G. W. Trucks, G. E. Schlegel, G. E. Scuseria, M. A. Robb, J. R. Cheeseman, G. Scalmani, V. Barone, B. Mennucci, G. A. Petersson, H. Nakatsuji, M. Caricato, X. Li, P. Hratchian, A. F. Izmaylov, J. Bloino, G. Zheng, J. L. Sonnenberg, M. Hada, M. Ehara, K. Toyota, R. Fukuda, J. Hasegawa, M. Ishida, T. Nakajima, Y. Honda, O. Kitao, H. Nakai, T. Vreven, J. A. J. Montgomery, J. E. Peralta, F. Ogliaro, M. Bearpark, J. J. Heyd, E. Brothers, K. N. Kudin, V. N. Staroverov, T. Keith, R. Kobayashi, J. Normand, K. Raghavachari, A. Rendell, J. C. Burant, S. S. Iyengar, J. Tomasi, M. Cossi, N. Rega, J. M. Millam, M. Klene, J. E. Knox, J. B. Cross, V. Bakken, C. Adamo, J. Jaramillo, R. Gomperts, R. E. Stratmann, O. Yazyev, A. J. Austin, R. Cammi, C. Pomelli, J. W. Ochterski, R. L. Martin, K. Morokuma, V. G. Zakrzewski, G. A. Voth, P. Salvador, J. J. Dannenberg, S. Dapprich, A. D. Daniels, O. Farkas, J. B. Foresman, J. V. Ortiz, J. Cioslowski, D. J. Fox, *Gaussian09, Revision D.01*, Gaussian Inc., Wallingford CT, **2013**.
- [136] L. Yang, D. R. Powell, R. P. Houser, *Dalton Trans.* **2007**, 955–964.
- [137] A. Hoffmann, S. Herres-Pawlis, *Chem. Commun.* **2014**, *50*, 403–405.
- [138] A. W. Addison, T. Nageswara Rao, J. Reedijk, J. van Rijn, G. C. Verschoor, *J. Chem. Soc., Dalt. Trans.* **1984**, 1349–1356.
- [139] R. S. Himmelwright, N. C. Eickman, C. D. LuBien, K. Lerch, E. I. Solomon, *J. Am. Chem. Soc.* **1980**, *102*, 7339–7344.
- [140] K. Heirwegh, H. Borghinon, R. Lontie, *Biochim. Biophys. Acta* **1961**, *48*, 506–517.
- [141] *Calculated by A. Hoffmann*, **2014**.
- [142] E. D. Glendening, J. K. Badenhoop, A. E. Reed, J. E. Carpenter, J. A. Bohmann, C. M. Morales, C. R. Landis, F. Weinhold, *NBO 6.0*, Theoretical Chemistry Institute, University of Wisconsin: Madison, **2013**.

- [143] R. L. Martin, *J. Chem. Phys.* **2003**, *118*, 4775–4777.
- [144] C. Citek, C. T. Lyons, E. C. Wasinger, T. D. P. Stack, *Nat. Chem.* **2012**, *4*, 317–322.
- [145] *In Collaboration with the Work Group of Prof. Ivanović-Burmazović, Measured by M. Dürr*, Friedrich-Alexander-Universität Erlangen-Nürnberg, **2014**.
- [146] A. A. Hummer, A. Rompel, *Metallomics* **2013**, *5*, 597–614.
- [147] R. Stumm von Bordwehr, *Ann. Phys.* **1989**, *14*, 377.
- [148] *In Collaboration with Prof. M. Bauer*, Universität Paderborn, **2014**.
- [149] G. Bunker, *Introduction to XAFS. A Practical Guide to X-Ray Absorption Fine Structure Spectroscopy*, Cambridge University Press, Cambridge, **2010**.
- [150] K. C. C. Kharas, D.-J. Liu, H. J. Robota, *Catal. Today* **1995**, *26*, 129–145.
- [151] A. B. Ene, M. Bauer, T. Archipov, E. Roduner, *Phys. Chem. Chem. Phys.* **2010**, *12*, 3620–6531.
- [152] L.-S. Kau, D. J. Spira-Solomon, J. E. Penner-Hahn, K. O. Hodgson, E. I. Solomon, *J. Am. Chem. Soc.* **1987**, *109*, 6433–6442.
- [153] J. L. Dubois, P. Mukherjee, A. M. Collier, J. M. Mayer, E. I. Solomon, B. Hedman, T. D. P. Stack, K. O. Hodgson, *J. Am. Chem. Soc.* **1997**, *2*, 8578–8579.
- [154] G. Y. Park, M. F. Qayyum, J. Woertink, K. O. Hodgson, B. Hedman, A. A. Narducci Sarjeant, E. I. Solomon, K. D. Karlin, *J. Am. Chem. Soc.* **2012**, *134*, 8513–8524.
- [155] S. E. Allen, R. R. Walvoord, R. Padilla-Salinas, M. C. Kozlowski, *Chem. Rev.* **2013**, *113*, 6234–6458.
- [156] K. V. N. Esguerra, Y. Fall, L. Petitjean, J.-P. Lumb, *J. Am. Chem. Soc.* **2014**, *136*, 7662–7668.
- [157] J. E. Bulkowski, *Binucleating Ligand-Metal Complexes as Oxidation Catalysts*, **1985**, US4545937 A.
- [158] S. I. Bailey, I. M. Ritchie, Z. Hong-Guang, *Bioelectrochem. Bioenerg.* **1988**, *19*, 521–531.
- [159] H.-J. Teuber, S. Benz, *Chem. Ber.* **1967**, *100*, 2077–2092.
- [160] C. Wilfer, P. Liebhäuser, H. Erdmann, A. Hoffmann, S. Herres-Pawlis, *Eur. J. Inorg. Chem.* **2015**, 494–502.
- [161] S. Trofimenko, J. C. Calabrese, J. S. Thompson, *Inorg. Chem.* **1987**, *26*, 1507–1514.
- [162] A. Hoffmann, U. Flörke, S. Herres-Pawlis, *Eur. J. Inorg. Chem.* **2014**, 2296–2306.

- [163] F. Weinhold, C. Landis, *Valency and Bonding - A Natural Bond Orbital Donor-Acceptor Perspective*, Cambridge University Press, New York, **2005**.
- [164] E. D. Glendening, C. R. Landis, F. Weinhold, *J. Comput. Chem.* **2013**, *34*, 1429–1437.
- [165] G. M. Whitesides, B. Grzybowski, *Science (80-.)*. **2002**, *295*, 2418–2421.
- [166] A. Klug, *Angew. Chem. Int. Ed. Engl.* **1983**, *22*, 565–582.
- [167] D. Philp, J. F. Stoddart, *Angew. Chemie Int. Ed. English* **1996**, *35*, 1154–1196; *Angew. Chem.* **1996**, *108*, 1242–1286.
- [168] *Measured by A. Hoffmann*, **2014**.
- [169] R. L. Martin, *J. Chem. Phys.* **2003**, *118*, 4775–4777.
- [170] P. Liebhäuser, *Kinetik Der Sauerstoffaktivierung Und -Übertragung von N-Donorligandkupferkomplexen*, Masterarbeit an Der Fakultät Für Chemie Der Ludwig-Maximilians-Universität München, **2015**.
- [171] W. Macyk, A. Franke, G. Stochel, *Coord. Chem. Rev.* **2005**, *249*, 2437–2457.
- [172] *The Regional Transport of Ozone. New EPA Rulemaking on Nitrogen Oxide Emissions*, United States Environmental Protection Agency, **1998**.
- [173] N. F. Curtis, Y. M. Curtis, *Inorg. Chem.* **1965**, *4*, 804–809.
- [174] G. J. van Driel, W. L. Driessen, J. Reedijk, *Inorg. Chem.* **1985**, *24*, 2919–2925.
- [175] G. J. Kleywegt, W. G. R. Wiesmeijer, G. J. Van Driel, W. L. Driessen, J. Reedijk, J. H. Noordik, *J. Chem. Soc., Dalt. Trans.* **1985**, 2177–2184.
- [176] M. D. Lechner, Ed., *D'ans Lax Taschenbuch Für Chemiker Und Physiker*, Springer Verlag, Berlin, **1992**.
- [177] U. Förstermann, *Biol. Chem.* **2006**, *387*, 1521–1533.
- [178] U. Förstermann, I. Gath, P. Schwarz, E. I. Closs, H. Kleinert, *Biochem. Pharmacol.* **1995**, *50*, 1321–1332.
- [179] T. W. Hayton, P. Legzdins, W. B. Sharp, *Chem. Rev.* **2002**, *102*, 935–992.
- [180] K. G. Caulton, *Coord. Chem. Rev.* **1975**, *14*, 317–355.
- [181] J. M. Fletcher, I. L. Jenkins, F. M. Lever, F. S. Martin, A. R. Powell, R. Todd, *J. Inorg. Nucl. Chem.* **1955**, *1*, 378–401.
- [182] D. S. Pandey, U. C. Agarwala, *Inorg. Chim. Acta* **1989**, *159*, 197–200.

- [183] K. R. Laing, W. R. Roper, *J. Chem. Soc. A* **1970**, 1967–1971.
- [184] M. S. Askari, B. Girard, M. Murugesu, X. Ottenwaelde, *Chem. Commun. (Camb)*. **2011**, 47, 8055–8057.
- [185] P. L. Holland, *Dalton Trans.* **2010**, 39, 5415–5425.
- [186] M. J. Frisch, G. W. Trucks, G. E. Schlegel, G. E. Scuseria, M. A. Robb, J. R. Cheeseman, G. Scalmani, V. Barone, B. Mennucci, G. A. Petersson, H. Nakatsuji, M. Caricato, X. Li, P. Hratchian, A. F. Izmaylov, J. Bloino, G. Zheng, J. L. Sonnenberg, M. Hada, M. Ehara, K. Toyota, R. Fukuda, J. Hasegawa, M. Ishida, T. Nakajima, Y. Honda, O. Kitao, H. Nakai, T. Vreven, J. A. J. Montgomery, J. E. Peralta, F. Ogliaro, M. Bearpark, J. J. Heyd, E. Brothers, K. N. Kudin, V. N. Staroverov, T. Keith, R. Kobayashi, J. Normand, K. Raghavachari, A. Rendell, J. C. Burant, S. S. Iyengar, J. Tomasi, M. Cossi, N. Rega, J. M. Millam, M. Klene, J. E. Knox, J. B. Cross, V. Bakken, C. Adamo, J. Jaramillo, R. Gomperts, R. E. Stratmann, O. Yazyev, A. J. Austin, R. Cammi, C. Pomelli, J. W. Ochterski, R. L. Martin, K. Morokuma, V. G. Zakrzewski, G. A. Voth, P. Salvador, J. J. Dannenberg, S. Dapprich, A. D. Daniels, O. Farkas, J. B. Foresman, J. V. Ortiz, J. Cioslowski, D. J. Fox, *Gaussian09, Revision C.01*, Gaussian Inc., Wallingford CT, **2010**.
- [187] R. S. Srivastava, M. A. Khan, K. M. Nicholas, *J. Am. Chem. Soc.* **2005**, 127, 7278–7279.
- [188] R. S. Srivastava, N. R. Tarver, K. M. Nicholas, *J. Am. Chem. Soc.* **2007**, 129, 15250–15258.
- [189] A. Hoffmann, U. Flörke, S. Herres-Pawlis, *Inorg. Chem. Commun.* **2012**, 22, 154–157.
- [190] U. Herber, A. Hoffmann, C. Lochenie, B. Weber, S. Herres-Pawlis, *Z. Naturforsch. B* **2014**, 69b, 1206–1214.
- [191] D. L. Reger, J. E. Collins, D. L. Jameson, R. K. Castellano, *Inorg. Synth.* **1998**, 32, 63–65.
- [192] D. L. Jameson, R. K. Castellano, D. L. Reger, J. E. Collins, W. B. Tolman, C. J. Tokar, *Inorg. Synth.* **1998**, 32, 51–63.
- [193] D. L. Jameson, R. K. Castellano, *Inorg. Synth.* **1998**, 32, 51.
- [194] T. Astley, A. J. Canty, M. A. Hitchman, G. L. Rowbottom, B. W. Skelton, A. H. White, *J. Chem. Soc., Dalt. Trans.* **1991**, 1981–1990.
- [195] G. J. Kleywegt, W. G. R. Wiesmeijer, G. J. Van Driel, W. L. Driessen, J. Reedijk, J. H. Noordik, *J. Chem. Soc., Dalt. Trans.* **1985**, 2177–2184.
- [196] J. Leonhard, B. Lygo, G. Procter, *Praxis in Der Organischen Chemie*, VCH Verlagsgesellschaft, Weinheim, **1996**.
- [197] Z. Otwinowski, W. Minor, in *Int. Tables Crystallogr. Vol. F* (Ed.: M.G. Rossmann), Kluwer Academic Publishers, Dordrecht/Boston/London, **2001**, pp. 226–235.

- [198] Bruker, *SMART (Version 5.62), SAINT (Version 6.02), SHELXTL (Version 6.10), SADABS (Version 2.03)*, AXS Inc., Madison, Wisconsin, USA, **2002**.
- [199] Bruker, *XPREP*, Bruker AXS Inc., Madison, Wisconsin, USA, **2007**.
- [200] G. M. Sheldrick, *Acta Crystallogr., Sect. A* **1990**, *46*, 467–473.
- [201] C. B. Hübschle, G. M. Sheldrick, B. Dittrich, *J. Appl. Cryst.* **2011**, *44*, 1281–1284.
- [202] G. M. Sheldrick, *SHELXL*, University Of Göttingen, Göttingen, Germany, **1997**.
- [203] J. Tao, J. P. Perdew, V. N. Staroverov, G. E. Scuseria, *Phys. Rev. Lett.* **2003**, *91*, 146401–1 – 146401–4.
- [204] J. P. Perdew, *Phys. Rev. B* **1986**, *33*, 8822–8824.
- [205] A. D. Becke, *Phys. Rev. A* **1988**, *38*, 3098–3100.
- [206] A. D. Becke, *J. Chem. Phys.* **1993**, *98*, 5648–5652.
- [207] S. I. Gorelsky, *AOMix: Program for Molecular Orbital Analysis*, [Http://www.sg-chem.net/](http://www.sg-chem.net/), **1997**.
- [208] S. I. Gorelsky, S. Ghosh, E. I. Solomon, *J. Am. Chem. Soc.* **2006**, *128*, 278–290.
- [209] Y. Shi, A. M. Arif, R. D. Ernst, *Polyhedron* **2011**, *30*, 1899–1905.
- [210] G. Fries, J. Kirchhoff, G. Koehler, *Preparation of Pyrazoles by Treatment of 1,3-Dicarbonyl Compound Bisacetals with Hydrazines under Simultaneous Separation of Resulting Hydroxy Compound by Distillation and Chemical Reprocessing of the Organic Aqueous Phase.*, **2002**, DE 10057194C2.
- [211] L. Achremowicz, *Synth. Commun.* **1996**, *26*, 1681–1684.
- [212] H.-D. Hardt, *Z. Anorg. Allg. Chem.* **1959**, *301*, 87–96.
- [213] Y. Inada, Y. Nakano, M. Inamo, M. Nomura, S. Funahashi, *Inorg. Chem.* **2000**, *39*, 4793–4801.
- [214] A. Company, S. Palavicini, I. Garcia-Bosch, R. Mas-Ballesté, L. Que Jr., E. V Rybak-Akimova, L. Casella, X. Ribas, M. Costas, L. Que Jr, *Chem. Eur. J.* **2008**, *14*, 3535–3538.
- [215] S. E. Howson, L. E. N. Allan, N. P. Chmel, G. J. Clarkson, R. J. Deeth, A. D. Faulkner, D. H. Simpson, P. Scott, *Dalton Trans.* **2011**, *40*, 10416–10433.
- [216] A. L. Spek, *PLATON, A Multipurpose Crystallographic Tool*, Utrecht University, Utrecht, The Netherlands, **2008**.
- [217] A. L. Spek, *Acta Crystallogr., Sect. D Biol. Crystallogr.* **2009**, *65*, 148–155.

7 Appendix

Table 29. Crystallographic data collection and refinement information for L1 and C1.

	L1 (so035)	C1 (rv453)
Empirical formula	C ₁₉ H ₂₈ N ₆	C ₁₉ H ₂₈ Cl ₂ CuN ₆
Formula weight [g mol ⁻¹]	340.47	474.91
Crystal size [mm]	0.37 × 0.31 × 0.10	0.09 × 0.04 × 0.04
<i>T</i> [K]	173(2)	173(2)
Crystal system	triclinic	triclinic
Space group	<i>P</i> $\bar{1}$	<i>P</i> $\bar{1}$
<i>a</i> [Å]	6.3373(4)	7.6934(6)
<i>b</i> [Å]	10.2663(4)	8.0918(7)
<i>c</i> [Å]	14.8859(7)	18.1881(15)
α [°]	84.201(4)	89.787(2)
β [°]	87.172(4)	88.0722(2)
γ [°]	88.343(3)	84.734(2)
<i>V</i> [Å ³]	961.53(7)	1126.85(16)
<i>Z</i>	2	2
$\rho_{\text{calcd.}}$ [g cm ⁻³]	1.176	1.400
μ [mm ⁻¹]	0.074	1.223
λ [Å]	0.71073	0.71073
<i>F</i> (000)	368	494
<i>hkl</i> range	-6/7, -12/10, ± 18	± 9 , ± 10 , ± 22
Reflections collected	5216	20053
Independent reflections	3882	4623
<i>R</i> _{int.}	0.0149	0.0511
Reflections observed	3882	4623
Number of Parameters	233	260
<i>R</i> ₁ [$ I \geq 2\sigma(I)$]	0.0499	0.0460
<i>wR</i> ₂ (all data)	0.1350	0.1128
Goodness-of-fit	1.037	1.085
Largest diff. peak, hole [eÅ ⁻³]	-0.213, 0.229	-0.512, 0.882

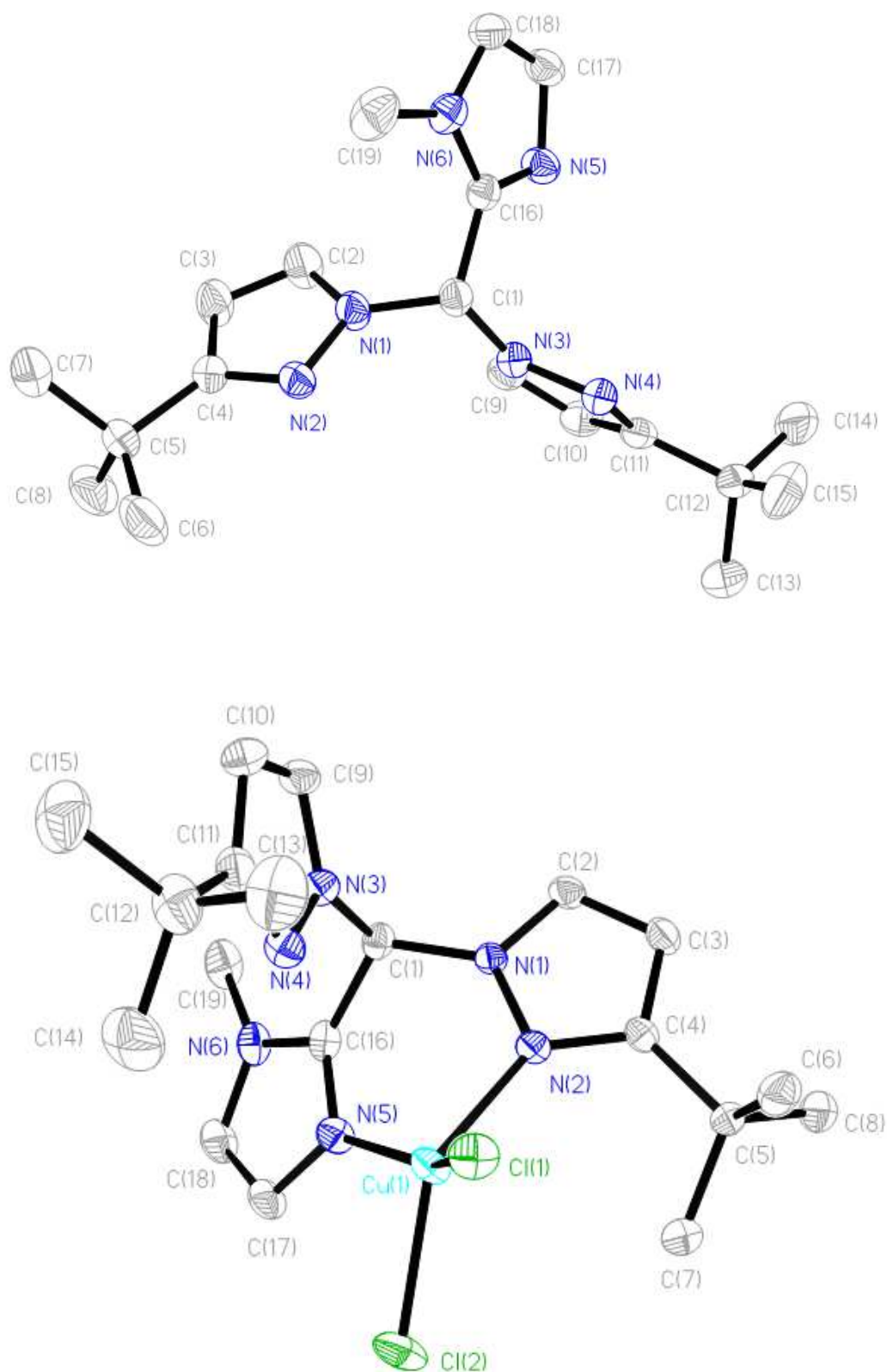


Figure 54. Molecular structure of $\text{HC}(3\text{-}t\text{BuPz})_2(1\text{-Melm})$ (L1, top) and $[\text{CuCl}_2\{\text{HC}(3\text{-}t\text{BuPz})_2(1\text{-Melm})\}]$ (C1, bottom). Thermal ellipsoids represent 50% particular probability.

Table 30. Crystallographic data collection and refinement information for C2 and C3.

	C2 (qn245)	C3 (qq075)
Empirical formula	C ₂₄ H ₂₉ ClCuN ₅	C ₂₀ H ₂₇ ClCuN ₅
Formula weight [g mol ⁻¹]	486.51	436.46
Crystal size [mm]	0.16 × 0.13 × 0.10	0.18 × 0.17 × 0.11
<i>T</i> [K]	200(2)	200(2)
Crystal system	orthorhombic	monoclinic
Space group	<i>Pnma</i>	<i>P2₁/c</i>
<i>a</i> [Å]	15.017(3)	15.9899(4)
<i>b</i> [Å]	15.970(3)	16.4751(4)
<i>c</i> [Å]	10.398(2)	16.5686(5)
α [°]	90	90
β [°]	90	94.819(2)
γ [°]	90	90
<i>V</i> [Å ³]	2493.7(8)	4349.3(2)
<i>Z</i>	4	8
$\rho_{\text{calcd.}}$ [g cm ⁻³]	1.296	1.333
μ [mm ⁻¹]	1.003	1.141
λ [Å]	0.71073	0.71073
<i>F</i> (000)	1016	1824
<i>hkl</i> range	±18, ±19, −11/12	±19, ±19, −19/20
Reflections collected	15160	38340
Independent reflections	2403	8081
<i>R</i> _{int.}	0.0412	0.0400
Reflections observed	2403	8081
Number of Parameters	163	499
<i>R</i> ₁ [<i>I</i> ≥ 2σ(<i>I</i>)]	0.0318	0.0358
<i>wR</i> ₂ (all data)	0.0851	0.0916
Goodness-of-fit	1.083	1.080
Largest diff. peak, hole [eÅ ⁻³]	−0.302, 0.269	−0.443, 0.479

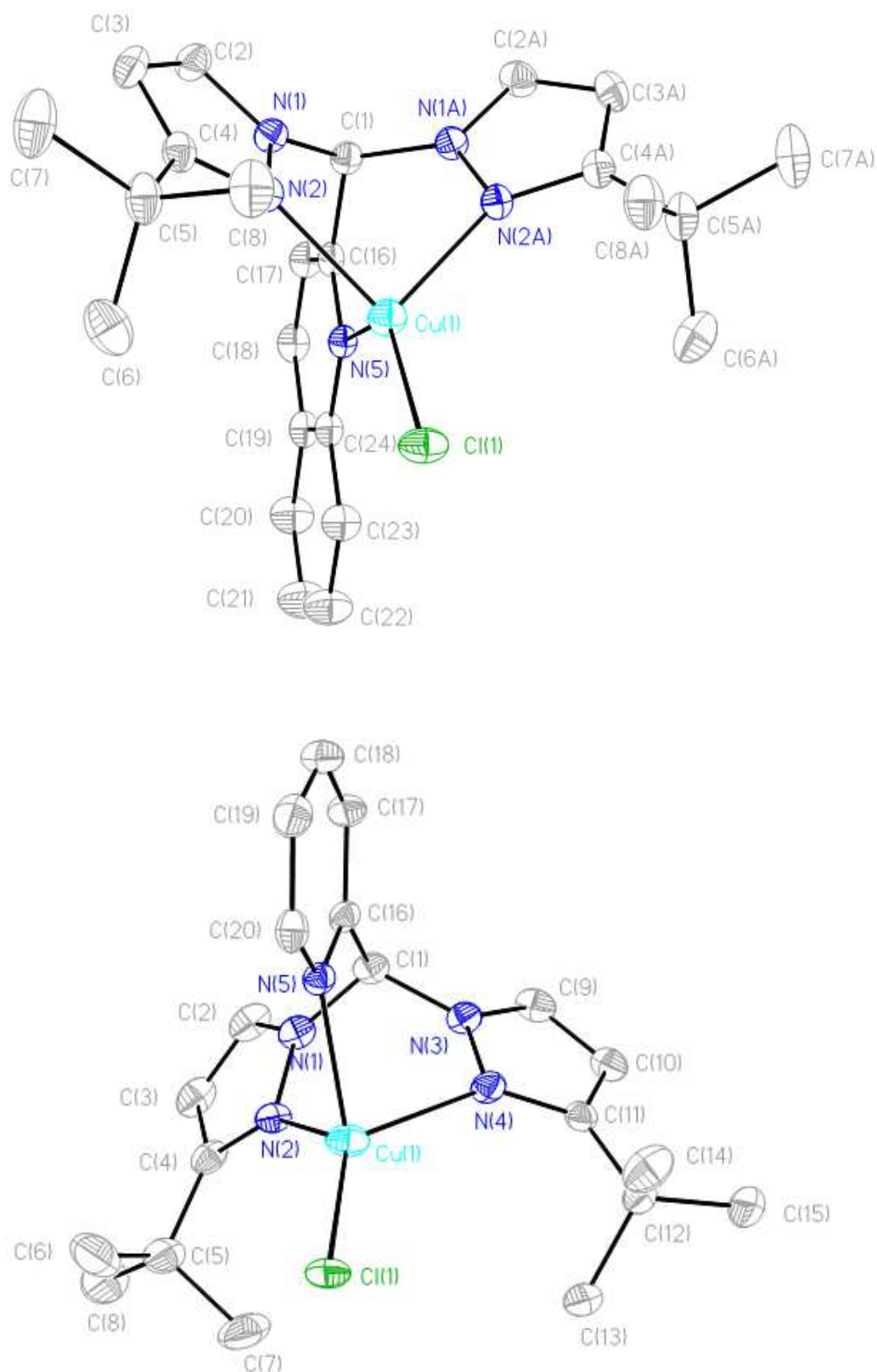


Figure 55. Molecular structure of $[\text{CuCl}\{\text{HC}(3\text{-}t\text{BuPz})_2(\text{Qu})\}]$ (C2, top) and $[\text{CuCl}\{\text{HC}(3\text{-}t\text{BuPz})_2(\text{Py})\}]$ (C3, bottom). Thermal ellipsoids represent 50% particular probability.

Table 31. Crystallographic data collection and refinement information for C4 and C5.

	C4 (rv360)	C5 (qq032)
Empirical formula	C ₂₀ H ₂₇ Br ₂ CuN ₅	C ₂₀ H ₂₇ CoN ₇ O ₆
Formula weight [g mol ⁻¹]	560.83	520.42
Crystal size [mm]	0.17 × 0.11 × 0.09	0.210 × 0.19 × 0.087
<i>T</i> [K]	173(2)	200(2)
Crystal system	monoclinic	monoclinic
Space group	<i>P</i> 2 ₁ / <i>c</i>	<i>P</i> 2 ₁ / <i>c</i>
<i>a</i> [Å]	8.0820(6)	15.6689(4)
<i>b</i> [Å]	17.3088(14)	9.7832(2)
<i>c</i> [Å]	32.561(2)	17.8367(4)
α [°]	90	90
β [°]	91.680(2)	95.4430(10)
γ [°]	90	90
<i>V</i> [Å ³]	4553.0(6)	2721.89(11)
<i>Z</i>	8	4
$\rho_{\text{calcd.}}$ [g cm ⁻³]	1.636	1.270
μ [mm ⁻¹]	4.485	0.674
λ [Å]	0.71073	0.71073
<i>F</i> (000)	2248	1084
<i>hkl</i> range	±10, ±21, −36/40	±18, ±11, ±21
Reflections collected	50615	42299
Independent reflections	9286	5058
<i>R</i> _{int.}	0.0327	0.0393
Reflections observed	9286	5058
Number of Parameters	517	313
<i>R</i> ₁ [<i>I</i> ≥ 2σ(<i>I</i>)]	0.0776	0.0348
<i>wR</i> ₂ (all data)	0.1794	0.0896
Goodness-of-fit	1.262	1.061
Largest diff. peak, hole [eÅ ⁻³]	−0.851, 2.053	−0.222, 0.360

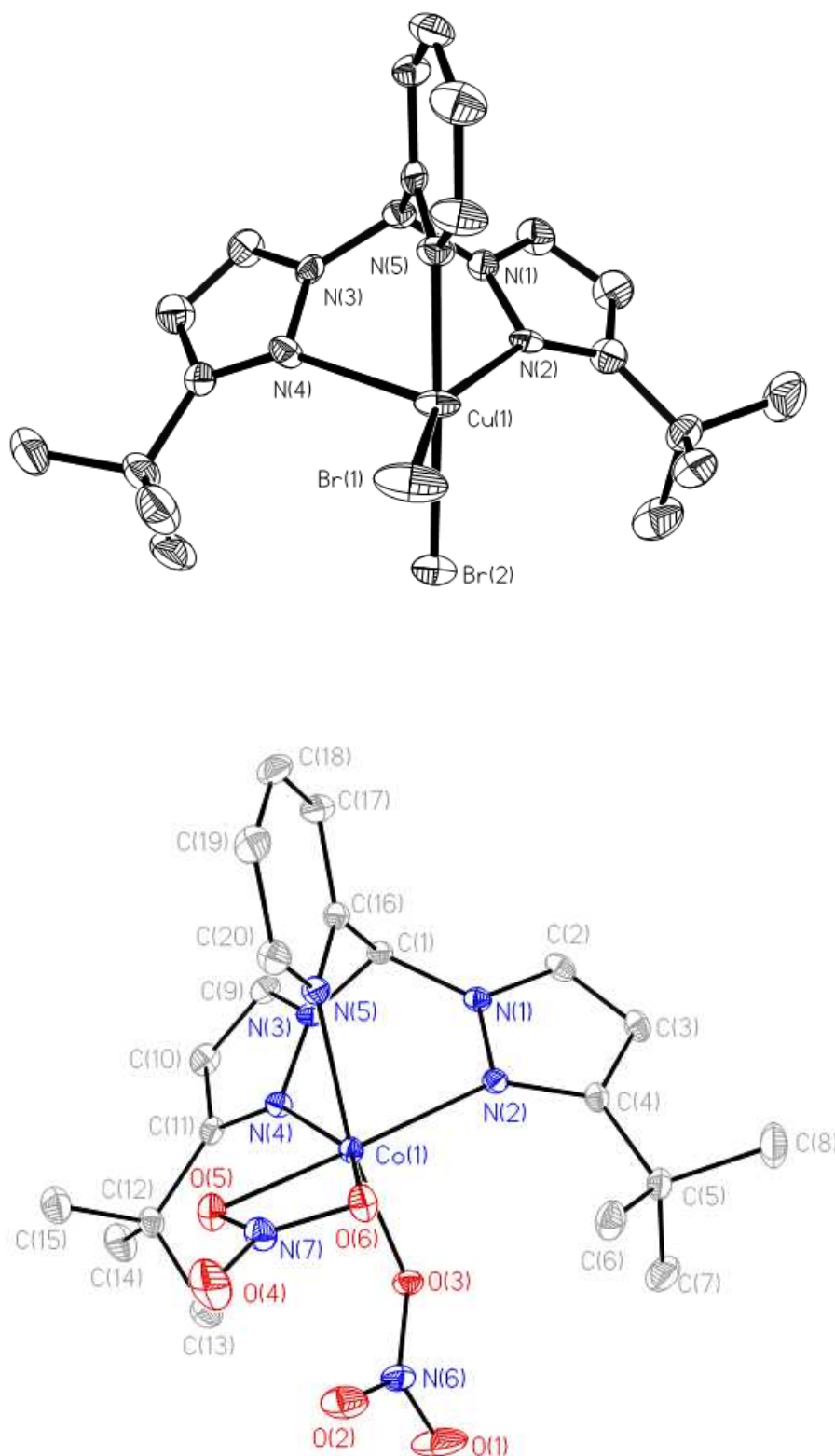


Figure 56. Molecular structure of $[\text{CuBr}_2\{\text{HC}(3\text{-tBuPz})_2(\text{Py})\}]$ (C4, top) and $[\text{Co}(\text{NO}_3\text{-}\kappa^2\text{OO}')\{\text{HC}(3\text{-tBuPz})_2(\text{Py})\}]\cdot\text{CH}_2\text{Cl}_2$ (C5, bottom). In C5 it was not possible to model the disordered solvent molecules of CH_2Cl_2 in an adequate manner, so the data set was treated with the SQUEEZE facility of PLATON.^[216,217] Thermal ellipsoids represent 50% particular probability.

Table 32. Crystallographic data collection and refinement information for C6 and C7.

	C6 (qq060)	C7 (rq005)
Empirical formula	C ₃₉ H ₅₂ Co ₂ N ₁₄ O ₁₃	C ₁₈ H ₂₃ N ₇ O ₆ Zn
Formula weight [gmol ⁻¹]	1042.81	498.80
Crystal size [mm]	0.12 × 0.09 × 0.05	0.09 × 0.08 × 0.08
<i>T</i> [K]	200(2)	173(2)
Crystal system	triclinic	triclinic
Space group	<i>P</i> $\bar{1}$	<i>P</i> $\bar{1}$
<i>a</i> [Å]	9.2772(5)	9.1885(3)
<i>b</i> [Å]	9.4075(6)	9.5114(3)
<i>c</i> [Å]	15.9758(9)	14.6006(5)
α [°]	90.453(4)	78.654(2)
β [°]	96.796(3)	77.695(2)
γ [°]	118.972(3)	61.603(2)
<i>V</i> [Å ³]	1207.81(12)	1089.93(6)
<i>Z</i>	1	2
$\rho_{\text{calcd.}}$ [gcm ⁻³]	1.434	1.520
μ [mm ⁻¹]	0.762	1.177
λ [Å]	0.71073	0.71073
<i>F</i> (000)	542	516
<i>hkl</i> range	-11/10, ± 11 , -18/19	± 11 , ± 12 , ± 18
Reflections collected	11617	21065
Independent reflections	4210	4967
<i>R</i> _{int.}	0.0421	0.0484
Reflections observed	4210	4967
Number of Parameters	329	293
<i>R</i> ₁ [$ I \geq 2\sigma(I)$]	0.0610	0.0339
<i>wR</i> ₂ (all data)	0.1549	0.0732
Goodness-of-fit	1.036	1.036
Largest diff. peak, hole [eÅ ⁻³]	-0.445, 2.755*	-0.411, 0.523

* The rest electron density is located 2.5 Å from C11.

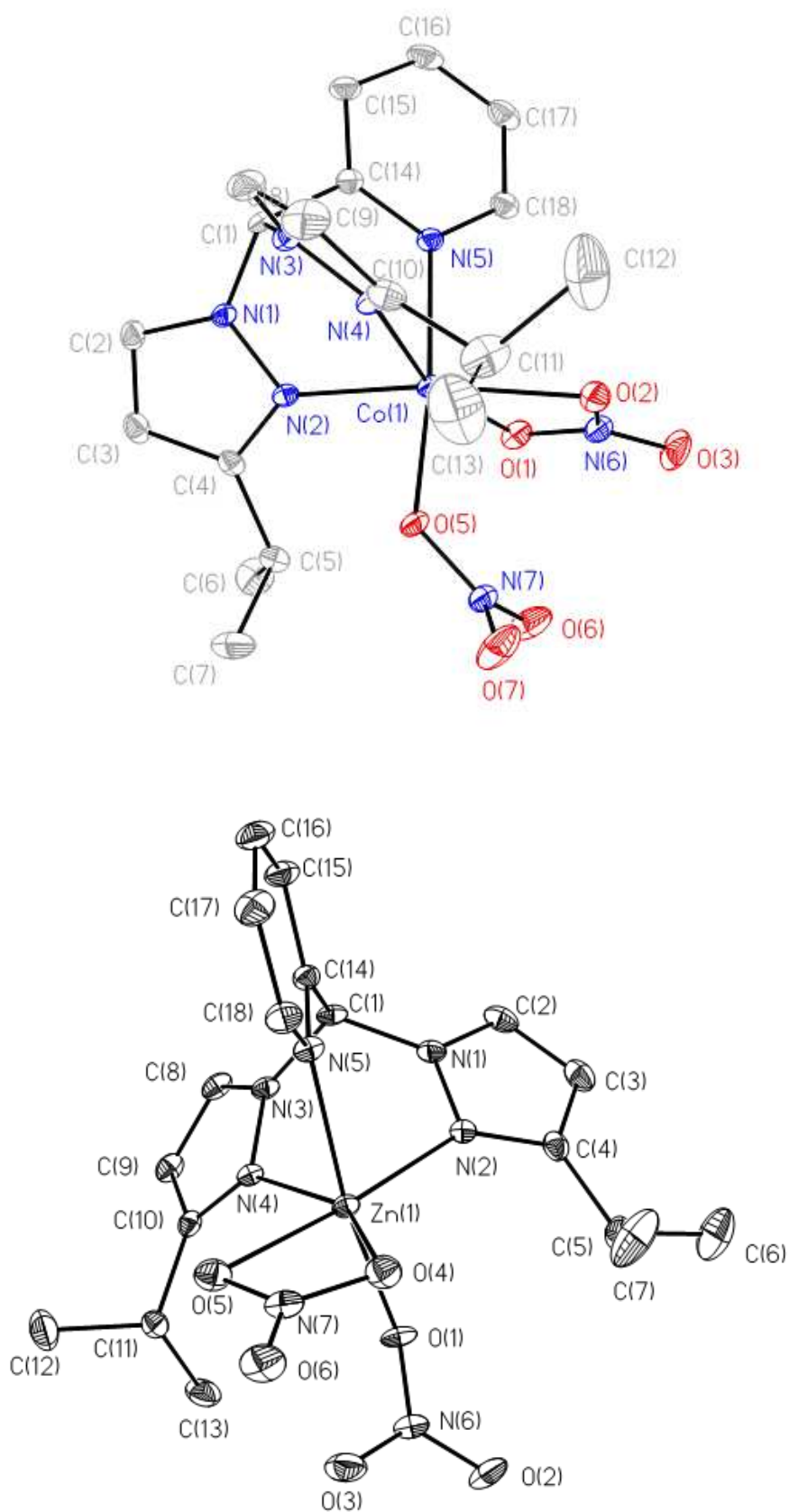


Figure 57. Molecular structure of $[\text{Co}(\text{NO}_3\text{-}\kappa\text{O})(\text{NO}_3\text{-}\kappa^2\text{OO}')\{\text{HC}(3\text{-}i\text{PrPz})_2(\text{Py})\}]$ (C6, top) and $[\text{Zn}(\text{NO}_3\text{-}\kappa\text{O})(\text{NO}_3\text{-}\kappa^2\text{OO}')\{\text{HC}(3\text{-}i\text{PrPz})_2(\text{Py})\}]$ (C7, bottom). Thermal ellipsoids represent 50% particular probability.

Table 33. Crystallographic data collection and refinement information for L2 and L3'.

	L2 (qo110)	L3' (qo117)
Empirical formula	C _{71.94} H _{78.90} N ₁₅	C ₁₈ H ₂₃ N ₅
Formula weight [g mol ⁻¹]	1153.68	309.41
Crystal size [mm]	0.42 × 0.15 × 0.07	0.40 × 0.24 × 0.16
<i>T</i> [K]	173(2)	293(2)
Crystal system	triclinic	triclinic
Space group	<i>P</i> $\bar{1}$	<i>P</i> $\bar{1}$
<i>a</i> [Å]	10.8373(10)	11.2219(11)
<i>b</i> [Å]	16.4284(15)	12.1606(13)
<i>c</i> [Å]	20.0020(19)	13.9505(13)
α [°]	75.454(8)	77.982(9)
β [°]	85.936(8)	73.924(8)
γ [°]	80.012(8)	74.881(9)
<i>V</i> [Å ³]	3393.4(5)	1746.9(3)
<i>Z</i>	2	4
$\rho_{\text{calcd.}}$ [g cm ⁻³]	1.129	1.176
μ [mm ⁻¹]	0.069	0.073
λ [Å]	0.71073	0.71073
<i>F</i> (000)	1231	664
<i>hkl</i> range	-13/5, -19/18, -24/23	-12/13, \pm 14, -16/14
Reflections collected	17601	9083
Independent reflections	12248	6454
<i>R</i> _{int.}	0.0678	0.0362
Reflections observed	12248	6454
Number of Parameters	824	423
<i>R</i> ₁ [$ I \geq 2\sigma(I)$]	0.0911	0.0574
<i>wR</i> ₂ (all data)	0.2724	0.1605
Goodness-of-fit	0.989	1.131
Largest diff. peak, hole [eÅ ⁻³]	-0.360, 0.351	-0.346, 0.199

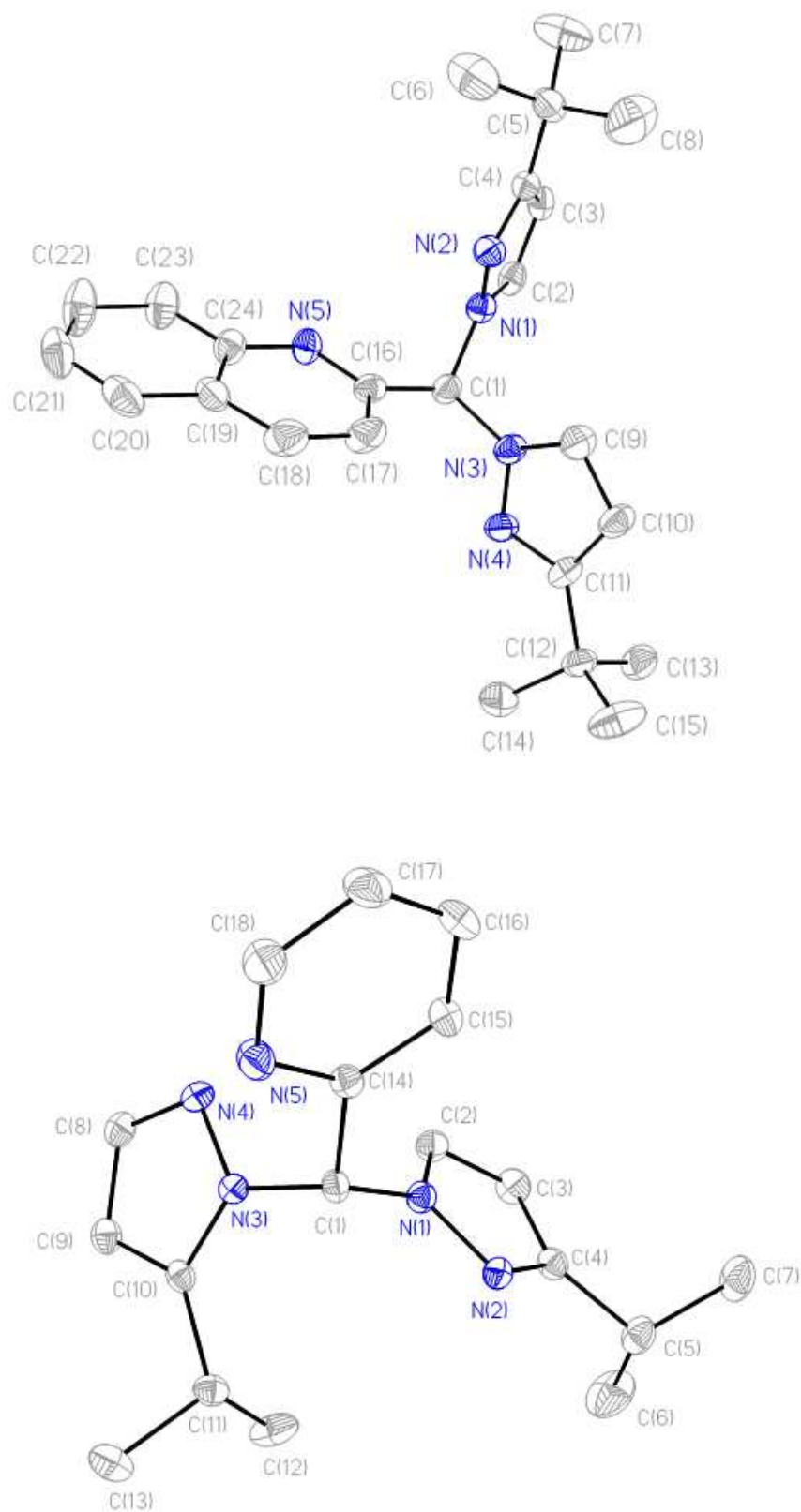


Figure 58. Molecular structure of $\text{HC}(3\text{-}t\text{BuPz})_2(\text{Qu})$ (L2, top) and of $\text{HC}(3\text{-}i\text{PrPz})(5\text{-}i\text{PrPz})(\text{Qu})$ (L3', bottom). In L2 three molecules are present, two of which have one threefold disordered *t*Bu-group each. Refinement of those was not possible due to the minor quality of the data set.

Thermal ellipsoids represent 50% particular probability.

Table 34. Crystallographic data collection and refinement information for C8 and C9.

	C8 (qv083)	C9 (qq074)
Empirical formula	$\text{C}_{30}\text{H}_{34}\text{Co}_2\text{N}_{14}\text{O}_{14}$	$\text{C}_{34}\text{H}_{26}\text{CoF}_6\text{N}_{10}\text{O}_6\text{S}_2$
Formula weight [g mol^{-1}]	932.57	907.70
Crystal size [mm]	$0.13 \times 0.10 \times 0.07$	$0.24 \times 0.10 \times 0.08$
T [K]	100(2)	200(2)
Crystal system	monoclinic	monoclinic
Space group	$C2/c$	$P2_1/c$
a [Å]	15.4948(7)	10.7845(3)
b [Å]	14.3870(7)	8.0116(2)
c [Å]	18.9064(9)	22.4651(7)
α [°]	90	90
β [°]	109.813(2)	101.7930(10)
γ [°]	90	90
V [Å ³]	3965.2(3)	1900.04(9)
Z	4	2
$\rho_{\text{calcd.}}$ [g cm^{-3}]	1.562	1.587
μ [mm^{-1}]	0.920	0.651
λ [Å]	0.71073	0.71073
$F(000)$	1912	922
hkl range	$\pm 18, \pm 17, \pm 22$	$\pm 13, \pm 9, \pm 27$
Reflections collected	28344	15280
Independent reflections	3692	3529
$R_{\text{int.}}$	0.0355	0.0311
Reflections observed	3692	3529
Number of Parameters	264	268
R_1 [$ I \geq 2\sigma(I)$]	0.0467	0.0321
wR_2 (all data)	0.1061	0.0843
Goodness-of-fit	1.076	1.045
Largest diff. peak, hole [e Å^{-3}]	-0.451, 0.511	-0.290, 0.367

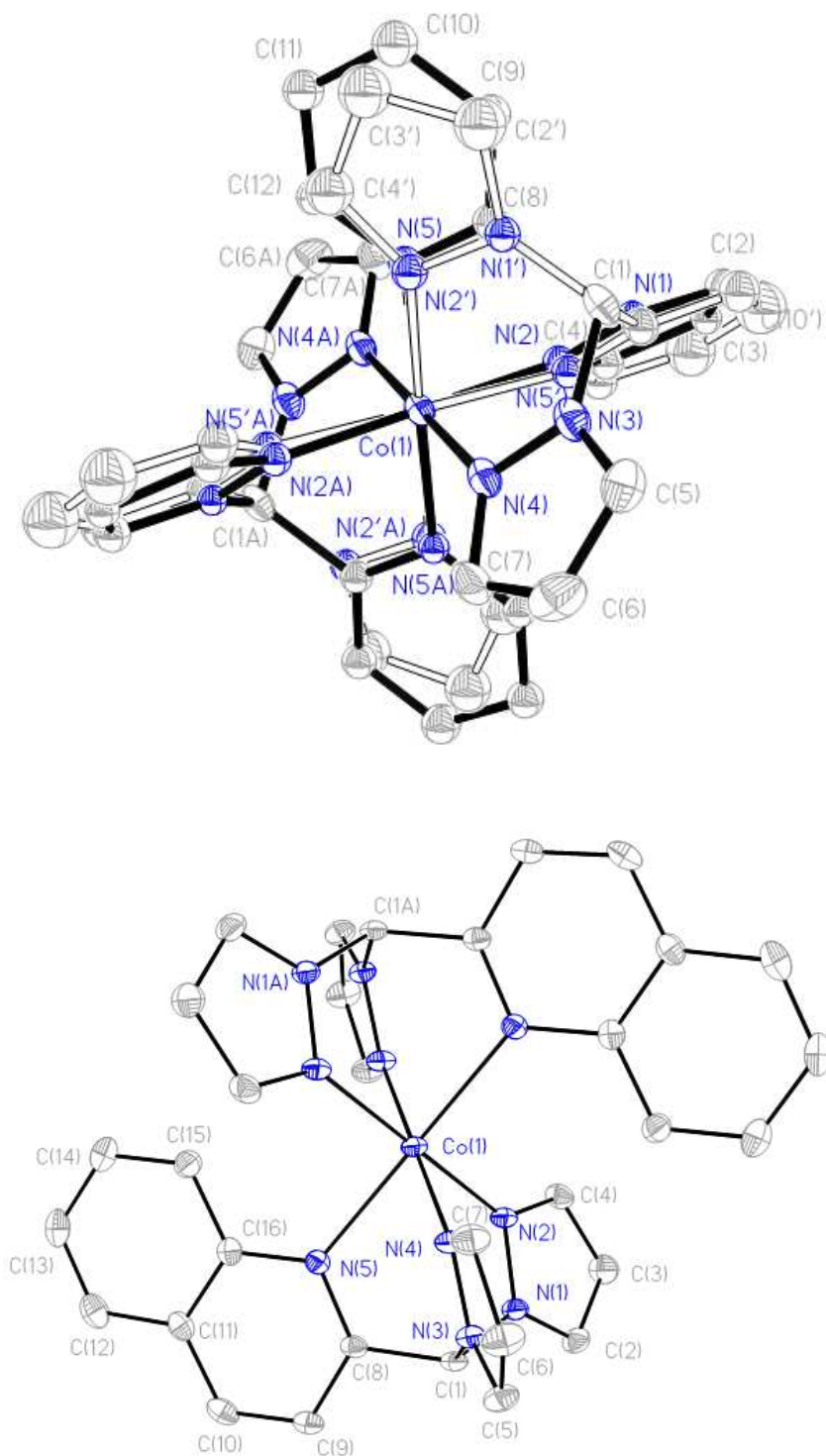


Figure 59. Molecular structure of $[\text{Co}\{\text{HC}(\text{Pz})_2(\text{Py})\}_2][\text{Co}(\text{NO}_3)_4] \cdot \text{C}_3\text{H}_6\text{O}$ (C8, top) and of $[\text{Co}\{\text{HC}(\text{Pz})_2(\text{Qu})\}_2][(\text{OTf})_2]$ (C9, bottom). In C8 it was not possible to model the disordered solvent molecules of acetone in an adequate manner, the data set was treated with the SQUEEZE facility of PLATON.^[216,217] Thermal ellipsoids represent 50% particular probability.

Table 35. Crystallographic data collection and refinement information for C10 and C11.

	C10 (ro029)	C11 (qo119)
Empirical formula	C ₄₆ H ₅₈ CoN ₁₂ O ₈	C ₂₄ H ₃₅ Cl ₂ CoN ₅ O
Formula weight [gmol ⁻¹]	965.97	539.40
Crystal size [mm]	0.30 × 0.25 × 0.10	0.40 × 0.12 × 0.02
<i>T</i> [K]	100(2)	173(2)
Crystal system	monoclinic	monoclinic
Space group	<i>P</i> 2 ₁ / <i>c</i>	<i>P</i> 2 ₁ / <i>c</i>
<i>a</i> [Å]	10.5869(6)	21.5887(18)
<i>b</i> [Å]	12.0375(7)	8.2140(5)
<i>c</i> [Å]	18.5244(10)	15.8355(11)
α [°]	90	90
β [°]	101.362(5)	107.000(8)
γ [°]	90	90
<i>V</i> [Å ³]	2314.5(2)	2685.4(3)
<i>Z</i>	2	4
$\rho_{\text{calcd.}}$ [gcm ⁻³]	1.386	1.334
μ [mm ⁻¹]	0.438	0.863
λ [Å]	0.71073	0.71073
<i>F</i> (000)	1018	1132
<i>hkl</i> range	-10/13, -15/12, -21/13	-23/26, -9/8, ± 19
Reflections collected	13391	13797
Independent reflections	4703	4965
<i>R</i> _{int.}	0.0304	0.0431
Reflections observed	4703	4965
Number of Parameters	310	304
<i>R</i> ₁ [<i>I</i> ≥ 2σ(<i>I</i>)]	0.0336	0.0500
<i>wR</i> ₂ (all data)	0.0826	0.1212
Goodness-of-fit	1.052	1.100
Largest diff. peak, hole [eÅ ⁻³]	-0.341, 0.293	-0.590, 0.614

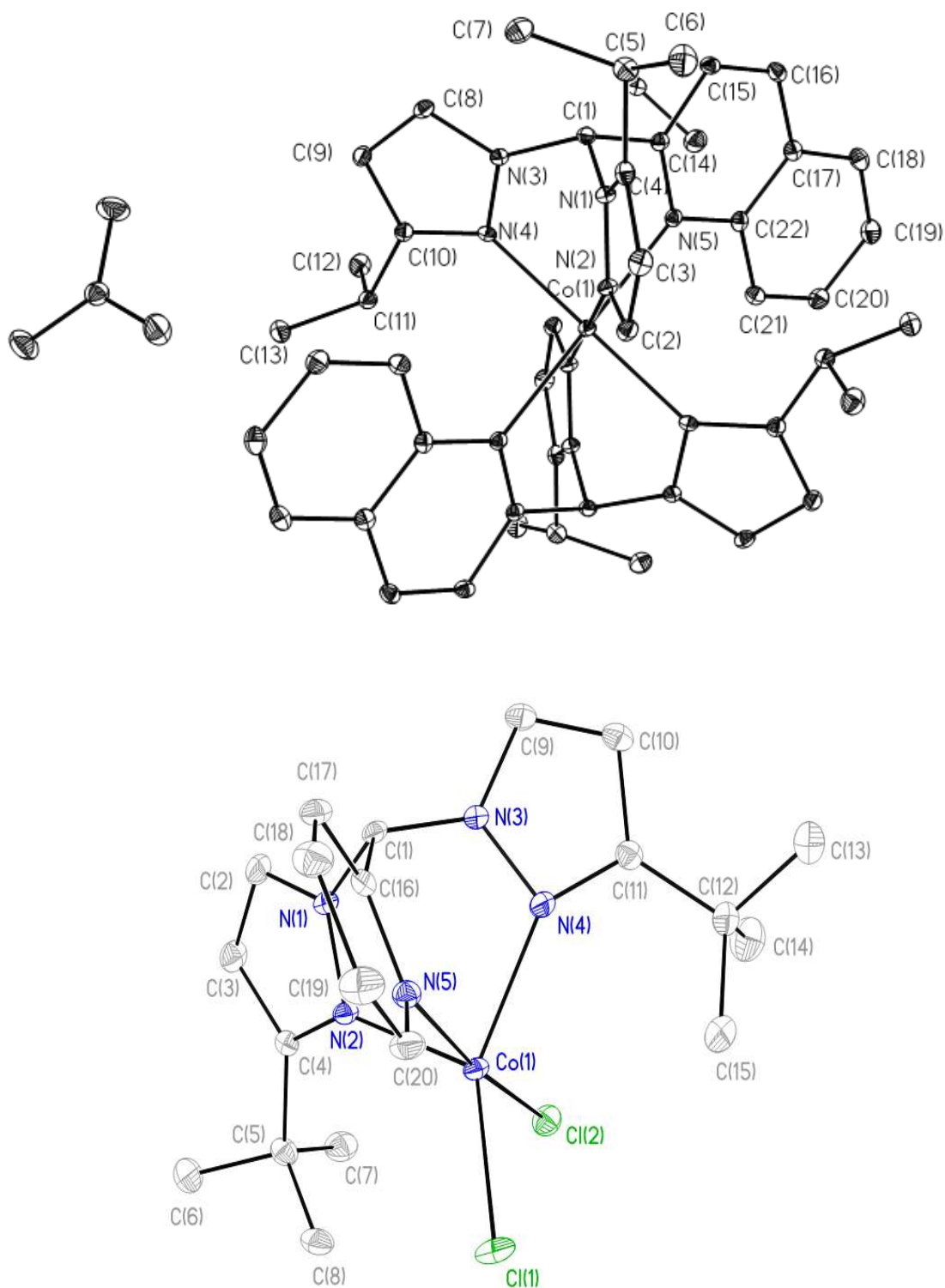


Figure 60. Molecular structure of $[\text{Co}\{\text{HC}(i\text{PrPz})_2(\text{Qu})\}_2][(\text{NO}_3)_2] \cdot 2\text{MeOH}$ (C10, top) and of $[\text{CoCl}_2\{\text{HC}(\text{Pz})_2(\text{Py})\}] \cdot \text{THF}$ (C11, bottom). Thermal ellipsoids represent 50% particular probability.

Overview of Ligands and Complexes

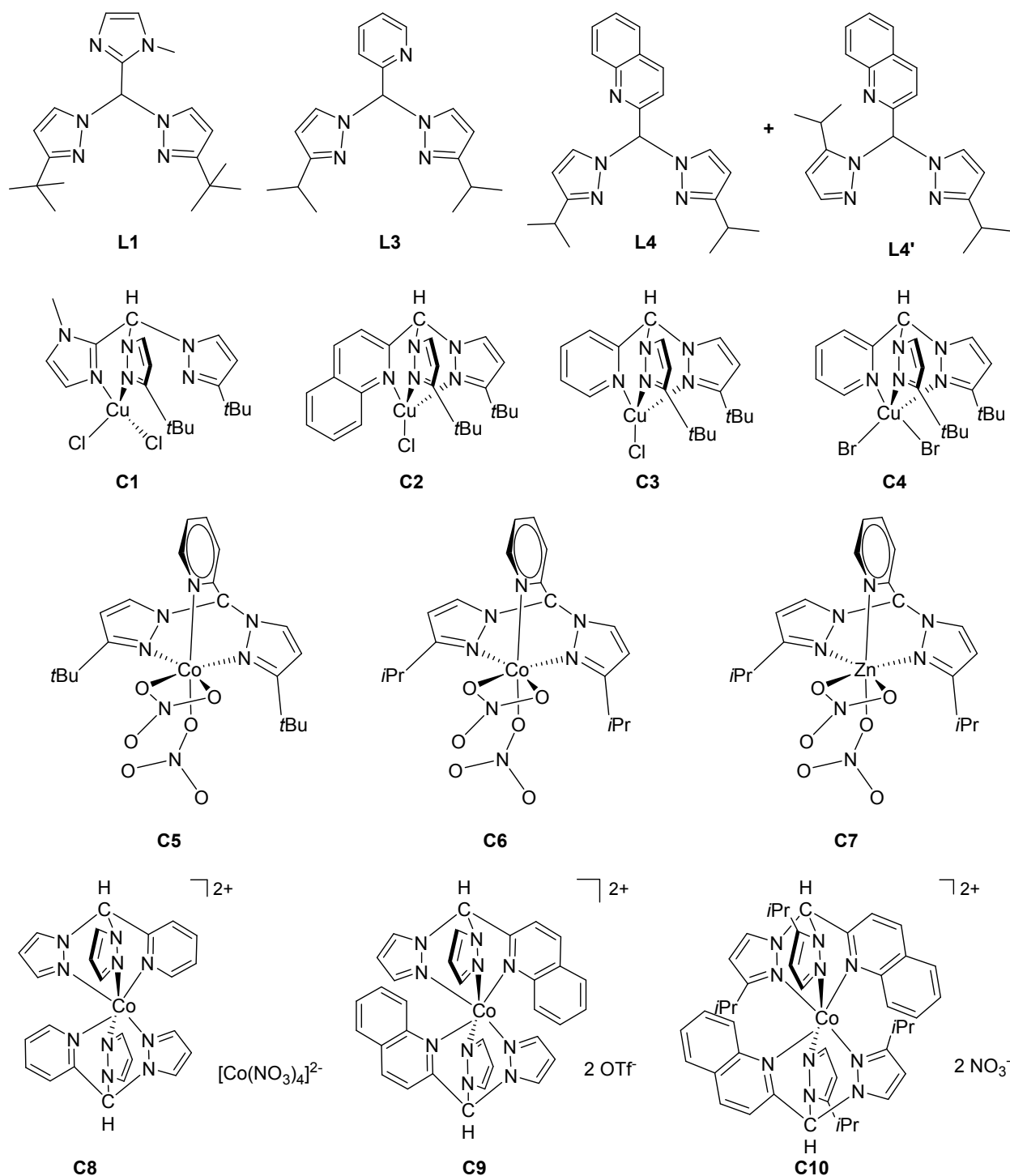


Figure 61. Overview of all newly synthesised bis(pyrazolyl)methane ligands and transition metal bis(pyrazolyl)methane complexes.

Publications

Biomimetic Hydroxylation Catalysis Through Self-Assembly of a Bis(pyrazolyl)methane Copper-Peroxo Complex

C. Wilfer, P. Liebhäuser, H. Erdmann, A. Hoffmann, S. Herres-Pawlis, *Eur. J. Inorg. Chem.* **2015**, 494–502.

Efficient biomimetic hydroxylation catalysis with a bis(pyrazolyl)-imidazolylmethane copper-peroxide complex

C. Wilfer, P. Liebhäuser, A. Hoffmann, H. Erdmann, O. Grossmann, R. Schepper, R. Dick, M. Bauer, M. Dürr, I. Ivanović-Burmazović, S. Herres-Pawlis, *Chem. Eur. J.* **2015**, manuscript in preparation.

Bis(pyrazolyl)methane transition metal nitrato complexes: a donor study

C. Wilfer, D. Ziegler, A. Hoffmann, S. Herres-Pawlis, *Z. Anorg. Allg. Chem.* **2015**, manuscript in preparation.

Contribution to conferences

2014

Presentations:

5th EuCheMS Chemistry Congress in Istanbul

C. Wilfer, H. Erdmann, O. Grossmann, A. Hoffmann, S. Herres-Pawlis, „Hydroxylation of phenols using tyrosinase models“

Koordinationschemie Tagung in Kaiserslautern

C. Wilfer, H. Erdmann, O. Grossmann, A. Hoffmann, S. Herres-Pawlis, „Bis(pyrazolyl)methan-Kupferkomplexe als Precursor für die Aktivierung von Sauerstoff“

Posters:

5th EuCheMS Chemistry Congress in Istanbul

C. Wilfer, A. Hoffmann, S. Herres-Pawlis, „Bis(pyrazolyl)methanes as ligands for transition metal nitrate complexes

Agichem (Anglo German Inorganic Chemistry) 9th International Conference on Inorganic Chemistry in Edinburgh

C. Wilfer, H. Erdmann, O. Grossmann, A. Hoffmann, S. Herres-Pawlis, „Towards a more efficient phenol hydroxylation using tyrosinase models“

2013

Posters:

MRIC (Medicinal Redox Inorganic Chemistry) Konferenz in Erlangen

C. Wilfer, P. Liebhäuser, R. Rahimoff, A. Hoffmann, S. Herres-Pawlis, „Bis(pyrazolyl)methane-copper complexes as precursors for the activation of oxygen and NO“

Bioanorganisches Symposium an der LMU München

C. Wilfer, P. Liebhäuser, R. Rahimoff, A. Hoffmann, S. Herres-Pawlis, „Bis(pyrazolyl)methane-copper complexes as precursors for the activation of oxygen and NO“

Koordinationschemie Tagung in Bayreuth

C. Wilfer, D. Ziegler, P. Liebhäuser, A. Hoffmann, S. Herres-Pawlis, „Bis(pyrazolyl)methane als Liganden für Komplexe mit Cobalt und Kupfer“

2012

Poster:

16. Vortragstagung der Wöhler-Vereinigung in Göttingen

C. Wilfer, C. Sondermann, A. Metz, A. Hoffmann, S. Herres-Pawlis, „Bis(pyrazolyl)methane als Liganden für Komplexe mit Metallen der ersten Übergangsmetallreihe“